# A VIRTUAL TEST BED FOR PEBB-BASED SHIP POWER SYSTEMS

## ANNUAL TECHNICAL REPORT

Report # VTB9706001
*June 1997*

DISTRIBUTION STATEMENT A
Approved for public release
Distribution Unlimited

**Submitted**

**by**

Roger Dougal, *Project Director*
on behalf of the project team

**ONR Grant N00014-96-1-0926**

Volume III

19970714 119

**University of South Carolina**
Dept. of Electrical and Computer Engineering
Columbia, SC 29208

# PUBLICATIONS INDEX

Volume III

"A time domain model for flicker analysis", A.P. Sakis Meliopoulos and G. J. Cokkinides, IPST '97, October 1997.

"Wavelet-based transient analysis", A.P. Sakis Meliopoulos and Chien-Hsing Lee, 29th North American Power Symposium, Oct 13-14, 1997.

"An efficient and accurate method of incorporating magnetic saturation in the physical-variable models of synchronous machines" S. D. Pekarek and E.A. Walters,

"A fast and efficient multi-rate technique for detailed simulation of AC/DC power systems", S. D. Pekarek, O. Wasynczuk, H.J. Hegner,

"Digital tracking control for PWM systems with unacceptable zeros", M. Al-Numay and D. Taylor, submitted to IEEE Trans. on Circuits and Systems - special issue on Simulation, Theory, and Design of Switched-analog Networks.

"Adaptive control of DC motor drives with converter nonlinearities" W. Khan and D. Taylor, submitted to Intern. Journal of Control

"Adaptive control of DC motor drives with inverter nonlinearities" W. Khan and D. Taylor, submitted to Intern. Journal of Control

"Modeling and control of digital PWM systems using averaging" M. Al-Numay and D. Taylor, submitted to IEEE Trans. on Control Systems Technology

"Polymer current limiters for low-voltage power distribution systems", M. H. McKinney, C.W. Brice, and R.A. Dougal, IEEE Conf on Industrial and Commercial Power Systems, May 1997, Philadelphia, PA.

"Global Asymptotic stability of indirect field-oriented speed control of induction motors", L. Gokdere, M. A. Simaan, and C. W. Brice, submitted to Automatica

"A passivity-based controller for saturated induction motors" L. Gokdere, M. A. Simaan, and C. W. Brice, submitted to IEEE Trans on Control Sys Tech

"Incorporation of magnetic saturation effects into passivity-based control of induction motors", L. Gokdere, M. A. Simaan, and C. W. Brice, submitted to IEEE Trans. on Industrial Electronics

"A comparison of passivity-based and input-output linearization controllers for induction motors" L. Gokdere, M. A. Simaan, and C. W. Brice, accepted for presentation at IEEE Emerging Technologies and Factory Automation Conf., Sept. 9-12, 1997, Los Angeles, CA.

"Speed estimators for indirect field-oriented control of induction motors" L. Gokdere, M.A. Simaan, and C.W. Brice, accepted for IEEE Emerging Tech and Factory Automation Conf., Sept. 9-12, 1997, Los Angeles, CA.

"A passivity-based controller for high-performance motion control of induction motors", L. Gokdere, M. A. Simaan, and C. W. Brice, accepted for presentation at IEEE Power Electronics Specialists Conf, June 22-2- St. Louis, MO.

# A Time Domain Model for Flicker Analysis

A. P. Sakis Meliopoulos, Fellow

Georgia Institute of Technology
School of Electrical and Computer Engineering
Atlanta, GA 30332-0250

George J. Cokkinides

University of South Carolina
Department of Electrical and Computer
Engineering
Columbia, SC 29208

**Abstract** This paper presents a time domain model of an electric power system for the purpose of studying voltage magnitude variations due to the operation of an arc furnace. The time domain model of the arc consists of the nonlinear characteristics of the arc and the associated absorbed energy. The rms value of the voltage can be computed anywhere in the system. The voltage variation is compared to flicker threshold values as defined in standards. Typical results in a test system are presented in the paper.

## 1. Introduction

Operation of nonlinear loads cause distortion of the sinusoidal waveform of the voltage and current which are quantified with harmonics. If the nonlinear load is also varying with time, as is the case of arc furnace loads, the rms value of the electric load is also varying. Lighting, which is affected by the voltage variations, may flicker which cause a certain degree of unpleasantness. This phenomenon has been known since the early days of power systems. Advances in power system technology and interconnections resulted in large power systems and the minimization of flicker type behaviour of a power system.

## 2. Modeling of Power System Devices

Models of power system elements are derived in direct phase quantities (a, b, c, and n (neutral) for three phase neutrals or L1, L2 and NN (neutral) for secondary service systems). The modeling procedure starts from a set of algebraic-differential-integral equations which describe a power system element. These equations are transformed into (a) a quadratic state space model or (b) a quadratic frequency domain model. These models are used to obtain the overall network solution with a Newton type algorithm. Details of the model and network solution are presented next followed by examples.

### *2.1 Time Domain Device Model*

Any power system device is described with a set of algebraic-differential-integral equations. It is always possible to cast these equations in the following general form:

$$\begin{bmatrix} i \\ 0 \end{bmatrix} = \begin{bmatrix} f_1(\dot{v}, \dot{y}, v, y, u) \\ f_2(\dot{v}, \dot{y}, v, y, u) \end{bmatrix} \qquad (1)$$

where
$i$ : vector of terminal currents,
$v$ : vector of terminal voltages,
$y$ : vector of device internal state variables
$u$ : vector of independent controls.

Note that this form includes two sets of equations which are named *external equations* and *internal equations* respectively. The terminal currents appear only in the external equations. Similarly, the device states consist of two sets: *external states* (i.e. terminal voltages, $v(t)$ ) and *internal states* ( i.e. $y(t)$ ). The set of equations (1) is consistent in the sense that the number of external states and the number of internal equations equals the number of external and internal equations respectively.

Equations (1) are integrated using a suitable numerical integration method. Assuming an integration time step h, the result of the integration is approximated with a second order equation of the form:

$$\begin{bmatrix} i(t) \\ 0 \end{bmatrix} = \begin{bmatrix} a_{11} & a_{12} \\ a_{21} & a_{22} \end{bmatrix} \begin{bmatrix} v(t) \\ y(t) \end{bmatrix} + \frac{1}{2} \mathrm{diag}(v(t), y(t)) \begin{bmatrix} b_{11} & b_{12} \\ b_{21} & b_{22} \end{bmatrix} \begin{bmatrix} v(t) \\ y(t) \end{bmatrix} + \frac{1}{2} \begin{bmatrix} c_{11} & c_{12} \\ c_{21} & c_{22} \end{bmatrix} \mathrm{diag}(v(t), y(t)) \begin{bmatrix} v(t) \\ y(t) \end{bmatrix} + \begin{bmatrix} b_1(t-h) \\ b_2(t-h) \end{bmatrix} \qquad (2)$$

where $b_1(t\text{-}h)$, $b_2(t\text{-}h)$ are past history functions.

### *2.3 Example: Arc Model*

The arc model consists of a nonlinear relationship between the arc current and arc voltage, i.e.

$$i(t) = k_1 (v(t)/v_{01})^{\alpha_1} + k_2 (v(t)/v_{02})^{\alpha_2}$$

where $i(t)$ is the arc current
$v(t)$ is the arc voltage
$k_1$, $\alpha_1$, $k_2$, $\alpha_2$, $v_{01}$,and $v_{02}$ are model parameters

## 3. Network Solution

The network solution is obtained by application of Kirchoff's current law at each node of the system. This procedure results in the set of equations (3). To these equations, the internal equations are appended resulting to the following set of equations.

$$\sum_k A^k i^k(t) = I_{inj} \qquad (3)$$

internal equations of all devices (4)

where $I_{inj}$ is a vector of nodal current injections, $A^k$ is a component incidence matrix with:

$$\left\{A_{ij}^{k}\right\} = 1, \text{ if terminal j of component k is connected to node i}$$
$$= 0, \text{ otherwise}$$

$i^k(t)$ are the terminal currents of component k.

The component k terminal voltage $v^k(t)$ is related to the nodal voltage vector v(t) by:

$$v^k(t) = (A^k)^T v(t) \qquad (5)$$

Upon substitution of device equations (2), the set of equations (3) and (4) become a set of quadratic equations. These equations are solved using Newton's method. Specifically, the solution is given by the following expression.

$$\begin{bmatrix} v(t) \\ y(t) \end{bmatrix} = \begin{bmatrix} v^0(t) \\ y^0(t) \end{bmatrix} - \left\{ \begin{bmatrix} A_{11} & A_{12} \\ A_{21} & A_{22} \end{bmatrix} + \tfrac{1}{2}\operatorname{diag}\left[ \begin{bmatrix} B_{11} & B_{12} \\ B_{21} & B_{22} \end{bmatrix} \operatorname{diag}(v^0(t), y^0(t))\mathbf{1} \right] \right.$$
$$\left. + \tfrac{1}{2}\operatorname{diag}(v^0(t), y^0(t)) \begin{bmatrix} B_{11} & B_{12} \\ B_{21} & B_{22} \end{bmatrix} + \begin{bmatrix} C_{11} & C_{12} \\ C_{21} & C_{22} \end{bmatrix} \operatorname{diag}(v^0(t), y^0(t)) \right\}^{-1} \begin{bmatrix} B_1^0 \\ B_2^0 \end{bmatrix} \qquad (6)$$

where :

$v^0(t), y^0(t)$ are the values of the state variables at the previous iteration, $B_1^0, B_2^0$ represents the mismatch of the system equations of the previous iteration, and $\mathbf{1}$ is a column vector with all entries equal to 1.

Note that at each time step, the quadratic device model is an approximation of the nonlinear device equations. For this reason, the above procedure utilizes an iterative algorithm which is applied at each time step. The algorithm is illustrated in Figure 1.

## 4. Applications

The proposed method has been applied to an example power systems with an arc furnace. The single line diagram of the system is illustrated in Figure 2. For this system we compare the harmonics and flicker at BUS10, BUS20, and BUS30. The computed flicker is compared to the allowable limits as described in [13]. For convenience the permissible flicker curves are presented in Figure 3.

Figure 4 illustrates the time wavform and the rms value (over a sliding window of 16.6667 mseconds) of the voltage at buses BUS20 and BUS30 (see Figure 2). Figure 5 illustrates the rms values of the voltages at the three buses of the system (BUS20, BUS30 and BUS32KV) as well as the variation of the electric real power absorbed by the furnace. Note that the power varies with a frequency of 5 Hz. The maximum power is 18.3 MW per phase and the minimum is 13.1 MW per phase. Note that in the model we can simulate any variation of the arc power, including random variations. However, for the simulation shown we elected to use a periodic variation with frequency 5 Hz. The rms values of the voltages vary in the ranges (61.2-64.3 kV), (58.8-62.7 kV) and (15.5-17.0 kV) for the buses BUS20, BUS30 and BUS32KV respectively. The percentage variations are 4.06, 6.63 and 9.68% respectively. It is important to note that the rms value of the voltage variation is high near the furnace and decreases for buses further away from the furnace. This is to be expected in a system that does not have capacitor banks. In systems with capacitor banks, however, the voltage variation profile may be different. With reference to Figure 3, the computed voltage variations will be noticed as flicker above the threshold of perception (at 5 Hz the threshold of perception is about 1.3%).

## 5. Summary and Conclusions

A time domain model for computing flicker due to changing electric loads, such as electric furnace loads, has been presented. The model is based on a quadratic equivalent representation of each element in the system and subsequent simultaneous solution of all equations. When there are nonlinear elements, such as an electric furnace, this approach yields a method with quadratic convergence characteristics. The result is an accurate and efficient computational method. The solution provides the waveforms of voltages and currents anywhere in the system. From the waveforms, any other desirable quantity can be computed such as rms values, real power, reactive power, distortion power, etc. Typical results have been presented in the paper. Our experience with this method indicates that the use of quadratic equivalent representation for each element of the system results in a robust real time simulation method.

## 6. References

1. Gyugyi, L., "Solid-State Control of AC Power Transmission", EPRI Proceedings: FACTS Conference I, 1992.
2. Bohmann L.J. and Lasseter, R.H. "Stability and Harmonics in Thyristor Controlled Reactors," *IEEE Trans. on Power Delivery*, Vol 5, No. 2, pp 1175-1181, April 1990.
3. Xu, W.W., Dommel, H.W. and Marti, J.R. "A Synchronous Machine Model for Three-Phase Harmonic Analysis and EMTP Initialization", *IEEE Tran. on PWRS*, Vol 6, No. 4, Nov. 1991, pp 1530-1538.
4. Semlyen, A., Eggleston J.F. and Arrillaga, J. "Admittance Matrix Model of a Synchronous Machine for Harmonic Analysis", *IEEE Tran. on PWRS*, Vol 2, No. 4, Nov. 1987, pp 833-840.
5. Tang, Y. "Power Systems Stability in the Presence of FACTS Elements" Ph.D. Thesis, Georgia Tech, May 1995.
6. Mahmoud, A.A., Shultz, R.D. " A Method for Analyzing Harmonic Distribution in AC Power Systems," *IEEE Trans*. PAS-101, No. 6, pp 1815-1824, June 1982.
7. Dommel H.W., Yan, A. and Wei, S., "Harmonic From Transformer Saturation", *IEEE Trans. on Power Delivery*, Vol. PWRD-1, No. 2, April 1986, pp 206-214.
8. Xia, D., Heydt, G.T. "Harmonic Power Flow Studies, Part I: Formulation and Solution, Part II: Implementation and Practical Application," *IEEE Trans*. PAS-101, No. 6, pp 1257-1270, June 1982.
9. Christoforidis, G.P. "Harmonic Analysis of Power Systems Connected to Converter Substations," Ph.D. Thesis, Georgia Tech, May 1990.
10. Beides, H., Meliopoulos, A. P. and Zhang, F. "Modeling and Analysis of Power System Under Periodic Steady State Controls", *IEEE 35th Midwest Symposium on Circuit and Systems.*
11. Brogan, W.L., *Modern Control Theory*, Prentice Hall, New Jersey, 1991, pp348.

12. Franklin, G.F., Power, J.D., and Workman, M.L., *Digital Control of Dynamic Systems*, Addison-Wesley, 1990, pp 71-73
13. IEEE Std 141-1986, IEEE Recommended Practice for Electric Power Distribution for Industrial Plants.
14. IEEE Std 1159-1995, IEEE Recommended Practice for Monitoring Electric Power Quality.
15. IEEE Std 1250-1995, IEEE Guide for Service to Equipment Sensitive to Momentary Voltage Disturbances.
16. ANSI/IEEE Std 519-1981, IEEE Guide for Harmonic Control and Reactive Compensation of Static Power Converters.

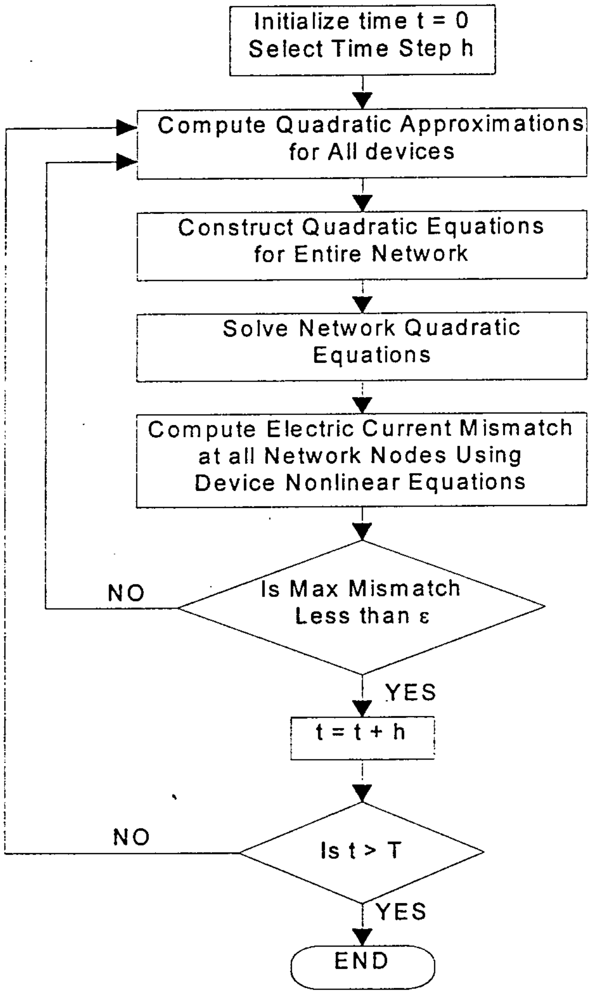
Initialize time t = 0
Select Time Step h
Compute Quadratic Approximations for All devices
Construct Quadratic Equations for Entire Network
Solve Network Quadratic Equations
Compute Electric Current Mismatch at all Network Nodes Using Device Nonlinear Equations
NO
Is Max Mismatch Less than ε
YES
t = t + h
NO
Is t > T
YES
END

**Figure 1. Network Solver Algorithm**

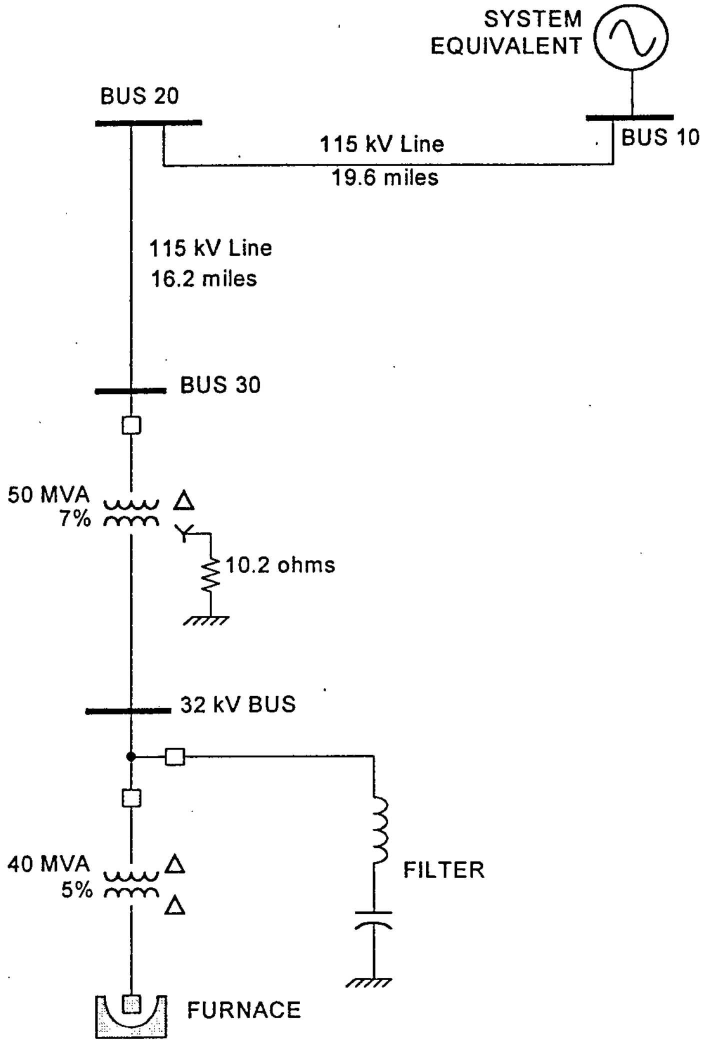
SYSTEM
EQUIVALENT
BUS 20
115 kV Line
19.6 miles
BUS 10
115 kV Line
16.2 miles
BUS 30
50 MVA
7%
Δ
Y
10.2 ohms
32 kV BUS
40 MVA
5%
Δ
Δ
FILTER
FURNACE

**Figure 2. Example Test System**

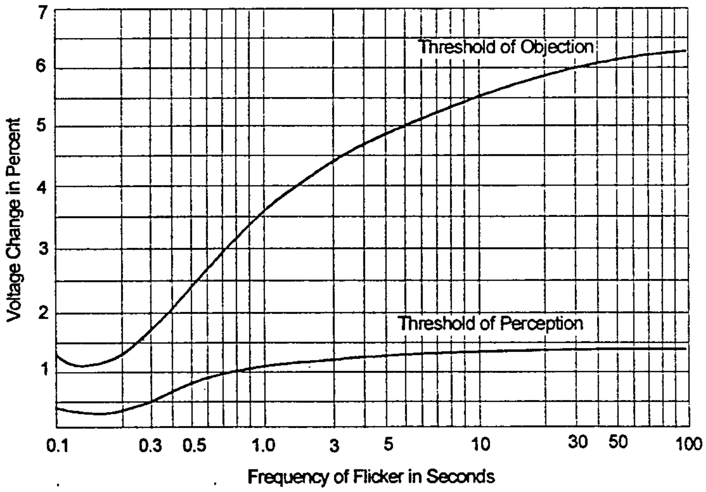

**Figure 3. Range of Observable and Objectionable Voltage Flicker Versus Time (from reference [13])**

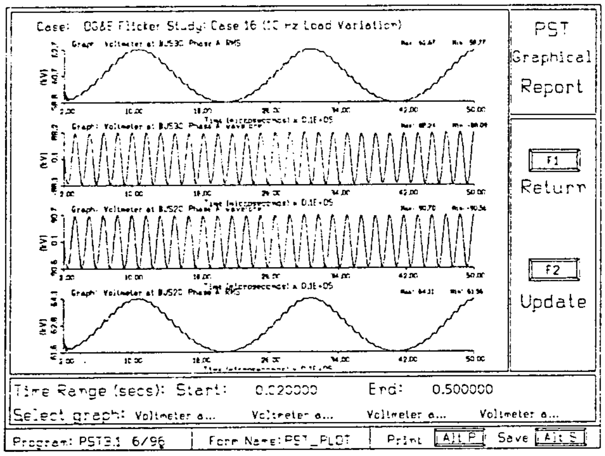
Case: OG&E Flicker Study: Case 16 (10 Hz Load Variation)
Graph: Voltmeter at BUS30 Phase A RMS
Graph: Voltmeter at BUS30 Phase A waveform
Graph: Voltmeter at BUS20 Phase A waveform
Graph: Voltmeter at BUS20 Phase A RMS
(kV)
Time (microseconds) x 0.1E+05
2.00
10.00
18.00
26.00
34.00
42.00
50.00
PST
Graphical
Report
F1
Return
F2
Update
Print
Alt P
Save
Alt S

Time Range (secs): Start: 0.020000 End: 0.500000

Select graph: Voltmeter a... Voltmeter a... Voltmeter a... Voltmeter a...

Program: PST3.1 6/96 | Form Name: PST_PLOT

**Figure 4. Waveform and RMS Variation of the BUS20 and BUS30 Voltage**

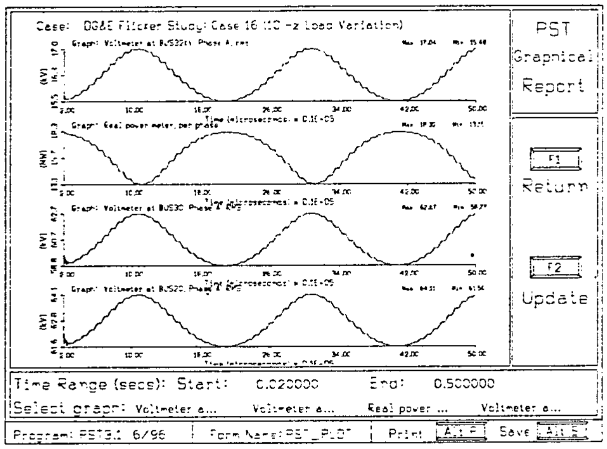
Case: OG&E Flicker Study: Case 16 (10 Hz Load Variation)
Graph: Voltmeter at BUS32KV Phase A rms
Graph: Real power meter, per phase
Graph: Voltmeter at BUS30 Phase A RMS
Graph: Voltmeter at BUS20 Phase A RMS
(kV)
(MW)
Time (microseconds) x 0.1E+05
2.00
10.00
18.00
26.00
34.00
42.00
50.00
PST
Graphical
Report
F1
Return
F2
Update
Print
Alt P
Save
Alt S

Time Range (secs): Start: 0.020000 End: 0.500000

Select graph: Voltmeter a... Voltmeter a... Real power ... Voltmeter a...

Program: PST3.1 6/96 | Form Name: PST_PLOT

**Figure 5. RMS Variation of the BUS20, BUS30 and BUS32KV Voltage and Furnace Real Power**

## Acknowledgments

The work reported in this paper has been partially supported by the ONR Grant No. N00014-96-1-0926. This support is gratefully acknowledged.

## Biographies

**A. P. Sakis Meliopoulos** (M '76, SM '83, F '93) was born in Katerini, Greece, in 1949. He received the M.E. and E.E. diploma from the National Technical University of Athens, Greece, in 1972; the M.S.E.E. and Ph.D. degrees from the Georgia Institute of Technology in 1974 and 1976, respectively. In 1971, he worked for Western Electric in Atlanta, Georgia. In 1976, he joined the Faculty of Electrical Engineering, Georgia Institute of Technology, where he is presently a professor. He is active in teaching and research in the general areas of modeling, analysis, and control of power systems. He has made significant contributions to power system grounding, harmonics, and reliability assessment of power systems. He is the author of the books, Power Systems Grounding and Transients, Marcel Dekker, June 1988, Ligthning and Overvoltage Protection, Section 27, Standard Handbook for Electrical Engineers, McGraw Hill, 1993, and the monograph, Numerical Solution Methods of Algebraic Equations, EPRI monograph series. Dr. Meliopoulos is a member of the Hellenic Society of Professional Engineering and the Sigma Xi.

**G. J. Cokkinides** (M78). Dr. Cokkinides' interests include power system simulation and control, electromagnetic system modeling, measurement instrumentation, and CAD software development. Current research projects include the development of a power system ground impedance measurement device based on a custom microprocessor controlled multichannel data acquisition system, the development of a GPS synchronized measurement system for the estimation of the harmonic state of a bulk power transmission system, development of a CAD tools for characterization of microelectronic components, development of a comprehensive FEM based tool for dynamic structural analysis.

# Wavelet Based Transient Analysis

A. P. Sakis Meliopoulos, Fellow
Chien-Hsing Lee, Student Member

School of Electrical and Computer Engineering
Georgia Institute of Technology
Atlanta, GA 30332-0250

**Abstract:** This paper proposes a systematic way to analyze power system transient problems using wavelet transforms. We name this approach WBTA (Wavelet Based Transient Analysis). The methodology is being implemented using Daubechies wavelets. The results obtained using this method are compared to the solution computed from a numerical time domain analysis. A concise description of this method will be presented.

Key Words: Wavelet Transforms, Daubechies wavelets, transient.

## 1.0 Introduction

Electric power systems are subject to many types of disturbances that result in transients. Electrical transients result in abnormal voltages (overvoltages) and abnormal currents (overcurrents). For example, physical phenomena such as lightning may generate transient overvoltages and abnormal conditions such as electrical faults (e.g., single line to ground, line to line, etc.) may generate overcurrents. Overcurrents may damage power equipment due to excessive heat dissipation, while overvoltages may result in flashovers or insulation breakdown, device outages, and eventual deterioration of power system reliability. Figure 1.1 shows several common transient signals occurring in electric power systems [1]. From the time horizon, we see that the transients are often of short duration. For example, the transient period is on the order of milliseconds for a line switching transient.

There are a number of methods used to study electrical transients. As shown in Figure 1.2, these methods are categorized into either the time domain or the integral transform domain [1]. In the time domain, the mathematical solution comes directly from solving the differential equations, or by representing the system with its equivalent resistive companion circuit which is then solved numerically. There are many commercialized user-friendly software packages designed to analyze electrical transients numerically such as the ElectroMagnetic Transients Program (EMTP) and the Alternative Transients Program (ATP). The EMTP provides many advantages over other harmonic and transient simulation programs such as allowing the user to complete steady-state and transient simulations with the same model.

In the integral transform domain, the Fourier, Laplace and Z transforms are used. The Fourier transform and the Laplace transform are very closely related. The Laplace transform has certain advantages over the Fourier transform. Among these are the ease of computing transforms, the simplicity of the transforms themselves, the ease of including initial conditions in the solution of differential equations, the insight into system performance that is possible through use of the complex frequency concept, and the ability to deal with time functions that are not absolutely integrable [2]. However, Fourier transforms are still required for certain types of signals and for system analysis problems. For example, the Fourier transform provides information concerning the frequency composition of transient waveforms. A method which incorporates desirable components of both domains is the Wavelet transform. Wavelet transforms have certain advantages for analyzing transient signals, which will be further explored here.

In this paper, the wavelet based approach is proposed to solve transient problems. The Daubechies wavelet is embedded within the wavelet transform scheme. Concept of wavelet transforms using Daubechies wavelet is introduced in Section 2. The proposed approach is described in Section 3. The result of study case using this proposed approach is shown in Section 4. Conclusions are drawn in Section 5.

| Type | Waveshape | Time Horizon |
|---|---|---|
| Transformer Inrush Current | 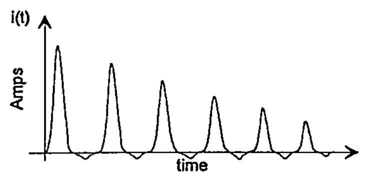 | up to one second |
| Lightning Surge Voltage | 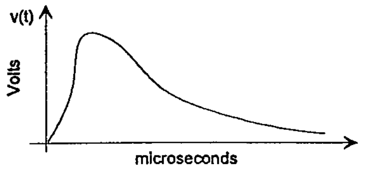 | Microseconds |
| Line Switching Transient | 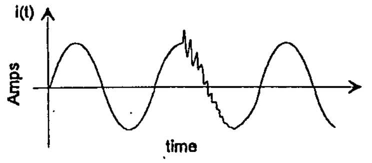 | Milliseconds |

**Figure 1.1 Examples of Transient Signals in Power Systems.**

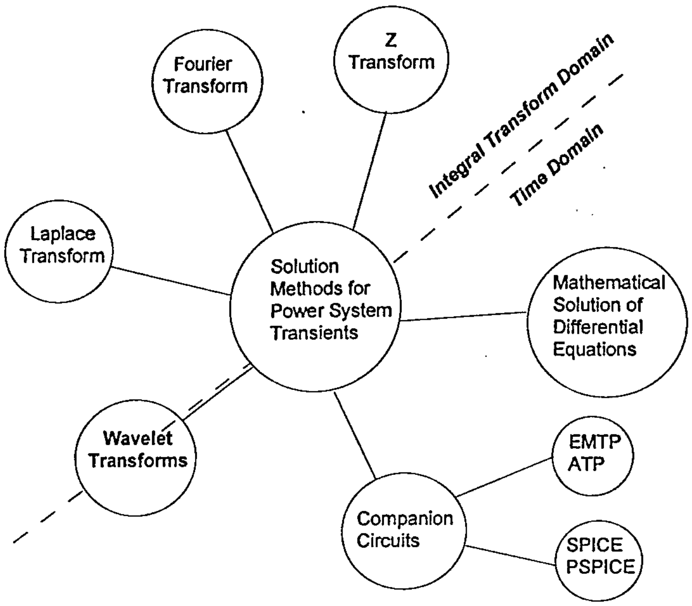
Fourier Transform
Z Transform
Integral Transform Domain
Time Domain
Laplace Transform
Solution Methods for Power System Transients
Mathematical Solution of Differential Equations
Wavelet Transforms
EMTP ATP
Companion Circuits
SPICE PSPICE

**Figure 1.2 Solution Methods for Transient Analysis.**

## 2.0 Introduction of Wavelet Transforms

### Wavelet Series Expansion of an Arbitrary Function f(x)

Consider a wavelet series expansion that holds for the interval $0 \le x < 1$. Note that x is a non-dimensional variable resulting from a normalization procedure. For example, consider the independent variable t (time) and an interval of interest [0, T]. Then we define $x = t/T$, where x is a normalized variable. The interval of interest is $0 \le x < 1$. The wavelet expansion of an arbitrary function f(x) in $0 \le x < 1$ can be written as [3]

$$f(x) = \sum_j a_j w_j(x) \qquad (2.1)$$

where

$a_j$ are unknown coefficients,

$w_j(x)$ are known functions (family of Daubechies' wavelets).

In equation 2.1, $w_1(x)$ is equal to $\phi(x)$ which is generated recursively from the following equation [4]

$$\phi(x) = \sum_k c_k \phi(2x-k) \qquad (2.2)$$

where k is any integer, positive, zero or negative. The c's are the Daubechies' coefficients and $\phi(x)$ is called the scaling function. $w_2(x)$ is equal to w(x) which is derived from $\phi(x)$ with the following equation [4]

$$w(x) = \sum_k (-1)^k c_k \phi(2x+k-N+1) \qquad (2.3)$$

where N is the number of Daubechies coefficient and w(x) is called the wavelet function. Note the scaling function and the wavelet function generally do not have a closed form. Figure 2.1 shows an example of the scaling and wavelet functions for N = 4.

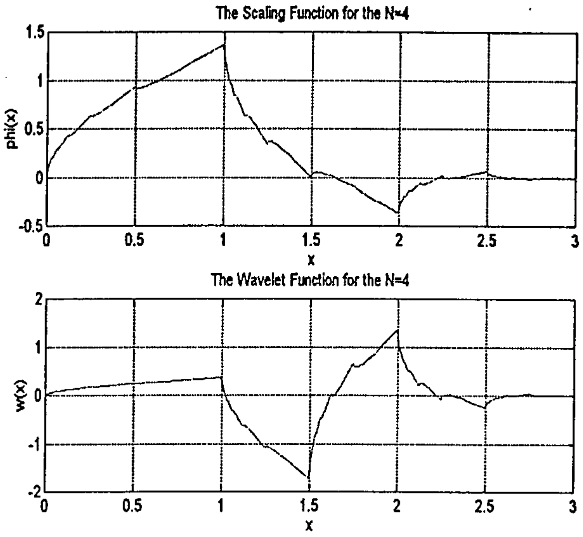

**Figure 2.1 The Scaling and Wavelet Functions with Four Daubechies Coefficients.**

Subsequently, the functions $w_3(x)$, $w_4(x)$,... $w_j(x)$ are derived with scaling and translation operations as follows:

$$\begin{aligned} w_3(x) &= w(2x), \\ w_4(x) &= w(2x-1), \\ w_5(x) &= w(4x), \\ w_6(x) &= w(4x-1), \\ w_7(x) &= w(4x-2), \\ w_8(x) &= w(4x-3), \\ &\vdots \end{aligned}$$

The coefficients $a_1$, $a_2$, ... represent the amplitudes of each of the contributing wavelets in a similar manner to the Fourier series coefficients which are the amplitudes of the various sine and cosine terms in the classical Fourier analysis.

The selected family of Daubechies' wavelets are orthogonal, i.e. $< w_i(x), w_j(x) > = 0$ for $i \neq j$, which means the inner product of $w_i(x)$ and $w_j(x)$ is equal to zero except when i = j. The coefficients $a_1$, $a_2$, ... can be found by multiplying equation 2.1 by $w_i(x)$ and integrating from x = 0 to x = 1 to get

$$\int_0^1 w_i(x) f(x) dx = \int_0^1 w_i(x) \sum_j a_j w_j(x) dx$$

thus, for i = j, we have

$$a_j = \frac{\int_0^1 w_j(x) f(x) dx}{\int_0^1 w_j^2(x) dx} \qquad (2.4)$$

### Reconstruction of an Arbitrary Function f(x)

Since we have determined the coefficients, $a_j$, the reconstructed function $\tilde{f}(x)$ of f(x) can now be reconstructed as follows

$$
\begin{aligned}
\tilde{f}(x) = {} & a_1\phi(x) + && \uparrow \text{level } 0\\
& a_2 w(x) + && \uparrow \text{level } 1\\
& a_3 w(2x) + a_4 w(2x-1) + && \uparrow \text{level } 2\\
& a_5 w(2^{3-1}x) + a_6 w(2^{3-1}x-1) + \ldots + a_8 w(2^{3-1}x-3) + && \uparrow \text{level } 3\\
& a_9 w(2^{4-1}x) + a_{10} w(2^{4-1}x-1) + \ldots + a_{16} w(2^{4-1}x-7) + && \uparrow \text{level } 4\\
& a_{17} w(2^{5-1}x) + a_{18} w(2^{5-1}x-1) + \ldots + a_{32} w(2^{5-1}x-15) + && \uparrow \text{level } 5\\
& a_{33} w(2^{6-1}x) + a_{34} w(2^{6-1}x-1) + \ldots + a_{64} w(2^{6-1}x-31) + && \uparrow \text{level } 6\\
& a_{65} w(2^{7-1}x) + a_{66} w(2^{7-1}x-1) + \ldots + a_{128} w(2^{7-1}x-63) + && \uparrow \text{level } 7\\
& \qquad \ldots
\end{aligned}
$$

The accuracy of the reconstructed is dependent on the number of wavelet levels used. The original function can be approximated more accurately by increasing the number of levels. For example, the use of one wavelet level to reconstruct $\tilde{f}(x)$ is given by

$$\tilde{f}(x) = a_1\phi(x) + a_2 w(x) = \tilde{f}_1(x)$$

Reconstruction using two wavelet levels is then

$$\tilde{f}(x) = \tilde{f}_1(x) + a_3 w(2x) + a_4 w(2x-1) = \tilde{f}_2(x)$$

For a total of M wavelet levels, the reconstruction is

$$
\begin{aligned}
\tilde{f}(x) &= \tilde{f}_{M-1}(x) + a_{2^{M-1}+1} w(2^{M-1}x) + a_{2^{M-1}+2} w(2^{M-1}x-1) + \\
&\quad \ldots + a_{2^M} w(2^{M-1}x - 2^{M-1} + 1)\\
&= \tilde{f}_M(x)
\end{aligned}
$$

Therefore, the higher the level of reconstruction, the closer the reconstructed function is to the original.

## 3.0 The Proposed Approach

In section 1, several different methods for solving transient problems were introduced. An alternative method to those techniques proposed is the use of wavelet transforms. We name this approach WBTA (Wavelet Based Transient Analysis). A concise description of this method is presented below.

WBTA is a systematic way to analyze power system transient problems using wavelet transforms. It consists of three steps:

1) Develop a wavelet companion equivalent circuit for each system component, such as resistor, inductor, and capacitor
2) Construct the wavelet equivalent network for the entire system and determine the coefficients of the wavelet components for all node voltages of the equivalent system.
3) Construct the actual voltages and currents from the wavelet component solution

## 3.1 Wavelet Companion Equivalent Circuit

The basic methodology for transient analysis using wavelet transforms has been formulated in section 3.0. The methodology is being implemented using Daubechies wavelets. The derivation of a wavelet companion equivalent circuit for resistors, inductors, and capacitors is described.

| Network Element | Wavelet Equivalent Current Model |
|---|---|
| 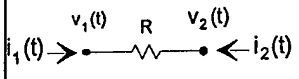 a1 | $\hat{i}_1(x) = \frac{1}{R}\sum_j (a_{1j} - a_{2j}) w_j(x)$<br>$\hat{i}_2(x) = -\frac{1}{R}\sum_j (a_{1j} - a_{2j}) w_j(x)$<br>a |
| 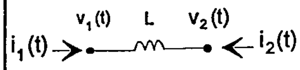 b1 | $\hat{i}_1(x) = \frac{T}{L}\sum_j (\sum_r (a_{1r} - a_{2r})\alpha_{rj}) w_j(x)$<br>$\hat{i}_2(x) = -\frac{T}{L}\sum_j (\sum_r (a_{1r} - a_{2r})\alpha_{rj}) w_j(x)$<br>b |
| 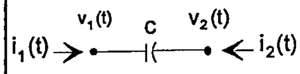 c1 | $\hat{i}_1(x) = \frac{C}{T}\sum_j (\sum_r (a_{1r} - a_{2r})\beta_{rj}) w_j(x)$<br>$\hat{i}_2(x) = -\frac{C}{T}\sum_j (\sum_r (a_{1r} - a_{2r})\beta_{rj}) w_j(x)$<br>c |

Figure 3.1 Wavelet Equivalent Companion Circuit

Resistance

Consider a resistor as illustrated in Figure 3.1a1. The current/voltage relationship for the resistor is

$$i_1(t) = \frac{1}{R}\left[v_1(t) - v_2(t)\right], 0 \le t < T$$

For convenience, the time interval of interest [0, T] is normalized with the transformation x = t/T. The interval of interest for variable x is [0, 1]. Upon replacement of variable t with x, the resistor equation becomes

$$i_1(xT) = \frac{1}{R}\left[v_1(xT) - v_2(xT)\right], \qquad 0 \le x < 1$$

Define $\hat{i}_1(x) = i_1(xT), \hat{v}_1(x) = v_1(xT)$ and $\hat{v}_2(x) = v_2(xT)$. Then, assume the wavelet expansion of $\hat{v}_1(x)$ and $\hat{v}_2(x)$ in $0 \le x < 1$ can be written as

$$\hat{v}_1(x) = \sum_j a_{1j} w_j(x), \qquad 0 \le x < 1 \qquad (3.1)$$

$$\hat{v}_2(x) = \sum_j a_{2j} w_j(x), \qquad 0 \le x < 1 \tag{3.2}$$

where

$a_{1j}$, $a_{2j}$ are unknown coefficients,
$w_j(x)$ are known functions (family of Daubechies' wavelets).

The current flowing through the resistor is

$$\hat{i}_1(x) = \frac{1}{R}\,[\hat{v}_1(x) - \hat{v}_2(x)], 0 \le x < 1 \tag{3.3}$$

By substituting equations 3.1 and 3.2 into equation 3.3, we have

$$\hat{i}_1(x) = \frac{1}{R}\sum_j (a_{1j} - a_{2j}) w_j(x), 0 \le x < 1 \tag{3.4}$$

Note, $\hat{i}_2(x) = -\hat{i}_1(x) = -\frac{1}{R}\sum_j (a_{1j} - a_{2j}) w_j(x)$.

Inductance

Consider an inductor as illustrated in Figure 3.1b1. The current/voltage relationship for the inductor is

$$i_1(t) = \frac{1}{L}\int_0^t [v_1(\tau) - v_2(\tau)]d\tau, \quad 0 \le t < T$$

with initial condition $i_1(0) = 0$

For convenience, the time interval of interest [0, T] is normalized with the transformation $x = t/T$. The interval of interest for variable x is [0, 1]. Upon replacement of variables t with x, the inductor equation becomes

$$i_1(xT) = \frac{1}{L}\int_0^{xT} (v_1(\lambda T) - v_2(\lambda T))T d\lambda, \qquad 0 \le x < 1$$

Define $\hat{i}_1(x) = i_1(xT)$, $\hat{v}_1(x) = v_1(xT)$ and $\hat{v}_2(x) = v_2(xT)$. Then, assume the wavelet expansion of $\hat{v}_1(x)$ and $\hat{v}_2(x)$ in $0 \le x < 1$ can be written as

$$\hat{v}_1(x) = \sum_j a_{1j} w_j(x), \qquad 0 \le x < 1 \tag{3.5}$$

$$\hat{v}_2(x) = \sum_j a_{2j} w_j(x), \qquad 0 \le x < 1 \tag{3.6}$$

where

$a_{1j}$, $a_{2j}$ are unknown coefficients,
$w_j(x)$ are known functions (family of Daubechies' wavelets).

The current flowing through the inductor is

$$\hat{i}_1(x) = \frac{1}{L}\int_0^x (\hat{v}_1(\lambda) - \hat{v}_2(\lambda))T d\lambda, 0 \le x < 1 \tag{3.7}$$

By substituting equations 3.5 and 3.6 into equation 3.7, we have

$$\hat{i}_1(x) = \frac{T}{L}\int_0^x \left[\sum_j a_{1j} w_j(\lambda) - \sum_j a_{2j} w_j(\lambda)\right] d\lambda$$

$$= \frac{T}{L}\sum_j (a_{1j} - a_{2j}) \int_0^x w_j(\lambda) d\lambda \tag{3.8}$$

Define $f_j(x) = \int_0^x w_j(\lambda) d\lambda$, $0 \le x < 1$, where $f_j(x)$ is a known function. Thus, $f_j(x)$ can be written in terms of the wavelet expansion as follows.

$$f_j(x) = \sum_m \alpha_{jm} w_m(x), \quad 0 \le x < 1 \tag{3.9}$$

where

$\alpha_{jm}$ are known coefficients,
$w_m(x)$ are known functions (family of Daubechies' wavelets).

By substituting equation 3.9 into equation 3.8, we have

$$\hat{i}_1(x) = \frac{T}{L}\sum_j (a_{1j} - a_{2j}) \sum_m \alpha_{jm} w_m(x), 0 \le x < 1$$

$$= \frac{T}{L}\sum_m \left[\sum_j (a_{1j} - a_{2j})\alpha_{jm}\right] w_m(x) \tag{3.10}$$

In order to have the same index as the resistor model, the indices j and m are replaced by r and j respectively. Thus, equation 3.10 becomes

$$\hat{i}_1(x) = \frac{T}{L}\sum_j \left[\sum_r (a_{1r} - a_{2r})\alpha_{rj}\right] w_j(x) \tag{3.11}$$

Note, $\hat{i}_2(x) = -\hat{i}_1(x) = -\frac{T}{L}\sum_j \left[\sum_r (a_{1r} - a_{2r})\alpha_{rj}\right] w_j(x)$

Capacitance

Consider a capacitor as illustrated in Figure 3.1c1. The current/voltage relationship for the capacitor is

$$i_1(t) = C\frac{d}{dt}[v_1(t) - v_2(t)], 0 \le t < T$$

with initial conditions $v_1(0) = v_2(0) = 0$,

For convenience, the time interval of interest [0, T] is normalized with the transformation $x = t/T$. The interval of interest for variable x is [0, 1]. Upon replacement of variable t with x, the capacitor equation becomes

$$i_1(xT) = C\frac{d}{Tdx}[v_1(xT) - v_2(xT)]$$

Define $\hat{i}_1(x) = i_1(xT)$, $\hat{v}_1(x) = v_1(xT)$ and $\hat{v}_2(x) = v_2(xT)$. Then, assume the wavelet expansion of $\hat{v}_1(x)$ and $\hat{v}_2(x)$ in $0 \le x < 1$ can be written as

$$\hat{v}_1(x) = \sum_j a_{1j} w_j(x), 0 \le x < 1 \tag{3.12}$$

$$\hat{v}_2(x) = \sum_j a_{2j} w_j(x), 0 \le x < 1 \tag{3.13}$$

where

$a_{1j}$, $a_{2j}$ are unknown coefficients,
$w_j(x)$ are known functions (family of Daubechies' wavelets).

The current flowing through the capacitor is

$$\hat{i}_1(x) = C\frac{d}{Tdx}\left[\hat{v}_1(x) - \hat{v}_2(x)\right], 0 \le x < 1 \tag{3.14}$$

By substituting equations 3.12 and 3.13 into equation 3.14, we have

$$\begin{aligned}\hat{i}_1(x) &= \frac{C}{T}\frac{d}{dx}\left[\sum_j a_{1j}w_j(x) - \sum_j a_{2j}w_j(x)\right] \\ &= \frac{C}{T}\sum_j (a_{1j} - a_{2j})\frac{d}{dx}\left[w_j(x)\right]\end{aligned} \tag{3.15}$$

Define $g_j(x) = \frac{d}{dx}w_j(x)$, $0 \le x < 1$, where $g_j(x)$ is a known function. Thus, $g_j(x)$ can be written in terms of the wavelet expansion as follows.

$$g_j(x) = \sum_m \beta_{jm}w_m(x), 0 \le x < 1 \tag{3.16}$$

where

$\beta_{jm}$ are known coefficients,
$w_m(x)$ are known functions (family of Daubechies' wavelets).

By substituting equation 3.16 into equation 3.15, we have

$$\begin{aligned}\hat{i}_1(x) &= \frac{C}{T}\sum_j (a_{1j} - a_{2j}) \sum_m B_{jm}w_m(x), 0 \le x < 1 \\ &= \frac{C}{T}\sum_m\left[\sum_j (a_{1j} - a_{2j})\beta_{jm}\right]w_m(x)\end{aligned} \tag{3.17}$$

In order to have the same index as the resistor and inductor models, the indices j and m are replaced by r and j respectively. Thus, equation 3.17 becomes

$$\hat{i}_1(x) = \frac{C}{T}\sum_j\left[\sum_r (a_{1r} - a_{2r})\beta_{rj}\right]w_j(x) \tag{3.18}$$

Note, $\hat{i}_2(x) = -\hat{i}_1(x) = -\frac{C}{T}\sum_j\left[\sum_r (a_{1r} - a_{2r})\beta_{rj}\right]w_j(x)$

### 3.2 Wavelet Component Network Analysis

Consider a system state with its state defined by the vector of voltages at all nodes of the system,

$$v(t) = \begin{bmatrix} v_1(t) \\ v_2(t) \\ \vdots \\ v_n(t) \end{bmatrix} \tag{3.19}$$

Subsequently, each voltage, i.e. the voltage at node i is expressed as a linear combination of wavelets resulting from the expansion of the voltage into the wavelet space, i.e.

$$v_i(x) = \sum_j a_{ij}w_j(x) \tag{3.20}$$

By substituting equation 3.20 into equation 3.19, the vector of voltages at all nodes of the system is expressed with:

$$v(x) = U\,w(x) \tag{3.21}$$

where

$$U = \begin{bmatrix} a_{11} & a_{12} & \cdots & a_{12^M} \\ \vdots & \ddots & \cdots & \vdots \\ \vdots & \vdots & \ddots & \vdots \\ a_{n1} & a_{n2} & \cdots & a_{n2^M} \end{bmatrix} \text{ and } w(x) = \begin{bmatrix} w_1(x) \\ w_2(x) \\ \vdots \\ w_{2^M}(x) \end{bmatrix}$$

Note that n is the total number of nodes in a system, M is the total number of wavelet levels and w(x) are the family of Daubechies' wavelets [3].

Next consider a device k which is part of the system. In general, the input/output relationship for a device k (or the current-voltage relationship) is:

$$i_{mk}(x) = A_{mk}v(x) + B_{mk}\dot{v}(x) + C_{mk}\int v(\lambda)d\lambda \tag{3.22}$$

where

m is the node number,
k is the device number, and
$A_{mk}$, $B_{mk}$, and $C_{mk}$ are appropriate constant matrices

Upon substitution of equation 3.21 into equation 3.22, we have

$$i_{mk}(x) = A_{mk}Uw(x) + B_{mk}U\dot{w}(x) + C_{mk}U\int w(\lambda)d\lambda \tag{3.23}$$

By using the second order finite difference approximation and the trapezoidal numerical integration method, equation 3.23 can be approximated as

$$i_{mk}(x) \cong \sum_j g_{mkj}(U)w_j(x) \tag{3.24}$$

Kirchoff's Current Law at node m yields

$$\sum_k i_{mk}(x) = 0$$

Thus,

$$\sum_k\sum_j g_{mkj}(U)w_j(x) = 0 \tag{3.25}$$

Since equation 3.25 needs to be valid for all x, then

$$\sum_k g_{mkj}(U) = 0, \qquad j = 1,2,\ldots,2^M \tag{3.26}$$

Note that above procedure yields n x $2^M$ equations. Solution of these equations yields the unknown coefficients $a_{ij}$, i = 1, 2, ..., n, j = 1, 2, ..., $2^M$. The actual voltage at a node i is computed now from equation 3.20.

Examples of transient analysis using WBTA will be illustrated in the next section. The accuracy of this approach is computed by comparing the wavelet based solution to the time domain solution from a time domain network solver.

## 4.0 Study Cases of Transient Analysis

Examples 4.1 to 4.4 investigate solutions obtained using the equivalent wavelet models for the basic circuit elements. The problem statements are: Assume the initial voltage at each node is zero. Then, at time t = 0, a lightning strike occurs at node 1 which is modeled by a current source $i_s(t) = i_0(e^{-\alpha_1 t} - e^{-\alpha_2 t})$ where $\alpha_1 = 0.06 \times 10^6$ sec$^{-1}$, $\alpha_2 = 1.2 \times 10^6$ sec$^{-1}$, and $i_0 = 1.0$ kA. Compute the voltage waveform at each node over a duration T = 12.8 μsec using WBTA with the total number of M, M-1, M-2, and M-3 wavelet levels where M = 7. Then the same problem will be solved using a numerical time domain analysis. The two solutions will be compared.

**Example 4.1:** Consider a simple system consisting of a resistor R = 50 Ω and a capacitor C = 0.001 μF as shown in Figure 4.1.

**Example 4.2:** Consider a simple system consisting of a resistor R = 40 Ω and an inductor L = 100 μH as shown in Figure 4.2.

**Example 4.3:** Consider a simple system consisting of a resistor R = 50 Ω, a capacitor C = 0.001 μF, and an inductor L = 100 μH as shown in Figure 4.3.

**Example 4.4:** Consider a simple system consisting of resistors, inductors and capacitors where $R_1$ = 30 Ω, $R_2$ = 40 Ω, $R_3$ = 20 Ω, $R_4$ = 50 Ω, $L_1$ = 100 μH, $L_2$ = 90 μH , and $C_1$ = $C_2$ = 0.001 μF as shown in Figure 4.4.

Figures 4.5, 4.6 and 4.7 show the voltage waveform at node 1 using Wavelet Based Transient Analysis (WBTA) for the total number of 7, 6, 5, and 4 wavelet levels of the system from Figure 4.1 to 4.3, respectively. The numerical time domain analysis solution is also plotted for comparison. Tables 4.1, 4.2 and 4.3 show the comparison of the solution found using WBTA as compared to a Numerical Time Domain Analysis (NTDA).

Figure 4.8, 4.9, 4.10, and 4.11 show the voltage waveform at each node of the system in Figure 4.4 using Wavelet Based transient Analysis (WBTA) for the total number of 7, 6, 5, and 4 wavelet levels. The numerical time domain analysis solution is also plotted for comparison. Table 4.4 shows the comparison of the solution found using WBTA as compared to a Numerical Time Domain Analysis (NTDA).

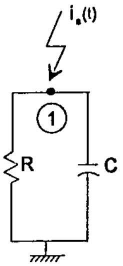

**Figure 4.1 A Resistor and Capacitor Circuit.**

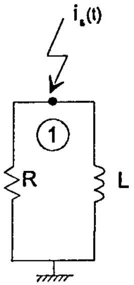

**Figure 4.2 A Resistor and Inductor Circuit.**

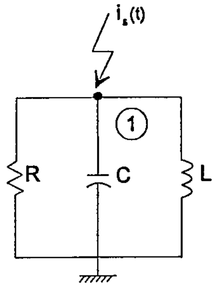

**Figure 4.3 A Resistor, Capacitor and Inductor Circuit.**

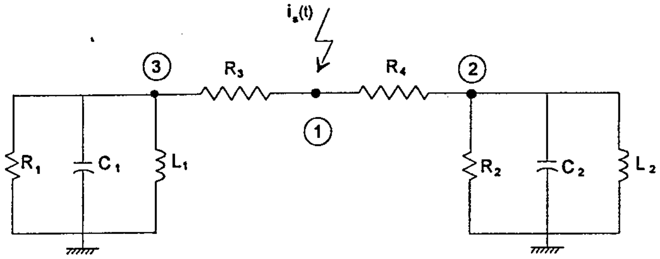

**Figure 4.4 A System Consisting of Resistors, Inductors and Capacitors.**

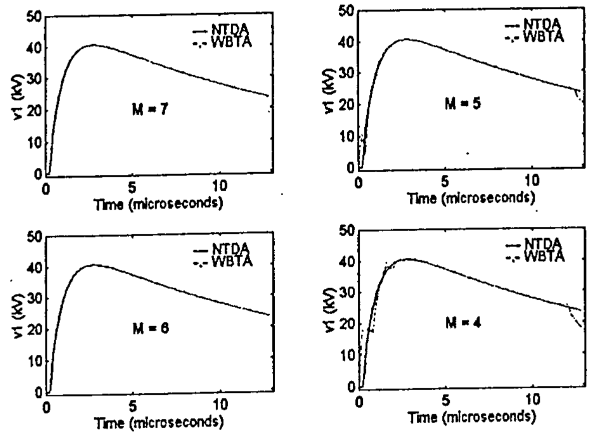

Figure 4.5 Voltage Waveforms at Node 1 for WBTA and NTDA in Figure 4.1.

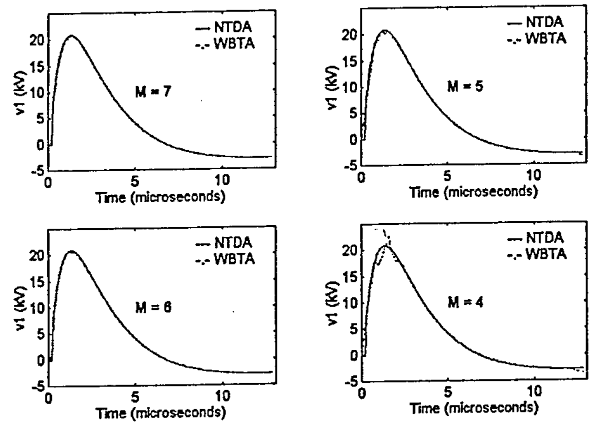

Figure 4.6 Voltage Waveforms at Node 1 for WBTA and NTDA in Figure 4.2

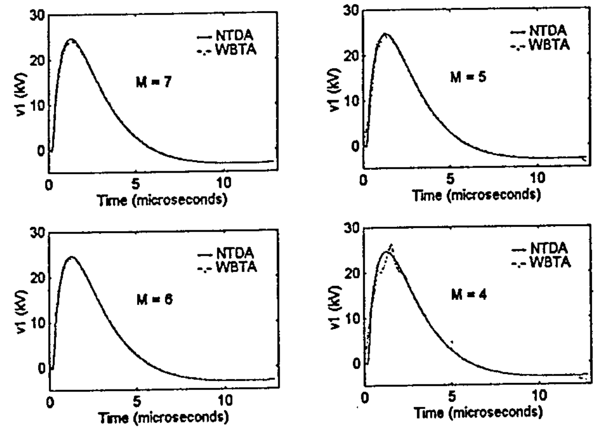

Figure 4.7 Voltage Waveforms at Node 1 for WBTA and NTDA in Figure 4.3.

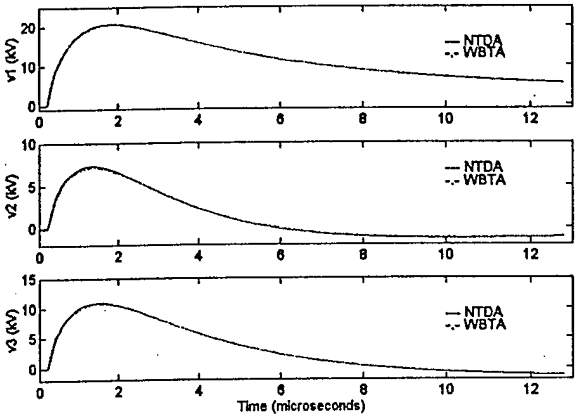

Figure 4.8 Voltage Waveforms for WBTA Using 7 Wavelet Levels and NTDA in Figure 4.4.

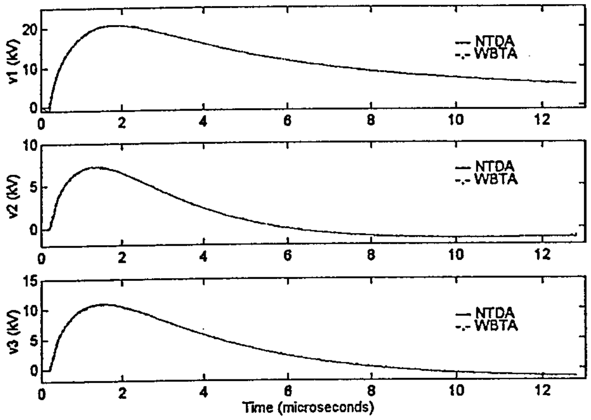

Figure 4.9 Voltage Waveforms for WBTA Using 6 Wavelet Levels and NTDA in Figure 4.4.

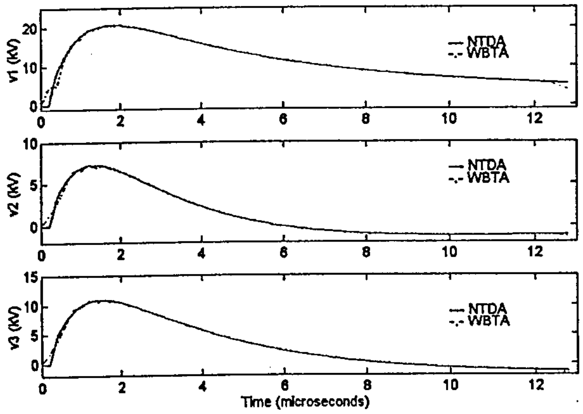

Figure 4.10 Voltage Waveforms for WBTA Using 5 Wavelet Level and NTDA in Figure 4.4.

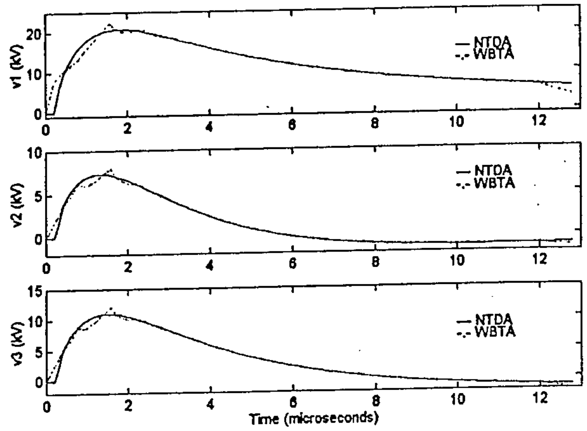

Figure 4.11 Voltage Waveforms for WBTA Using 4 Wavelet Levels and NTDA in Figure 4.4.

Table 4.1 Comparison of WBTA Result to NTDA.

| Total Number of Wavelet Levels Used | R.M.S. Error (p.u.) | Max. Abs. Error (p.u.) |
|---|---|---|
| 7 | 0.0056 | 0.0635 |
| 6 | 0.0090 | 0.0998 |
| 5 | 0.0399 | 0.3388 |
| 4 | 0.0784 | 0.5764 |

Table 4.2 Comparison of WBTA Result to NTDA.

| Total Number of Wavelet Levels Used | R.M.S. Error (p.u.) | Max. Abs. Error (p.u.) |
|---|---|---|
| 7 | 0.0138 | 0.0351 |
| 6 | 0.0208 | 0.1350 |
| 5 | 0.0575 | 0.4961 |
| 4 | 0.0795 | 0.6205 |

Table 4.3 Comparison of WBTA Result to NTDA.

| Total Number of Wavelet Levels Used | R.M.S. Error (p.u.) | Max. Abs. Error (p.u.) |
|---|---|---|
| 7 | 0.0293 | 0.0164 |
| 6 | 0.0231 | 0.1507 |
| 5 | 0.0599 | 0.4359 |
| 4 | 0.0991 | 0.6275 |

Table 4.4 Comparison of WBTA Result to NTDA.

| | Voltage at Node 1 | | Voltage at Node 2 | | Voltage at Node 3 | |
|---|---|---|---|---|---|---|
| Total Number of Wavelet Levels | R.M.S Error (p.u.) | Max. Abs. Error (p.u.) | R.M.S Error (p.u.) | Max. Abs. Error (p.u.) | R.M.S Error (p.u.) | Max. Abs. Error (p.u.) |
| 7 | 0.0069 | 0.0442 | 0.0260 | 0.1569 | 0.0177 | 0.1154 |
| 6 | 0.0091 | 0.0824 | 0.0213 | 0.1315 | 0.0132 | 0.0756 |
| 5 | 0.0481 | 0.3834 | 0.0561 | 0.4136 | 0.0469 | 0.3757 |
| 4 | 0.0789 | 0.6179 | 0.0889 | 0.5749 | 0.0737 | 0.5245 |

## 5.0 Summary and Conclusions

The results of the wavelet based and a numerical time domain analysis appear to be slightly different. The resulting differences are caused by the numerical approximation of integral and differential of Daubechies wavelet functions. The computation speed of using the proposed method appears to be faster than using a numerical time domain analysis.

## 6.0 Bibliography

[1] A. W. Galli, G. T. Heydt, and P. F. Riberio, *"Exploring the Power of Wavelet Analysis"*, IEEE Computer Applications in Power, vol. 9, no.4, Oct 1996, pp 37-41.

[2] M. Cooper, *Continuous & Discrete Signal & System Analysis*, Saunders College Publishing, A Division of Holt, Rinehart and Winton, Inc 1991.

[3] D. E. Newland, *An Introduction to Random Vibrations, Spectral and Wavelet Analysis*, 3rd ed., Longman Scientific and Technical (co-published in U.S. by John Wiley and Sons), 1993, pp295-370.

[4] J. R. Williams and K. Amaratunga, "Introduction to wavelets in engineering", *International Journal for Numerical Methods in Engineering*, vol. 37, 1994, pp2365-2388.

[5] I. Daubechies, "Orthonormal bases of compactly supported wavelets", *Communications on Pure and Applied Mathematics*, vol. 41, 1988, pp909-996.

## Biographies

**A. P. Sakis Meliopoulos** (M '76, SM '83, F '93) was born in Katerini, Greece, in 1949. He received the M.E. and E.E. diploma from the National Technical University of Athens, Greece, in 1972; the M.S.E.E. and Ph.D. degrees from the Georgia Institute of Technology in 1974 and 1976, respectively. In 1971, he worked for Western Electric in Atlanta, Georgia. In 1976, he joined the Faculty of Electrical Engineering, Georgia Institute of Technology, where he is presently a professor. He is active in teaching and research in the general areas of modeling, analysis, and control of power systems. He has made significant contributions to power system grounding, harmonics, and reliability assessment of power systems. He is the author of the books, Power Systems Grounding and Transients, Marcel Dekker, June 1988, Ligthning and Overvoltage Protection, Section 27, Standard Handbook for Electrical Engineers, McGraw Hill, 1993, and the monograph, Numerical Solution Methods of Algebraic Equations, EPRI monograph series. Dr. Meliopoulos is a member of the Hellenic Society of Professional Engineering and the Sigma Xi.

**Chien-Hsing Lee** (M '94) was born in Taiwan on June 13, 1967. He received the Diploma of Electrical Engineering from National Kaohsiung Institute of Technology, Taiwan, the B.S. degree in electrical engineering from Arizona State University, Tempe, AZ, and the M.S.E.E degree from the Georgia Institute of Technology in 1987, 1993 and 1995, respectively. He is currently pursuing his Ph.D. degree at the Georgia Institute of Technology. His research interests are power system grounding analysis, power system transient modeling, applications of wavelet in power systems.

# An Efficient and Accurate Method of Incorporating Magnetic Saturation in the Physical-Variable Models of Synchronous Machines

S. D. Pekarek, Member and E. A. Walters, Student Member
School of Electrical and Computer Engineering
Purdue University
West Lafayette, IN 47907

*Abstract* - **In recent research, it has been shown that a physical-variable voltage-behind-reactance form of the synchronous machine model can be derived which is more numerically efficient than existing physical-variable models. In this research, a new voltage-behind-reactance model is derived which incorporates the effects of magnetic saturation. This model is shown to have the same numerical advantages of the unsaturated model, and is readily implemented in either circuit-based or differential-equation based simulation languages. An example system is provided which demonstrates the accuracy and efficiency of this model over a wide-range in operating conditions.**

## I. INTRODUCTION

In [1], a new synchronous machine model is presented which is shown to have significant advantages relative to existing models. It is readily implemented in either circuit-based languages or in differential-equation-based languages using the state model generation algorithm in [2]. This model is based upon standard representations and no approximations are made in its derivation. However, the numerical implementation is significantly more efficient than existing physical-variable models. In the example system studied, the given model gives rise to a 1700% increase in simulation speed with no discernible loss in accuracy.

In this paper, a new voltage-behind-reactance model is derived in which the effects of magnetic saturation are included. This model is based upon the technique of representing the derivative of the flux linkage versus current curve as an arctangent function described in [3]. It is readily implemented in circuit-based languages or in differential-equation based languages using the state model generation algorithm. Although it is substantially more accurate than existing physical-variable models; its implementation is no less computationally efficient. An example system is provided which demonstrates the accuracy and numerical efficiency of this model.

## II. VOLTAGE BEHIND REACTANCE REPRESENTATION

The dynamic equations of the synchronous machine are often expressed in the rotor frame of reference as [5]

$$v_{qs}^r = r_s i_{qs}^r + \omega_r \lambda_{ds}^r + p\lambda_{qs}^r \tag{1}$$

$$v_{ds}^r = r_s i_{ds}^r - \omega_r \lambda_{qs}^r + p\lambda_{ds}^r \tag{2}$$

$$v_{os} = r_s i_{os} + p\lambda_{os} \tag{3}$$

$$v_j = r_j i_j + p\lambda_j \; j = kq1 \ldots kqM, kd1 \ldots kdN, fd \tag{4}$$

where

$$\lambda_{qs}^r = L_{ls} i_{qs}^r + \lambda_{mq}^r \tag{5}$$

$$\lambda_{ds}^r = L_{ls} i_{ds}^r + \lambda_{md}^r \tag{6}$$

$$\lambda_j = L_{lj} i_j + \lambda_{mq}^r \; j = kq1 \ldots kqM \tag{7}$$

$$\lambda_j = L_{lj} i_j + \lambda_{md}^r \; kd1 \ldots kdN, fd \tag{8}$$

and

$$\lambda_{mq}^r = L_{mq}\left(i_{qs}^r + \sum_{j=1}^{M} i_{kqj}\right) \tag{9}$$

$$\lambda_{md}^r = L_{md}\left(i_{ds}^r + i_{fd} + \sum_{j=1}^{N} i_{kdj}\right) \tag{10}$$

Here, it is assumed the rotor contains $M$ amortissur windings in the $q$-axis, in addition to $N$ amortissuer and one field winding in the $d$-axis.

In order to optimize the efficiency of machine-converter simulations, a new synchronous machine model was recently set forth in [1]. In this model, the stator voltage equations are expressed in terms of physical variables as

$$\begin{aligned}\mathbf{v}_{abcs} = {} & \mathbf{r}_s''(\theta_r)\mathbf{i}_{abcs} + \mathbf{L}_{abcs}''(\theta_r)p\mathbf{i}_{abcs} + \\ & [p\mathbf{L}_{abcs}''(\theta_r)]\mathbf{i}_{abcs} + \mathbf{e}_{abcs}''\end{aligned} \tag{11}$$

The resistance and inductance matrices are given by

$$\mathbf{r}_{abcs}''(\theta_r) = \begin{bmatrix} r_S(2\theta_r) & r_M\left(2\theta_r - \frac{2\pi}{3}\right) & r_M\left(2\theta_r + \frac{2\pi}{3}\right) \\ r_M\left(2\theta_r - \frac{2\pi}{3}\right) & r_S\left(2\theta_r - \frac{4\pi}{3}\right) & r_M(2\theta_r) \\ r_M\left(2\theta_r + \frac{2\pi}{3}\right) & r_M(2\theta_r) & r_S\left(2\theta_r + \frac{4\pi}{3}\right) \end{bmatrix} \tag{12}$$

where

$$r_S(\cdot) = r_s + r_a - r_b\cos(\cdot) \tag{13}$$

$$r_M(\cdot) = -\frac{r_a}{2} - r_b\cos(\cdot) \tag{14}$$

$$r_a = \frac{r_d'' + r_q''}{3} - \frac{2}{3}r_s \tag{15}$$

$$r_b = \frac{r_d'' - r_q''}{3} \tag{16}$$

$$r_q'' = r_s + L_{mq}''^{2}\left(\sum_{j=1}^{M}\frac{r_{kqj}}{L_{lkqj}^2}\right) \tag{17}$$

$$r_d'' = r_s + \frac{L_{md}''^{2} r_{fd}}{L_{lfd}^2} + L_{md}''^{2}\left(\sum_{j=1}^{N}\frac{r_{kdj}}{L_{lkdj}^2}\right) \tag{18}$$

$$\mathbf{L}''_{abcs}(\theta_r) = \begin{bmatrix} L_S(2\theta_r) & L_M\left(2\theta_r - \frac{2\pi}{3}\right) & L_M\left(2\theta_r + \frac{2\pi}{3}\right) \\ L_M\left(2\theta_r - \frac{2\pi}{3}\right) & L_S\left(2\theta_r - \frac{4\pi}{3}\right) & L_M(2\theta_r) \\ L_M\left(2\theta_r + \frac{2\pi}{3}\right) & L_M(2\theta_r) & L_S\left(2\theta_r + \frac{4\pi}{3}\right) \end{bmatrix} \tag{19}$$

where

$$L_S(\cdot) = L_s + L_a - L_b\cos(\cdot) \tag{20}$$

$$L_M(\cdot) = -\frac{L_a}{2} - L_b\cos(\cdot) \tag{21}$$

$$L_a = \frac{L''_{mq} + L''_{md}}{3} \tag{22}$$

$$L_b = \frac{L''_{md} - L''_{mq}}{3} \tag{23}$$

and the back emf is expressed

$$\mathbf{e}''_{abcs} = [\mathbf{K}^r_s]^{-1} \begin{bmatrix} e''_q \\ e''_d \\ 0 \end{bmatrix} \tag{24}$$

where

$$e''_q = \omega_r \lambda''_d + \left( \sum_{j=1}^{M} \frac{L''_{mq} r_{kqj}}{L^2_{lkqj}} (\lambda''_q - \lambda_{kqj}) \right) \tag{25}$$

$$e''_d = -\omega_r \lambda''_q + \sum_{j=1}^{N} \frac{L''_{md} r_{kdj}}{L^2_{lkdj}} (\lambda''_d - \lambda_{kdj}) + \tag{26}$$

$$v_{fd}\frac{L''_{md}}{L_{lfd}} + \frac{L''_{md} r_{fd}}{L^2_{lfd}} (\lambda''_d - \lambda_{fd})$$

Here it is assumed that all rotor quantities are referred to the stator using the appropriate turns ratio. Double primes represent the subtransient quantities of the machine.

The stator voltage equations given by (11), along with the rotor voltage equations

$$p\lambda_j = -\frac{r_j}{L_{lj}}(\lambda_j - \lambda_{mq}) + v_j ;\ j = kq1, \dots kqM \tag{27}$$

$$p\lambda_j = -\frac{r_j}{L_{lj}}(\lambda_j - \lambda_{md}) + v_j ;\ j = fd,\ kd1, \dots kdN \tag{28}$$

where $\lambda_{mq}$ and $\lambda_{md}$ are given by

$$\lambda_{mq} = L''_{mq}\left( i^r_{qs} + \sum_{j=1}^{M} \frac{\lambda_{kqj}}{L_{lkqj}} \right) \tag{29}$$

$$\lambda_{md} = L''_{md}\left( i^r_{ds} + \frac{\lambda_{fd}}{L_{lfd}} + \sum_{j=1}^{N} \frac{\lambda_{kdj}}{L_{lkdj}} \right) \tag{30}$$

define the so-called voltage-behind-reactance (VBR) model of the synchronous machine. It is important to note that no approximations were made in its derivation. Neglecting numerical error, the solution of the corresponding equations should yield the same time-domain response as the coupled-circuit model upon which it is based. Moreover, no assumptions have been made in regard to the stator winding configuration. The windings may be connected in wye, delta, or the individual windings may be supplied to isolated converter circuits. With only minor modification, the model may be extended to include machines with an arbitrary number of stator phases.

When implementing the VBR model, only the stator branches and nodes are included when defining the circuit topology. The rotor voltage equations are expressed explicitly in state model form with rotor flux linkages as state variables. The subtransient voltages represent outputs of the rotor model and are incorporated in the stator circuit as dependent sources. The stator branch currents are transformed into the rotor reference frame and represent inputs to the rotor state model. A circuit/block diagram of the VBR model is given in Fig. 2 In [1], it was shown that the VBR model is significantly more efficient than standard circuit-based models. For the example system, a 1700% increase in simulation speed was documented. The increased efficiency results from the fact that the rotor equations are not expressed in a coupled-circuit form. Therefore, the size of the matrices used in circuit-based approaches (both differential-equation based and discrete-circuit based) is significantly reduced and the eigenstructure of the resulting system is more numerically stable [1].

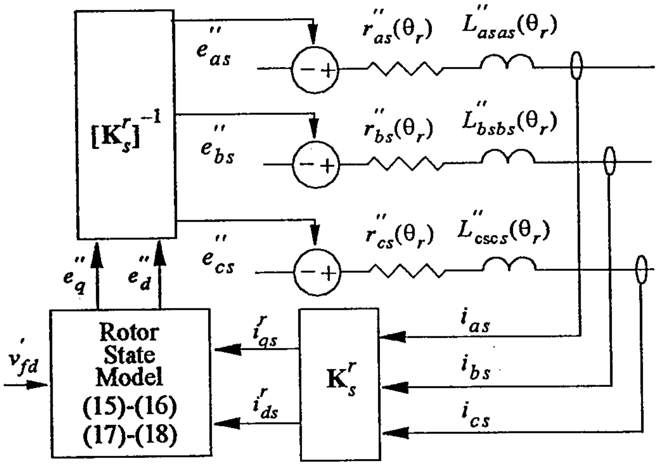

Fig. 1 Voltage-behind-reactance machine mode (saturation neglected)l.

## III. INCORPORATING MAGNETIC SATURATION IN THE Q-D REFERENCE FRAME

Several techniques exist for incorporating magnetic saturation in the q-d synchronous machine model. Traditional approaches [6] have used iterative techniques or polynomial approximations to include the effects of saturation. More recently, magnetic circuits have been derived and duality used to form equivalent electrical representations of saturated parts of the machine [7]-[9]. These models have been shown to provide accurate representations of magnetic saturation; however, obtaining the necessary parameters often requires finite element analysis or magnetic search coils to be mounted in the machine. A new method of incorporating saturation in the q-d model of the synchronous machine was described in [3]. Therein, an arctangent function is used to approximate the derivative of the magnetizing current versus flux linkage curve. From this, an explicit function is derived relating the magnetizing current to the magnetizing flux linkage in either axis of the machine. The advantage of this method is that i) the current versus flux curve is approximated over a large operating region ii) it is non-iterative iii) saturation is represented using only four parameters, all having physical significance iv) no noise in estimating derivatives. It is useful to provide a brief description of this method before deriving the physical variable models.

In [3], the magnetizing current $i_{md}$ is expressed as a function of the magnetizing flux linkage,

$$i_{md}(\lambda_{md}) = F(\lambda_{md}) \tag{31}$$

In order to derive the function, a plot of the $d$-axis magnetizing current versus flux linkage curve of a 3.7 kW machine is shown in Fig. 2 [3]. The slope of this curve is constant in the unsaturated region, undergoes a transition, and finally is constant in the highly-saturated region. Thus, as described in [3], it is reasonable to expect the slope of this curve may be approximated by an arctangent function of the form

$$\frac{\partial F(\lambda^r_{md})}{\partial \lambda^r_{md}} = \frac{2}{\pi} M_d \operatorname{atan}(\tau_T(\lambda^r_{md} - \lambda_T)) + M_a \tag{32}$$

where $M_d$ and $M_a$ are related to the initial and final slopes of the saturation function by

$$M_d = \frac{M_f - M_i}{2} \tag{33}$$

$$M_a = \frac{M_f + M_i}{2} \tag{34}$$

and $\tau_T$ and $\lambda_T$ define the tightness of the transition from initial slope to final slope and the point of transition, respectively. Integrating (32) subject to the condition that zero magnetizing flux yields zero magnetizing current, the function $F(\lambda_{md})$ may be expressed

$$\begin{aligned} F(\lambda^r_{md}) = {} & \frac{2M_d}{\pi}[(\lambda_{md} - \lambda_T)\operatorname{atan}(\tau_T(\lambda^r_{md} - \lambda_T)) + \tau_T \operatorname{atan}(-\tau_T\lambda_T)] \\ & + \frac{M_d}{\pi\tau_T}[\ln(1 + \tau_T^2\lambda_T^2) - \ln(1 + \tau_T^2(\lambda^r_{md} - \lambda_T)^2)] + M_a\lambda^r_{md} \end{aligned} \tag{35}$$

A similar function may be derived if saturation is assumed in the $q$-axis. As shown in Fig. 2, (35) provides an excellent fit to the experimentally measured curve. The parameters used to model the saturation of this machine are listed in Table 1 . A method for incorporating this function (nonliterary) in the $q$-$d$ model of the synchronous machine is described in [3].

## IV. VOLTAGE BEHIND REACTANCE REPRESENTATION WITH MAGNETIC SATURATION INCLUDED

In the VBR model described in Section II, the stator and rotor systems are effectively partitioned. The rotor circuits are expressed in state-model form, while the stator circuits are expressed in a circuit-based form. This results from the fact that in the unsaturated model, the magnetizing flux linkages can be separated into stator and rotor components. For example, the $d$-axis magnetizing flux linkage may be expressed

Fig. 2 Measured and fitted $d$-axis magnetizing current versus magnetizing flux

$$\lambda^r_{md} = L''_{md}(i^r_{ds}) + L''_{md}\left(\frac{\lambda_{fd}}{L_{lfd}} + \sum_{j=1}^{N}\frac{\lambda_{kdj}}{L_{lkdj}}\right) \tag{36}$$

A linear partitioning cannot be applied to the saturated model because the magnetizing flux linkages are no longer linear functions of the stator and rotor currents (or flux linkages). In order to express the stator voltage equations in a voltage-behind-reactance form, a new partitioning must be derived in which the nonlinearity of the magnetizing flux linkages is portrayed in both the stator and rotor equations.

This can be achieved by first expressing the $d$-axis magnetizing current as the fitted function of the magnetizing flux linkage ((31)- (35)). From this, the derivative of the magnetizing current may be expressed in terms of the derivative of the magnetizing flux linkage as

$$pi^r_{md} = \frac{\partial F_{md}(\lambda^r_{md})}{\partial \lambda^r_{md}} p\lambda^r_{md} = pi^r_{ds} + pi_{fd} + \sum_{j=1}^{N} pi_{kdj} \tag{37}$$

In this research, a salient-pole machine is considered and thus magnetic saturation is included in only the $d$-axis. Experimental results verify this assumption. A parallel approach can be used in modeling round rotor machines. Therefore, the derivative of the q-axis magnetizing current may be expressed

$$pi^r_{mq} = \frac{1}{L_{mq}} p\lambda^r_{mq} = pi^r_{qs} + \sum_{j=1}^{M} pi_{kqj} \tag{38}$$

Taking the derivative of the rotor flux linkages and substituting for the derivatives of the rotor currents, (37) and (38) may be rewritten as

$$\frac{1}{L_{mq}} p\lambda^r_{mq} = pi^r_{qs} + \sum_{j=1}^{M} p\left(\frac{\lambda_{kqj} - \lambda^r_{mq}}{L_{lkqj}}\right) \tag{39}$$

$$\frac{\partial F(\lambda^r_{md})}{\partial \lambda^r_{md}} p\lambda^r_{md} = pi^r_{ds} + p\left(\frac{\lambda_{fd} - \lambda^r_{md}}{L_{lfd}}\right) + \sum_{j=1}^{N} p\left(\frac{\lambda_{kdj} - \lambda^r_{md}}{L_{lkdj}}\right) \tag{40}$$

bringing the derivatives of the magnetizing flux linkages to one side yields

$$p\lambda^{r}_{mq} = L''_{mq}\left[pi^{r}_{qs} + \sum_{j=1}^{M} p\left(\frac{\lambda_{kqj}}{L_{lkqj}}\right)\right] \tag{41}$$

$$p\lambda^{r}_{md} = L''_{md}(\lambda^{r}_{md})\left[pi^{r}_{ds} + p\left(\frac{\lambda_{fd}}{L_{lfd}}\right) + \sum_{j=1}^{N} p\left(\frac{\lambda_{kdj}}{L_{lkdj}}\right)\right] \tag{42}$$

where

$$L''_{mq} = \left[\frac{1}{L_{mq}} + \sum_{j=1}^{M}\frac{1}{L_{lkqj}}\right]^{-1} \tag{43}$$

$$L''_{md}(\lambda^{r}_{md}) = \left[\frac{\partial F(\lambda^{r}_{md})}{\partial \lambda^{r}_{md}} + \frac{1}{L_{lfd}} + \sum_{j=1}^{N}\frac{1}{L_{lkdj}}\right]^{-1} \tag{44}$$

Substituting (41) and (42) into (1) and (2), the stator voltage equations may be rewritten as

$$v^{r}_{qs} = r_s i^{r}_{qs} + \omega_r(L_{ls} i^{r}_{ds} + \lambda_{md}) + L''_{q} p i^{r}_{qs} + L''_{mq}\sum_{j=1}^{M}\frac{p\lambda_{kqj}}{L_{lkqj}} \tag{45}$$

$$v^{r}_{ds} = r_s i^{r}_{ds} - \omega_r(L_{ls} i^{r}_{qs} + \lambda_{mq}) + L''_{d}(\lambda^{r}_{md}) p i^{r}_{ds} \tag{46}$$

$$+ L''_{d}(\lambda^{r}_{md})\frac{p\lambda_{fd}}{L_{lfd}} + L''_{d}(\lambda^{r}_{md})\sum_{j=1}^{N}\frac{p\lambda_{kdj}}{L_{lkdj}}$$

where

$$L''_{q} = L_{ls} + L''_{mq} \tag{47}$$

$$L''_{d}(\lambda^{r}_{md}) = L_{ls} + L''_{mq}(\lambda^{r}_{md}) \tag{48}$$

Expressions for the derivatives of the rotor flux linkages are obtained by manipulating the rotor flux-linkage equations (7)-(8). Using

$$i_j = \frac{1}{L_{lj}}(\lambda_j - \lambda_{mq})\,;\; j = kq1, \ldots kqM \tag{49}$$

$$i_j = \frac{1}{L_{lj}}(\lambda_j - \lambda_{md})\,;\; j = fd, kd1, \ldots kdN \tag{50}$$

for the rotor currents and substituting the resulting expressions into (45) and (46) yields, after algebraic manipulation, an exact voltage-behind-reactance form of the stator voltage equations

$$v^{r}_{qs} = r_s i^{r}_{qs} + \omega_r L_{ls} i^{r}_{ds} + L''_{q} p i^{r}_{qs} + e_q \tag{51}$$

$$v^{r}_{ds} = r_s i^{r}_{ds} - \omega_r L_{ls} i^{r}_{qs} + L''_{d}(\lambda^{r}_{md}) p i^{r}_{ds} + e_d \tag{52}$$

$$e_q = \omega_r \lambda_{md} + \left(\sum_{j=1}^{M}\frac{L''_{mq} r_{kqj}}{L^{2}_{lkqj}}(\lambda^{r}_{mq} - \lambda_{kqj})\right) \tag{53}$$

$$e_d = -\omega_r \lambda_{mq} + \sum_{j=1}^{N}\frac{L''_{md} r_{kdj}}{L^{2}_{lkdj}}(\lambda^{r}_{md} - \lambda_{kdj}) + \tag{54}$$

$$v_{fd}\frac{L''_{md}}{L_{lfd}} + \frac{L''_{md} r_{fd}}{L^{2}_{lfd}}(\lambda^{r}_{md} - \lambda_{fd})$$

These equations may be transformed to physical variables by applying the inverse of Park's transformation to (3), (45) and (46), which yields,

$$\mathbf{v}_{abcs} = \mathbf{r}_s \mathbf{i}_{abcs} + \mathbf{L}_{abcs}(\theta_r, \lambda^{r}_{md}) p \mathbf{i}_{abcs} \tag{55}$$

$$+ \omega_r \frac{\partial}{\partial \theta_r}(\mathbf{L}_{abcs}(\theta_r, \lambda^{r}_{md}))\mathbf{i}_{abcs} + \mathbf{e}_{abcs}$$

where $\mathbf{r}_s$ is a diagonal matrix of the stator winding resistances and

$$\mathbf{e}_{abcs} = [\mathbf{K}^{r}_{s}]^{-1}\begin{bmatrix} e_q \\ e_d \\ 0 \end{bmatrix} \tag{56}$$

The inductance matrix is given by

$$\mathbf{L}_{abcs}(\theta_r, \lambda^{r}_{md}) = \begin{bmatrix} L_S(2\theta_r) & L_M\left(2\theta_r - \frac{2\pi}{3}\right) & L_M\left(2\theta_r + \frac{2\pi}{3}\right) \\ L_M\left(2\theta_r - \frac{2\pi}{3}\right) & L_S\left(2\theta_r - \frac{4\pi}{3}\right) & L_M(2\theta_r) \\ L_M\left(2\theta_r + \frac{2\pi}{3}\right) & L_M(2\theta_r) & L_S\left(2\theta_r + \frac{4\pi}{3}\right) \end{bmatrix} \tag{57}$$

where

$$L_S(\cdot) = L_s + L_a(\lambda^{r}_{md}) - L_b(\lambda^{r}_{md})\cos(\cdot) \tag{58}$$

$$L_M(\cdot) = -\frac{L_a(\lambda^{r}_{md})}{2} - L_b(\lambda^{r}_{md})\cos(\cdot) \tag{59}$$

$$L_a(\lambda^{r}_{md}) = \frac{L''_{mq} + L''_{md}(\lambda^{r}_{md})}{3} \tag{60}$$

$$L_b(\lambda^{r}_{md}) = \frac{L''_{md}(\lambda^{r}_{md}) - L''_{mq}}{3} \tag{61}$$

The stator voltage equations given by (55), along with the magnetizing flux linkage equations (41) and (42), and rotor voltage equations

$$p\lambda_j = -\frac{r_j}{L_{lj}}(\lambda_j - \lambda_{mq}) + v_j\,;\; j = kq1, \ldots kqM - 1 \tag{62}$$

$$p\lambda_j = -\frac{r_j}{L_{lj}}(\lambda_j - \lambda_{md}) + v_j\,;\; j = fd, kd1, \ldots kdN - 1 \tag{63}$$

define the so-called voltage-behind-reactance saturation (VBRS) model of the synchronous machine. It is important to note that the magnetizing flux linkages replace one of the rotor flux linkages as state variables in each axis. In this derivation no assumptions have been made in regard to the stator winding configuration. The windings may be connected in wye, delta, or the individual windings may be supplied to isolated converter circuits. With only minor modification, the model may be extended to include machines with an arbitrary number of stator phases.

The VBRS model is compatible with both circuit-based or differential-equation based programming languages. The implementation is similar to the VBR model in that only the stator branches and nodes are included when defining the circuit topology. The derivatives of the $q$- and $d$-axis magnetizing flux linkages, the $M-1$ $q$-axis and $N-1$ $d$-axis amortissuer rotor voltage equations, and the field voltage equation, are expressed explicitly in state model form with magnetizing and rotor flux inkages as state variables. The magnetizing and rotor flux linkges represent outputs of the airgap-rotor model and are incorporated in the stator circuit as dependent voltage sources. The stator branch currents and their derivatives are transformed into the otor reference frame and represent inputs to the airgap-rotor state model. A circuit/block diagram of the VBRS model is given in Fig. 3.

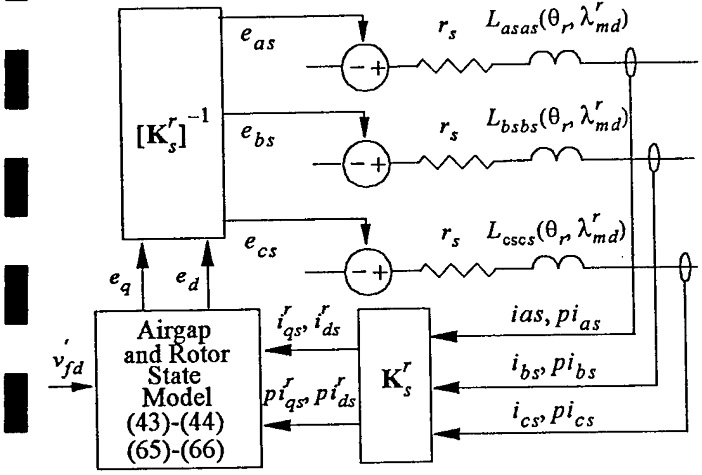

Fig. 3 Voltage-behind-reactance machine model (saturation included).

## V. SATURATION MODEL VERIFICATION

In order to illustrate the accuracy of the VBRS model, an experimental system consisting of a 3.7 kW synchronous machine connected to a line-commutated converter was simulated. A circuit diagram of this system is shown in Fig. 4. The synchronous machine parameters, as determined by standstill frequency response testing, as well as the saturation model parameters, are summarized in Table 1. .

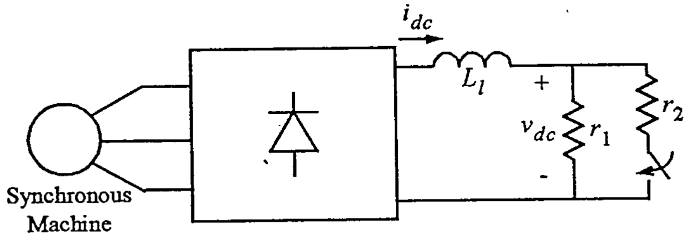

Fig. 4 Step Load Test Configuration

| | | |
|---|---|---|
| $r_s$ = 382 mΩ | $L_{ls}$ = 0.83 mH | $L_{mq}$ = 13.5 mH |
| $r_{kd1}$ = 40.47 Ω | $L_{lkd1}$ = 4.73 mH | $r_{kq1}$ = 31.8 Ω |
| $r_{kd2}$ = 1.31 kΩ | $L_{lkd2}$ = 3.68 mH | $r_{kq2}$ = 0.923 Ω |
| $r_{fd}$ = 122 mΩ | $L_{lfd}$ = 2.54 mH | $\frac{N_s}{N_{fd}}$ = 0.0269 |
| $L_{md}$ = 39.27 mH | $L_{lkq1}$ = 6.13 mH | $L_{lkq2}$ = 3.4 mH |
| $M_a$ = 140 | $M_d$ = 120 | 4 Poles |
| $\lambda_T$ = 0.5 | $\tau_T$ = 29 | |

Table 1: Synchronous machine parameters.

In the first computer study, it is assumed that the system is initially operating in the steady state with a base load resistance of 66.11 Ω connected to the dc output terminals. A second load resistance of 57.9 Ω is then connected in parallel with the original load. The machine is operated at a fixed electrical speed of 377 rad/sec with a constant field voltage of 0.6896 V as the switch is closed. The VBR and VBRS models were implemented in ACSL [4] using the state model generation algorithm described in [2]. The simulated response of both the VBR and VBRS model is shown along with the experimentally measured response in Fig. 5. As shown, the measured and simulated responses are in excellent agreement. In this system, the field current is low, and thus the unsaturated and saturated models yield the same response. In calculating the responses depicted in Fig. 5, Gear's algorithm was used with a maximum and minimum time step of $1 \times 10^{-4}$ and $1 \times 10^{-7}$ sec, respectively. The local truncation error, which is used to determine the actual time step, was set to $1 \times 10^{-4}$ for all state variables. When a change in topology (change in diode conduction state) is sensed, the time step is reduced and the preceding calculation is repeated so as to limit the uncertainty in switching time to less than the minimum time step. Following each topological change, the time step is set to its minimum value and the integration algorithm is reset. Subsequent time steps are adjusted in accordance with Gear's criteria [12]. The CPU time needed to calculate the VBRS and VBR responses on a 200 Mhz Pentium-based PC were 12.29 and 12.55 sec., respectively.

In the second computer study, the machine is operated with a constant field voltage of 2.84 V as the switch is closed. In this experiment, the field resistance drifted slightly from the previous experiment to 0.135 . The load resistance changed slightly to values of 67.03 and 57.9 Ω respectively. The simulated response of the VBRS model is shown along with the experimentally measured response in Fig. 6. The response of the VBR model in which saturation was not represented is again included. As shown, the measured and the simulated VBRS responses are in excellent agreement. However, the response predicted by the VBR model is significantly less accurate. In this system, the field current is much larger than in the previous study, and thus the machine is operating in a saturated region. This is particularly evident in the responses of the rectifier output voltage and the field current. The CPU time needed to calculate the VBRS and VBR responses were 12.40 and 12.59 sec., respectively. From this it is seen that the VBRS model is more accurate and is as numerically efficient as the VBR model.

## VI. SUMMARY

A new physical-variable voltage-behind-reactance model of the synchronous machine is derived in which the effects of magnetic saturation are included. This models is flexible with regard to the stator winding configuration, and is compatible with circuit-based and differential-equation-based simulation approaches. Experimental results are included in which the accuracy of the model is demonstrated over a wide range of operating conditions.

## VII. ACKKNOWLEDGEMENTS

This work was supported in part by P. C. Krause and Associates under contract N00024-93-C-4180 with Naval Surface Warfare Center and in part by University of South Carolina under Grant No. N00014-96-1-0926 with Office of Naval Research.

## VIII. REFERENCES

[1] S. D. Pekarek, O. Wasynczuk, H. J. Hegner "An Efficient and Accurate Model for the Simulation and Analysis of Synchronous Machine/Converter Systems," accepted for publication in *IEEE Transactions on Energy Conversion*, PE #

[2] O. Wasynczuk and S. D. Sudhoff, "Automated State Model Generation Algorithm for Power Circuits and Systems," Paper 96 WM 259-2 PWRC presented at the IEEE Power Engineering Society Winter Meeting, Baltimore, MD, Jan. 21-25, 1996.

[3] K. A. Corzine, B. T. Kuhn, S. D. Sudhoff, H.J. Hegner, "An Improved Method For Incorporating Magnetic Saturation In The Q-D Synchronous Machine Model," Submitted to IEEE Transactions on Energy Conversion, January 1996.

[4] Mitchell and Gauthier Associates, Advanced Continuous Simulation Language Reference Manual," Concord, MA, 1993.

[5] P. C. Krause, O. Wasynczuk, and S. D. Sudhoff, **Analysis of Electric Machinery**, IEEE Press, Piscataway, NJ, 1995.

[6] C. H. Thomas, Discussion of "Analogue Computer Representation of Synchronous Generators in Voltage-Regulation Studies," *Transactions of AIEE* (Power Apparatus and Systems), vol. 75, December 1956, pp. 1182-1184.

[7] G. R. Slemon, "An Equivalent Circuit Approach to Analysis of Synchronous Machines With Saliency and Saturation," *IEEE Transactions of Energy Conversion*, vol. 5, no. 3, September 1990, pp. 538-545.

[8] J. O. Ojo, T. A. Lipo, "An Improved Model for Saturated Salient Pole Synchronous Motors," *IEEE Transactions on Energy Conversion*, vol. 4, no. 1, March 1989, pp. 135-142.

[9] I. Boldea and S. A. Nasar, "A General Equivalent Circuit (GEC) of Electric Machines," *IEEE Transactions on Energy Conversion*, Vol. 3, no. 3, September 1988, pp. 689-695.

[10] S. D. Sudhoff, "Waveform Reconstruction From the Average-Value Model of Line-Commutated Converter - Synchronous Machine Systems," *IEEE Transactions on Energy Conversion*, Vol. 8, No. 3, pp. 404-410, September 1993.

[11] L. O. Chua, P-M Lin, **Computer Aided Analysis of Electronic Circuits: Algorithms and Computational Techniques**, Prentice-Hall, Englewood Cliffs, New Jersey, 1975.

[12] C. W. Gear, **Numerical Initial Value Problems in Ordinary Differential Equations**, Prentice Hall, NJ, 1971.

**Steven D. Pekarek** was born in Oak Park, Illinois on December 22, 1968. He received the B.S.E.E, M.S.E.E, and Ph.D. degrees from Purdue University in 1991, 1993, and 1996, respectively, and is currently a post-doctoral research engineer. His interests include electric machines and automatic control.

**Eric A. Walters** was born in Sullivan, Indiana on April 28, 1972. He received the B.S.E.E, M.S.E.E, degrees from Purdue University in 1994, 1995 respectively, and is currently pursuing his Ph.D. His interests include power electronics and electric machines.

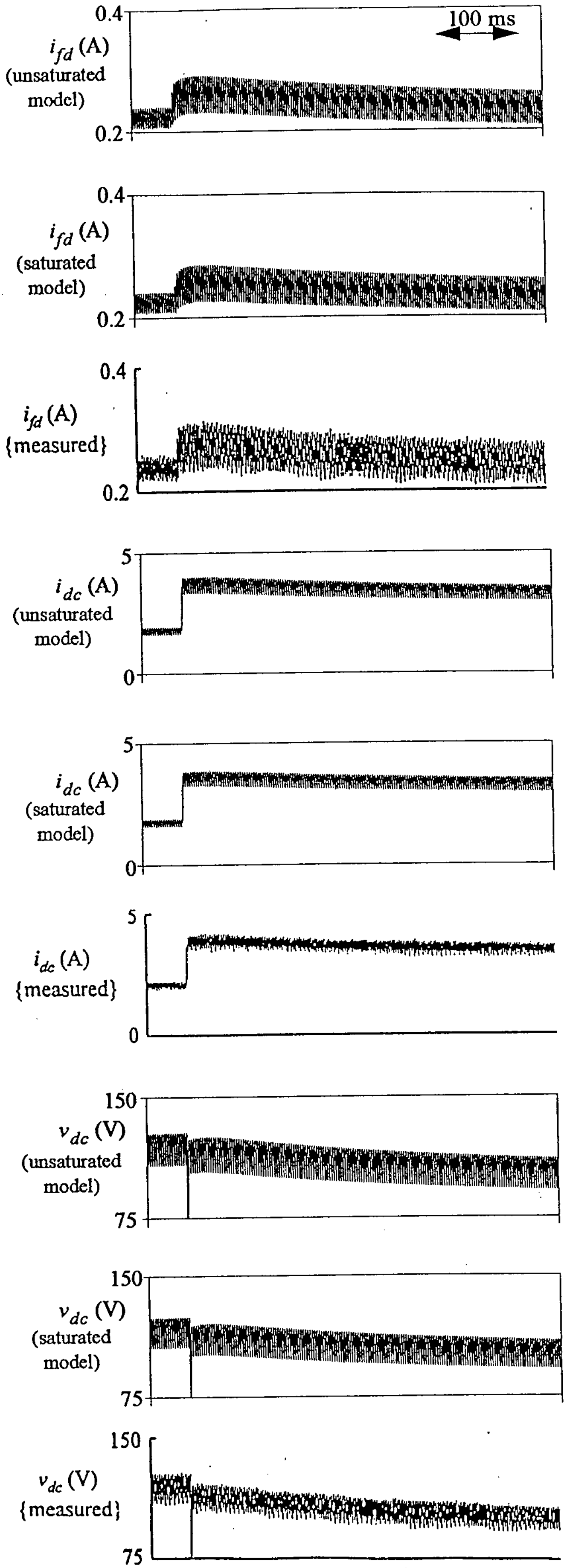

Fig. 5 System dynamics (low field current case)

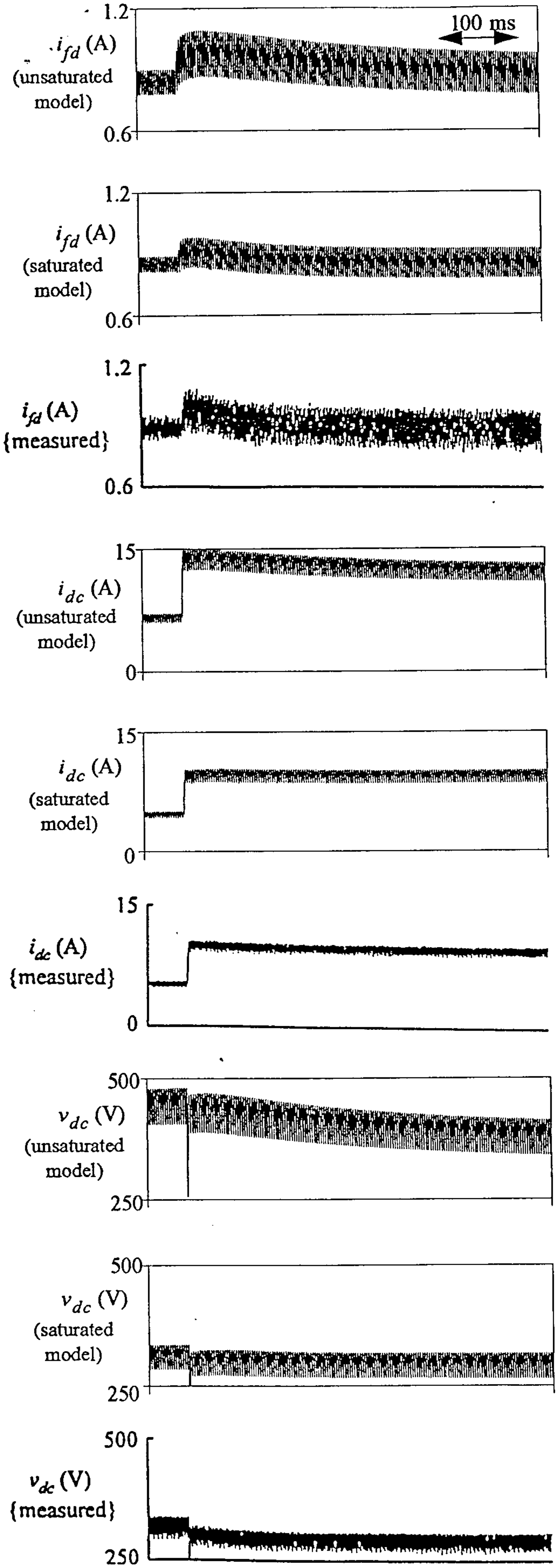

Fig. 6 System dynamics (high field current)

# A Fast and Efficient Multi-Rate Technique For Detailed Simulation of AC/DC Power Systems

S. D. Pekarek, Member
O. Wasynczuk, Senior Member
School of Electrical and Computer Engineering
Purdue University
West Lafayette, Indiana

H. J. Hegner, Member
Naval Surface Warfare Center
Annapolis, Maryland

*Abstract* - **A technique to perform multi-rate simulations of AC/DC power systems is presented which is readily implemented in either circuit-based or differential-equation-based simulation languages. In this method, the partitioning of the system is accomplished using an exact voltage-behind-reactance model of the synchronous machine. It is therefore easy to implement and does not require eigensystem partitioning algorithms. The partitioned system is integrated separately, and thus any fixed-step or variable-step integration algorithm can be used to solve the fast and slow systems respectively. An example synchronous machine-converter system is provided which demonstrates a 350% increase in simulation speed over the most efficient single-rate simulations with little observable loss in accuracy.**

## I. INTRODUCTION

It is well known that an inherent stiffness exists in the dynamics of most power systems. The stiffness results from the differences in the dynamics of the stator network, the rotor circuits, and the rotor mechanical system. The techniques used to efficiently solve these systems have traditionally fallen into one of two general categories. In the first category, stiffly-stable variable-step numerical integration algorithms, such as Gear's [1] are used. Although there are several strict definitions used to characterize an algorithm as stiffly-stable, the main property is the ability to vary the integration step size over a wide range of values while maintaining numerical stability. Stiffly-stable algorithms are often applied to the simulation of power systems. Although effective, their efficiency can be significantly reduceds when simulating AC/DC power systems which include switching circuits (converters, inverters). In these systems, switching results in a change in topology of the stator-network and possible discontinuities in the state variables. If variable-step integration algorithms are used, the time step is reduced to its minimum value and the integration algorithm is reset each time a change in topology occurs. In addition, because several of the states associated with the fast dynamics contain switching transients, the fast dynamics may continue to be dominant over the entire course of integration and therefore the maximum integration time-step that can be used to solve the system is limited.

In the second category, time-scale separation techniques are applied. Therein, the system is decoupled into states with fast and slow dynamics respectively. Once partitioned, different methods can be used to solve the resulting equations. One such method that has been used is multi-rate integration [2]-[5] wherein different time steps are used to solve the fast and slow systems, respectively. These methods have been applied to simulations of power systems with successful results [4]-[5]. Although effective, their use has been limited by the fact that multi-rate integration algorithms are not included in most commercially available simulation packages, such as Spice [6], Saber [7], EMTP [8], etc. Therefore, the system analyst, must establish and program these algorithms.

In this paper, a technique to perform multi-rate simulations of switched power networks is described. The partitioning of the system is based upon the exact voltage-behind-reactance model of the synchronous machine derived in [10]. Applying this method, any standard fixed- or variable-step integration algorithm can be used to solve the fast or slow systems respectively. Therefore, it is compatible with existing commercial dynamic simulation software (both circuit-based or differential-equation based), and does not require any integration algorithm programming by the system analyst. An example synchronous machine-converter system is provided which demonstrates a 350% increase in simulation speed over the most efficient single-rate simulations with little observable loss in accuracy.

## II. MULTI-RATE SIMULATION

The solution of power system dynamic equations is typically accomplished using numerical integration. The numerical integration of a system of differential equations

$$p\mathbf{x} = \mathbf{f}(\mathbf{x}, t) \tag{1}$$

is achieved using either explicit (Runge-Kutta, Forward-Euler, Taylor) or implicit algorithms (Adams Moulton, Gear's, Backward-Euler). If explicit algorithms are used, (1) is discretized into a form

$$\mathbf{x}_{n+1} = \mathbf{x}_n + h\sum_{i=0}^{m} a_i\mathbf{f}(\mathbf{x}_{n-i}) \tag{2}$$

where the values of the $a_i$'s are dependent upon the chosen algorithm. If implicit algorithms are used, (1) is discretized into a form

$$\mathbf{x}_{n+1} = \mathbf{x}_n + h\sum_{i=-1}^{m} a_i\mathbf{f}(\mathbf{x}_{n-i}) \tag{3}$$

The term implicit refers to the presence of $\mathbf{x}_{n+1}$ on both sides of the equal sign in (3). Both explicit and implicit algorithms can have fixed time-steps, or the time-step may be allowed to change (variable-step) throughout the integration. The stability properties of these algorithms vary; however; stiffly-stable algorithms, such as Gear's, are always implicit. Thus, although the time-step can be increased by orders of magnitude through a simulation, the solution of the implicit equations can be computationally intensive for large systems. Furthermore, when simulating systems which include switching circuits, (Fig. 1), switching results in a change in topology of the stator-network and possible discontinuities in the state variables. If variable-step integration algorithms are used, the time step is reduced to its minimum value and the integration algorithm is reset each time a change in topology occurs. In addition, because several of the states associated with the fast dynamics contain switching transients, the fast dynamics may continue to be dominant over the entire course of integration and therefore the maximum integration time-step that can be used to solve the system is limited.

An alternative technique that has been applied to efficiently solve stiff systems is multi-rate integration. Therein, a system of differential equations

$$p\mathbf{x} = \mathbf{f}(\mathbf{x}, t) \tag{4}$$

is expressed in decoupled form as

$$p\mathbf{x} = \begin{bmatrix} p\mathbf{x}_f \\ p\mathbf{x}_s \end{bmatrix} = \begin{bmatrix} \mathbf{f}_f(\mathbf{x}_f, \mathbf{x}_s, t) \\ \mathbf{f}_s(\mathbf{x}_f, \mathbf{x}_s, t) \end{bmatrix} \tag{5}$$

where $\mathbf{x}_f$ and $\mathbf{x}_s$ are vectors containing the states with fast and slow dynamics respectively. The partitioning is most readily accomplished if there is apriori knowledge of the system. However, transformations have been derived in which the model is partitioned based upon the calculated eigenvalues of the linearized model [2]-[3]. Once partitioned, different time steps are used to solve the fast and slow systems, respectively. It is interesting to consider the numerical problems that must be addressed when solving a partitioned system using different time steps. Although the problems are present regardless of the integration algorithms used, it is convenient to assume that both the fast and slow equations of the partitioned model in (5) are solved using a second-order Runge-Kutta algorithms. Therein, the systems is solved using discrete equations of the form.

$$\mathbf{x}_{f(n+1)} = \mathbf{x}_{f(n)} + \frac{h_1}{2}(\mathbf{k}_{f1} + \mathbf{k}_{f2}) \tag{6}$$

$$\mathbf{x}_{s(n+1)} = \mathbf{x}_{s(n)} + \frac{h_2}{2}(\mathbf{k}_{s1} + \mathbf{k}_{s2}) \tag{7}$$

where

$$\mathbf{k}_{f1} = \mathbf{f}_f(\mathbf{x}_{f(n)}, \mathbf{x}_s(t_{f(n)}), t_{f(n)}) \tag{8}$$

$$\mathbf{k}_{f2} = \mathbf{f}_f(\mathbf{x}_{f(n)} + h_1\mathbf{k}_{f1}, \mathbf{x}_s(t_{f(n)} + h_1), t_{f(n)} + h_1) \tag{9}$$

$$\mathbf{k}_{s1} = \mathbf{f}_s(\mathbf{x}_f(t_{s(n)}), \mathbf{x}_{s(n)}(t_{s(n)}), t_{s(n)}) \tag{10}$$

$$\mathbf{k}_{f2} = \mathbf{f}_f(\mathbf{x}_f(t_{s(n)} + h_2), \mathbf{x}_{s(n)} + h_2\mathbf{k}_{s1}, t_{s(n)} + h_2) \tag{11}$$

Here $h_1$ and $h_2$ represent the time steps of the fast and slow systems, respectively. Since $h_1 \neq h_2$, difficulties arise because the time step of the slow system does not correspond to that of the fast system. In order to advance the fast system to the next step, $f_f$ must be evaluated at different points on the interval from $t_{f(n)}$ to $t_{f(n+1)}$. However, because the slow states are integrated at a different rate, their values may not be known at these points. The same problem occurs when advancing the slow system to the next step.

Imbedded forms of various integration algorithms have been derived in which these problems are addressed [2]-[5]. In the imbedded Runge-Kutta scheme described in [2], a polynomial approximation is used to determine the values of the slow states needed to advance the fast system. The fast system is then integrated to the points needed to advanced the slow system.

Although imbedded algorithms have been shown to be an effective means of applying multi-rate techniques, most commercially available simulation software does not contain provisions to apply these methods. Imbedded algorithms must be established by the system analyst. Furthermore, the flexibility of using imbedded schemes is limited since the same integration algorithm is used to solve the fast and slow dynamics of the system.

Additional problems are encountered when attempting to apply standard multi-rate techniques in circuit-based or differential-equation based languages in which algorithmic state model generation is used. In circuit-based languages the differential equations are discretized at the branch level providing an algebraic equation relating branch voltages and currents at any given instant of time to their past values. A state model is never formed; inductors and capacitors are replaced by discrete-circuit equivalent models which are functions of the specific integration algorithm that is chosen. Therefore, partitioning the system algorithmically would involve separating the system based upon the values of the inductances and capacitances in the circuit. If imbedded algorithms are applied, the inductive or capacitive branches would be at a different instants in time, making it difficult to solve for the branch currents and voltages of the entire system. In differential-equation based languages in which the algorithmic state model generation is applied, the eigenvalues of the system can be calculated. However, in machine-converter circuits the eigenvalues are functions of rotor position and the switching of the converter. An algorithmic method of partitioning the system can be developed; however, the partitioning routine must be applied at each time step in the integration algorithm. Therefore, there is significant overhead in both calculating and partitioning the eigensystem at each time step.

## III. PHYSICAL-VARIABLE VOLTAGE-BEHIND-REACTANCE MODEL OF SYNCHRONOUS MACHINE-CONVERTER SYSTEMS

To optimize the efficiency of machine-converter simulations, a new synchronous machine model was recently set forth in [10]. In this model, the stator voltage equations are expressed in terms of physical variables as

$$\mathbf{v}_{abcs} = \mathbf{r}_s''(\theta_r)\mathbf{i}_{abcs} + p[\mathbf{L}_{abcs}''(\theta_r)\mathbf{i}_{abcs}] + \mathbf{e}_{abcs}'' \tag{12}$$

where the resistance matrix is given by

$$\mathbf{r}_{abcs}''(\theta_r) = \begin{bmatrix} r_S(2\theta_r) & r_M\left(2\theta_r - \frac{2\pi}{3}\right) & r_M\left(2\theta_r + \frac{2\pi}{3}\right) \\ r_M\left(2\theta_r - \frac{2\pi}{3}\right) & r_S\left(2\theta_r - \frac{4\pi}{3}\right) & r_M(2\theta_r) \\ r_M\left(2\theta_r + \frac{2\pi}{3}\right) & r_M(2\theta_r) & r_S\left(2\theta_r + \frac{4\pi}{3}\right) \end{bmatrix} \tag{13}$$

with

$$r_S(\cdot) = r_s + r_a - r_b\cos(\cdot) \tag{14}$$

$$r_M(\cdot) = -\frac{r_a}{2} - r_b\cos(\cdot) \tag{15}$$

$$r_a = \frac{r_d'' + r_q''}{3} - \frac{2}{3}r_s \tag{16}$$

$$r_b = \frac{r_d'' - r_q''}{3} \tag{17}$$

and

$$r_q'' = r_s + L_{mq}''^2\left(\sum_{j=1}^{m}\frac{r_{kqj}}{L_{lkqj}^2}\right) \tag{18}$$

$$r_d'' = r_s + \frac{L_{md}''^2 r_{fd}}{L_{lfd}^2} + L_{md}''^2 \left( \sum_{j=1}^{N} \frac{r_{kdj}}{L_{lkdj}^2} \right) \tag{19}$$

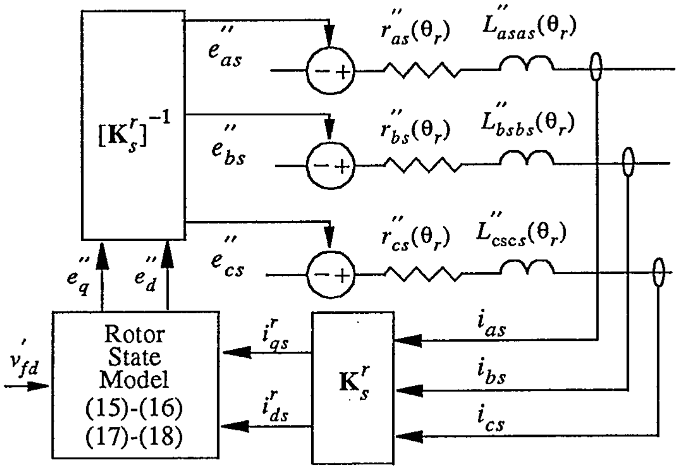

Fig. 1 Voltage-behind-reactance machine model.

The inductance matrix is expressed as

$$\mathbf{L}_{abcs}''(\theta_r) = \begin{bmatrix} L_S(2\theta_r) & L_M\left(2\theta_r - \frac{2\pi}{3}\right) & L_M\left(2\theta_r + \frac{2\pi}{3}\right) \\ L_M\left(2\theta_r - \frac{2\pi}{3}\right) & L_S\left(2\theta_r - \frac{4\pi}{3}\right) & L_M(2\theta_r) \\ L_M\left(2\theta_r + \frac{2\pi}{3}\right) & L_M(2\theta_r) & L_S\left(2\theta_r + \frac{4\pi}{3}\right) \end{bmatrix} \tag{20}$$

where

$$L_S(\cdot) = L_s + L_a - L_b\cos(\cdot) \tag{21}$$

$$L_M(\cdot) = -\frac{L_a}{2} - L_b\cos(\cdot) \tag{22}$$

$$L_a = \frac{L_{mq}'' + L_{md}''}{3} \tag{23}$$

$$L_b = \frac{L_{md}'' - L_{mq}''}{3} \tag{24}$$

In (13)-(23), $L_{md}''$ and $L_{mq}''$ represent the subtransient magnetizing inductances of the machine, which are defined by

$$L_{mq}'' = \frac{1}{\frac{1}{L_{md}} + \sum^{M} \frac{1}{L_{lkqj}}} \tag{25}$$

$$L_{md}'' = \frac{1}{\frac{1}{L_{md}} + \frac{1}{L_{lfd}} + \sum^{n} \frac{1}{L_{lkdj}}} \tag{26}$$

The back emf on the stator windings is a function of the rotor flux linkages which may be represented as

$$\mathbf{e}_{abcs}'' = [\mathbf{K}_s^r]^{-1} \begin{bmatrix} e_q'' \\ e_d'' \\ 0 \end{bmatrix} \tag{27}$$

where

$$e_q'' = \omega_r \lambda_d'' + \left( \sum_{j=1}^{M} \frac{L_{mq}'' r_{kqj}}{L_{lkqj}^2} (\lambda_q'' - \lambda_{kqj}) \right) \tag{28}$$

$$e_d'' = -\omega_r \lambda_q'' + \sum_{j=1}^{N} \frac{L_{md}'' r_{kdj}}{L_{lkdj}^2} (\lambda_d'' - \lambda_{kdj}) + \tag{29}$$

$$v_{fd} \frac{L_{md}''}{L_{lfd}} + \frac{L_{md}'' r_{fd}}{L_{lfd}^2} (\lambda_d'' - \lambda_{fd})$$

The stator voltage equations given by (6), along with the rotor voltage equations

$$p\lambda_j = -\frac{r_j}{L_{lj}}(\lambda_j - \lambda_{mq}) + v_j;\ j = kq1, \ldots kqM \tag{30}$$

$$p\lambda_j = -\frac{r_j}{L_{lj}}(\lambda_j - \lambda_{md}) + v_j;\ j = fd,\ kd1, \ldots kdN \tag{31}$$

where $\lambda_{mq}$ and $\lambda_{md}$ are given by

$$\lambda_{mq} = L_{mq}'' \left( i_{qs}^r + \sum_{i=1}^{M} \frac{\lambda_{kqj}}{L_{lkqj}} \right) \tag{32}$$

$$\lambda_{md} = L_{md}'' \left( i_{ds}^r + \frac{\lambda_{fd}}{L_{lfd}} + \sum_{i=1}^{N} \frac{\lambda_{kdj}}{L_{lkdj}} \right) \tag{33}$$

define the so-called voltage-behind-reactance (VBR) model of the synchronous machine. It is important to note that no approximations are made in its derivation. Moreover, no assumptions have been made in regard to the stator winding configuration. The windings may be connected in wye, delta, or the individual windings may be supplied to isolated converter circuits. With only minor modification, the model may be extended to include machines with an arbitrary number of stator phases.

When implementing the VBR model, the stator branches and nodes are included when defining the circuit topology. The rotor voltage equations are expressed explicitly in state model form with rotor flux linkages as state variables. The subtransient voltages represent outputs of the rotor model and are incorporated in the stator circuit as dependent voltage sources. A diagram of this approach for an example machine-converter system is shown in Fig. 1. In [10] it was shown that the VBR model is significantly more efficient than standard circuit-based models. This is due to the fact that the rotor equations are not expressed in a coupled-circuit form. Rather, they are expressed in state model form with flux linkages as state variables. Therefore the size of the matrices used in circuit-based approaches (both differential-equation based and discrete-circuit based) is significantly reduced and the eigenstructure of the resulting system has been shown to be more numerically stable [10].

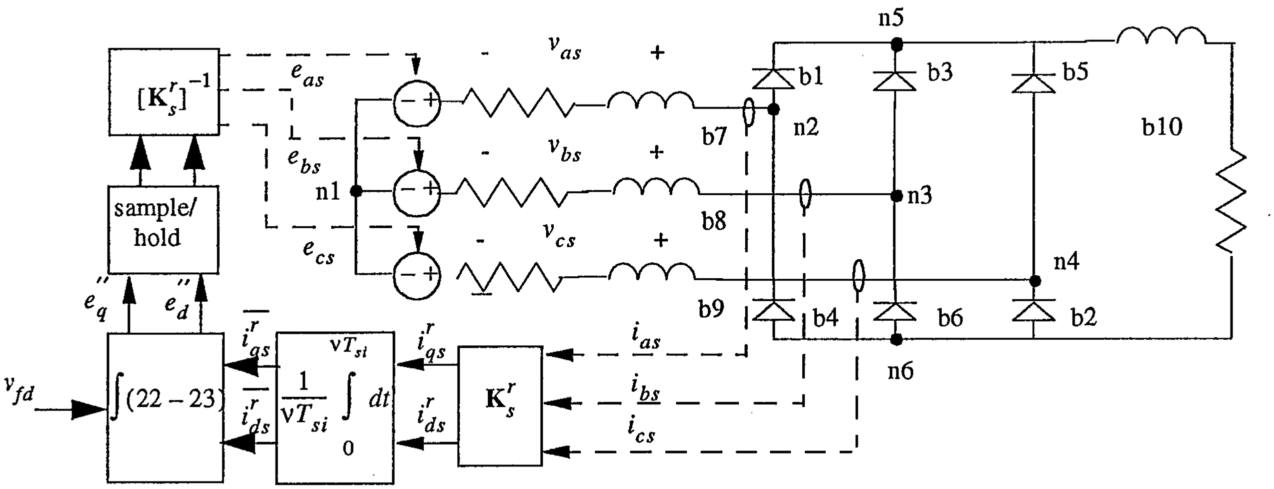

Fig. 2 Multi-rate integration of synchronous machine/power systems.

## IV. MULTI-RATE SIMULATION OF SWITCHED POWER NETWORKS

The VBR model described by (12), (30) and (31) as well as several properties of switched networks provide a means to apply a multi-rate integration method using standard integration routines that is compatible with both circuit-based and differential- equation based languages. Additionally, different integration algorithms can be utilized to solve the partitioned system.

Using the VBR model described in Fig. 1, the stator-network equations can be derived algorithmically while the rotor dynamic equations are derived analytically. This not only provides an efficient method of solving the system, it provides a convenient means of separating the stator and rotor dynamic systems. In most networks, the stator and rotor states are characterized by different time scales. The stator-network currents have small time constants relative to the rotor flux linkages. Furthermore, the stator currents are characterized by discontinuities which result from the converter switching. These discontinuities result in a reduction in the time-step selected by most variable-step integration algorithms (Gear's, Adams-Moulton, etc.). The rotor flux linkages typically have larger time constants, and they do not contain the discontinuities resulting from the converter switching.

The example synchronous machine connected to a line-commutated converter shown in Fig. 1 provides a convenient example that can be used to describe the implementation of a new multi-rate integration approach. For simplicity, and without loss in generality, it is assumed that a synchronous machine is connected to an uncontrolled diode converter and the system operates in conduction Mode . A typical converter output voltage waveform is shown in Fig. 2. The output voltage is periodic with a period of $T_{si} = \frac{\pi}{3\omega_r}$ sec, where $\omega_r$ is the electrical angular velocity of the rotor. The period $T_{si}$ is herein defined as the switching interval. As shown in Fig. 2, $T_{si}$ consists of two subintervals, labeled $t_{cond}$ and $t_{com}$. The interval $t_{cond}$ represents the time in which only two valves of the converter (one in upper and lower half respectively) are conducting. The interval $t_{com}$ represents the time in which the current is switched from one diode to another in either the upper or lower part of the converter. The length of time spent in either mode is dependent upon the commutating inductance and the output current. However, for constant rotor speed, the total switching interval remains fixed

$T_{si}$ is an interval that can be useful in facilitating multi-rate integration approaches. In most systems, the rotor dynamics have time constants that are much greater than $T_{si}$. Therefore, the subtransient voltages, $e_q''$ and $e_d''$, which represent inputs to the stator network equations and outputs of the rotor equations in the partitioned state model, can assumed to be constant over a switching interval, and in some cases multiple intervals. Because of this, the fast system can be integrated over a switching interval without the need to estimate the values of the slow states. After the stator network equations are integrated over the interval using any fixed- or variable-step integration algorithm, the values of the transformed stator currents are input to the rotor equations which are then updated using a possibly different fixed-or variable-step integration routine. It should be noted that the transformed currents $i_{qs}^r$ and $i_{ds}^r$ that represent inputs to the rotor equations contain switching harmonics. In order to reduce the effects of the switching transients on the rotor calculations, average values of the currents can be used to advance the rotor states. A block diagram of this technique is shown in Fig. 3. Here the assumption that the rotor back emfs $e_q''$ and $e_d''$ remain constant over a switching interval (or a fraction or multiple switching interval) is represented as a sample and hold block. It will be shown in the next section that there are machines in which the rotor dynamics are as fast or faster than the stator dynamics. In these instances, it can still be useful to have the stator and rotor dynamics partitioned, since the rotor flux linkages are smoother functions than the stator-network currents. In these instances the rotor equations are updated at a fraction of the switching interval, rather than multiples of the switching interval.

There are several advantages of this method over standard multi-rate approaches; namely (i) it is readily implemented with standard integration routines (ii) it does not require algorithmic partitioning of the state model (iii) it is fully compatible with circuit-based or differential equation based languages.

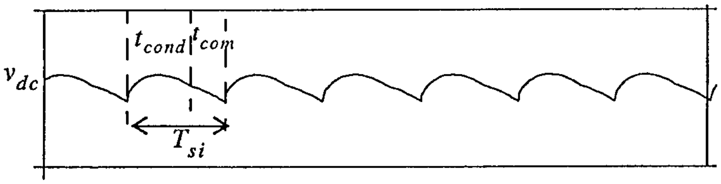

Fig. 3 Output voltage of a six pulse rectifier (Mode 1).

## V. COMPUTER STUDY

In order to illustrate the advantages of the new multi-rate technique, an experimental system consisting of a 3.7 kW synchronous machine connected to a line-commutated converter was simulated. A circuit diagram of this system is shown in Fig. 1. The synchronous machine parameters, as determined by standstill frequency response testing, are summarized in Table 1.

**Table 1: Synchronous machine parameters.**

| | | |
|---|---|---|
| $r_s = 382\ \mathrm{m}\Omega$ | $L_{ls} = 1.12$ mH | $L_{mq} = 24.9$ mH |
| $r_{kd1} = 140\ \Omega$ | $L_{lkd1} = 9.87$ mH | $r_{kq1} = 5.07\ \Omega$ |
| $r_{kd2} = 1.19\ \mathrm{k}\Omega$ | $L_{lkd2} = 4.91$ mH | $r_{kq2} = 1.06\ \Omega$ |
| $r_{kd3} = 1.58\ \Omega$ | $L_{lkd3} = 4.52$ mH | $r_{kq3} = 447\ \mathrm{m}\Omega$ |
| $r_{fd} = 112\ \mathrm{m}\Omega$ | $L_{lfd} = 1.53$ mH | $\frac{N_s}{N_{fd}} = 0.0269$ |
| $L_{md} = 39.3$ mH | $L_{lkq1} = 4.21$ mH | $L_{lkq2} = 3.5$ mH |
| $L_{lkq3} = 26.2$ mH | 4 Poles | |

In the computer studies, it is assumed that the system is initially operating in the steady state with a base load resistance of 21 Ω connected to the dc output terminals. A second load resistance of 4.04 Ω is then connected in parallel with the original load. The simulation was implemented in ACSL [9] using the state model generation algorithm to establish the state equations of the stator-converter. The solution was calculated using five methods. In each of the first four, multi-rate integration was not applied; rather, the stator and rotor dynamic equations were solved using a single integration routine. The particular algorithm, the specified time step, and the cpu times necessary to calculate the response are given in Table 2. The fifth solution was calculated using the multi-rate technique described above. Calculating this response, the stator-network equations were solved using a fixed-step Backward Euler algorithm. The rotor response was solved using a variable-step Gear's algorithm. The choice of these algorithms is described below. The integration of the stator-network equations can be included as part of any circuit-based or differential-equation based automated state model generation algorithm. In this particular example, the stator-network equations were solved within the automated state model generation algorithm by using the Backward-Euler discretized form of the algorithmically derived state model described in [11]

$$p\mathbf{i}_x = -\mathbf{L}_x^{-1}(\mathbf{r}_x + p\mathbf{L}_x)\mathbf{i}_x + \mathbf{B}_b\mathbf{e}_{br} \qquad (34)$$

which can be expressed in a closed-form discrete equation

$$\mathbf{i}_x(n+1) = [I + h(\mathbf{L}_x^{-1}(\mathbf{r}_x + p\mathbf{L}_x))]^{-1}[\mathbf{i}_x(n) - h\mathbf{L}_x^{-1}\mathbf{B}_b\mathbf{e}_{br}] (35)$$

The solution of the state equations within the state-model generation algorithm can be useful when solving large-scale systems, since the symmetry of the matrices $\mathbf{L}_x$ and $\mathbf{r}_x$ can be used to reduce the computation required to solve the discretized system.

As stated previously, any fixed- or variable-step algorithm can be used to solve the stator-network or the rotor dynamic equations. In most power systems, the stator-network will have a much faster dynamic response than that of the rotor circuits. However, in this particular system, there is a stiffness within the rotor circuit dynamics. The stiffness results from the wide range in values of the amortisseur winding resistances. Although a modal partitioning of the rotor dynamic system could be performed, and the fast rotor dynamics solved within the stator-network block or in a separate integration block, Gear's algorithm is chosen. The inefficiencies of Gear's algorithm in solving switched power networks was described previously; however, it is noted that the rotor circuits do not contain switching elements. Therefore, Gear's algorithm can be used to efficiently solve the stiff rotor system.

In this system the stator-network dynamics are much less stiff than the rotor dynamics, thus a fixed-step Backward-Euler algorithm was chosen because it is computationally efficient compared to higher order fixed-step algorithms and does not have the inefficiencies of variable-step algorithms which result from the switching of the converter.

Because the rotor circuits contain fast dynamics, it was assumed that the subtransient back emfs $e_q''$ and $e_d''$ that are outputs of the rotor block and inputs to the stator-network block remain constant only over approximately a tenth of the switching interval. Therefore, the multi-rate integration was achieved by integrating the stator-network equations (using Backward-Euler)at a fixed time step of $5 \cdot 10^{-4}$ over an interval $0.1T_{si}$, during which the rotor flux linkages were assumed constant. The average of the transformed currents $\overline{i_{qs}^r}$ and $\overline{i_{ds}^r}$ over the interval $0.1T_{si}$ were then input to the rotor dynamic equations which were integrated (using Gear's) over $0.1T_{si}$, and the cycle repeated

Comparing the cpu times of the five simulation methods, it is seen that the multi-rate technique is over 350% faster than fastest single-rate method (in this example Gear's). There is a significant difference in the simulation times of the single-rate algorithms which results from the difference in the numerical properties of the algorithms. Of the three, only Gear's is stiffly-stable [13]. The single-step Runge-Kutta and variable-step Adam's Moulton are less efficient because a smaller time-step must be used to ensure numerical stability. The significant increase in the efficiency of the multi-rate method results from the reduction of the numerical integration inefficiencies associated with converter switching. In the multi-rate integration approach, Gear's algorithm is used to solve only the rotor system. Therefore, the time-step selected is not effected by the switching of the converter. A plot of the time step selected by Gear's algorithm for both single-rate and the multi-rate simulations are shown in Figs. 4-5.

The responses predicted using the single-rate and multi-rate algorithms are shown in Figs. 6-7, respectively. From these plots it is seen that the long-term dynamic response predicted by the multi-rate algorithm is in excellent agreement with those of the single-rate algorithms. Comparing the overall response, there are slight differences in the switching dynamics, particularly in the field current of the synchronous machine. These differences result from the fact that the averaged stator currents are used as inputs to the rotor dynamic equations. By using averaged currents, a portion of the switching harmonics are eliminated. .

**Table 2:**

| Integration Algorithm | **Time-Step** | CPU Time |
|---|---|---|
| Runge-Kutta-Fehlberg | $10^{-6} < h < 10^{-8}$ | 135 s |
| Adams-Moulton | $10^{-7} < h < 10^{-4}$ | 47 s |
| Gear's | $10^{-7} < h < 10^{-4}$ | 18 s |
| Multi-rate<br>Stator/network - Bckwd Euler<br>Rotor - Gear | $h = 5 \bullet 10^{-5}$<br>$10^{-7} < h < 10^{-4}$ | 5 s |

## VI. SUMMARY

A new multi-rate integration technique for simulation of AC/DC power systems has been derived. This technique is computationally more efficient than single-rate algorithms, can be implemented in circuit-based or differential equation-based languages, and uses standard integration algorithms.

## ACKKNOWLEDGEMENTS

This work was supported in part by P. C. Krause and Associates under contract N00024-93-C-4180 with Naval Surface Warfare Center and in part by University of South Carolina under Grant No. N00014-96-1-0926 with Office of Naval Research.

## VII. REFERENCES

[1] C. W. Gear, **Numerical Initial Value Problems in Ordinary Differential Equations**, Prentice Hall, NJ, 1971.Analogy, Inc., "Introduction to the Saber Simulator," Beaverton, Oregon, 1991.

[2] P. V. Girijashankar, D. L. Hetrick, W. N. Keepin, O. A. Pulisinki, "A Technique for Efficient Simulation of Large Dynamic Systems," *Proceedings of the 1980 Joint Automatic Control Conference*, Vol. 1, Section WP9-A.

[3] L. Anderson, "Order Reduction in the Numerical Simulation of Time-Varying Two-Time-Scale Control Systems," *Proceedings of the 1980 Joint Automatic Control Conference*, Vol. 1, Section WP9-E.

[4] M. L. Crow and J. G. Chen, "The Multirate Simulation of FACTS Devices in Power System Dynamics," *IEEE Transactions on Power Systems*, Vol. 11, No. 1, February 1996.

[5] J. G. Chen and M. L. Crow, "The Multirate Method for Simulation of Power SYstem Dynamics," *IEEE Transactions on Power Systems*, Vol. 9, No. 3, August 1994.

[6] L. W. Nagel and D. O. Pederson, "Simulation Program with Integrated Circuit Emphasis," University of California Electronic Research Laboratory, Memorandum EAL-M382, April 1973.

[7] Saber Reference Manual

[8] EMTP Reference Manual

[9] ACSL Reference Manual

[10] S. D. Pekarek, O. Wasynczuk, H. J. Hegner, "An Efficient and Accurate Model for the Simulation and Analysis of Synchronous Machine/Converter Systems," accepted for publication in the *IEEE Transactions on Energy Conversion.*

[11] O. Wasynczuk and S. D. Sudhoff, "Automated State Model Generation Algorithm for Power Circuits and Systems," Paper 96 WM 259-2 PWRC presented at the IEEE Power Engineering Society Winter Meeting, Baltimore, MD, Jan. 21-25, 1996.

[12] P. C. Krause, O. Wasynczuk, and S. D. Sudhoff, **Analysis of Electric Machinery**, IEEE Press, Piscataway, NJ, 1995.

[13] L. O. Chua, P-M Lin, **Computer Aided Analysis of Electronic Circuits: Algorithms and Computational Techniques**, Prentice-Hall, Englewood Cliffs, New Jersey, 1975.

**Steven D. Pekarek** was born in Cicero, Illinois on December 22, 1968. He received the B.S.E.E, M.S.E.E, degrees from Purdue University in 1991, 1993 respectively, and is currently pursuing his Ph.D. His interests include electric machines and automatic control.

**Oleg Wasynczuk** (M' 76, SM'88) was born in Chicago, Illinois on June 26, 1954. He received the B.S.E.E. degree from Bradley University in 1976 an the M.S. and Ph.D. degrees from Purdue University in 1977 and 1979, respectively. Since 1979, he has been at Purdue where he is presently a Professor of Electrical and Computer Engineering. Dr. Wasynczuk is a member of Eta Kappa Nu, Tau Beta Pi and Phi Kappa Phi and is a Senior member of the IEEE Power Engineering Society.

**H. J. Hegner** (S' 88, M'89) received the B.S.E.E. degree from the Virginia Polytechnic Institute and State University in 1983 and the M.S.E.E. degree from Purdue University in 1992. He is currently a member of the U.S. Navy Advanced Surface Machinery Programs in which he serves as a team leader of the DC Zonal Electric System Program. For the past 16 years, he has specialized in electrical systems and components for U.S. Navy shipboard systems.

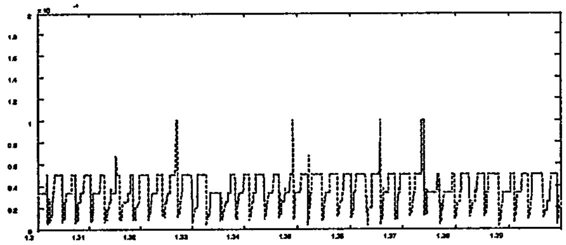

Fig. 4 Integration time step selected by Gear's algorithm in integration of entire system.

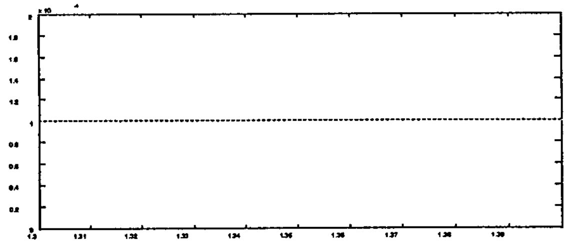

Fig. 5 Integration time step selected by Gear's algorithm in integration of rotor dynamic equations.

# Digital Tracking Control for PWM Systems with Unacceptable Zeros*

Mohammed Al-Numay and David G. Taylor†

Georgia Institute of Technology
School of Electrical and Computer Engineering
Atlanta, GA 30332-0250 USA

E-mail: david.taylor@ece.gatech.edu
Phone: 404-894-8910
Fax: 404-894-4641

Submitted to IEEE Transactions on Circuits and Systems
Special Issue on Simulation, Theory and Design of Switched-Analog Networks

### Abstract

Perfect output tracking, which requires inversion of the input-output dynamics, is not always a practical control objective. Difficulties are encountered for systems with zeros which are unstable, or stable but lightly damped. When the zeros are unacceptable in the above sense, perfect output tracking would require the control to be either unbounded, or bounded but highly oscillatory. In this paper, an approximate output tracking control design method is introduced for pulse-width modulated (PWM) systems with unacceptable zeros. The design method is applied to the nonlinear sampled-data model of the PWM system, and is based on output redefinition. Although the new approach leads to approximate rather than perfect output tracking, it guarantees bounded and non-oscillatory responses.

## 1 Introduction

Pulse-width modulated (PWM) systems are switch-controlled systems with dynamic models that depend on the status of the switch. Sampled-data modeling techniques provide a natural means to represent the behavior of such systems over each switching cycle. Sampled-data models for switchmode power converters were first developed in [16] and later extended in [15] and [19]. More recent related work appears in [9] and [6].

One of the motivations for modeling PWM systems is to design model-based PWM controllers. Digital controller implementations may be designed using either a direct approach or an indirect approach. The direct design approach is based on the discrete-time sampled-data model and thus explicitly accounts for the switching frequency, whereas the indirect design

---

[*] This work was supported in part by the National Science Foundation under grant ECS-9158037, by the Office of Naval Research under grant N00014-96-1-0926, and by a graduate fellowship funded through King Saud University of Riyadh, Saudi Arabia.

[†] All correspondence should be addressed to this author.

approach is based on a continuous-time model which is typically derived using averaging approximations. Examples of both types of digital controllers exist in the literature; e.g. a direct digital design is reported in [8] whereas an indirect digital design is discussed in [18].

This paper addresses the problem of digital control design for a class of PWM systems, using large-signal sampled-data models. One possible design method is based on inversion of the discrete-time input-output relation. Although such inverse control offers potentially high performance, its implementation is problematic for two reasons.

First, the sampled-data model exhibits input nonlinearities, and hence iterative numerical search must be used to determine the control input. This first issue has been addressed by the authors in [1] for simple PWM systems and in [2] for more general PWM systems, using piecewise-linear approximations of the nonlinearities. By solving for the inverse control using piecewise-linear Newton iteration, accurate control is achieved with very low computation and with moderate storage.

Second, difficulties are encountered when implementing inverse control for systems with zeros which are unstable, or stable but lightly damped [12, 5, 10]. This second issue is the main subject of the present paper; preliminary results are reported by the authors in [3]. When the zeros are unacceptable in the above sense, perfect output tracking would require the control to be either unbounded, or bounded but highly oscillatory. Clearly, in either case, inverse control for perfect tracking is not a practical solution for systems with unacceptable zeros.

In this paper, an approximate output tracking control design method is introduced for PWM systems with unacceptable zeros. The design method is applied to the nonlinear sampled-data model of the PWM system. The original system is approximated by one with acceptable zeros, and the approximate system's inverse control is applied to the original system. Although this approach leads to approximate rather than perfect output tracking, it guarantees bounded and non-oscillatory control signals. The approximation step involves redefinition of the system output, in such a way as to eliminate all unacceptable zeros while leaving all acceptable zeros in their original locations.

## 2 Modeling

This paper considers PWM systems of the form

$$\dot{x}(t) = \begin{cases} A_1 x(t) + b_1 u(t) & , \ kT \le t < kT + d_k T \\ A_2 x(t) + b_2 u(t) & , \ \text{otherwise} \end{cases} \tag{2.1}$$

$$y(t) = c' x(t) \tag{2.2}$$

where $x \in R^n$ is the state vector, $y \in R$ is a scalar output (e.g. the signal to be controlled), $u \in R$ is a scalar input (e.g. a voltage or current source), and $'$ denotes transpose. As indicated, the circuit dynamics switch between two topologies, $(A_1, b_1)$ and $(A_2, b_2)$, with switching period $T$ and duty ratio $d_k \in [0, 1]$, where $k$ represents the discrete-time index. The source input will be assumed to be piecewise-constant, i.e. $u(t) = u_k$ for all $kT \le t < (k+1)T$.

Note that the model (2.1)–(2.2) implicitly assumes that the control processor and the PWM switch operate at the same frequency. This assumption was made only to simplify the presentation. It is possible to carry out all steps of the paper using instead a model which assumes that the control input is updated every $N$ switching periods, where $N$ represents the integer ratio of switching frequency to control frequency. The conflicting requirements of relatively fast switching with relatively slow control computation could then be resolved by selecting an appropriate $N > 1$. See [13] for details.

## 2.1 Sampled-Data Model

Using sampled-data modeling techniques [14, 15, 19], it is easy to show that the discrete-time evolution of the state $x_k := x(kT)$ and output $y_k := y(kT)$ is governed by

$$
\begin{aligned}
x_{k+1} &= F(d_k)x_k + G(d_k)u_k && (2.3)\\
y_k &= c'x_k && (2.4)
\end{aligned}
$$

where the input nonlinearities $F(\cdot)$ and $G(\cdot)$ are given by

$$
\begin{aligned}
F(d) &:= \Phi_2((1-d)T)\Phi_1(dT) && (2.5)\\
G(d) &:= \Phi_2((1-d)T)\Gamma_1(dT) + \Gamma_2((1-d)T) && (2.6)
\end{aligned}
$$

and where $\Phi_i(\cdot)$ and $\Gamma_i(\cdot)$ are defined by

$$
\Phi_i(t) := e^{A_i t} \qquad \Gamma_i(t) := \int_0^t e^{A_i \tau} b_i \, d\tau \tag{2.7}
$$

It is important to understand that the control input for this model is the duty ratio $d_k$, not the source input $u_k$ which for many applications is constant. It is assumed that this nonlinear model has well-defined relative degree $r$ at $(\bar{d}, \bar{x}, \bar{u})$, i.e. $1 \leq r \leq n$ is the smallest integer such that

$$
\frac{\partial y_{k+r}}{\partial d_k} \neq 0 \tag{2.8}
$$

for all points near $(\bar{d}, \bar{x}, \bar{u})$.

## 2.2 Zero Dynamics

The model (2.3)–(2.4) exactly reproduces the sample-to-sample trajectory of the system, as no approximations have been made. Unfortunately, both the input nonlinearities and the zero dynamics of this model can present difficulties in the control design process. The primary concern in this paper is to account for the possibility of unacceptable zero dynamics. This focus is well motivated since, due to the influence of sampling, sampled-data models possessing unacceptable zero dynamics are frequently encountered in practice [4].

In determining whether the zero dynamics is acceptable or unacceptable, it suffices to consider the eigenvalues of the zero dynamics' linear approximation. These eigenvalues coincide with the zeros of the transfer function associated with the linear approximation of (2.3)–(2.4). Hence, the next modeling step is to evaluate the transfer function, in order to avoid the explicit calculation of the nonlinear system's normal form and zero dynamics.

The equilibrium points of (2.3)–(2.4) are parameterized by constant duty ratio $\bar{d} \in [0,1]$ and constant source input $\bar{u} \in R$, i.e.

$$\begin{aligned} \bar{x} &= F(\bar{d})\bar{x} + G(\bar{d})\bar{u} && (2.9) \\ \bar{y} &= c'\bar{x} && (2.10) \end{aligned}$$

Associated with any such equilibrium point is a small-signal model which describes the approximately linear dynamics of the system in a neighborhood of the equilibrium point. Denoting the deviations from equilibrium values by

$$\tilde{x} := x - \bar{x} \quad \tilde{u} := u - \bar{u} \quad \tilde{d} := d - \bar{d} \quad \tilde{y} := y - \bar{y} \tag{2.11}$$

the corresponding small-signal linear approximate model is given by

$$\begin{aligned} \tilde{x}_{k+1} &= \tilde{F}\tilde{x}_k + \tilde{G}\tilde{u}_k + \tilde{H}\tilde{d}_k && (2.12) \\ \tilde{y}_k &= c'\tilde{x}_k && (2.13) \end{aligned}$$

where

$$\begin{aligned} \tilde{F} &:= F(\bar{d}) && (2.14) \\ \tilde{G} &:= G(\bar{d}) && (2.15) \\ \tilde{H} &:= T\Phi_2((1-\bar{d})T)((A_1 - A_2)(\Phi_1(\bar{d}T)\bar{x} + \Gamma_1(\bar{d}T)\bar{u}) + (b_1 - b_2)\bar{u}) && (2.16) \end{aligned}$$

The transfer function from $\tilde{d}$ to $\tilde{y}$ is given by

$$\frac{N_a(z)N_u(z)}{D(z)} := c'(zI - \tilde{F})^{-1}\tilde{H} \tag{2.17}$$

where $D(z)$ is the denominator polynomial, and the numerator polynomial $N_a(z)N_u(z)$ has been factored into acceptable and unacceptable components. Note that $N_u(z)$ contains every zero on or outside the unit circle, as well as stable but otherwise unacceptable zeros such as those on the real axis near $z = -1$. The total number of unacceptable zeros is assumed to be $m := \deg\{N_u(z)\}$.

## 2.3 Output Redefinition

The objective is to find a nonlinear model which is a reasonably close approximation of (2.3)–(2.4), yet which has zeros given by $N_a(z)$ rather than by $N_a(z)N_u(z)$. The approach taken requires redefinition of the output, but involves no alteration of the state dynamics. Given (2.17), it is clear that the zeros given by $N_u(z)$ may be removed while, at the same time, the magnitude and phase of the transfer function may be maintained at dc, by simply replacing

$N_u(z)$ with $N_u(1)$. Hence, this suggests that an approximate model possessing the desired properties can be found by computing the unique vector $\hat{c}$ such that

$$\hat{c}'(zI-\tilde{F})^{-1}\tilde{H} = \frac{N_a(z)N_u(1)}{D(z)} \tag{2.18}$$

The approximate transfer function (2.18) exactly matches the true transfer function (2.17) at dc, and hence the approximation error is guaranteed to be small for all sufficiently low frequencies. The frequency range over which the approximation error is acceptable can be quantified by enforcing the condition $N_u(e^{j\omega T}) \approx N_u(1)$.

Given $\hat{c}$, a nonlinear model which approximates the original nonlinear model (2.3)–(2.4) is defined by

$$\begin{aligned} x_{k+1} &= F(d_k)x_k + G(d_k)u_k && (2.19)\\ \hat{y}_k &= (c-\hat{c})'\bar{x} + \hat{c}'x_k && (2.20) \end{aligned}$$

Since (2.20) is derived on the basis of a local approximation, it may be desirable to schedule $\hat{c}$ and $\bar{x}$ such that they vary with the operating point. The equilibrium output $\bar{\hat{y}}$ of the approximate nonlinear model coincides with the equilibrium output $\bar{y}$ of the original nonlinear model. The small-signal model associated with the approximate nonlinear model is simply

$$\begin{aligned} \tilde{x}_{k+1} &= \tilde{F}\tilde{x}_k + \tilde{G}\tilde{u}_k + \tilde{H}\tilde{d}_k && (2.21)\\ \tilde{\hat{y}}_k &= \hat{c}'\tilde{x}_k && (2.22) \end{aligned}$$

which indeed yields the desired approximate transfer function (2.18) rather than the true transfer function (2.17).

Since there are $m$ fewer zeros in (2.18) than in (2.17), the approximate nonlinear model (2.19)–(2.20) has (loosely speaking) relative degree $\hat{r} := r+m$ at $(\bar{d},\bar{x},\bar{u})$. Yet this relative degree is not well-defined in the sense that, although $1 \le \hat{r} \le n$ is the smallest integer such that

$$\frac{\partial \hat{y}_{k+\hat{r}}}{\partial d_k} \neq 0 \tag{2.23}$$

at $(\bar{d},\bar{x},\bar{u})$, smaller integers may satisfy this inequality at neighboring points. This means that an additional approximation, called regularization [11, 5], will be needed before the approximate nonlinear model (2.19)–(2.20) may be used for inverse control calculations. The intuitive explanation of this additional approximation is as follows: if a step response test is used to determine the delay of the system, and a very small response is measured at $k=\hat{r}-1$ with a larger response at $k=\hat{r}$, then the delay is assumed to be equal to $\hat{r}$ rather than $\hat{r}-1$.

## 3 Control

For simplicity, this section considers the case when the power source is constant, i.e. when $u_k \equiv \bar{u}$. The control algorithms can be easily re-derived to consider the more general case if desired, provided that preview information on $u_k$ is available. The output control problem is to find the duty ratio $d_k$ which will force the sampled output $y_k$ to match a desired discrete-time output trajectory $y_k^d$. As mentioned previously, this control problem is not well-posed for systems having unacceptable zeros, in which case some type of approximate control performance is sought. The subscript notation

$$\tilde{F}_i := \begin{cases} I + \tilde{F} + \cdots + \tilde{F}^i & , i \geq 0 \\ 0 & , \text{otherwise} \end{cases} \tag{3.1}$$

will prove useful below, when defining the nonlinear controllers.

## 3.1 Perfect Tracking Control

Associated with the original nonlinear model (2.3)–(2.4) are families of scalar functions, defined by

$$F_{Pi}(d,x) := c'\tilde{F}_{i-2}\tilde{G}\bar{u} + c'\tilde{F}^{i-1}\left(F(d)x + G(d)\bar{u}\right) \tag{3.2}$$

$$J_{Pi}(d,x) := \frac{\partial c'\tilde{F}^{i-1}(F(d)x + G(d)\bar{u})}{\partial d} \tag{3.3}$$

for $i = 1, \ldots, n$. It can be shown that (2.3)–(2.4) has well-defined relative degree $r$ at $(\bar{d}, \bar{x})$ if

$$J_{Pi}(d,x) \begin{cases} = 0 & , i < r \text{ near } (\bar{d}, \bar{x}) \\ \neq 0 & , i = r \text{ at } (\bar{d}, \bar{x}) \end{cases} \tag{3.4}$$

in which case the input-output relation is given by

$$y_{k+r} = F_{Pr}(d_k, x_k) \tag{3.5}$$

Inversion of this relation is not practical if the system's zero dynamics is unacceptable.

The nonlinear perfect tracking controller is implicitly defined by solutions of the scalar nonlinear equation

$$y_{k+r}^d = F_{Pr}(d_k, x_k) \tag{3.6}$$

for $d_k$, given $x_k$ and $y_{k+r}^d$. The input nonlinearities prohibit a closed-form solution; however, for sake of illustration, note that the equivalent control objective translated to the linear approximate model would yield the explicit linear inverse control

$$\tilde{d}_k = \frac{\tilde{y}_{k+r}^d - c'\tilde{F}^r\tilde{x}_k}{c'\tilde{F}^{r-1}\tilde{H}} \tag{3.7}$$

Numerical search procedures will be given for implementation of the general nonlinear perfect tracking control.

## 3.2 Approximate Tracking Control

Associated with the approximate nonlinear model (2.19)–(2.20) are families of scalar functions, defined by

$$\begin{aligned} F_{Ai}(d,x) &:= (c-\hat{c})'\,\bar{x} + \hat{c}'\tilde{F}_{i-2}\tilde{G}\bar{u} + \hat{c}'\tilde{F}^{i-1}\,(F(d)x + G(d)\bar{u}) & (3.8)\\ J_{Ai}(d,x) &:= \frac{\partial \hat{c}'\tilde{F}^{i-1}(F(d)x + G(d)\bar{u})}{\partial d} & (3.9) \end{aligned}$$

for $i = 1, \ldots, n$. Although (2.19)–(2.20) cannot be expected to have a well-defined relative degree at $(\bar{d}, \bar{x})$, it is reasonable to regularize by neglecting certain small input-output couplings. Since $m$ zeros have been eliminated at $(\bar{d}, \bar{x})$ by the output redefinition, it is guaranteed that

$$J_{Ai}(\bar{d},\bar{x}) \begin{cases} = 0 & , \ i < \hat{r} \\ \neq 0 & , \ i = \hat{r} \end{cases} \tag{3.10}$$

Regularization is achieved by assuming that $J_{Ai}(d,x) = 0$ for $i < \hat{r}$ at all points near $(\bar{d}, \bar{x})$ as well, which leads to an approximate input-output relation given by

$$\hat{y}_{k+\hat{r}} \approx F_{A\hat{r}}(d_k, x_k) \tag{3.11}$$

Inversion of this relation involves cancellation of only acceptable zeros, by construction.

Since $\hat{y}$ is a reasonable approximation of $y$ at low frequencies, the nonlinear approximate tracking controller is implicitly defined by solutions of the scalar nonlinear equation

$$y^d_{k+\hat{r}} = F_{A\hat{r}}(d_k, x_k) \tag{3.12}$$

for $d_k$, given values for $x_k$ and $y^d_{k+\hat{r}}$. Like the perfect tracking control, the approximate tracking control for the nonlinear system cannot be expressed in closed-form due to the input nonlinearities, However, if one was content to apply a linear approximate tracking control designed on the same principle but neglecting the nonlinearities, then the algorithm would be explicitly written as

$$\tilde{d}_k = \frac{\tilde{y}^d_{k+\hat{r}} - \hat{c}'\tilde{F}^{\hat{r}}\tilde{x}_k}{\hat{c}'\tilde{F}^{\hat{r}-1}\tilde{H}} \tag{3.13}$$

In the remaining subsections, numerical iterative procedures for approximately computing the nonlinear tracking controllers will be described.

## 3.3 Nonlinear Newton Iteration

The standard nonlinear (NL) Newton iteration could be used to solve (3.6) or (3.12) in recursive fashion. The solution process begins by taking an initial guess $d_k^{(0)}$ of the solution $d_k$. Given this duty ratio, one applies the iteration

$$d_k^{(j+1)} = d_k^{(j)} - \frac{F_{Pr}(d_k^{(j)}, x_k) - y^d_{k+r}}{J_{Pr}(d_k^{(j)}, x_k)} \tag{3.14}$$

where

$$J_{Pr}(d,x) = c'\tilde{F}^{r-1}T\Phi_2((1-d)T)((A_1-A_2)(\Phi_1(dT)x+\Gamma_1(dT)\bar{u})+(b_1-b_2)\bar{u}) \tag{3.15}$$

for perfect tracking control, or the iteration

$$d_k^{(j+1)} = d_k^{(j)} - \frac{F_{A\hat{r}}(d_k^{(j)}, x_k) - y_{k+\hat{r}}^d}{J_{A\hat{r}}(d_k^{(j)}, x_k)} \tag{3.16}$$

where

$$J_{A\hat{r}}(d,x) = \hat{c}'\tilde{F}^{\hat{r}-1}T\Phi_2((1-d)T)((A_1-A_2)(\Phi_1(dT)x+\Gamma_1(dT)\bar{u})+(b_1-b_2)\bar{u}) \tag{3.17}$$

for approximate tracking control. The outcome of the iteration is a new candidate solution $d_k^{(1)}$. Iteration continues until either the step-size $d_k^{(j+1)} - d_k^{(j)}$ is within the stopping tolerance, or until the maximum number of permissible iterations has taken place. Convergence from an arbitrary initial guess $d_k^{(0)}$ is not guaranteed, unless backtracking is used to limit the length of the Newton step [17].

The NL solution method involves a great deal of computation. Increased accuracy is achieved only by increasing the number of terms in the series approximations of $\Phi_i(\cdot)$ and $\Gamma_i(\cdot)$, which implies increasing the computation per iteration in a linear fashion. For any fixed number of terms in the series, the growth in computation per iteration with respect to $n$ is cubic.

## 3.4 Piecewise-Linear Newton Iteration

To avoid the need for repeated evaluations of $\Phi_i(\cdot)$ and $\Gamma_i(\cdot)$, a new piecewise-linear (PL) approach, inspired by [7], has been suggested in [1, 2]. The input nonlinearities appearing in either (3.6) or (3.12) will be replaced by corresponding PL approximations. For an $N$-segment PL approximation over the domain $d \in [0,1]$, the index $\sigma = 1, \ldots, N$ locates any particular segment of interest. To insure that the PL approximations coincide with the input nonlinearities at segment boundaries, the coefficients of the approximation are related to functions identified in the original nonlinear system (2.3)–(2.4) or its nonlinear approximation (2.19)–(2.20) as necessary. The parameterized PL functions used to approximate the nonlinearities are given by

$$F_{Pr}(d,x) \approx \left(\alpha_\sigma^P d + \beta_\sigma^P\right) x + \left(\gamma_\sigma^P d + \delta_\sigma^P\right) \bar{u} \tag{3.18}$$

for perfect tracking control, or by

$$F_{A\hat{r}}(d,x) \approx \left(\alpha_\sigma^A d + \beta_\sigma^A\right) x + \left(\gamma_\sigma^A d + \delta_\sigma^A\right) \bar{u} + \epsilon \tag{3.19}$$

for approximate tracking control.

A PL version of Newton's iteration is the recommended numerical method to solve either (3.6) or (3.12) in recursive fashion. The solution process begins by taking an initial guess $\sigma^{(0)}$

of the segment containing the solution $d_k$. Given this segment, the iteration is given by

$$d_k^{(j+1)} = \frac{y^d_{k+r} - (\beta^P_{\sigma(j)} x_k + \delta^P_{\sigma(j)} \bar{u})}{\alpha^P_{\sigma(j)} x_k + \gamma^P_{\sigma(j)} \bar{u}} \tag{3.20}$$

for perfect tracking control, or by

$$d_k^{(j+1)} = \frac{y^d_{k+\hat{r}} - (\beta^A_{\sigma(j)} x_k + \delta^A_{\sigma(j)} \bar{u} + \epsilon)}{\alpha^A_{\sigma(j)} x_k + \gamma^A_{\sigma(j)} \bar{u}} \tag{3.21}$$

for approximate tracking control. The iteration will produce a new candidate solution $d_k^{(1)}$ and a corresponding new candidate segment $\sigma^{(1)}$. Iteration continues until either $d_k^{(j+1)}$ belongs to segment $\sigma^{(j)}$ or until the maximum number of permissible iterations has taken place. The convergence properties of PL Newton iterations are discussed in [7]; the only form of non-convergence is cyclic divergence, which can be detected and overcome without difficulty. In the present application, even cyclic divergence did not occur.

The above PL solution procedure is more reliable numerically and more efficient compared to the NL solution procedure. Accuracy improves as the number of segments $N$ is increased, but computation per iteration is independent of $N$, so the only penalty for increasing $N$ is a corresponding linear increase in memory storage. For any fixed $N$, the computation per iteration exhibits linear growth with respect to $n$.

## 4 Examples

Three examples serve to illustrate the theory introduced in this paper. The circuit diagrams for three power electronic converters are shown in Fig. 4.1. Assuming in each case that load voltage is the output, the buck converter will be shown to possess a stable but otherwise unacceptable zero, whereas the boost and buck-boost converters will be shown to possess an unstable, and hence unacceptable, zero. Consequently, each converter benefits from the output redefinition technique recommended in this paper.

### 4.1 Converter Models

The buck converter is defined by

$$A_1 = \begin{bmatrix} 0 & -\frac{1}{L} \\ \frac{1}{C} & -\frac{1}{RC} \end{bmatrix} \quad b_1 = \begin{bmatrix} \frac{1}{L} \\ 0 \end{bmatrix} \quad A_2 = \begin{bmatrix} 0 & -\frac{1}{L} \\ \frac{1}{C} & -\frac{1}{RC} \end{bmatrix} \quad b_2 = \begin{bmatrix} 0 \\ 0 \end{bmatrix} \quad c = \begin{bmatrix} 0 \\ 1 \end{bmatrix} \tag{4.1}$$

The boost converter is defined by

$$A_1 = \begin{bmatrix} 0 & 0 \\ 0 & -\frac{1}{RC} \end{bmatrix} \quad b_1 = \begin{bmatrix} \frac{1}{L} \\ 0 \end{bmatrix} \quad A_2 = \begin{bmatrix} 0 & -\frac{1}{L} \\ \frac{1}{C} & -\frac{1}{RC} \end{bmatrix} \quad b_2 = \begin{bmatrix} \frac{1}{L} \\ 0 \end{bmatrix} \quad c = \begin{bmatrix} 0 \\ 1 \end{bmatrix} \tag{4.2}$$

The buck-boost converter is defined by

$$A_1 = \begin{bmatrix} 0 & 0 \\ 0 & -\frac{1}{RC} \end{bmatrix} \quad b_1 = \begin{bmatrix} \frac{1}{L} \\ 0 \end{bmatrix} \quad A_2 = \begin{bmatrix} 0 & \frac{1}{L} \\ -\frac{1}{C} & -\frac{1}{RC} \end{bmatrix} \quad b_2 = \begin{bmatrix} 0 \\ 0 \end{bmatrix} \quad c = \begin{bmatrix} 0 \\ 1 \end{bmatrix} \tag{4.3}$$

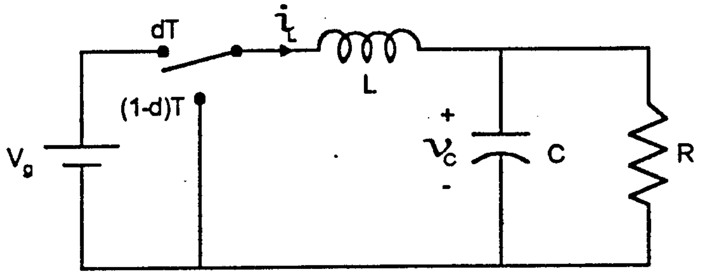
dT
$i_L$
L
(1-d)T
$V_g$
+
$v_C$
-
C
R

Buck Converter

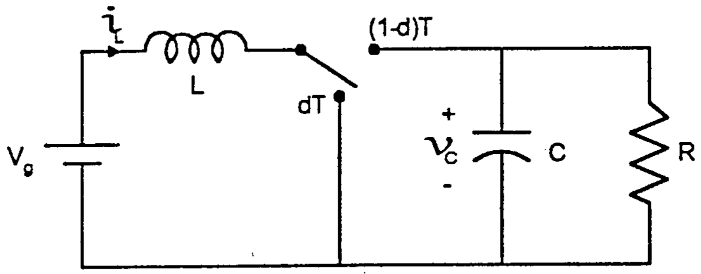
$i_L$
L
(1-d)T
dT
$V_g$
+
$v_C$
-
C
R

Boost Converter

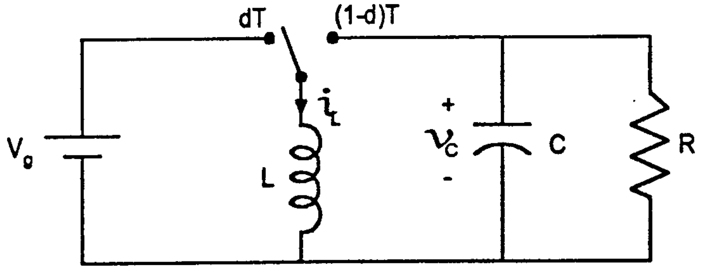
dT
(1-d)T
$i_L$
$V_g$
L
+
$v_C$
-
C
R

Buck-Boost Converter

Figure 4.1: Common switchmode power converters.

For all three converters, $x_1$ is the inductor current, $x_2$ is the capacitor voltage, the circuit component values are $R = 10\ \Omega$, $L = 2$ mH, $C = 200\ \mu$F, and the constant voltage source is $\bar{u} = 100$ V. For the buck converter the switching period is $T = 50\ \mu s$, whereas for the boost and buck-boost converters the switching period is $T = 200\ \mu s$. Note that these parameter values were chosen for illustration purposes only; the control design methods of this paper can be applied equally well for other parameter values.

## 4.2 Zero Locations

The locus of the (real) zero versus switching period $T$ is shown in Fig. 4.2, for all three converters. The zero locations are computed from the converters' transfer functions evaluated at $\bar{d} = 0.5$. The limiting zero locations, for small and large $T$, are as predicted in [4]. From these plots, it is clear that the buck converter is minimum phase for all values of $T$, yet has a zero near $-1$ for the smaller values of $T$ which are of greatest interest. On the other hand, one can see that the boost and buck-boost converters are non-minimum phase for the smaller values of $T$ which are of greatest interest. To be more precise, the buck converter zero corresponding to $\bar{d} = 0.5$ is located at $z = -0.9876$, the boost converter zero corresponding to $\bar{d} = 0.5$ is located at $z = 1.3281$, and the buck-boost converter zero corresponding to $\bar{d} = 0.5$ is located at $z = 1.8562$. The finite zero of all three converters is designated as unacceptable, and the control design proceeds with output redefinition.

## 4.3 Output Redefinition

In order to remove the unacceptable zero from the model prior to inverting the dynamics, it is necessary to determine the appropriate vector $\hat{c}$ from (2.18). Assuming that the equilibrium point of interest corresponds to $\bar{d} = 0.5$, the computations yield

$$\hat{c} = \begin{bmatrix} -0.1259 \\ 1.0126 \end{bmatrix} \qquad (c - \hat{c})' \bar{x} = -0.0392 \tag{4.4}$$

for the buck converter

$$\hat{c} = \begin{bmatrix} 0.9351 \\ 0.6553 \end{bmatrix} \qquad (c - \hat{c})' \bar{x} = 35.5671 \tag{4.5}$$

for the boost converter and

$$\hat{c} = \begin{bmatrix} -0.4843 \\ 0.8660 \end{bmatrix} \qquad (c - \hat{c})' \bar{x} = -5.2497 \tag{4.6}$$

for the buck-boost converter. A comparison of Bode plots for the original and approximate small-signal models, provided in Figs. 4.3–4.5, reveals that the approximation of $c$ by $\hat{c}$ does not significantly alter the frequency response within a low frequency range.

The consequence of output redefinition is further illustrated by comparing several scalar Jacobians. In Fig. 4.6, the Jacobians $J_{P1}$, $J_{A1}$ and $J_{A2}$ are each plotted for various equilibrium values $(\bar{d}, \bar{x})$. Note that near $\bar{d} = 0.5$, all three converters with output $y$ have well-defined

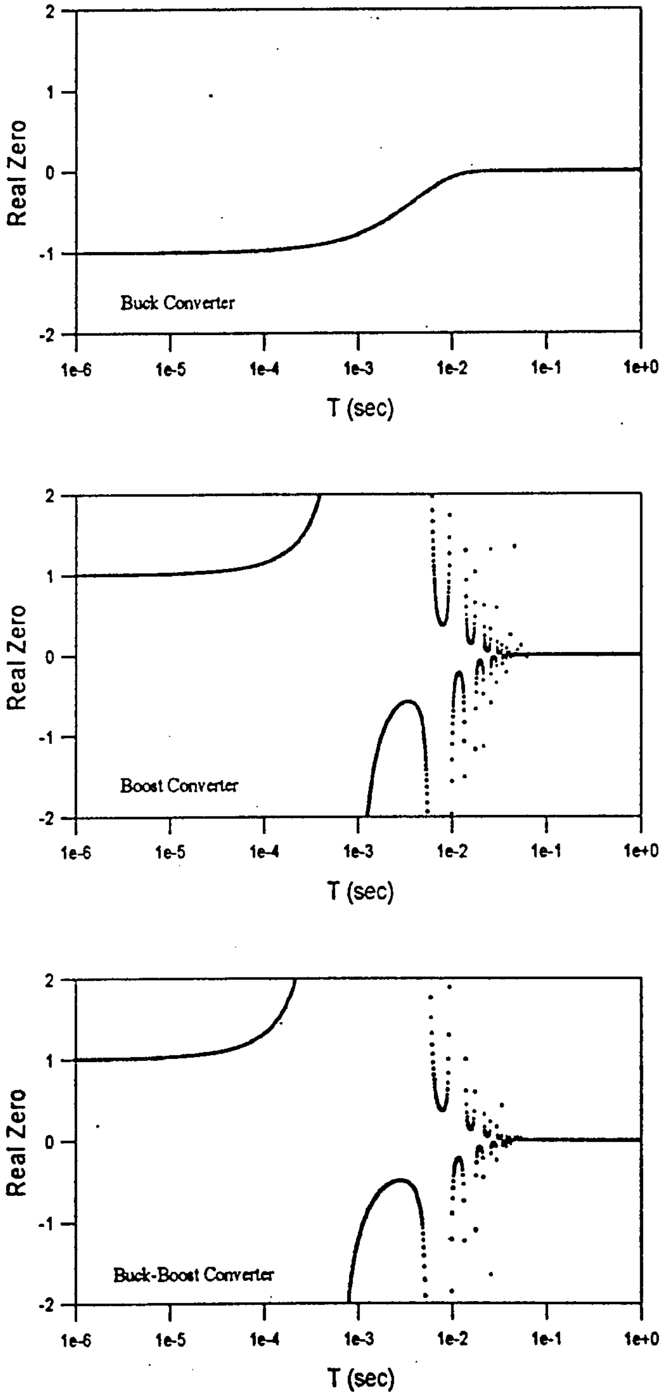

Figure 4.2: Zero locations of converter transfer functions.

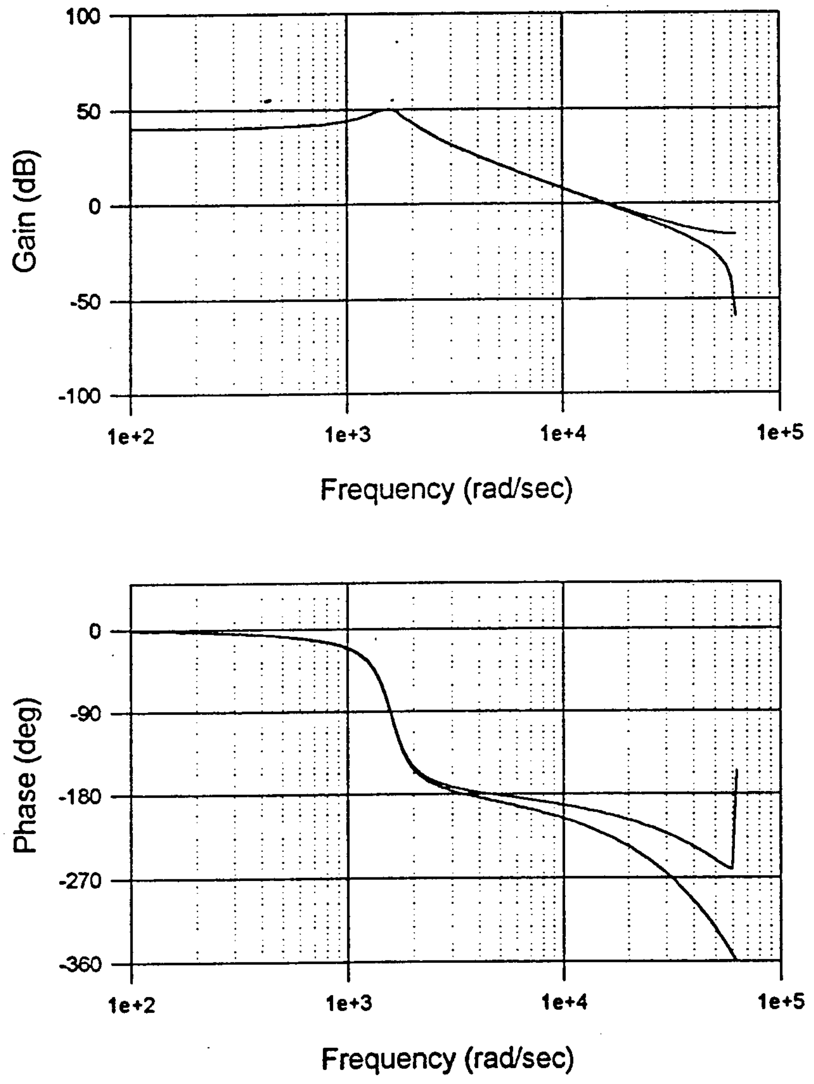

Figure 4.3: Bode plots for buck converter.

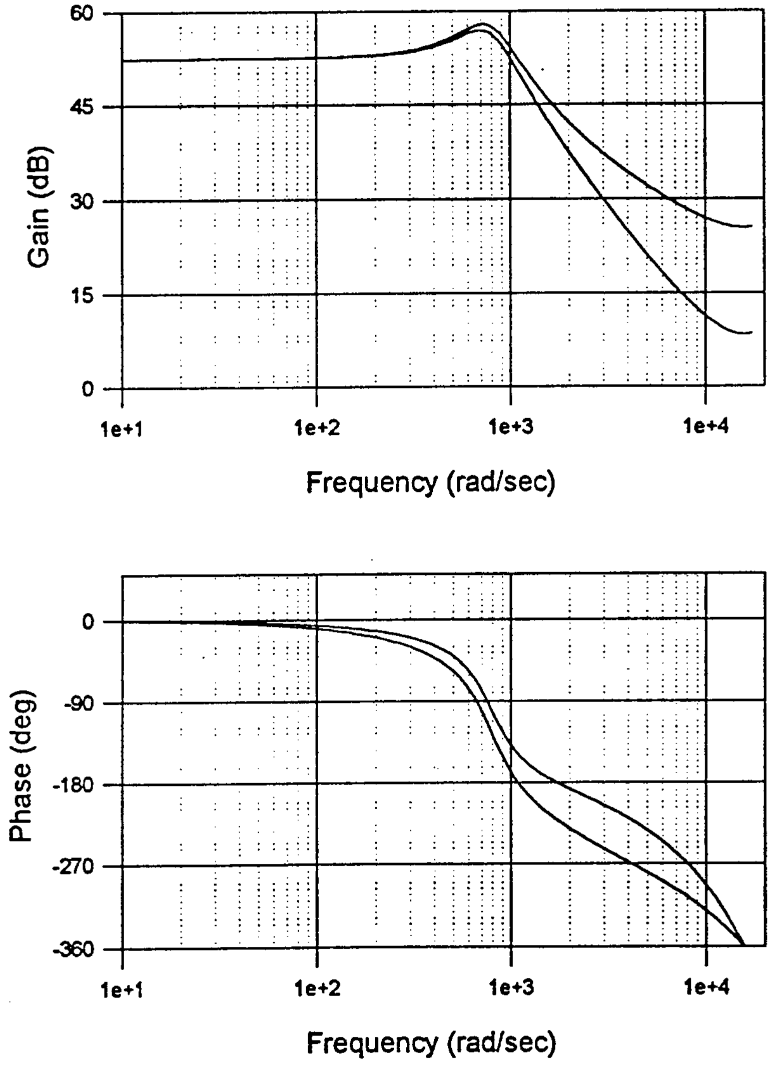

Figure 4.4: Bode plots for boost converter.

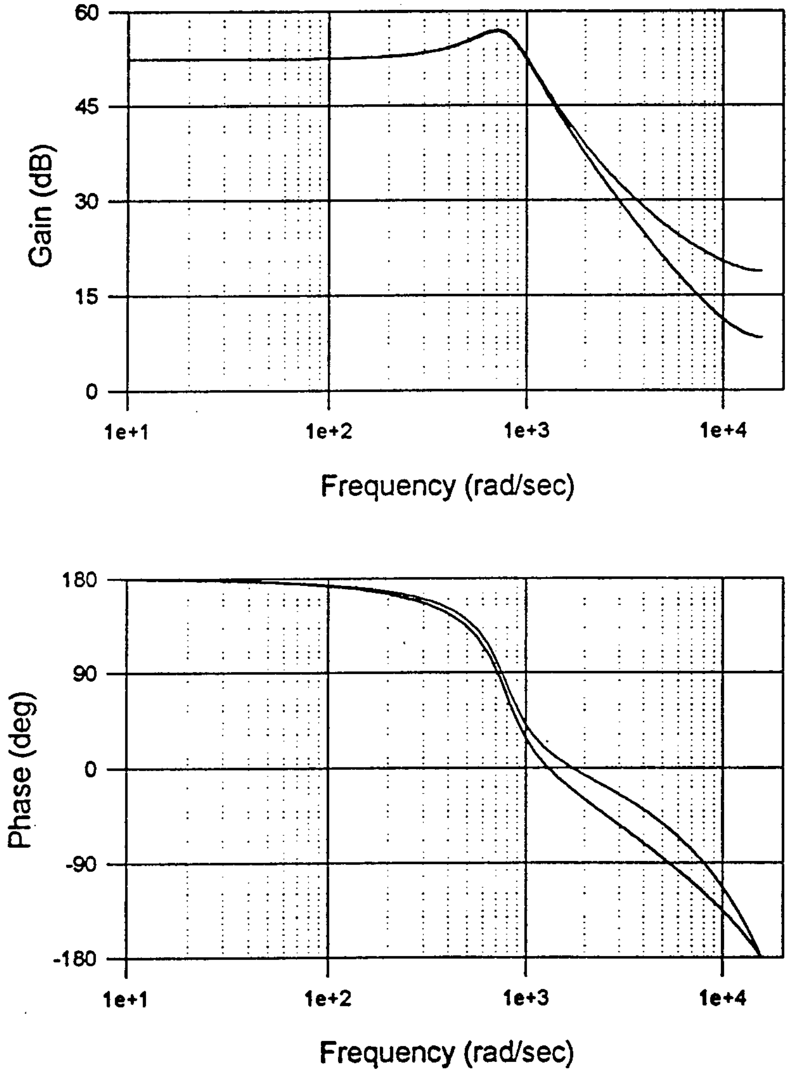

Figure 4.5: Bode plots for buck-boost converter.

relative degree $r = 1$, due to the fact that $J_{P1}$ is nonzero. At $\bar{d} = 0.5$, the value used for output redefinition, the relative degree of all three converters with output $\hat{y}$ should be $\hat{r} = 2$. This increase in relative degree (or, equivalently, this decrease in the number of zeros) is confirmed by the fact that $J_{A1}$ crosses zero at precisely $\bar{d} = 0.5$. However, since $J_{A1}$ is not identically zero in a neighborhood of $\bar{d} = 0.5$, the relative degree of two is not well-defined. This motivates a second approximation, in which the small but nonzero values of $J_{A1}$ near $\bar{d} = 0.5$ are neglected. The second approximation leads to an approximate two-step-ahead input-output relation, with Jacobian $J_{A2}$. Note that $J_{A2}$ is nonzero and dominates $J_{A1}$ in magnitude for all $\bar{d}$ near 0.5. Unfortunately, a relative degree singularity exists for the boost and buck-boost converters where $J_{A2}$ crosses zero, and hence the maximum duty ratios permitted for these two examples would be 0.6177 and 0.5951, respectively. By scheduling the output redefinition, this difficulty may be avoided.

### 4.4 Output Tracking

To illustrate the application of output redefinition methods for these converters, simulations were run using sinusoidal load voltage objectives. Specifically, the desired output sequence is given by

$$y_k^d = \begin{cases} 50 - 35\sin(120\pi(kT)) & ,\ \text{buck} \\ 200 - 55\sin(20\pi(kT)) & ,\ \text{boost} \\ -100 - 40\sin(20\pi(kT)) & ,\ \text{buck-boost} \end{cases} \tag{4.7}$$

The simulation results for perfect tracking control are displayed in Figs. 4.7–4.9. Note that in each simulation, cancellation of the converter's zero (as required for perfect tracking) leads to unacceptable behavior. For the buck converter, high-gain is needed which leads to numerical ill-conditioning and highly oscillatory behavior of the control input and inductor current; even the ability to achieve truly perfect tracking is not present due to control saturation. For the boost and buck-boost converters, the instability associated with the inversion of the system leads to unbounded inductor current; the control input remains bounded only because the converters are lossless with infinite dc gain as $d$ approaches 1.

The simulation results for approximate tracking control are displayed in Figs. 4.10–4.12. The desired trajectories for these simulations are the same as those used in the perfect tracking control simulations, in order to allow direct comparison. Although in all three cases the tracking performance is only approximate, rather than asymptotically perfect, note that the high-gain oscillatory effect has been removed in the buck converter response and that the unboundedness of the internal state has been removed in the boost and buck-boost converter responses.

## 5 Conclusions

This paper addresses the topic of digital tracking control design for PWM systems. Two concepts, namely output redefinition and piecewise-linear Newton iteration, contribute to the

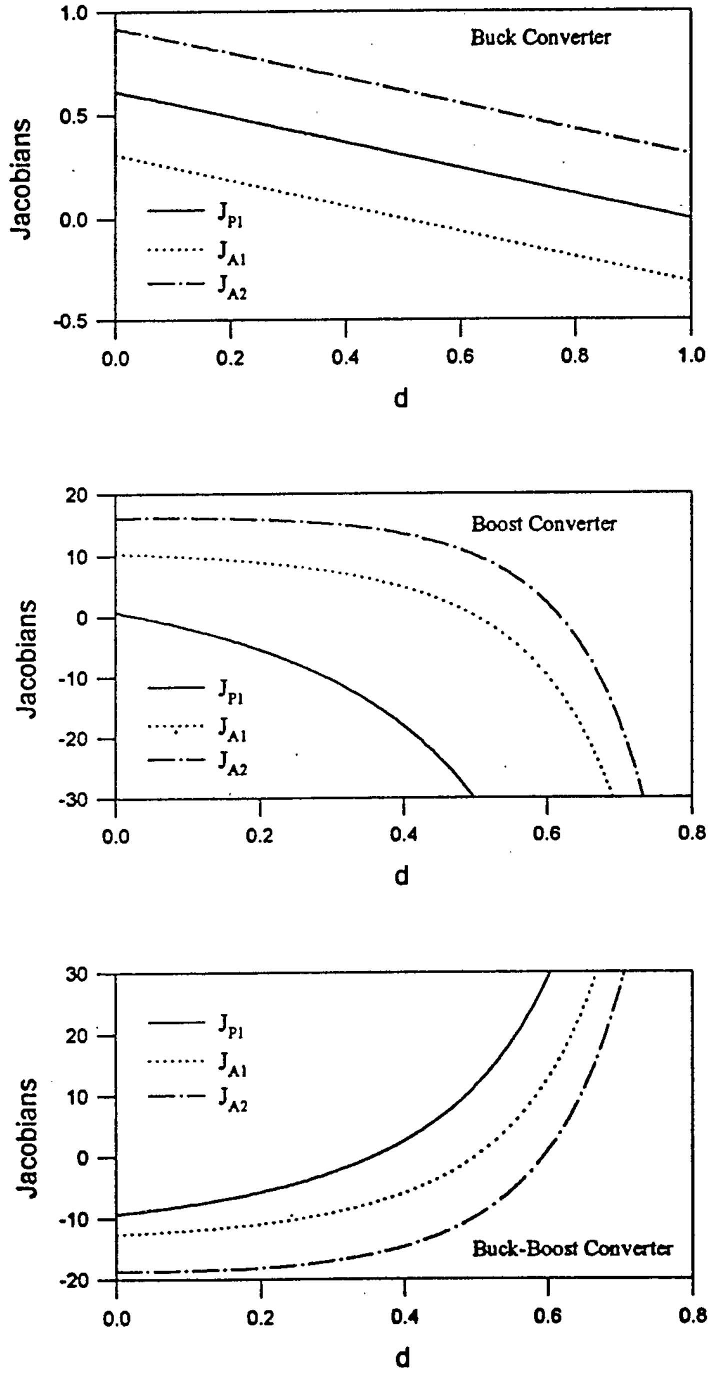

Figure 4.6: Jacobian values at various equilibrium points.

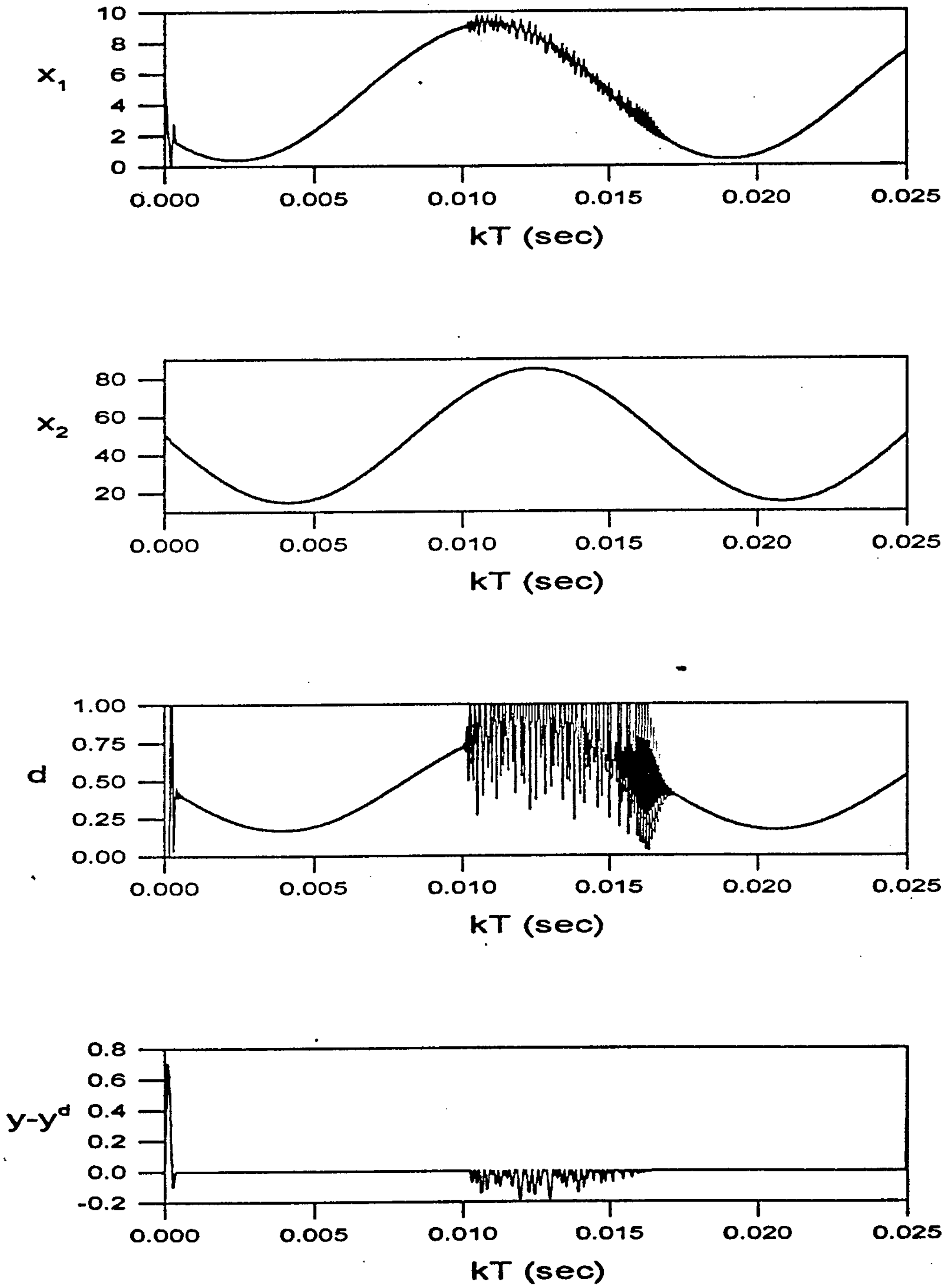

Figure 4.7: Perfect output tracking for buck converter.

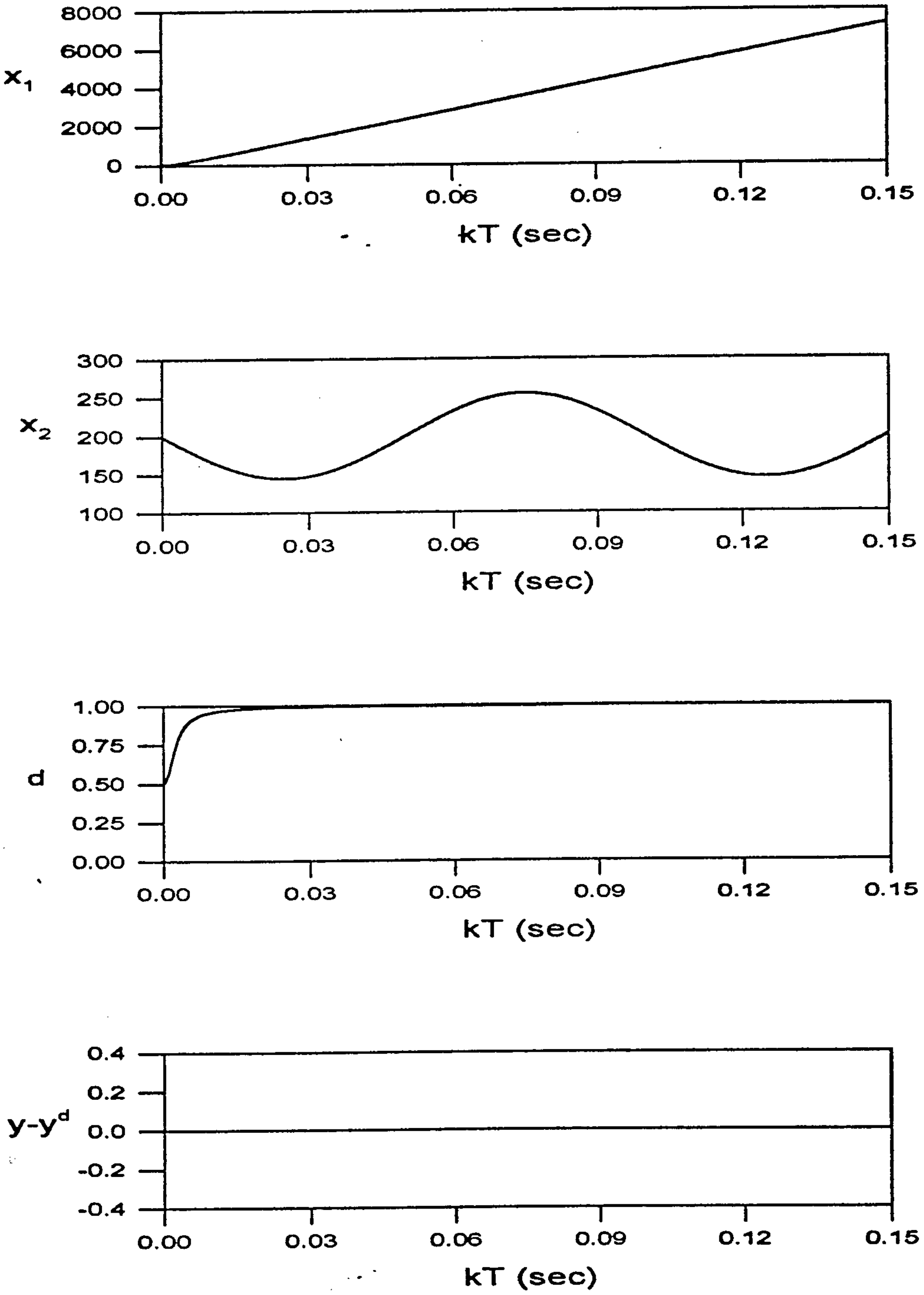

Figure 4.8: Perfect output tracking for boost converter.

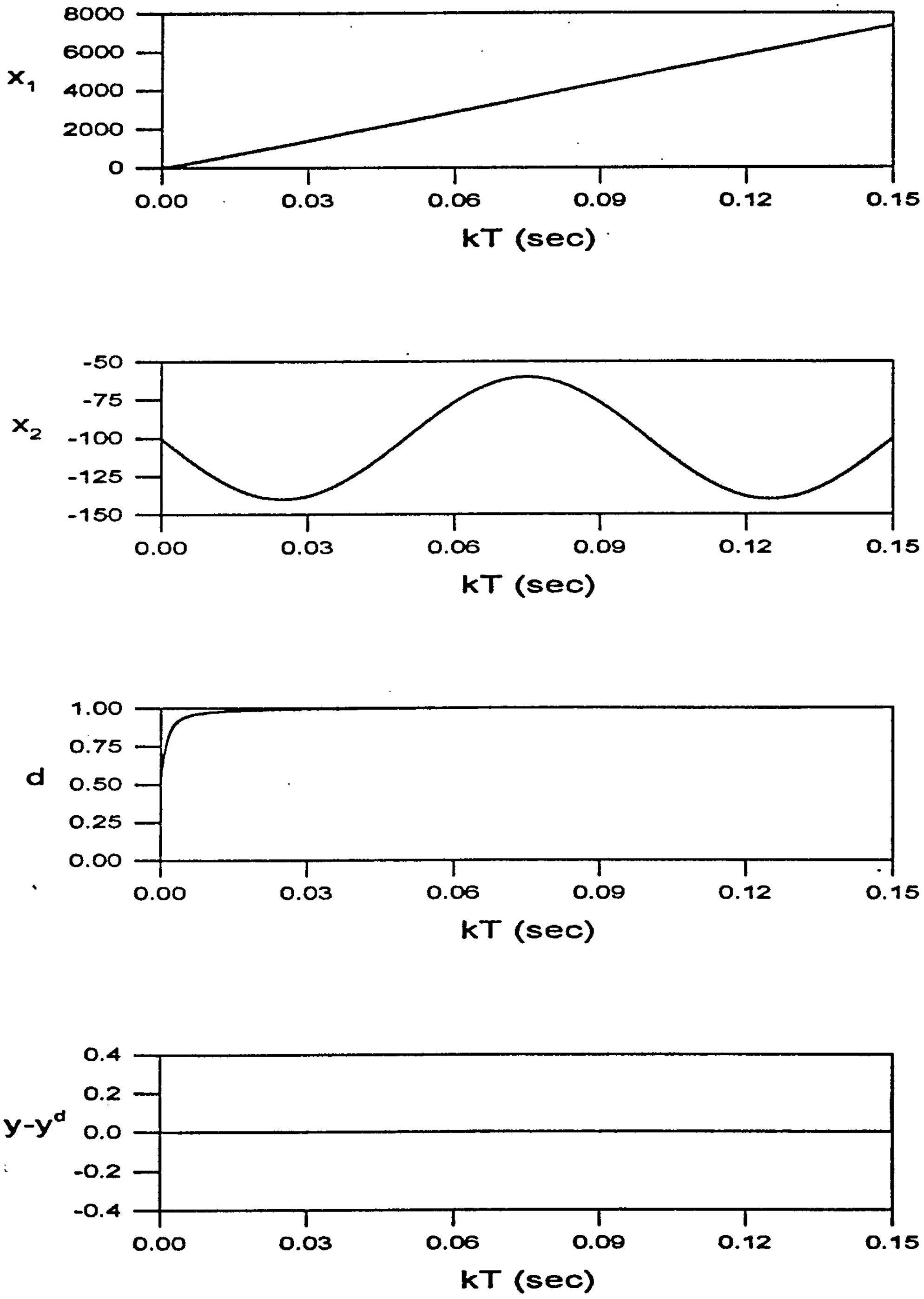

Figure 4.9: Perfect output tracking for buck-boost converter.

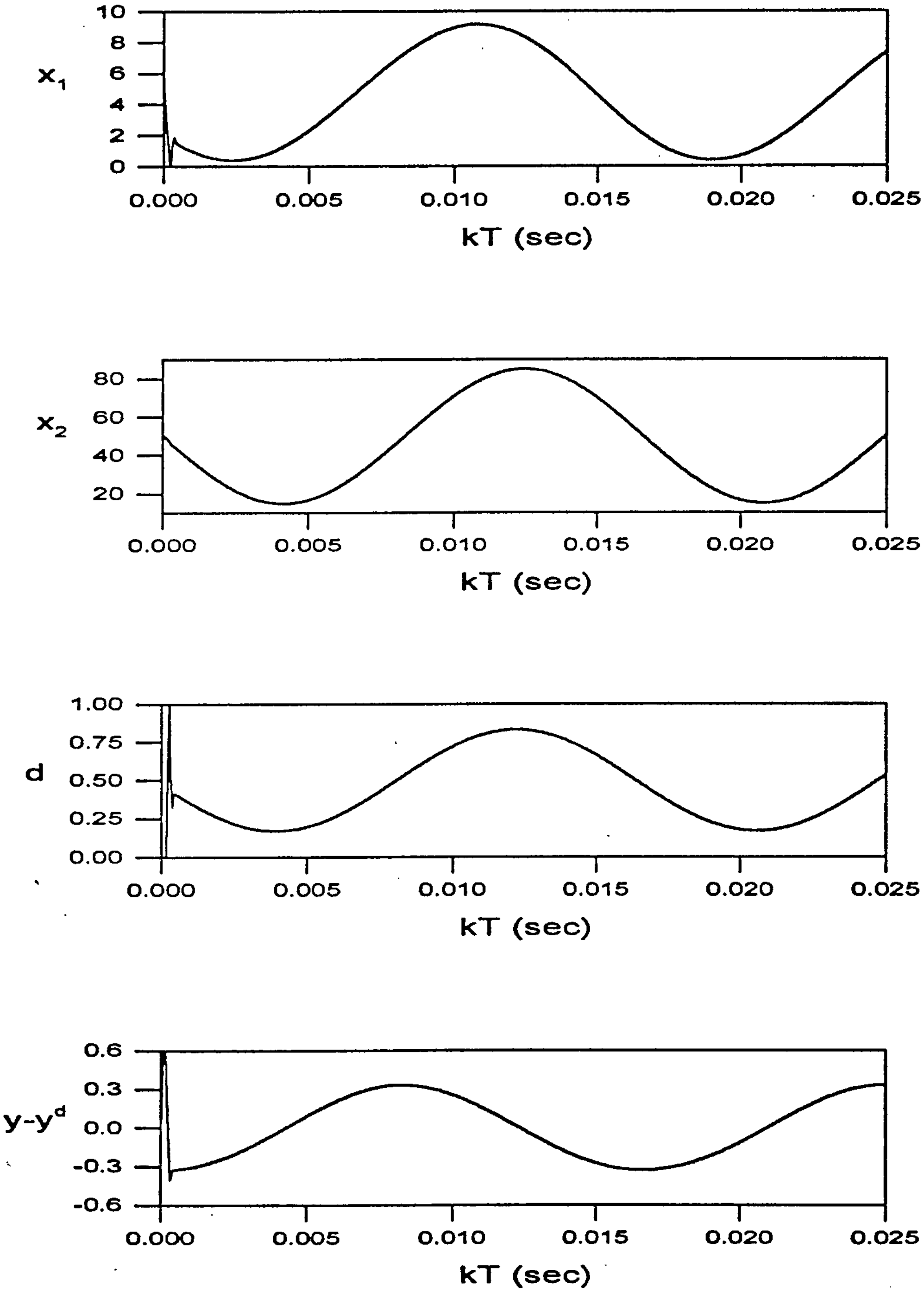

Figure 4.10: Approximate output tracking for buck converter.

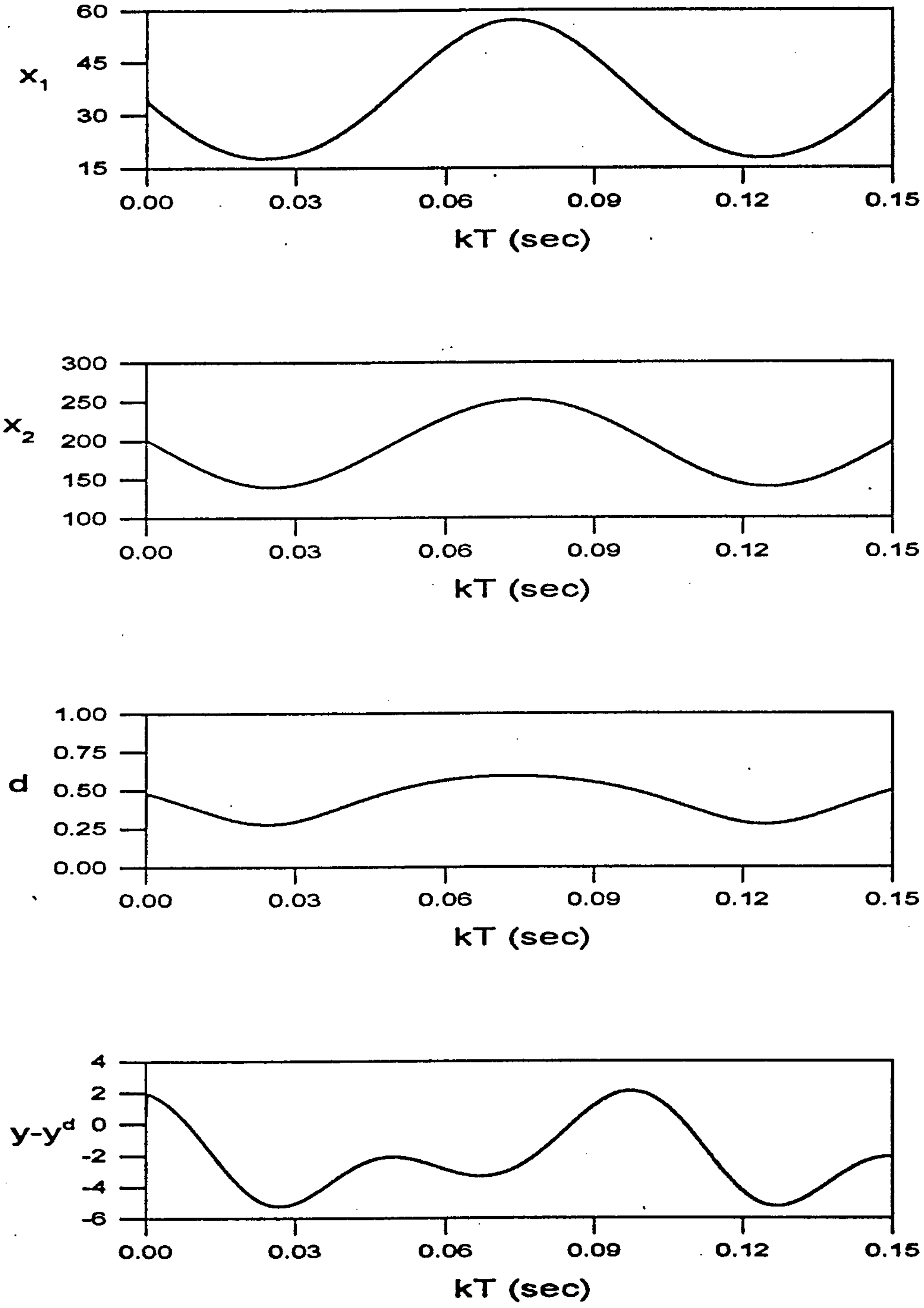

Figure 4.11: Approximate output tracking for boost converter.

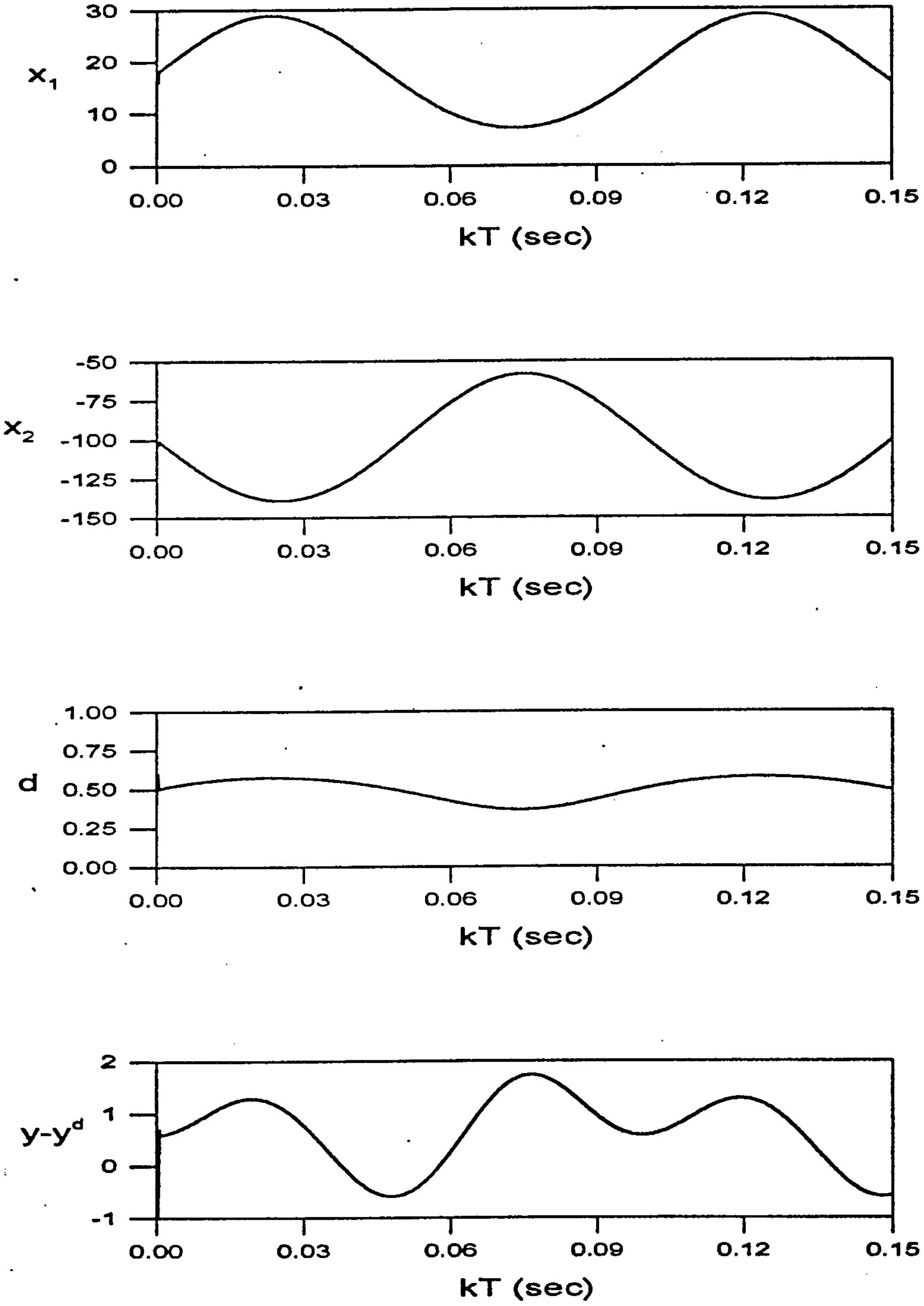

Figure 4.12: Approximate output tracking for buck-boost converter.

solution of this control problem. Power electronic converter examples are provided to illustrate the advantages of the proposed control design.

The key concept, output redefinition, is the main subject of the paper. Due to the effects of sampling, it is common to encounter sampled-data systems with unacceptable zero dynamics. For such systems, perfect output tracking is not a practical control objective. The only alternative is to design a controller which provides approximate tracking performance, while guaranteeing internal stability and reduction of oscillatory modes. The approach is simple: the original system is approximated by one with acceptable zeros, and the approximate system's inverse control is applied to the original system.

A secondary concept, piecewise-linear Newton iteration, also plays an important role in this paper. Since the sampled-data models of PWM systems inherently contain input nonlinearities, closed-form solutions for digital tracking controllers are not generally available. Instead, it is necessary to compute the appropriate duty ratio control inputs using a numerical search. A particularly efficient numerical method is the piecewise-linear Newton iteration, which is summarized in this paper. See [1, 2] for a more complete discussion of the piecewise-linear technique.

The results of this paper can be extended in several ways. Perhaps the most severe limitation of the proposed method is the need for accurate parameter knowledge. One possible remedy would be to augment the controller with an on-line parameter identification scheme. Another limitation which can arise is a relative degree singularity located at mid-range duty ratio values. Such a singularity would artificially limit the maximum permissible excursion of duty ratio and, hence, of desired output. This problem can be overcome by using scheduled output redefinition. It is also worth pointing out that alternative methods for transfer function approximation exist, leading to alternative forms of approximate tracking controllers. For example, it may be possible to shape the frequency response of the approximate design model, in order to meet specifications on the magnitude and/or phase error over a given frequency range. Finally, to avoid control saturation, it can be advantageous to relax the deadbeat tracking objective by designing linear error dynamics to achieve asymptotic transient response.

## References

[1] M. Al-Numay and D. G. Taylor, "Piecewise-Linear Methods for Digital Control of Input-Switched PWM Systems," *Proceedings of the IEEE International Symposium on Circuits and Systems*, Atlanta, GA, pp. 261–264, May 1996.

[2] M. Al-Numay and D. G. Taylor, "A Piecewise-Linear Method for Digital Control of PWM Systems," *Proceedings of the 27th IEEE Power Electronics Specialists Conference*, Baveno, Italy, pp. 803–809, June 1996.

[3] M. Al-Numay and D. G. Taylor, "Approximate Output Tracking Control for PWM Systems with Unacceptable Zeros," *Proceedings of the 1996 IEEE International Conference on Control Applications*, Dearborn, Michigan, pp. 498–503, September 1996.

[4] K. J. Astrom, P. Hagander and J. Sternby, "Zeros of Sampled Systems," *Automatica*, vol. 20, no. 1, pp. 31–38, 1984.

[5] L. Benvenuti, M. D. DiBenedetto and J. W. Grizzle, "Approximate Output Tracking for Nonlinear Non-Minimum Phase Systems with an Application to Flight Control," *International Journal of Robust and Nonlinear Control*, vol. 4, no. 3, pp. 397–414, 1994.

[6] J. M. Burdio and A. Martinez, "A Unified Discrete-Time State-Space Model for Switching Converters," *IEEE Transactions on Power Electronics*, vol. 10, no. 6, pp. 694–707, 1995.

[7] L. O. Chua and P. M. Lin, *Computer-Aided Analysis of Electronic Circuits: Algorithms and Computational Techniques*, Englewood Cliffs, NJ: Prentice Hall, 1975.

[8] M. E. Elbuluk, G. C. Verghese and J. G. Kassakian, "Sampled-Data Modeling and Digital Control of Resonant Converters," *IEEE Transactions on Power Electronics*, vol. 3, no. 3, pp. 344–354, 1988.

[9] L. Garcia de Vicuna, A. Poveda, L. Martinez, F. Guinjoan and J. Majo, "Computer-Aided Discrete-Time Large-Signal Analysis of Switching Regulators," *IEEE Transactions on Power Electronics*, vol. 7, no. 1, pp. 75–82, 1992.

[10] D. N. Godbole and S. S. Sastry, "Approximate Decoupling and Asymptotic Tracking for MIMO Systems," *IEEE Transactions on Automatic Control*, vol. 40, no. 3, pp. 441–450, 1995.

[11] J. Hauser, S. Sastry and P. Kokotovic, "Nonlinear Control via Approximate Input-Output Linearization: The Ball and Beam Example," *IEEE Transactions on Automatic Control*, vol. 37, no. 3, pp. 392–398, 1992.

[12] J. Hauser, S. Sastry and G. Meyer, "Nonlinear Control Design for Slightly Non-Minimum Phase Systems: Application to V/STOL Aircraft," *Automatica*, vol. 28, no. 4, pp. 665–679, 1992.

[13] F. Huliehel and S. Ben-Yaakov, "Low-Frequency Sampled-Data Models of Switched Mode DC-DC Converters," *IEEE Transactions on Power Electronics*, vol. 6, no. 1, pp. 55–61, 1991.

[14] J. G. Kassakian, M. F. Schlecht and G. C. Verghese, *Principles of Power Electronics*, Reading, MA: Addison-Wesley, 1991.

[15] F. C. Lee, R. P. Iwens, Y. Yu and J. E. Triner, "Generalized Computer-Aided Discrete Time-Domain Modeling and Analysis of DC-DC Converters," *IEEE Transactions on Industrial Electronics and Control Instrumentation*, vol. 26, no. 2, pp. 58–69, 1979.

[16] R. Prajoux, J. C. Marpinard and J. Jalade, "Accurate Mathematical Modeling of PWM Power Regulators," *NASA Technical Translation*, NASA TT F-15947, September 1974.

[17] W. H. Press, S. A. Teukolsky, W. T. Vetterling and B. P. Flannery, *Numerical Recipes in C*, 2nd Edition, New York, NY: Cambridge University Press, 1992.

[18] S. R. Sanders, G. C. Verghese and D. F. Cameron, "Nonlinear Control of Switching Power Converters," *Control: Theory and Advanced Technology*, vol. 5, no. 4, pp. 601–627, 1989.

[19] G. C. Verghese, M. E. Elbuluk and J. G. Kassakian, "A General Approach to Sampled-Data Modeling for Power Electronic Circuits," *IEEE Transactions on Power Electronics*, vol. 1, no. 2, pp. 76-89, 1986.

# Adaptive Control of DC Motor Drives with Converter Nonlinearities*

Wasim Khan and David G. Taylor

Georgia Institute of Technology
School of Electrical and Computer Engineering
Atlanta, GA 30332-0250 USA

Phone: (404) 894-8910
Fax: (404) 894-4641
Email: david.taylor@ece.gatech.edu

Submitted to International Journal of Control

### Abstract

Power electronic converters used in motor drives exhibit nonlinear behavior due to dead time and other circuit imperfections. Motors and their mechanical loads are often characterized by significant nonlinearities as well. Since the parameters describing the system are not always accurately known, improved motion control performance may be attempted by using nonlinear adaptive control methods. In this paper, the focus is on a dc motor fed by a full-bridge dc-dc converter. A linearizing adaptive motion controller is derived for the overall system, under the assumption that the parameters describing the converter, the motor, and its load, are all unknown. The controller guarantees global stability and asymptotic tracking.

## 1 Introduction

DC servo drives are typically powered by full-bridge dc-dc converters. Such converters can apply at most three voltage levels to the armature winding: the positive bus voltage, the negative bus voltage, and possibly zero voltage. Control is achieved by varying the duration of voltage levels applied within each switching cycle, using pulse width modulation (PWM). The resulting mechanical motion responds to the moving average of this two- or three-level voltage signal and, as a first approximation, this moving average depends linearly on the duty ratio command. On a more detailed level, the converter actually exhibits a nonlinear behavior due to dead time, imperfect transistor switches, parasitic capacitance in the circuit, etc.

Dead time is a time delay inserted between switch transitions to avoid shorting the voltage bus to ground. During the dead time the output voltage is not defined simply by the control logic, but also by the direction of current flowing through the armature winding. The anti-parallel diodes, which provide a closed path for the inductive load current, distort the voltage pulses during the dead time because their conduction leads to unintended voltage magnitudes. Switch imperfections include voltage drop,

---

*This work was supported in part by the National Science Foundation under grant ECS-9158037 and by the Office of Naval Research under grant N00014-96-1-0926.

and unequal turn on and turn off times. The voltage drop reduces the effective voltage applied across the motor terminals. The effect of unequal turn on and turn off times is similar to that of the dead time. Parasitic capacitance introduces a dynamic effect which limits the rates of rise and fall of the voltage pulses applied across the motor terminals. This dynamic effect can be approximated by an additional time delay. In certain operating regimes, the converter nonlinearities can introduce significant distortion into the armature voltage and, consequently, into the armature current. This current distortion may lead to unacceptable torque errors, in which case converter compensation is desired for improved performance.

Some compensation schemes addressing this problem, but for the case of three-phase dc-ac inverters, have recently appeared in the literature. In Mohan *et al.* (1989), voltage error introduced by the dead time is modeled and current control is suggested as a means of overcoming the distortion. In Sepe and Lang (1994), exhaustive measurements are made to characterize the distortion caused by the dead time and an approximate dead time inverse is used as a pre-processor to the inverter. The accuracy of the compensation depends entirely on the precision of the required off-line calibration. In Murai *et al.* (1987), the dead time interval is measured on-line and a correcting voltage pulse is added to the input voltage to compensate for the inverter nonlinearity. Such a scheme requires extra hardware circuitry. In Sukegawa *et al.* (1991), knowledge of the dead time is assumed and a corresponding correcting signal is added to the reference voltage commands in the dq frame of reference. No switch imperfections are considered. In Choi and Sul (1996), a more general compensation scheme is developed which accounts for the dead time, unequal turn on and turn off times, and the voltage drop across the inverter switches. However, at least two off-line tests are required to compute the appropriate voltage correction. Moreover, the currents are assumed to be well regulated.

Voltage distortion is due not only to dead time but is also influenced by other factors, like switch imperfections and circuit parameters. Consequently, off-line pre-calibration yields best results when performed on a converter/motor pair. The approaches which require pre-calibration are not only inflexible, they would also lead to performance degradation if the converter and/or motor parameters change slowly over time. Even without the complexities introduced by the converter nonlinearity, the design of high-performance motion controllers for motor drives is a challenging subject due to the lack of accurate mechanical load models for most applications. Parameters such as load inertia, load torque, and friction coefficients, are all typically unknown and will almost certainly change over time. Hence, in order to achieve a motion control response which is invariant with respect to the mechanical load, adaptive control methods are typically required. In all of the references cited above, the converter and the motor are treated as separate entities and no attempt is made to develop adaptive controllers or to guarantee stability of the overall design (see Sira-Ramirez *et al.* 1993 for adaptive control of buck, boost, and buck-boost converters).

In this paper, a technique motivated from Recker (1993) and Tao and Kokotovic (1994, 1996) is used for adaptive control of the converter-motor-load combination. The converter is modeled by a piecewise linear function. In order to avoid the need for pre-calibration, and to account for the possibility of slowly drifting system characteristics, the converter, motor and load parameters are considered to be unknown. Estimates of the unknown parameters are used by the adaptive controller to cancel the

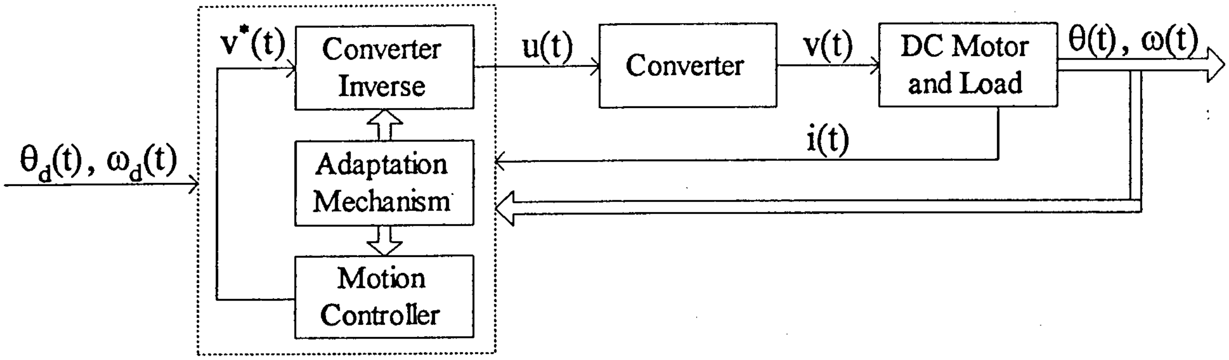

Figure 1.1: Structure of the adaptive control system.

converter nonlinearities and to achieve a motion control objective. The closed loop system is shown to be globally stable and to provide asymptotic tracking. Fig. 1.1 illustrates the overall structure of the control design, which accomodates either speed or position tracking control objectives.

## 2 DC Motor and Load

The dynamic model of a brush-commutated permanent-magnet dc motor, driving a simple mechanical load, can be expressed as

$$\dot{\theta}(t) = \omega(t) \tag{2.1}$$

$$J\dot{\omega}(t) = -B\omega(t) + Ki(t) \tag{2.2}$$

$$L\dot{i}(t) = -K\omega(t) - Ri(t) + v(t) \tag{2.3}$$

where $v(t)$ is the voltage applied to the armature, $i(t)$ is the armature current, $\omega(t)$ is the motor speed, and $\theta(t)$ is the motor position. The constant coefficients describing the motor are the torque constant $K$, the armature resistance $R$, and the armature inductance $L$. The constant coefficients describing the mechanical load are the total moment of inertia $J$ and the total viscous friction coefficient $B$. This simple load model is chosen for sake of simplicity; more complex load nonlinearities can be easily incorporated into the adaptive controller, provided that they are linearly parameterized functions of $\theta(t)$ and/or $\omega(t)$.

Armature current $i(t)$, motor speed $\omega(t)$ and (when necessary) motor position $\theta(t)$ are assumed to be measured. Although it is possible to eliminate measurement of internal signals (i.e. $i(t)$ for speed control or both $i(t)$ and $\omega(t)$ for position control) using methods described in Tao and Kokotovic (1994, 1996), such an approach is not recommended due to the significantly increased complexity of the controller. Measurement of $i(t)$ is both inexpensive and common industrial practice, and $\omega(t)$ is typically approximated from measurements of $\theta(t)$ rather than measured separately. As illustrated in Fig. 1.1, measurement of voltage $v(t)$ is not required for the control design. This is in contrast to the (non-adaptive) method used in Murai *et al.* (1987).

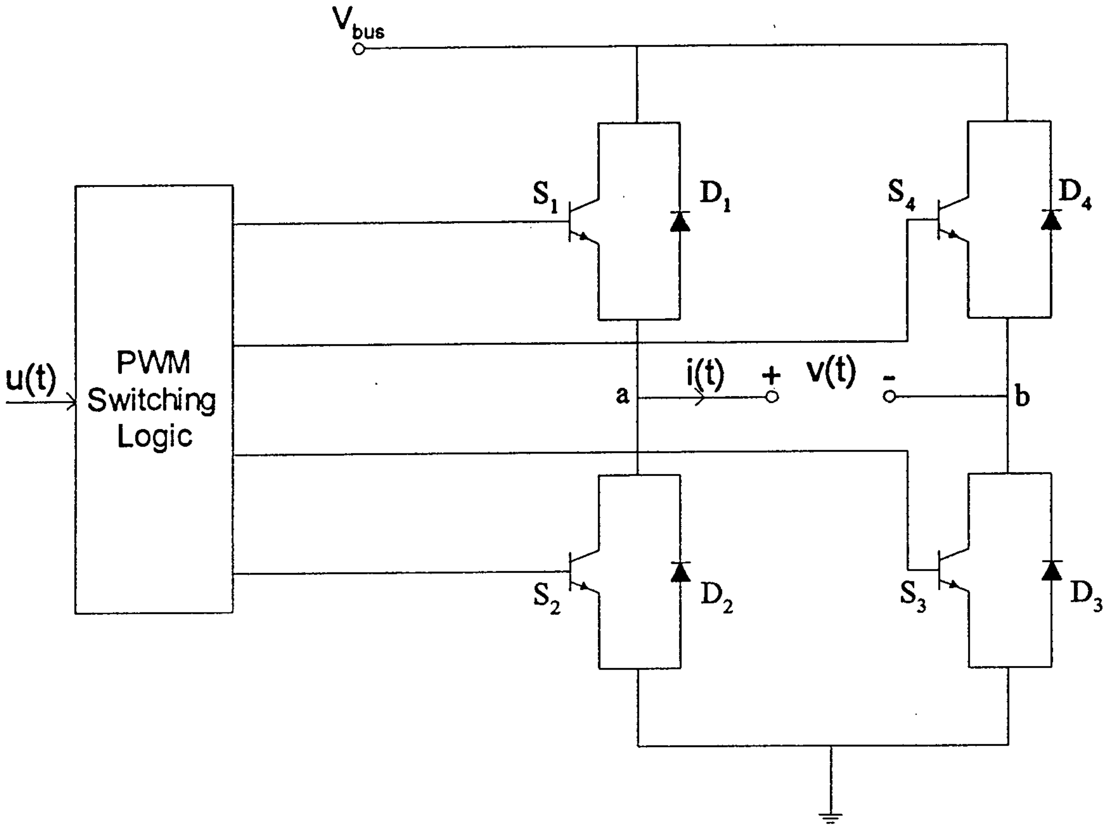

Figure 3.1: Full-bridge converter.

## 3 DC-DC Converter

A full-bridge dc-dc converter is shown in Fig. 3.1. This converter consists of two legs, each having two transistor switches $S_j$, and two diodes $D_j$. The motor winding is connected across the mid-point of each converter leg. The output voltage $v(t)$ can have at most three possible values as determined by the state of the transistor switches. For example, turning on switches $S_1$ and $S_3$ would apply $+V_{bus}$ while turning on $S_2$ and $S_4$ would establish $-V_{bus}$ across the motor winding. Zero voltage is applied if either $S_1$ and $S_4$ are on, or $S_2$ and $S_3$ are on. Turning on both switches in one leg, i.e. $S_1$ and $S_2$ or $S_3$ and $S_4$, would short the voltage bus to ground and must be avoided by including a dead time in the switching logic as described below.

Any average voltage level between $+V_{bus}$ and $-V_{bus}$, over each switching period $T$, can be produced by the converter. Consider the time interval $[kT, kT+T)$ where $k = 0, 1, 2, \cdots$, which is partitioned into two subintervals, $[kT, kT + d_kT)$ and $[kT + d_kT, kT + T)$, by the duty ratio $d_k \in [0, 1]$. The voltage $v(t)$ in each switching cycle will be $\{+V_{bus}, -V_{bus}\}$ for bipolar PWM, and either $\{+V_{bus}, 0\}$ or $\{-V_{bus}, 0\}$ for unipolar PWM. The average value of voltage produced during the $k$th cycle is computed from

$$\bar{v}_k = \frac{1}{T}\int_{kT}^{kT+T} v(t)\, dt \tag{3.1}$$

## 3.1 Converter Modeling

The voltage distortion introduced by the dead time can be explained with reference to the circuit diagram in Fig. 3.1 and the timing diagrams in Figs. 3.2 and 3.3 for the bipolar and the unipolar PWM respectively (see Mohan *et al.* 1989 also). The duration of the dead time $t_d$ has been exaggerated so that its effect can be seen clearly. The signal $u(t)$ is the input to the converter and represents the desired average value of the voltage output $v(t)$. In analog PWM implementations, $u(t)$ is compared to a triangular carrier waveform and the comparator output is latched once per switching cycle to produce $v_{\text{ideal}}(t)$, the desired terminal voltage waveform. In digital PWM implementations, the timing information contained in the waveform $v_{\text{ideal}}(t)$ is specified directly by the duty ratio, which in turn is computed from $u(t)$. For either implementation, the waveforms labeled $S_1$, $S_2$, $S_3$ and $S_4$ are logically derived from $u(t)$, but with the dead time inserted as necessary; these signals serve as the gate commands to the transistor switches.

Consider first Fig. 3.2 for the bipolar strategy. The desired voltage $v_{\text{ideal}}(t)$ switches between $+V_{bus}$ and $-V_{bus}$ and is thus a bipolar waveform. Switches $(S_1, S_3)$ and $(S_2, S_4)$ are operated as pairs. Positive voltage $+V_{bus}$ is applied by turning on $(S_1, S_3)$, while $(S_2, S_4)$ are turned off. Negative voltage $-V_{bus}$ is applied by turning on $(S_2, S_4)$, while $(S_1, S_3)$ are turned off. For either voltage polarity, dead time $t_d$ must be inserted between turn-off instants and turn-on instants. During the dead time, all switches are simultaneously turned off. Consequently, the direction of current $i(t)$ will determine the actual voltage $v(t)$ during the dead time. If $i(t) > 0$, diodes $(D_2, D_4)$ will conduct and $v(t) = -V_{bus}$ during the dead time. If $i(t) < 0$, diodes $(D_1, D_3)$ will conduct and $v(t) = +V_{bus}$ during the dead time. When $i(t) = 0$, the induced back-emf voltage appears across the converter terminals; this isolated open-circuit state will be disregarded. The actual $v(t)$ waveforms shown for the two current polarities clearly differ from the $v_{\text{ideal}}(t)$ waveform, due to dead time distortion.

Now consider Fig. 3.3 for the unipolar strategy. The desired voltage $v_{\text{ideal}}(t)$ switches between $+V_{bus}$ and 0 when positive voltage is requested, or between $-V_{bus}$ and 0 when negative voltage is requested, and is thus a unipolar waveform. There are two ways to apply zero voltage, by turning on $(S_1, S_4)$ with $(S_2, S_3)$ turned off, or by turning on $(S_2, S_3)$ with $(S_1, S_4)$ turned off. This degree of freedom can be exploited, so that voltage $v(t)$ may be produced at frequency $1/T$ while operating the switches at the lower frequency of $1/2T$. The period $2T$ switching logic may be described for the positive voltage case as follows. During the first $T$ interval, positive voltage $+V_{bus}$ is applied by turning on $(S_1, S_3)$ with $(S_2, S_4)$ turned off, and this is followed by a zero voltage state obtained by turning on $(S_1, S_4)$ with $(S_2, S_3)$ turned off. During the second $T$ interval, positive voltage $+V_{bus}$ is applied by turning on $(S_1, S_3)$ with $(S_2, S_4)$ turned off, and this is followed by a zero voltage state obtained by turning on $(S_2, S_3)$ with $(S_1, S_4)$ turned off. This mode of operation requires just 2 transitions (from all 4 switches) every $2T$ seconds; if one insists on a period $T$ switching logic with upper or lower switches used exclusively to reach the zero voltage state, then the requirement would be 4 transitions (from 2 of the switches) every $2T$ seconds. To avoid short-circuiting the dc input, dead time $t_d$ must be inserted between all turn-off instants and turn-on instants for a given leg. During the dead time, both switches of the given leg are simultaneously turned off. Consequently, the direction of current $i(t)$ will determine the actual voltage $v(t)$ during the dead time. The actual $v(t)$ waveforms for both current polarities are displayed in the

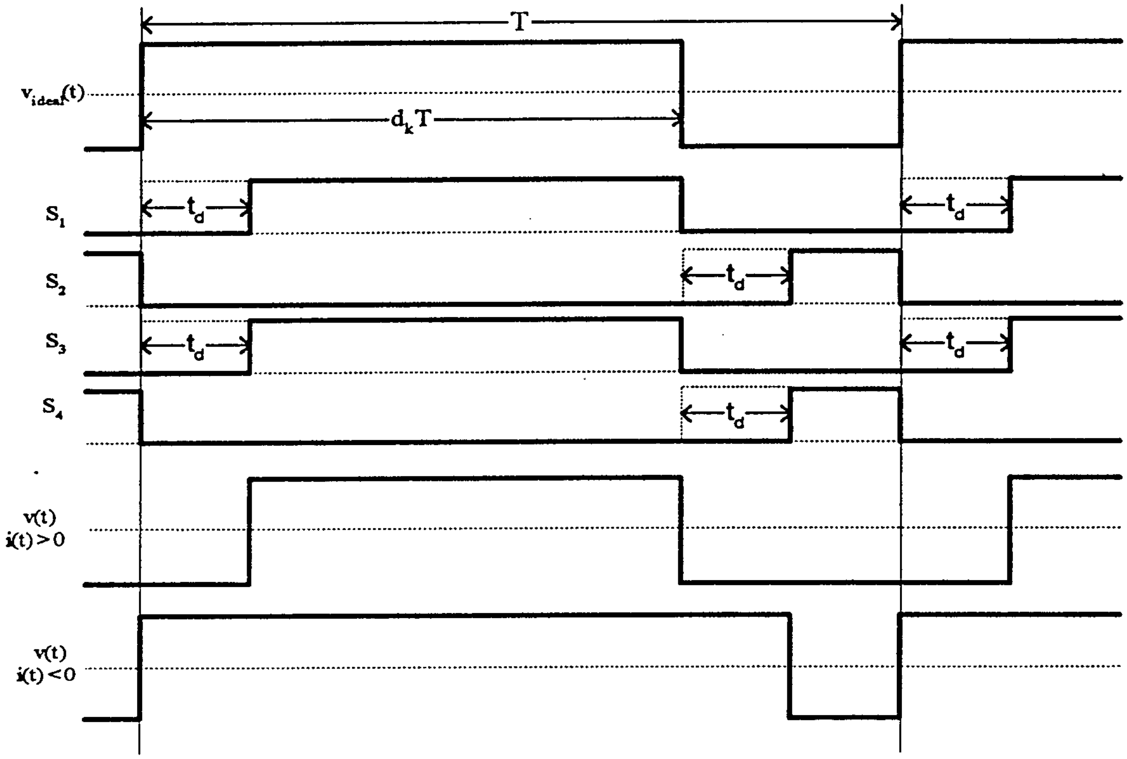

Figure 3.2: Bipolar PWM switching scheme.

figure, and comparison with $v_{\mathrm{ideal}}(t)$ reveals significant distortion.

The mathematical model of the converter is most easily derived under the assumptions that the transistors and diodes are ideal (i.e. that the only source of distortion is the dead time), and that $i(t)$ does not change signs within the $k$th switching cycle. The output voltage $v(t)$, in the presence of dead time, is modeled by

$$v(t) = \begin{cases} -\mathrm{sgn}(i_k)V_{bus} & , kT \le t < kT + t_d \\ +V_{bus} & , kT + t_d \le t < kT + d_kT \\ -\mathrm{sgn}(i_k)V_{bus} & , kT + d_kT \le t < kT + d_kT + t_d \\ -V_{bus} & , kT + d_kT + t_d \le t < kT + T \end{cases} \tag{3.2}$$

for the bipolar PWM and by

$$v(t) = \begin{cases} \frac{1}{2}\mathrm{sgn}(u_k)^2(\mathrm{sgn}(u_k) - \mathrm{sgn}(i_k))V_{bus} & , kT \le t < kT + t_d \\ \mathrm{sgn}(u_k)V_{bus} & , kT + t_d \le t < kT + d_kT \\ \frac{1}{2}\mathrm{sgn}(u_k)^2(\mathrm{sgn}(u_k) - \mathrm{sgn}(i_k))V_{bus} & , kT + d_kT \le t < kT + d_kT + t_d \\ 0 & , kT + d_kT + t_d \le t < kT + T \end{cases} \tag{3.3}$$

for the unipolar PWM, where the duty ratio is confined to the interval $d_k \in (\frac{t_d}{T}, 1 - \frac{t_d}{T})$. These mathematical expressions for $v(t)$ are obtained directly from the waveforms displayed in Figs. 3.2 and 3.3.

As previously mentioned, the objective is to operate the switches in such a way as to guarantee that the average output voltage during the $k$th cycle, $\bar{v}_k$, will be equal to the commanded value $u_k$. This objective is not easily achieved, even when the transistors and diodes are ideal. To understand why this

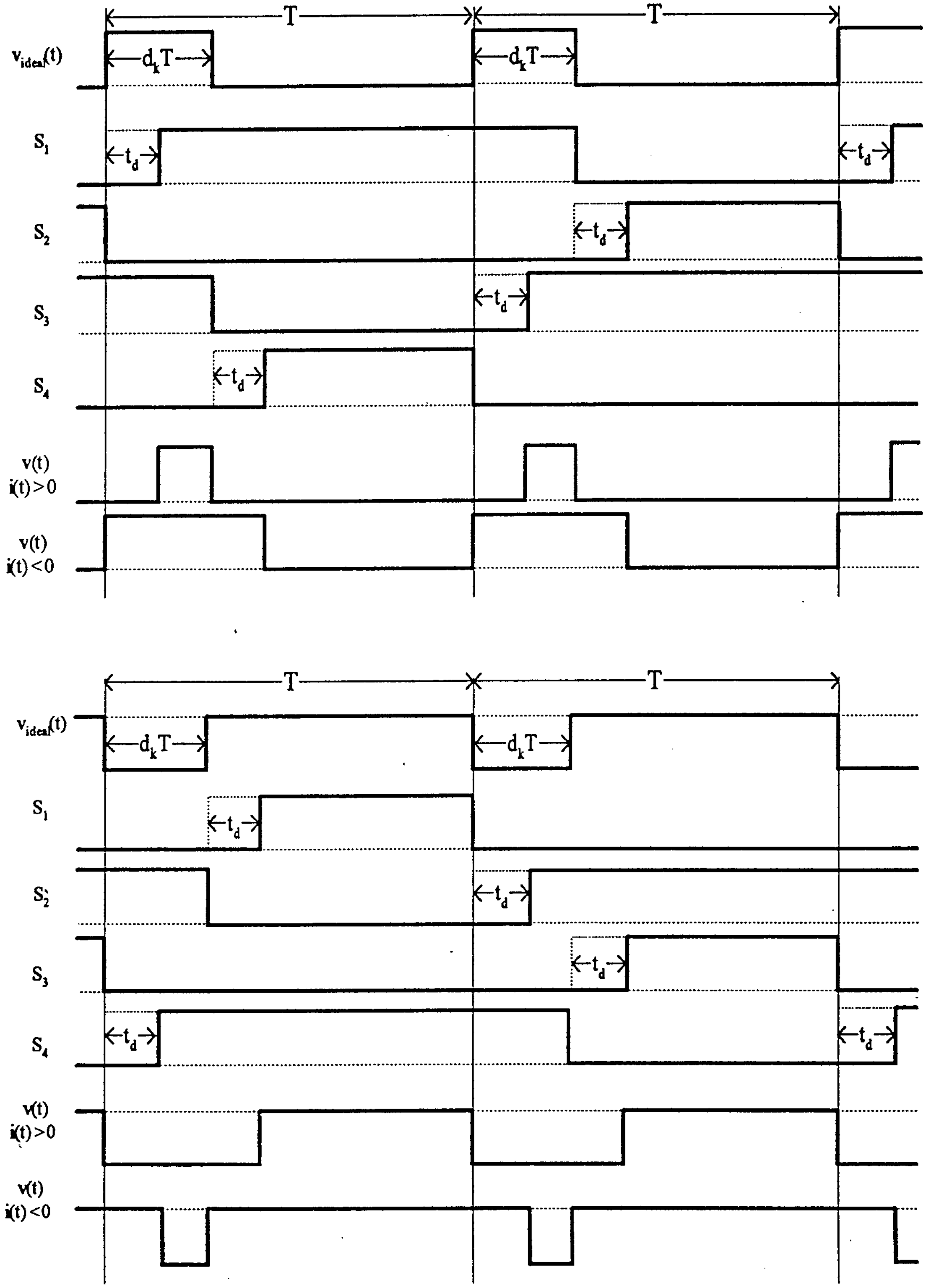
T
T
v_ideal(t)
d_kT
d_kT
S_1
t_d
t_d
S_2
t_d
S_3
t_d
S_4
t_d
v(t)
i(t)>0
v(t)
i(t)<0
T
T
v_ideal(t)
d_kT
d_kT
S_1
t_d
S_2
t_d
S_3
t_d
S_4
t_d
t_d
v(t)
i(t)>0
v(t)
i(t)<0

Figure 3.3: Unipolar PWM switching scheme.

is so, note that the $k$th cycle average output voltage computed from (3.1) is

$$\bar{v}_k = \begin{cases} V_{bus}\left((2d_k - 1) - 2\,\mathrm{sgn}(i_k)\frac{t_d}{T}\right) & \text{, bipolar PWM} \\ \mathrm{sgn}(u_k)V_{bus}\left(d_k - (1 - \mathrm{sgn}(u_k)(\mathrm{sgn}(u_k) - \mathrm{sgn}(i_k)))\frac{t_d}{T}\right) & \text{, unipolar PWM} \end{cases} \tag{3.4}$$

From (3.4), it is clear that precise knowledge of the bus voltage $V_{bus}$, the switching period $T$, and the dead time $t_d$ would be needed to select the duty ratio $d_k$ which gives the desired output $\bar{v}_k = u_k$. If such precise knowledge were available, then in principle the PWM switching logic in Fig. 3.1 could be programmed to implement

$$d_k = \begin{cases} \frac{1}{2}\left(\frac{1}{V_{bus}}u_k + 1\right) + \mathrm{sgn}(i_k)\frac{t_d}{T} & \text{, bipolar PWM} \\ \frac{1}{V_{bus}}|u_k| + (1 - \mathrm{sgn}(u_k)(\mathrm{sgn}(u_k) - \mathrm{sgn}(i_k)))\frac{t_d}{T} & \text{, unipolar PWM} \end{cases} \tag{3.5}$$

Of course, the dead time is not always known, especially for off-the-shelf converters, and the bus voltage may vary over time due to differing load conditions. If switching logic (3.5) is implemented by using estimates $\hat{t}_d$, $\hat{T}$ and $\hat{V}_{bus}$, then the average output voltage in (3.4) becomes

$$\bar{v}_k = \frac{V_{bus}}{\hat{V}_{bus}}u_k + \zeta_k\left(\frac{\hat{t}_d}{\hat{T}} - \frac{t_d}{T}\right)V_{bus} \tag{3.6}$$

where

$$\zeta_k = \begin{cases} 2\,\mathrm{sgn}(i_k) & \text{, bipolar PWM} \\ \mathrm{sgn}(u_k)^2\mathrm{sgn}(i_k) & \text{, unipolar PWM} \end{cases} \tag{3.7}$$

The effect of the direction of current flow is accounted for by the term $\zeta_k$, which takes values of $\pm 2$ for bipolar PWM or $\pm 1$ (or possibly 0) for unipolar PWM.

In summary, the static input-output model of the dc-dc converter is given by (3.6)–(3.7), which indicates that the average output voltage exhibits a jump discontinuity whenever the armature current reverses direction. Whenever the discontinuity is avoided, the input-output relationship of the converter is affine. In the ideal case when $\hat{V}_{bus} = V_{bus}$, $\hat{T} = T$, and $\hat{t}_d = t_d$, the desired operation $\bar{v}_k = u_k$ is achieved. However, if the dead time $t_d$ is neglected by setting $\hat{t}_d = 0$, the error in average output voltage will be proportional to $V_{bus}\frac{t_d}{T}$. Two implications immediately follow: even when fast switches with small $t_d$ are employed, the output error will grow larger as the switching frequency is increased, i.e. as $T$ is decreased; for any fixed $\frac{t_d}{T}$ ratio, the output error will grow in proportion to $V_{bus}$.

The static input-output model (3.6)–(3.7) has been derived for an ideal converter (with dead time). This model may be modified to account for various converter imperfections. In particular, switches are known to exhibit two types of delays. First, switches have turn-on and turn-off delays, $t_{\text{on}}$ and $t_{\text{off}}$, which account for the pure time delay between when a switch control signal changes state and when the switch begins to respond. Second, switches have voltage rise and fall times, $t_r$ and $t_f$, which account for the charging and discharging of parasitic capacitance. The consequence is that the output voltage waveforms labeled $v(t)$ in Figs. 3.2 and 3.3 would be both time delayed and approximately trapezoidal rather than square in shape.

Consider first the switch control signals $S_j$. All off-on transitions are delayed by $t_{\text{on}}$ and all on-off transitions are delayed by $t_{\text{off}}$. Examination of Figs. 3.2 and 3.3 indicates that these delays are accounted for by defining an effective dead time, i.e. by replacing $t_d$ in (3.6) with $t_d'$ where

$$t_d' = t_d + t_{\text{on}} - t_{\text{off}} \tag{3.8}$$

If $t_{\text{on}} = t_{\text{off}} = 0$, then the redefined (3.6) obviously reduces to (3.6) as a special case. If $t_{\text{on}} = t_{\text{off}} \neq 0$, then the redefined (3.6) also reduces to (3.6) as a special case, since the voltage waveforms simply exhibit a phase shift which does not influence their average values. On the other hand, if $t_{\text{on}} > t_{\text{off}}$, voltage distortion is increased.

The presence of parasitic capacitance limits the rates of rise and fall of the voltage pulses. It is reasonable to approximate the voltage transitions by linear ramps, leading to trapezoidal voltage waveforms instead of the square voltage waveforms shown in Figs. 3.2 and 3.3. Given that the rising and falling edges become ramps of duration $t_r$ and $t_f$, respectively, the trapezoidal waveform may be replaced by a square waveform with rising edge delayed by $\frac{1}{2}t_r$ and with falling edge delayed by $\frac{1}{2}t_f$, without affecting the average value. Alternatively, the trapezoidal waveform may be replaced by a square waveform with rising edge delayed and falling edge advanced by an equal time interval of $\frac{1}{4}(t_r - t_f)$. Hence, the effect of parasitic capacitance can be approximated by replacing $t_d$ in (3.6) with $t_d'$ where

$$t_d' = t_d + \frac{1}{4}(t_r - t_f) \tag{3.9}$$

Note that if both $t_r$ and $t_f$ are zero, or if $t_r$ and $t_f$ are nonzero but equal, then no change in (3.6) is required. Otherwise, this additional source of distortion is captured in the model by direct substitution. Naturally, the presence of both types of switching delays is accomodated by combining the additive terms in (3.8)–(3.9).

## 3.2 Piecewise Linear Converter Model

It is preferable for PWM converters to use a high switching frequency $1/T$, in order to reduce switching ripple. Under such circumstances, a standard averaging approximation may be made; the two- or three-level voltage $v(t)$ may be safely replaced by a continuous-time representation of average voltage $\bar{v}_k$ without significantly altering the response of the system. This averaging approximation will be used throughout the remainder of this paper.

Motivated in part by (3.6)–(3.7), the converter will be modeled in continuous-time by a general piecewise linear expression of the form

$$v(t) = \begin{cases} m_+(u(t) - b_+) & , \; i(t) > 0 \\ m_-(u(t) - b_-) & , \; i(t) < 0 \end{cases} \tag{3.10}$$

Fig. 3.4 illustrates the input-output behavior of the converter, using the parameterization of (3.10). The constant coefficients $m_+$, $m_-$, $b_+$ and $b_-$ depend on various converter parameters. For example, the converter models of the previous section can be put into the new format by defining the slopes

$$m_+ = m_- = \frac{V_{bus}}{\hat{V}_{bus}} \tag{3.11}$$

and the intercepts

$$b_+ = -b_- = \gamma \left( \frac{\hat{t}_d}{\hat{T}} - \frac{t_d}{T} \right) \hat{V}_{bus} \tag{3.12}$$

where $\gamma = -2$ for bipolar PWM and $\gamma = -1$ for unipolar PWM. In these parameter assignments, $t_d$ represents the effective dead time which includes the contributions due to turn-on delay, turn-off delay,

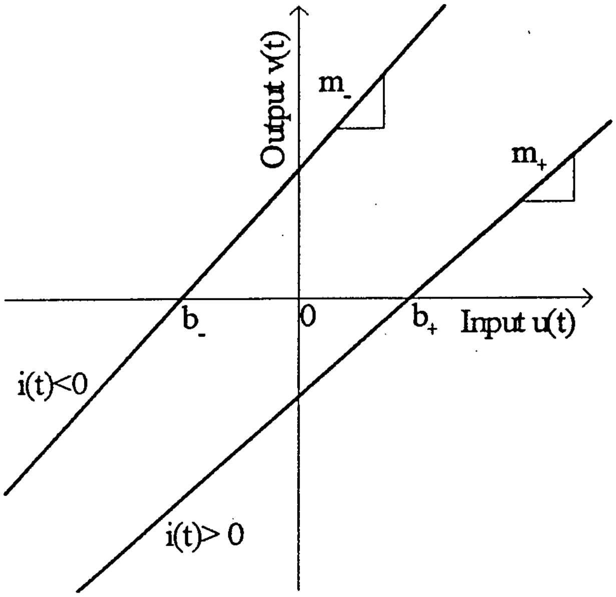

Figure 3.4: Piecewise linear model of the converter.

voltage rise time, and voltage fall time. Since $\text{sgn}(i(t))$ is determined by the direction of current only, it is thus available as a measurement even when the converter parameters are unknown.

The piecewise linear model (3.10) does not bother to model the $v(t) = u(t) = 0$ zero state of unipolar PWM converters; this zero state is achieved without switching and is easily implemented using if-then logic. For normal switching-based converter operation, (3.10) captures all features of (3.6)–(3.7) for both bipolar and unipolar PWM.

Note that the piecewise linear model (3.10) is more general in structure than required to capture the simple converter models described in the previous section. These simple converters have the property that $m_+ = m_-$ and $b_+ = -b_-$. The motivation for including the greater generality in (3.10) comes from the desire to account for additional secondary effects which create asymmetries with respect to the direction of current.

For example, the voltage drops of the transistor switches and diodes reduce the effective output voltage of the converter. The reduction in output voltage depends on the state of the switches and the current direction. When these voltage drops are accounted for, the magnitudes of $b_+$ and $b_-$ will be unequal (for both bipolar and unipolar PWM), and $m_+$ and $m_-$ will be unequal (for bipolar PWM only).

Another example is the existence of gain and offset errors in the circuitry that controls the switches. These errors could arise from the comparison circuit in analog PWM converters or from the sampling circuit in digital PWM converters. When these sources of error are included in the model, the magnitudes of $b_+$ and $b_-$ will again be unequal.

From these two examples, it is clear that the parameterization of (3.10) is sufficiently general to capture many converter imperfections. As the remainder of the paper will show, this extra level of generality does not significantly add to the complexity of the adaptive control system.

# 4 Adaptive Control Design

The control objective is to achieve asymptotic motion tracking with closed-loop stability, despite the presence of converter nonlinearities and parameter uncertainty. Adaptive input-output linearization is used as the basis for control design (see Sastry and Isidori 1989 and Kanellakopoulos *et al.* 1991). Since the controller includes on-line parameter estimation, detailed off-line measurements and pre-calibration are not necessary; moreover, the controller can automatically adjust to slowly drifting parameters. Refer to Fig. 1.1 for a block diagram of the overall control system.

## 4.1 Converter Inverse

As indicated in (3.10) and in Fig. 3.4, the converter is non-ideal in the sense that $v(t) \neq u(t)$. However, since the converter is characterized by an invertible static model, the nonlinearity cancellation technique of Recker (1993) and Tao and Kokotovic (1994, 1996) can be applied. Simpy put, the distortion introduced by the converter can be attenuated by preceding the converter with a so-called converter inverse. If the converter inverse is properly calibrated, all non-ideal features of the converter are cancelled, and $v(t)$ will be linearly proportional to the input of the converter inverse, $v^\star(t)$.

Note from (2.3) and (3.10) that the overall model contains products of converter parameters and motor parameter $1/L$. To provide a linear parameterization, (3.10) is rewritten in the form

$$\frac{1}{L}v(t) = \begin{cases} \vartheta_{C1}u(t) - \vartheta_{C2} & , \ i(t) > 0 \\ \vartheta_{C3}u(t) - \vartheta_{C4} & , \ i(t) < 0 \end{cases} \tag{4.1}$$

where

$$\vartheta_C = \left[ \begin{array}{cccc} \frac{m_+}{L} & \frac{m_+ b_+}{L} & \frac{m_-}{L} & \frac{m_- b_-}{L} \end{array} \right]^T \tag{4.2}$$

is the vector of unknown converter-dependent parameters. The adaptive converter inverse is defined as

$$u(t) = \begin{cases} \hat{\vartheta}_{C1}^{-1}(t)\left(v^\star(t) + \hat{\vartheta}_{C2}(t)\right) & , \ i(t) > 0 \\ \hat{\vartheta}_{C3}^{-1}(t)\left(v^\star(t) + \hat{\vartheta}_{C4}(t)\right) & , \ i(t) < 0 \end{cases} \tag{4.3}$$

where $v^\star(t)$ is the converter inverse input and $\hat{\vartheta}_C(t)$ represents the estimated value of $\vartheta_C$.

The relationship between the converter inverse input $v^\star(t)$ and the converter output voltage $v(t)$ is

$$\frac{1}{L}v(t) = v^\star(t) + W_C^T(t)\tilde{\vartheta}_C(t) \tag{4.4}$$

where the converter regressor vector is

$$\begin{aligned} W_C(t) &= \left[ \begin{array}{cccc} -\chi_+(t)u(t) & \chi_+(t) & -\chi_-(t)u(t) & \chi_-(t) \end{array} \right]^T & (4.5) \\ \chi_+(t) &= \begin{cases} 1 & , \ i(t) > 0 \\ 0 & , \ \text{otherwise} \end{cases} & (4.6) \\ \chi_-(t) &= \begin{cases} 1 & , \ i(t) < 0 \\ 0 & , \ \text{otherwise} \end{cases} & (4.7) \end{aligned}$$

and where $\tilde{\vartheta}_C(t) = \hat{\vartheta}_C(t) - \vartheta_C$ denotes parameter estimation error. Note that $W_C(t)$ depends only on $\text{sgn}(i(t))$ and $u(t)$, and can thus be computed without knowledge of $\vartheta_C$ and without measurement of $v(t)$. In the ideal case where $\hat{\vartheta}_C(t) = \vartheta_C$ for all $t \geq 0$, the converter output voltage obeys $\frac{1}{L}v(t) = v^\star(t)$.

## 4.2 Estimated Normal Form

The complete model of the dc motor drive, which includes the motor and load dynamics (2.1)–(2.3) as well as the cascade combination of the converter inverse and the converter (4.4), is given by

$$\dot\theta(t) = \omega(t) \tag{4.8}$$

$$\dot\omega(t) = -\vartheta_{L1}\omega(t) + \vartheta_{L2}i(t) \tag{4.9}$$

$$\dot i(t) = -\vartheta_{M1}\omega(t) - \vartheta_{M2}i(t) + v^\star(t) + W_C^T(t)\tilde\vartheta_C(t) \tag{4.10}$$

where the vector of unknown motor-dependent parameters is

$$\vartheta_M = [\ \tfrac{K}{L} \quad \tfrac{R}{L}\ ]^T \tag{4.11}$$

and the vector of unknown load-dependent parameters is

$$\vartheta_L = [\ \tfrac{B}{J} \quad \tfrac{K}{J}\ ]^T \tag{4.12}$$

To prepare for adaptive input-output linearization, consider the estimated acceleration defined by

$$\alpha(t) = -\hat\vartheta_{L1}(t)\omega(t) + \hat\vartheta_{L2}(t)i(t) \tag{4.13}$$

where $\hat\vartheta_L(t)$ is the estimated value of $\vartheta_L$. As shown in Kanellakopoulos *et al.* (1991), since all unknown parameters of the motor drive system are separated from the control input by no more than one integration, a change of variables from armature current to estimated acceleration will lead to certain advantages. In contrast, note that a change of variables from armature current to true acceleration (as suggested in Sastry and Isidori 1989) would instead lead to overparameterization and other disadvantages.

Using the change of variables suggested above, i.e. replacing armature current with estimated acceleration, the dc motor drive model is transformed into the estimated normal form

$$\dot\theta(t) = \omega(t) \tag{4.14}$$

$$\dot\omega(t) = \alpha(t) + \omega(t)\tilde\vartheta_{L1}(t) - i(t)\tilde\vartheta_{L2}(t) \tag{4.15}$$

$$\dot\alpha(t) = f_\omega(t) + f_i(t) + \hat\vartheta_{L2}(t)v^\star(t) + \hat\vartheta_{L2}(t)W_C^T(t)\tilde\vartheta_C(t) \tag{4.16}$$

where $\tilde\vartheta_L(t) = \hat\vartheta_L(t) - \vartheta_L$ represents parameter estimation error and

$$f_\omega(t) = \left(-\dot{\hat\vartheta}_{L1}(t) + \hat\vartheta_{L1}(t)\vartheta_{L1} - \hat\vartheta_{L2}(t)\vartheta_{M1}\right)\omega(t) \tag{4.17}$$

$$f_i(t) = \left(\dot{\hat\vartheta}_{L2}(t) - \hat\vartheta_{L1}(t)\vartheta_{L2} - \hat\vartheta_{L2}(t)\vartheta_{M2}\right)i(t) \tag{4.18}$$

Note that if one neglects parameter estimation errors, this new model is simply a chain of integrators with control input $v^\star(t)$ and functions $f_\omega(t)$ and $f_i(t)$ all located in the bottom equation.

## 4.3 Motion Controller

The motion controller is derived by applying input-output linearization after replacing all unknown parameters in the estimated normal form by their estimated values, yielding

$$v^\star(t) = \hat\vartheta_{L2}^{-1}(t)\left(-\hat f_\omega(t) - \hat f_i(t) + \Delta(t)\right) \tag{4.19}$$

where

$$\hat{f}_\omega(t) \quad = \quad \left(-\dot{\hat{\vartheta}}_{L1}(t) + \hat{\vartheta}_{L1}(t)\hat{\vartheta}_{L1}(t) - \hat{\vartheta}_{L2}(t)\hat{\vartheta}_{M1}(t)\right)\omega(t) \tag{4.20}$$

$$\hat{f}_i(t) \quad = \quad \left(\dot{\hat{\vartheta}}_{L2}(t) - \hat{\vartheta}_{L1}(t)\hat{\vartheta}_{L2}(t) - \hat{\vartheta}_{L2}(t)\hat{\vartheta}_{M2}(t)\right) i(t) \tag{4.21}$$

and where $\Delta(t)$ represents a linear error feedback. The design of $\Delta(t)$ depends on the control objective, e.g. either position control or speed control. In (4.20)–(4.21), $\hat{\vartheta}_M(t)$ is the estimated value of $\vartheta_M$ and, as usual, $\tilde{\vartheta}_M(t) = \hat{\vartheta}_M(t) - \vartheta_M$ will denote the corresponding parameter estimation error. Implementation of (4.20)–(4.21) will be achieved by replacing the terms $\dot{\hat{\vartheta}}_{L1}(t)$ and $\dot{\hat{\vartheta}}_{L2}(t)$ by the right-hand-sides of the corresponding update laws to be determined in the next section.

For position tracking control, with desired position trajectory $\theta_d(t)$, the outer feedback loop is given by

$$\Delta(t) = -c_\theta^T e_\theta(t) + \theta_d^{(3)}(t) \tag{4.22}$$

where the error vector is

$$e_\theta(t) = \begin{bmatrix} \theta(t) - \theta_d^{(0)}(t) \\ \omega(t) - \theta_d^{(1)}(t) \\ \alpha(t) - \theta_d^{(2)}(t) \end{bmatrix} \tag{4.23}$$

and where $c_\theta$ is a feedback gain vector chosen such that $s^3 + c_{\theta 3}s^2 + c_{\theta 2}s + c_{\theta 1}$ is a Hurwitz polynomial. The closed-loop error dynamics are

$$\dot{e}_\theta(t) = A_\theta e_\theta(t) + W_\theta^T(t)\tilde{\vartheta}(t) \tag{4.24}$$

where

$$A_\theta \quad = \quad \begin{bmatrix} 0 & 1 & 0 \\ 0 & 0 & 1 \\ -c_{\theta 1} & -c_{\theta 2} & -c_{\theta 3} \end{bmatrix} \tag{4.25}$$

$$W_\theta^T(t) \quad = \quad \begin{bmatrix} 0_{1\times 4} & 0 & 0 & 0 & 0 \\ 0_{1\times 4} & 0 & 0 & \omega(t) & -i(t) \\ \hat{\vartheta}_{L2}(t)W_C^T(t) & \hat{\vartheta}_{L2}(t)\omega(t) & \hat{\vartheta}_{L2}(t)i(t) & -\hat{\vartheta}_{L1}(t)\omega(t) & \hat{\vartheta}_{L1}(t)i(t) \end{bmatrix} \tag{4.26}$$

$$\tilde{\vartheta}(t) \quad = \quad \begin{bmatrix} \tilde{\vartheta}_C^T(t) & \tilde{\vartheta}_M^T(t) & \tilde{\vartheta}_L^T(t) \end{bmatrix}^T. \tag{4.27}$$

For speed tracking control, with desired speed trajectory $\omega_d(t)$, the outer feedback loop is given by

$$\Delta(t) = -c_\omega^T e_\omega(t) + \omega_d^{(2)}(t) \tag{4.28}$$

where the error vector is

$$e_\omega(t) = \begin{bmatrix} \omega(t) - \omega_d^{(0)}(t) \\ \alpha(t) - \omega_d^{(1)}(t) \end{bmatrix} \tag{4.29}$$

and where $c_\omega$ is a feedback gain vector chosen such that $s^2 + c_{\omega 2}s + c_{\omega 1}$ is a Hurwitz polynomial. The closed-loop error dynamics are

$$\dot{e}_\omega(t) = A_\omega e_\omega(t) + W_\omega^T(t)\tilde{\vartheta}(t) \tag{4.30}$$

where

$$
\begin{aligned}
A_\omega &= \begin{bmatrix} 0 & 1 \\ -c_{\omega 1} & -c_{\omega 2} \end{bmatrix} && (4.31) \\
W_\omega^T(t) &= \begin{bmatrix} 0_{1\times 4} & 0 & 0 & \omega(t) & -i(t) \\ \hat{\vartheta}_{L2}(t)W_C^T(t) & \hat{\vartheta}_{L2}(t)\omega(t) & \hat{\vartheta}_{L2}(t)i(t) & -\hat{\vartheta}_{L1}(t)\omega(t) & \hat{\vartheta}_{L1}(t)i(t) \end{bmatrix} && (4.32) \\
\tilde{\vartheta}(t) &= \begin{bmatrix} \tilde{\vartheta}_C^T(t) & \tilde{\vartheta}_M^T(t) & \tilde{\vartheta}_L^T(t) \end{bmatrix}^T && (4.33)
\end{aligned}
$$

## 4.4 Parameter Adaptation and Stability Analysis

As shown above, the combined effect of the cancellation loop and the pole placement loop is to achieve closed-loop error dynamics governed by

$$\dot{e}(t) = Ae(t) + W(t)^T\tilde{\vartheta}(t) \tag{4.34}$$

where $A$, $e(t)$, and $W(t)$ depend on the control objective. Now consider the Lyapunov function candidate

$$V(t) = e(t)^T Pe(t) + \tilde{\vartheta}^T(t)\Gamma^{-1}\tilde{\vartheta}(t) \tag{4.35}$$

where $\Gamma$ is a positive-definite symmetric adaptive gain matrix and $P$ is the positive-definite symmetric matrix which solves the Lyapunov equation

$$A^T P + PA = -Q \tag{4.36}$$

given any positive-definite symmetric matrix $Q$. Time differentiating both sides of (4.35) gives

$$\dot{V}(t) = -e^T(t)Qe(t) + 2\tilde{\vartheta}^T(t)\left(\Gamma^{-1}\dot{\tilde{\vartheta}}(t) + W(t)Pe(t)\right) \tag{4.37}$$

Selecting the parameter update law

$$\dot{\hat{\vartheta}}(t) = -\Gamma W(t)Pe(t) \tag{4.38}$$

reduces (4.37) to

$$\dot{V}(t) = -e^T(t)Qe(t) \leq 0 \tag{4.39}$$

Even though the update law (4.38) guarantees that $V(t)$ is non-increasing, it may lead to another problem. Specifically, note that the possibility of division by zero exists in both the converter inverse (4.3) and in the motion controller (4.19). However, under the reasonable assumption that positive constants $\vartheta_{C1}^0$, $\vartheta_{C3}^0$ and $\vartheta_{L2}^0$ are known such that

$$\vartheta_{C1} > \vartheta_{C1}^0 \quad \vartheta_{C3} > \vartheta_{C3}^0 \quad \vartheta_{L2} > \vartheta_{L2}^0 \tag{4.40}$$

it is possible to use projection on (4.38) in order to guarantee that division by zero will not occur while also guaranteeing that $\dot{V}(t) \leq 0$ continues to hold (see Ioannou and Sun 1996).

In summary, the complete adaptive control system consists of the adaptive converter inverse (4.3), the adaptive inner-loop of the motion controller (4.19), the adaptive outer-loop of the motion controller (4.22) or (4.28), and the parameter update law (4.38) modified by projection. A Lyapunov function $V(t)$ satisfying $\dot{V}(t) \leq 0$ has been found, which guarantees that tracking error $e(t)$ and parameter error

$\tilde{\vartheta}(t)$ are bounded and confined to a closed ellipsoidal region in the error space. Application of Barbalat's Lemma (see Ioannou and Sun 1996) allows the further conclusion that $e(t) \to 0$ as $t \to \infty$, i.e. that the tracking error converges to zero asymptotically. The boundedness of all signals in the closed-loop system, as well as the asymptotic tracking capability, are guaranteed for all bounded initial conditions and all bounded reference trajectories.

There are several special cases for which the adaptive control system simplifies. For example, if any parameter vector $\vartheta_C$, $\vartheta_M$, or $\vartheta_L$ is known a priori, then this known vector does not need to be estimated on-line. Instead, one would simply plug the known vector into the adaptive converter inverse or adaptive motion controller as necessary, and the corresponding update law would be disregarded.

## 5 Simulation Results

Two computer simulations were performed to support the results presented in this paper. In both simulations, all parameters of the converter-motor-load combination are assumed to be unknown, and the control objective is speed tracking. The converter parameters are: $m_+ = 0.8$, $b_+ = 5.5$, $m_- = 1.2$, and $b_- = -5$. The motor and load parameters are: $B = 0.5$, $J = 1$, $K = 5$, $R = 1.3$ and $L = 0.7$. Hence,

$$\begin{aligned}
\vartheta_C &= \begin{bmatrix} 1.143 & 6.286 & 1.714 & -8.571 \end{bmatrix}^T \\
\vartheta_M &= \begin{bmatrix} 7.143 & 1.857 \end{bmatrix}^T \\
\vartheta_L &= \begin{bmatrix} 0.5 & 5 \end{bmatrix}^T
\end{aligned}$$

The initial parameter estimates are chosen to be

$$\begin{aligned}
\hat{\vartheta}_C(0) &= \begin{bmatrix} 1 & 0 & 1 & 0 \end{bmatrix}^T \\
\hat{\vartheta}_M(0) &= \begin{bmatrix} 3.571 & 0.929 \end{bmatrix}^T \\
\hat{\vartheta}_L(0) &= \begin{bmatrix} 0.25 & 6 \end{bmatrix}^T
\end{aligned}$$

This choice corresponds to assuming an ideal converter, a unity inductance, and motor and load parameters equal (in most cases) to one-half of their true values. The gains are chosen to be

$$\begin{aligned}
c_\omega &= \begin{bmatrix} 144 & 24 \end{bmatrix}^T \\
P &= \begin{bmatrix} 10 & 1 \\ 1 & 0.2 \end{bmatrix} \\
\Gamma &= \operatorname{diag}\{0.2,\ 250,\ 0.2,\ 200,\ 50,\ 5,\ 5,\ 0.5\}
\end{aligned}$$

and the projection parameters are selected to be

$$\vartheta^0_{C1} = \frac{1}{3}\vartheta_{C1} \quad \vartheta^0_{C3} = \frac{1}{3}\vartheta_{C3} \quad \vartheta^0_{L2} = \frac{1}{3}\vartheta_{L2}$$

Although not necessary, projection was also used on all other parameter estimates to keep them positive or negative as appropriate; this option enhances parameter convergence. During the first 2 seconds, no parameter adaptation is performed and the controller uses the fixed initial parameter estimates.

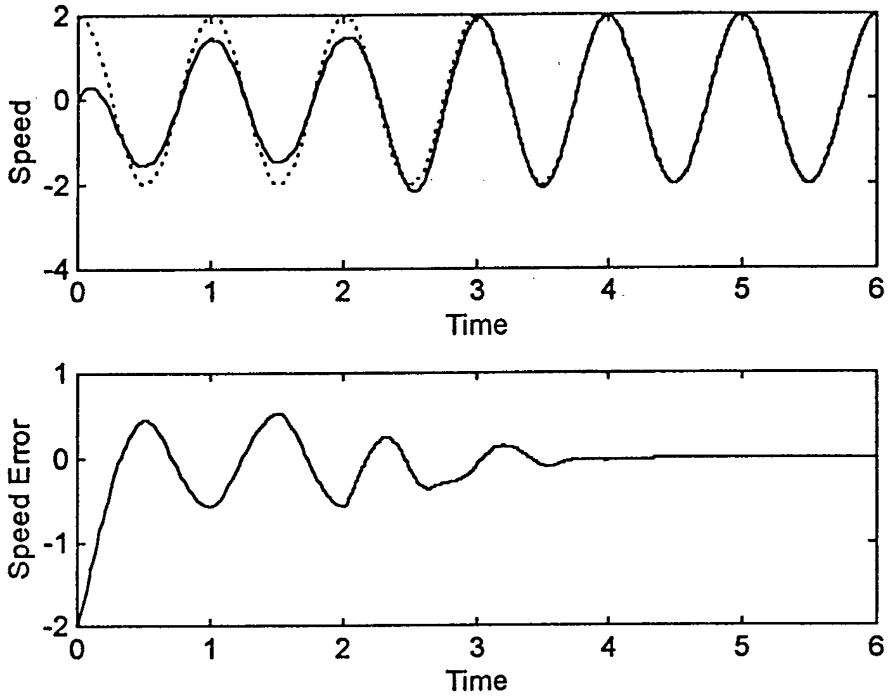

Figure 5.1: Case 1, speed and speed error.

In the first simulation, shown in Figs. 5.1–5.4, the motor is commanded to track the speed trajectory

$$\omega_d(t) = 2\cos(2\pi t)$$

During the first 2 seconds when adaptation is disabled, a large speed tracking error persists and the converter output voltage exhibits significant jump discontinuities. After a few seconds of adaptation, the speed error is reduced essentially to zero even though a nonzero error in converter output voltage remains at steady-state. The voltage jump discontinuities are, however, significantly reduced by the adaptation process. Note that the parameter estimation error does not converge to zero in this simulation.

In the second simulation, shown in Figs. 5.5–5.10, the motor is commanded to follow the desired speed

$$\omega_d(t) = 2\cos(2\pi t) + \sin(6\pi t)$$

In this case, the large speed and voltage errors present in the untuned response are both reduced practically to zero shortly after adaptation is enabled, as the parameter estimates converge to the true parameter values. This parameter convergence occurs because the desired trajectory is sufficiently rich in frequencies.

From both simulations, it is interesting to note that adaptation of the motor and load parameters occurs on a continuous basis (unless projection is activated), whereas adaptation of the converter parameters occurs piecewise in time according to the sign of the armature current.

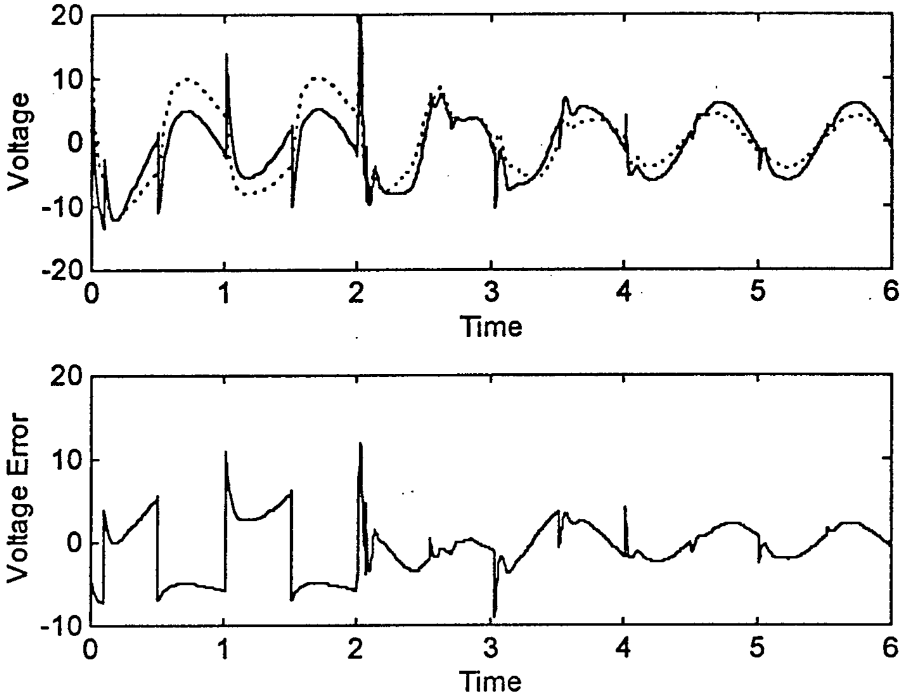

Figure 5.2: Case 1, desired and applied voltage.

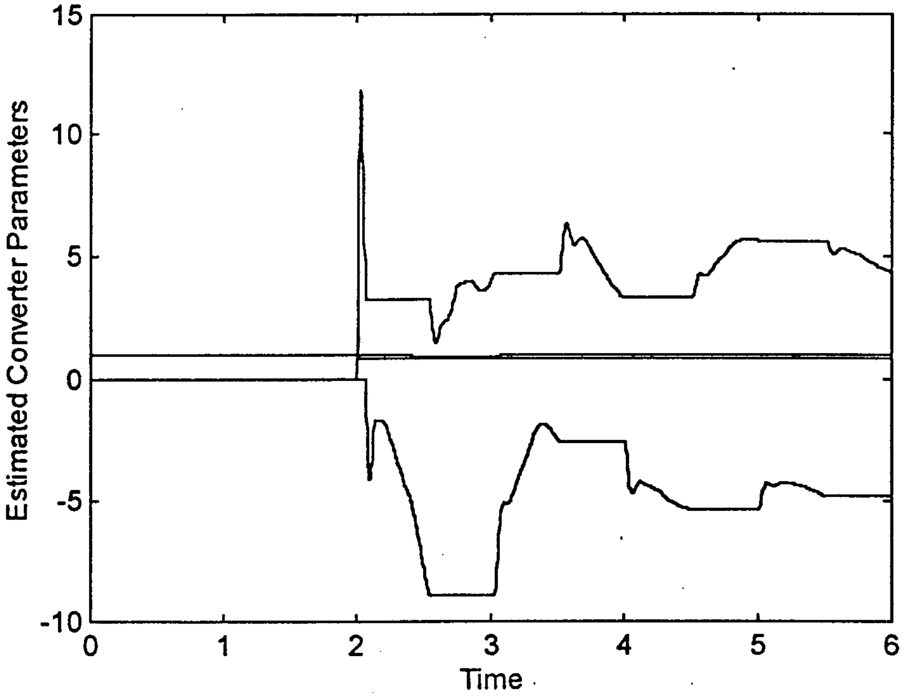

Figure 5.3: Case 1, estimated converter parameters.

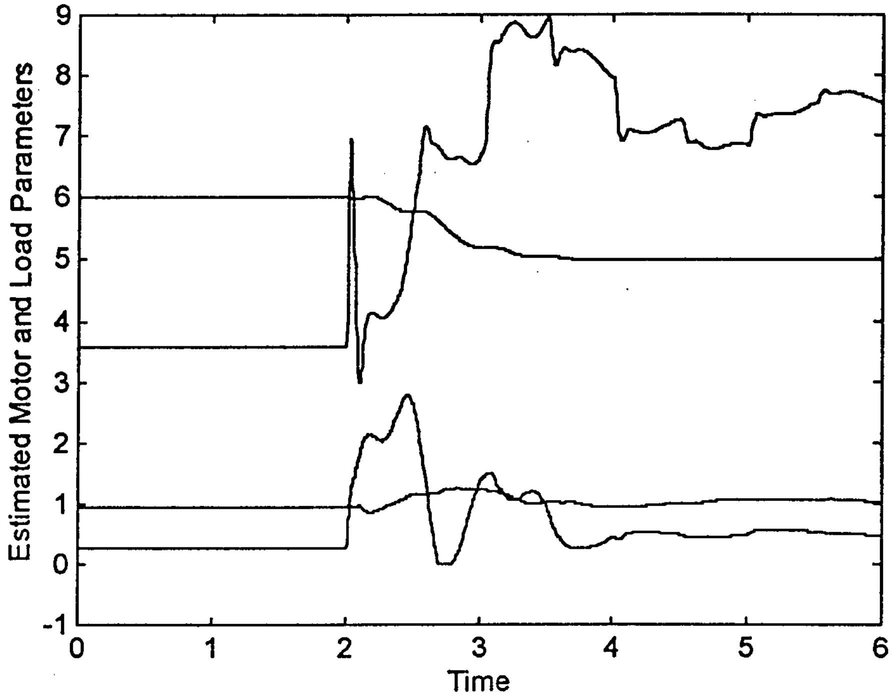

Figure 5.4: Case 1, estimated motor and load parameters.

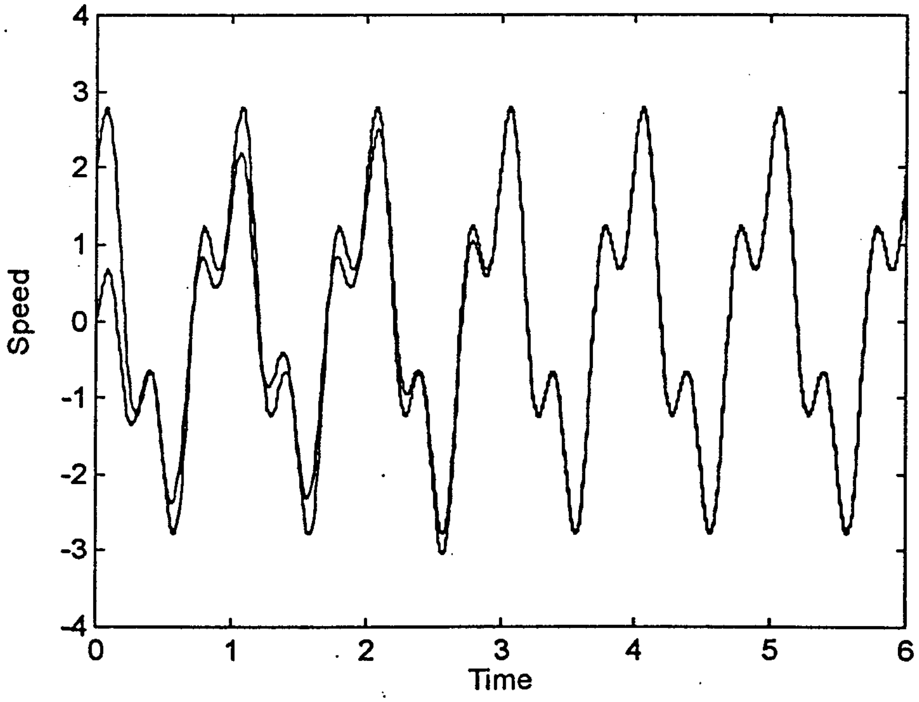

Figure 5.5: Case 2, actual and desired speed.

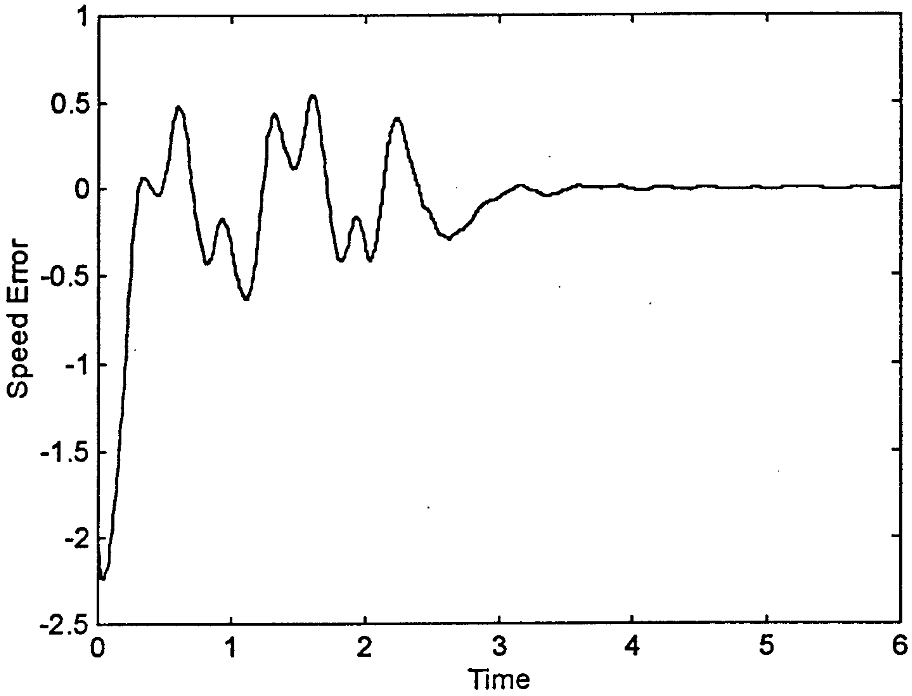

Figure 5.6: Case 2, speed error.

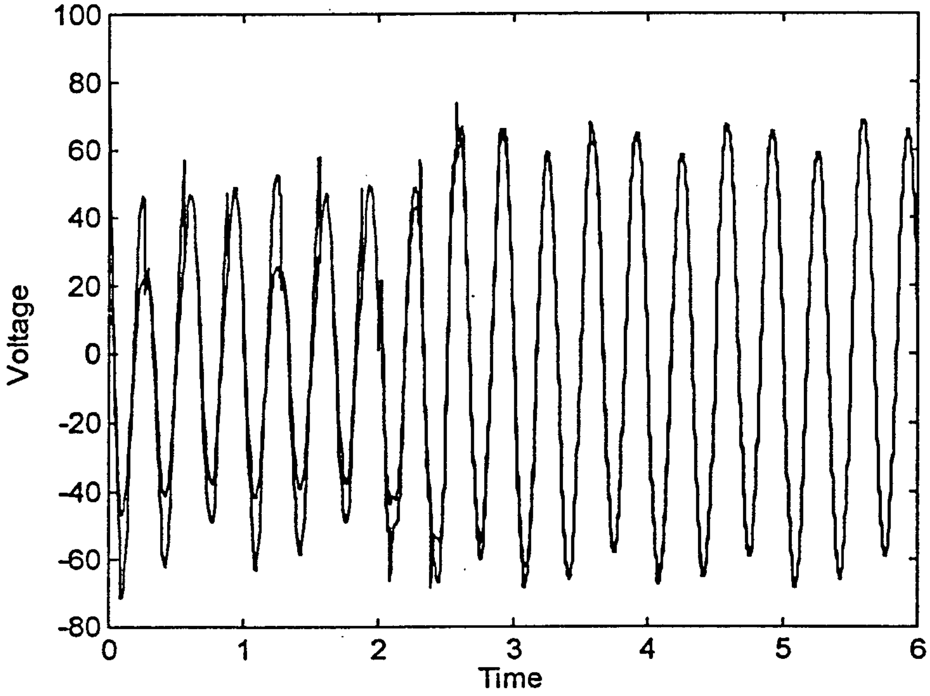

Figure 5.7: Case 2, actual and desired voltage.

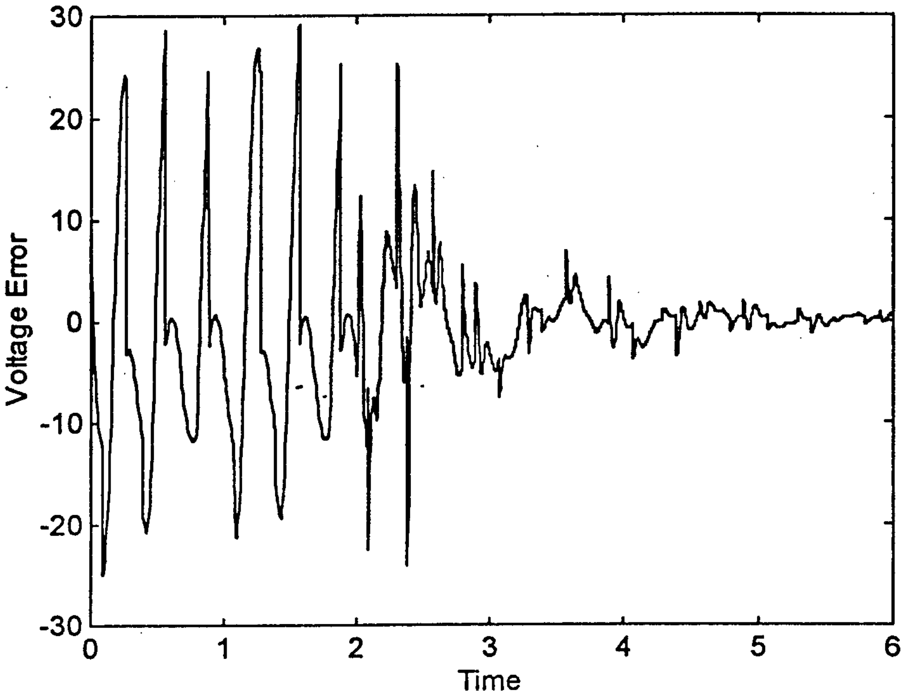

Figure 5.8: Case 2, voltage error.

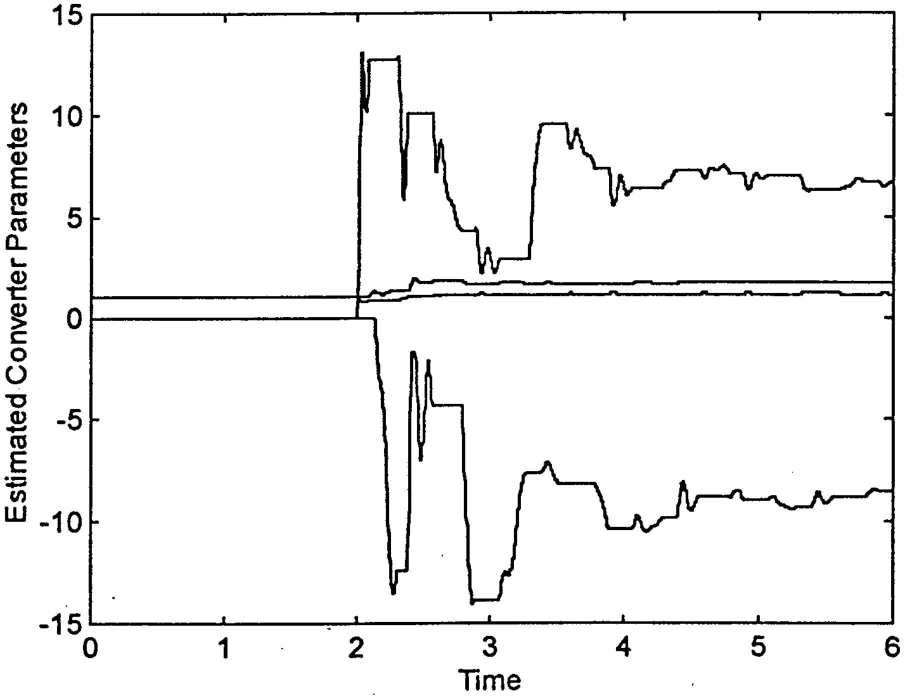

Figure 5.9: Case 2, estimated converter parameters.

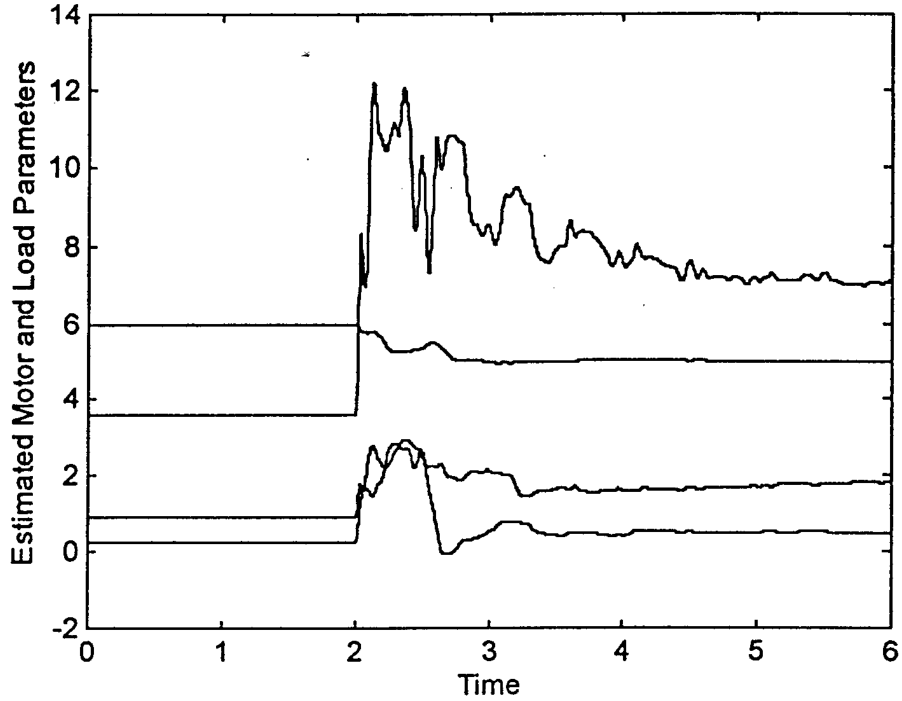

Figure 5.10: Case 2, estimated motor and load parameters.

## 6 Conclusion

This paper has presented a new state-feedback adaptive motion control scheme for converter-fed dc motor drives. The model on which the control scheme is based includes various converter nonlinearities, the electromechanical dynamics of the motor, and the mechanical load. The control scheme guarantees global stability, and provides asymptotic motion tracking, even when none of the parameters of the converter-motor-load combination are known.

Converter output voltage measurements are not required. By making use of full-state measurements, the need for filtering input-output signals is eliminated and the design of the adaptive controller is simplified. For the most general case, only eight parameters need to be estimated on-line. When converter symmetry is assumed, the number of parameters drops to just six.

Extension of the adaptive control scheme presented in this paper to inverter-fed ac motor drives is the subject of on-going research and will be reported elsewhere.

### REFERENCES

CHOI, J. W., AND SUL, S. K., 1996, Inverter output voltage synthesis using novel dead time compensation. *IEEE Transactions on Power Electronics*, **11**, 221–227.

IOANNOU, P. A., AND SUN, J., 1996, *Robust Adaptive Control* (Upper Saddle River, NJ: Prentice-Hall).

KANELLAKOPOULOS, I., KOKOTOVIC, P. V., AND MARINO, R., 1991, An extended direct scheme for robust adaptive nonlinear control. *Automatica*, **27**, 247–255.

MOHAN, N., UNDELAND, T. M., AND ROBBINS, W. P., 1989, *Power Electronics: Converters, Applications, and Design* (New York, NY: John Wiley & Sons).

MURAI, Y., WATANABE, T., AND IWASAKI, H., 1987, Waveform distortion and correction circuit for PWM inverters with switching lag-times. *IEEE Transactions on Industry Applications*, **23**, 881–886.

RECKER, D., 1993, *Adaptive Control of Systems Containing Piecewise Linear Nonlinearities*, Ph.D. Thesis, University of Illinois at Urbana-Champaign.

SASTRY, S. S., AND ISIDORI, A., 1989, Adaptive control of linearizable systems. *IEEE Transactions on Automatic Control*, **34**, 1123–1131.

SEPE, R. B., AND LANG, J. H., 1994, Inverter nonlinearities and discrete-time vector current control. *IEEE Transactions on Industry Applications*, **30**, 62–70.

SIRA-RAMIREZ, H., TARANTINO-ALVARADO, R., AND LLANES-SANTIAGO, O., 1993, Adaptive feedback stabilization in PWM-controlled DC-to-DC power supplies. *International Journal of Control*, **57**, 599–625.

SUKEGAWA, T., KAMIYAMA, K., MIZUNO, K., MATSUI, T., AND OKUYAMA, T., 1991, Fully digital, vector-controlled PWM VSI-fed AC drives with an inverter dead-time compensation strategy. *IEEE Transactions on Industry Applications*, **27**, 552–559.

TAO, G., AND KOKOTOVIC, P. V., 1994, Adaptive control of plants with unknown dead-zones. *IEEE Transactions on Automatic Control*, **39**, 59–68.

TAO, G., AND KOKOTOVIC, P. V., 1996, *Adaptive Control of Systems with Actuator and Sensor Nonlinearities*, to be published.

# Adaptive Control of AC Motor Drives with Inverter Nonlinearities*

Wasim Khan and David G. Taylor

Georgia Institute of Technology
School of Electrical and Computer Engineering
Atlanta, GA 30332-0250 USA

Phone: (404) 894-8910
Fax: (404) 894-4641
Email: david.taylor@ece.gatech.edu

Submitted to International Journal of Control

**Abstract**

An ac motor drive consists of a dc-ac inverter, an ac motor and some mechanical load. The inverter supplies electrical power in an appropriate form to the motor, which in turn provides the conversion to mechanical power needed to drive the load. All three components of the system are characterized by models which are nonlinear and contain unknown parameters. Improved motion control performance may thus be attempted by using nonlinear adaptive control methods. In this paper, a linearizing adaptive motion controller is derived for a representative ac motor drive, under the assumption that the parameters describing the inverter, the motor, and its load, are all unknown. The controller guarantees global stability and asymptotic tracking.

## 1 Introduction

Accurate control of ac motor drives is an important topic, due to the many advantages of brushless actuators for electric drive systems. Although several classes of ac motors exist, the three-phase permanent-magnet synchronous motor is often preferred in moderate-power high-performance motion control applications due to its high efficiency and unsurpassed power density. Within this family of motors, a popular choice is the version with sinusoidally distributed stator windings and a cylindrical surface-magnet rotor structure. For brevity, this paper will consider only this particular ac motor, though all of the critical concepts carry over to other ac motors without difficulty.

A complete ac motor drive consists of a dc-ac inverter, an ac motor and some mechanical load. The inverter supplies electrical power in an appropriate form to the motor, which in turn provides the conversion to mechanical power needed to drive the load. All three components of the system are characterized by models which are nonlinear and contain unknown parameters. One novel feature of this paper is an adaptive compensation of inverter nonlinearities. The existence of inverter nonlinearities stems from the presence of dead time, as well as switch imperfections and circuit parasitics. Dead time

---

*This work was supported in part by the National Science Foundation under grant ECS-9158037 and by the Office of Naval Research under grant N00014-96-1-0926.

is a time delay inserted between switch transitions to avoid shorting the voltage bus to ground. Switch imperfections include voltage drop, turn on delay and turn off delay. Parasitic capacitance limits the rates of rise and fall of inverter output voltages. If not properly compensated, these inverter nonlinearities will limit the achievable motion control performance.

Some inverter compensation schemes have recently appeared in the literature. In Mohan *et al.* (1989), voltage error introduced by the dead time is modeled and current control is suggested as a means of reducing the distortion. High-gain current control is not always available; moreover, its use can lead to a noisy non-smooth torque output. In Murai *et al.* (1987), the dead time interval is measured on-line and a correcting voltage pulse is added to the input voltage to compensate for the inverter nonlinearity. Such a scheme requires extra hardware circuitry and extra measurements. In Sukegawa *et al.* (1991), knowledge of the dead time is assumed and a corresponding correcting signal is added to the reference voltage commands. No switch imperfections are considered, and no guidance is provided to help determine the effective dead time. In Sepe and Lang (1994), exhaustive measurements are made to characterize the distortion caused by the dead time and an approximate dead time inverse is used as a pre-processor to the inverter. The accuracy of the compensation depends entirely on the precision of the required off-line calibration. In Choi and Sul (1996), a more general compensation scheme is developed which accounts for the dead time, unequal turn on and turn off times, and the voltage drop across the inverter switches. At least two off-line tests are required to compute the appropriate voltage correction, and the currents are assumed to be well regulated.

Most of the prior inverter compensation methods require off-line pre-calibration. Such methods yield best results when performed on an inverter/motor pair; their lack of modularity is inconvenient and inflexible. Considering that certain parameters of the ac motor and its load may also be unknown and will almost certainly change over time, nonlinear adaptive control methods are clearly well-motivated. However, in all of the references cited above, the inverter and the motor are treated as separate entities and no attempt is made to develop adaptive controllers or to guarantee stability of the overall design (see Sira-Ramirez *et al.* 1993, however, for adaptive control of purely electronic buck, boost, and buck-boost dc-dc converters).

In this paper, a technique motivated from Recker (1993) and Tao and Kokotovic (1996) is used for adaptive control of the inverter-motor-load combination. The inverter is modeled by a piecewise linear function. In order to avoid the need for pre-calibration, and to account for the possibility of slowly drifting system characteristics, the inverter, motor and load parameters are considered to be unknown. Estimates of the unknown parameters are used by the adaptive controller to cancel the inverter nonlinearities and to achieve a motion control objective. The closed loop system is shown to be globally stable and to provide asymptotic tracking. Fig. 1.1 illustrates the overall structure of the control design, which accomodates either position or velocity tracking control objectives. This paper extends the authors' recent work on the simpler problem of adaptive control design for dc motor drives with dc-dc converter nonlinearities (see Khan and Taylor 1996).

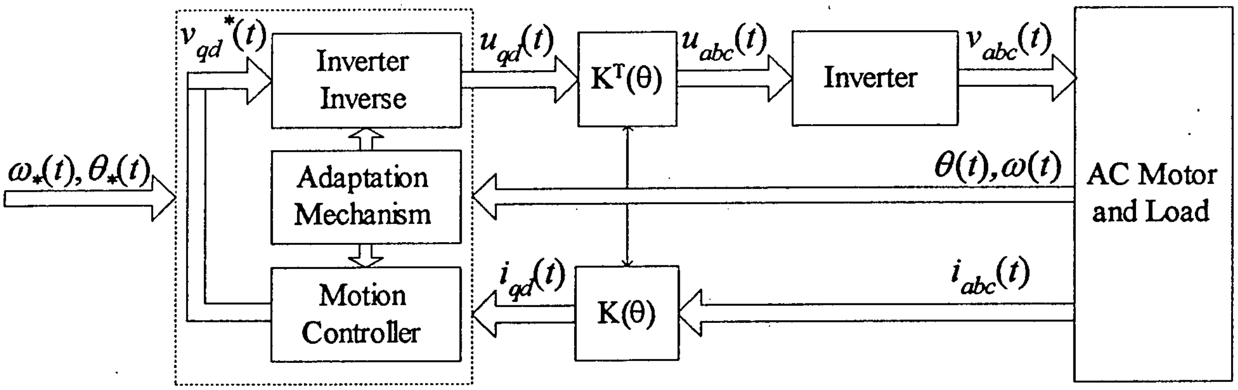

Figure 1.1: Structure of the adaptive control system.

## 2 AC Motor and Load

In many motion control applications, the three-phase permanent-magnet synchronous motor is used because of its high efficiency and unsurpassed power density. The particular version considered in this paper has sinusoidally distributed stator windings and a cylindrical surface-magnet rotor structure (see Krause 1986 for details). The voltage equations for this motor are expressed by

$$\begin{bmatrix} v_a(t) \\ v_b(t) \\ v_c(t) \end{bmatrix} = \begin{bmatrix} R & 0 & 0 \\ 0 & R & 0 \\ 0 & 0 & R \end{bmatrix} \begin{bmatrix} i_a(t) \\ i_b(t) \\ i_c(t) \end{bmatrix} + \begin{bmatrix} \dot{\lambda}_a(t) \\ \dot{\lambda}_b(t) \\ \dot{\lambda}_c(t) \end{bmatrix} \tag{2.1}$$

where $a$, $b$ and $c$ represent the three stator phases, $v_a(t)$, $v_b(t)$ and $v_c(t)$ are the phase voltages, $i_a(t)$, $i_b(t)$ and $i_c(t)$ are the phase currents, $\lambda_a(t)$, $\lambda_b(t)$ and $\lambda_c(t)$ are the phase flux-linkages, and $R$ is the phase resistance. If magnetic linearity is assumed, the phase flux-linkages can be expressed by

$$\begin{bmatrix} \lambda_a(t) \\ \lambda_b(t) \\ \lambda_c(t) \end{bmatrix} = \begin{bmatrix} L & -M & -M \\ -M & L & -M \\ -M & -M & L \end{bmatrix} \begin{bmatrix} i_a(t) \\ i_b(t) \\ i_c(t) \end{bmatrix} + \lambda_m \begin{bmatrix} \sin(N\theta(t)) \\ \sin(N\theta(t) - \frac{2\pi}{3}) \\ \sin(N\theta(t) + \frac{2\pi}{3}) \end{bmatrix} \tag{2.2}$$

where $\theta(t)$ is the rotor position, $L$ is the stator self-inductance, $M$ is the stator-to-stator mutual inductance, $\lambda_m$ is the magnitude of the flux established by the permanent-magnets, and $N$ is the number of pole pairs. From the flux-linkages (2.2), it can be shown that the torque of electrical origin is

$$T_e(t) = N\lambda_m(i_a(t)\cos(N\theta(t)) + i_b(t)\cos(N\theta(t) - \tfrac{2\pi}{3}) + i_c(t)\cos(N\theta(t) + \tfrac{2\pi}{3})) \tag{2.3}$$

Typically, the phase windings are wye-connected (with no neutral wire) and hence

$$i_a(t) + i_b(t) + i_c(t) = 0 \tag{2.4}$$

Combining (2.4) with (2.1) and (2.2) results in

$$v_a(t) + v_b(t) + v_c(t) = 0 \tag{2.5}$$

Note that (2.1)–(2.3) contain an explicit periodic dependence on rotor position. This dependence on rotor position can be eliminated by projecting the stator variables onto a reference frame fixed to the rotor. The matrix representation for this change of variables is given by

$$K(\theta(t)) = \sqrt{\frac{2}{3}} \begin{bmatrix} \cos(N\theta(t)) & \cos(N\theta(t) - \frac{2\pi}{3}) & \cos(N\theta(t) + \frac{2\pi}{3}) \\ \sin(N\theta(t)) & \sin(N\theta(t) - \frac{2\pi}{3}) & \sin(N\theta(t) + \frac{2\pi}{3}) \end{bmatrix} \tag{2.6}$$

It will be convenient to represent the phase voltages and phase currents in the vector form

$$v_{abc}(t) = \begin{bmatrix} v_a(t) \\ v_b(t) \\ v_c(t) \end{bmatrix} \qquad i_{abc}(t) = \begin{bmatrix} i_a(t) \\ i_b(t) \\ i_c(t) \end{bmatrix} \tag{2.7}$$

Similarly, the transformed voltages and currents will be represented in the vector form

$$v_{qd}(t) = \begin{bmatrix} v_q(t) \\ v_d(t) \end{bmatrix} \qquad i_{qd}(t) = \begin{bmatrix} i_q(t) \\ i_d(t) \end{bmatrix} \tag{2.8}$$

where $q$ and $d$ denote quadrature-axis and direct-axis components, respectively. Using these notations, the change of variables is given by

$$v_{qd}(t) = K(\theta(t))v_{abc}(t) \qquad i_{qd}(t) = K(\theta(t))i_{abc}(t) \tag{2.9}$$

and its inverse is given by

$$v_{abc}(t) = K^T(\theta(t))v_{qd}(t) \qquad i_{abc}(t) = K^T(\theta(t))i_{qd}(t) \tag{2.10}$$

After some tedious but straightforward algebra, the dynamic model of the permanent-magnet synchronous motor driving a simple mechanical load is given by

$$\begin{aligned} \dot{\theta}(t) &= \omega(t) && (2.11) \\ J\dot{\omega}(t) &= -B\omega(t) + N\lambda'_m i_q(t) && (2.12) \\ L'\dot{i}_q(t) &= -N(\lambda'_m + L'i_d(t))\omega(t) - Ri_q(t) + v_q(t) && (2.13) \\ L'\dot{i}_d(t) &= NL'i_q(t)\omega(t) - Ri_d(t) + v_d(t) && (2.14) \end{aligned}$$

where $\omega(t)$ denotes rotor velocity and where

$$L' = L + M \qquad \lambda'_m = \sqrt{\frac{3}{2}}\lambda_m \tag{2.15}$$

The constant coefficients describing the mechanical load are the total moment of inertia $J$ and the total viscous friction coefficient $B$. This load model is chosen for sake of simplicity; more complex load nonlinearities can be easily incorporated into the adaptive controller, provided that they are linearly parameterized functions of $\theta(t)$ and/or $\omega(t)$. Although this model remains nonlinear, the explicit dependence of the electrical equations on rotor position has been eliminated.

The vector of phase currents $i_{abc}(t)$, velocity $\omega(t)$ and position $\theta(t)$ are assumed to be measured. As illustrated in Fig. 1.1, measurement of the phase voltage vector $v_{abc}(t)$ is not required for the control design. This is in contrast to the (non-adaptive) method used in Murai *et al.* (1987).

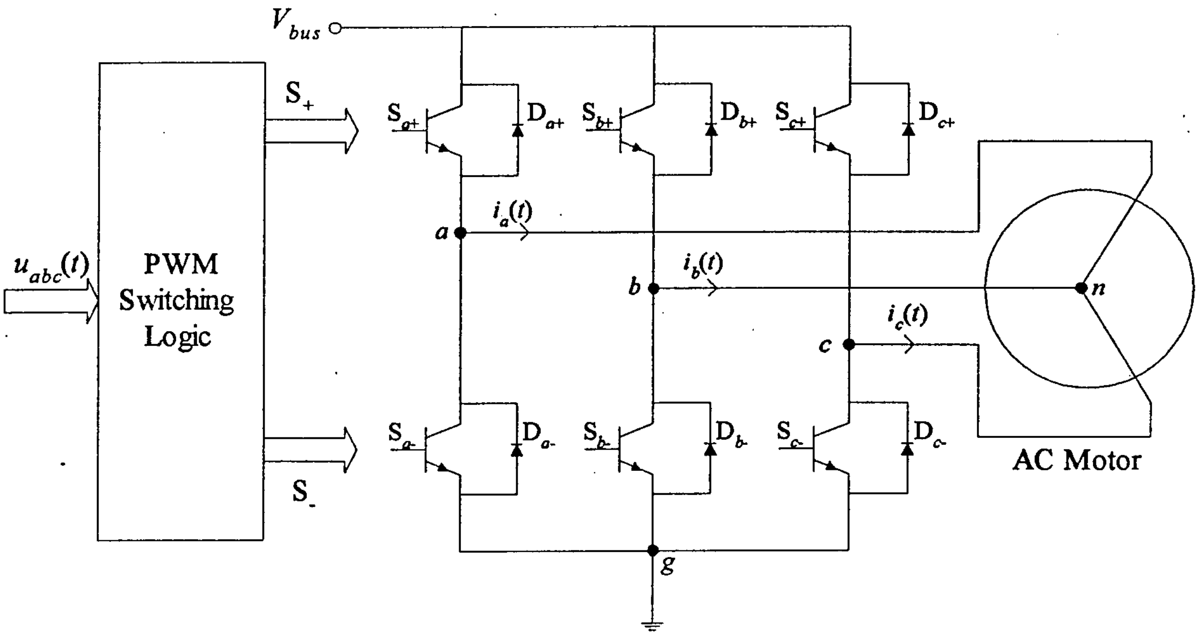

Figure 3.1: Three-phase inverter feeding a wye-connected ac motor.

# 3 Three-Phase Inverter

## 3.1 Basic Operation

A switch-mode dc-ac inverter feeding an ac motor is shown in Fig. 3.1. This inverter consists of three legs, each having two transistor switches $S_+$ and $S_-$, and two diodes $D_+$ and $D_-$. The motor terminals are connected to the mid-point of each inverter leg, denoted by $a$, $b$ and $c$. The motor phase windings are wye-connected, $n$ is the neutral point and $g$ is the inverter ground. The inverter leg voltages (with respect to ground $g$) are denoted by

$$v_{ABC}(t) = \begin{bmatrix} v_A(t) \\ v_B(t) \\ v_C(t) \end{bmatrix} = \begin{bmatrix} v_{ag}(t) \\ v_{bg}(t) \\ v_{cg}(t) \end{bmatrix} \tag{3.1}$$

and the motor phase voltages (with respect to neutral $n$) are denoted by

$$v_{abc}(t) = \begin{bmatrix} v_a(t) \\ v_b(t) \\ v_c(t) \end{bmatrix} = \begin{bmatrix} v_{an}(t) \\ v_{bn}(t) \\ v_{cn}(t) \end{bmatrix} \tag{3.2}$$

Note that $v_{abc}(t)$ has been consistently defined in the motor model and in the inverter model.

Application of Kirchoff's voltage law to the inverter-motor circuit in Fig. 3.1 yields a relationship between the inverter leg voltages $v_{ABC}(t)$ and the motor phase voltages $v_{abc}(t)$, namely

$$v_{abc}(t) = v_{ABC}(t) - v_{ng}(t) 1_3 \tag{3.3}$$

where $v_{ng}(t)$ is the voltage drop from the motor neutral $n$ to the inverter ground $g$ and

$$1_3 = \begin{bmatrix} 1 \\ 1 \\ 1 \end{bmatrix} \tag{3.4}$$

| # | $\tilde{v}_A$ | $\tilde{v}_B$ | $\tilde{v}_C$ | $\tilde{v}_a$ | $\tilde{v}_b$ | $\tilde{v}_c$ | $\tilde{v}_q$ | $\tilde{v}_d$ |
|---|---|---|---|---|---|---|---|---|
| 0 | 0 | 0 | 0 | 0 | 0 | 0 | 0 | 0 |
| 1 | 1 | 0 | 0 | 2 | $-1$ | $-1$ | $\cos(N\theta)$ | $\sin(N\theta)$ |
| 2 | 1 | 0 | 1 | 1 | $-2$ | 1 | $-\cos(N\theta - \frac{2\pi}{3})$ | $-\sin(N\theta - \frac{2\pi}{3})$ |
| 3 | 0 | 0 | 1 | $-1$ | $-1$ | 2 | $\cos(N\theta + \frac{2\pi}{3})$ | $\sin(N\theta + \frac{2\pi}{3})$ |
| 4 | 0 | 1 | 1 | $-2$ | 1 | 1 | $-\cos(N\theta)$ | $-\sin(N\theta)$ |
| 5 | 0 | 1 | 0 | $-1$ | 2 | $-1$ | $\cos(N\theta - \frac{2\pi}{3})$ | $\sin(N\theta - \frac{2\pi}{3})$ |
| 6 | 1 | 1 | 0 | 1 | 1 | $-2$ | $-\cos(N\theta + \frac{2\pi}{3})$ | $-\sin(N\theta + \frac{2\pi}{3})$ |
| 7 | 1 | 1 | 1 | 0 | 0 | 0 | 0 | 0 |

Table 3.1: Normalized voltages: $\tilde{v}_{ABC} = \frac{1}{V_{bus}} v_{ABC}$, $\tilde{v}_{abc} = \frac{3}{V_{bus}} v_{abc}$, $\tilde{v}_{qd} = \frac{3\sqrt{3/2}}{V_{bus}} v_{qd}$.

denotes a 3-vector of ones. Combining (2.5) with (3.3) yields

$$v_{ng}(t) = \frac{1}{3}(v_A(t) + v_B(t) + v_C(t)) \tag{3.5}$$

Substituting $v_{ng}(t)$ from (3.5) into (3.3) results in

$$v_{abc}(t) = C v_{ABC}(t) \tag{3.6}$$

where $C$ is the coupling matrix given by

$$C = \frac{1}{3}\begin{bmatrix} 2 & -1 & -1 \\ -1 & 2 & -1 \\ -1 & -1 & 2 \end{bmatrix} \tag{3.7}$$

From (3.6), one can directly compute the motor phase voltages $v_{abc}(t)$ appearing in (2.1) from the inverter leg voltages $v_{ABC}(t)$.

The basic operation of the three-phase inverter can be explained by considering a single inverter leg, say $a$. Turning on switch $S_{a+}$ and turning off switch $S_{a-}$ would establish $V_{bus}$ across terminals $a$ and $g$, i.e. $v_A(t) = V_{bus}$. On the other hand, turning on $S_{a-}$ and turning off $S_{a+}$ would apply zero voltage across $a$ and $g$, i.e. $v_A(t) = 0$. Turning on both $S_{a+}$ and $S_{a-}$ would short the voltage bus to ground and must be avoided by including a dead time in the switching logic. Turning off both $S_{a+}$ and $S_{a-}$ would yield $v_A(t) = V_{bus}$ if $i_a(t) < 0$ or $v_A(t) = 0$ if $i_a(t) > 0$, due to conduction of diode $D_{a+}$ or $D_{a-}$, respectively. Since each inverter leg can be in either of two states, the three-phase inverter as a whole can be in any of eight states. Table 3.1 summarizes these eight inverter states, using the relations in (3.6) and (2.9). Note that six symmetrically distributed nonzero voltage vectors and two zero voltage vectors can be produced in the $qd$ coordinates.

## 3.2 Pulse Width Modulation

Since only six nonzero voltage vectors in the $qd$ coordinates can be imposed by the inverter, precise control is best achieved through PWM strategies. The digital PWM strategy considered in this paper can be explained with reference to the timing diagram in Fig. 3.2, drawn specifically for phase $a$ (see also Mohan *et al.* 1989 and Holtz 1994). The timing diagram, which shows the $k$th sampling interval of fixed length $T$, has two interpretations. In the first interpretation, the rule for determining the ideal switching

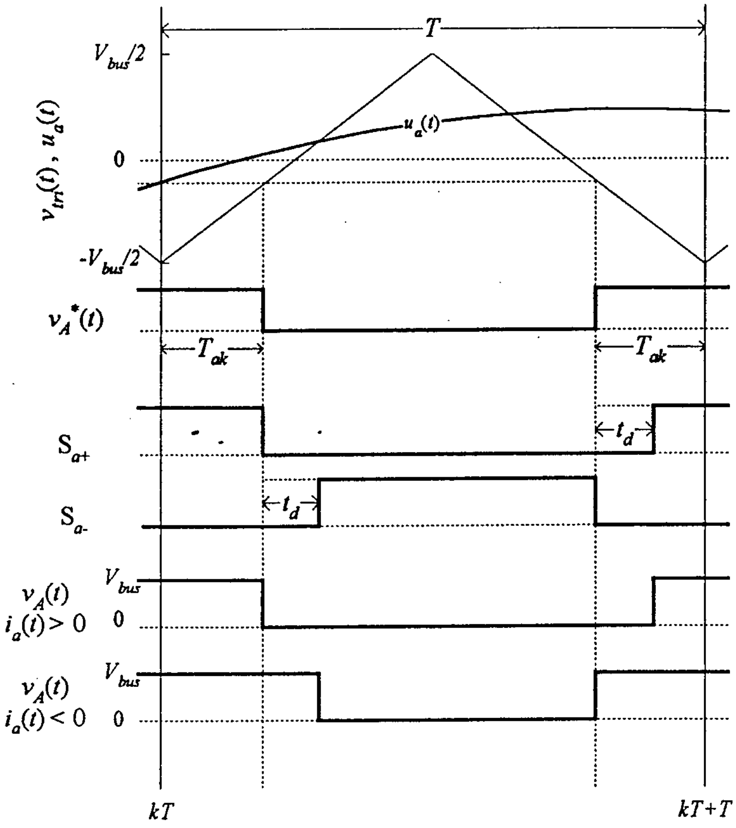

Figure 3.2: PWM switching scheme.

instants is defined by the uppermost plot which displays the triangular carrier waveform $v_{tri}(t)$ and the reference waveform $u_a(t)$. At the beginning of the sampling interval, $u_a(t)$ is sampled and compared to $v_{tri}(t)$ to determine time interval $T_{ak}$. Of course, $v_{tri}(t)$ need not exist as an analog signal here. In the second interpretation, the uppermost plot is disregarded and time interval $T_{ak}$ is simply an independent variable to be chosen later. The result of either interpretation is the logic signal $v_A^*(t)$, defined in terms of $T_{ak}$, which represents the ideal shape desired for $v_A(t)$.

To avoid the possibility of shorting the voltage bus to ground accidentally, all off-on transitions of the transistor switches are intentionally delayed by a dead time $t_d$. During the dead time, both switches are simultaneously turned off. Consequently, the direction of current $i_a(t)$ will determine the actual voltage $v_A(t)$ during the dead time. If $i_a(t) > 0$, diode $D_{a-}$ will conduct and $v_A(t) = 0$ during the dead time. If $i_a(t) < 0$, diode $D_{a+}$ will conduct and $v_A(t) = V_{bus}$ during the dead time. When $i_a(t) = 0$, an induced back-emf voltage appears at inverter node $a$; this isolated open-circuit state will be disregarded. The actual $v_A(t)$ waveforms shown for the two current polarities clearly differ from the $v_A^*(t)$ waveform, due to dead time distortion.

Now that Fig. 3.2 has been described in detail for phase $a$, it should be clear that the same discussion extends to the other phases in an obvious way. Considering the entire three-phase system, the inverter reference signals will be initially issued in the $qd$ coordinates and then transformed into the $abc$ coordinates, at which point the switching intervals for each inverter leg may be obtained. In vector form, these three sets of signals are

$$u_{qd}(t) = \begin{bmatrix} u_q(t) \\ u_d(t) \end{bmatrix} \qquad u_{abc}(t) = \begin{bmatrix} u_a(t) \\ u_b(t) \\ u_c(t) \end{bmatrix} \qquad T_{abck} = \begin{bmatrix} T_{ak} \\ T_{bk} \\ T_{ck} \end{bmatrix} \tag{3.8}$$

These vector notations will simplify the analysis and modeling results presented below.

The mathematical model of the inverter is most easily derived under the assumptions that the transistors and diodes are ideal (i.e. that the only source of distortion is the dead time), and that none of the motor phase currents changes sign within the $k$th switching cycle. Further simplification will be enabled by focusing on average voltage values rather than on instantaneous voltage values. To this end, recall that the average value of any voltage signal $v(t)$ produced during the $k$th cycle of operation is defined by

$$\bar{v}_k = \frac{1}{T} \int_{kT}^{kT+T} v(t)\ dt \tag{3.9}$$

According to Fig. 3.2, inverter leg voltage $v_A(t)$, in the presence of dead time, is modeled by

$$v_A(t) = \begin{cases} V_{bus} & ,\ kT \le t < kT + T_{ak} \\ \frac{1}{2}(1 - \mathrm{sgn}(i_{ak}))V_{bus} & ,\ kT + T_{ak} \le t < kT + T_{ak} + t_d \\ 0 & ,\ kT + T_{ak} + t_d \le t < kT + T - T_{ak} \\ \frac{1}{2}(1 - \mathrm{sgn}(i_{ak}))V_{bus} & ,\ kT + T - T_{ak} \le t < kT + T - T_{ak} + t_d \\ V_{bus} & ,\ kT + T - T_{ak} + t_d \le t < kT + T \end{cases} \tag{3.10}$$

where $t_d < T_{ak} < \frac{T}{2} - t_d$. Hence, the $k$th cycle average of inverter leg voltage $v_A(t)$ is

$$\bar{v}_{Ak} = \frac{V_{bus}}{T}\left(2T_{ak} - \mathrm{sgn}(i_{ak})t_d\right) \tag{3.11}$$

In fact, since Fig. 3.2 applies to each phase in an obvious way, it is clear that the $k$th cycle average of all inverter leg voltages is given by

$$\bar{v}_{ABCk} = \frac{V_{bus}}{T}\left(2T_{abck} - \mathrm{sgn}(i_{abck})t_d\right) \tag{3.12}$$

where

$$\mathrm{sgn}(i_{abck}) = \begin{bmatrix} \mathrm{sgn}(i_{ak}) \\ \mathrm{sgn}(i_{bk}) \\ \mathrm{sgn}(i_{ck}) \end{bmatrix} \tag{3.13}$$

This "open-loop" model for the inverter can be used to determine the effect of various switching strategies, once a rule for relating the time interval $T_{abck}$ to the reference signal $u_{abck}$ has been established.

One such rule has already been established by the comparator approach depicted in the uppermost plot of Fig. 3.2. By noting that

$$v_{tri}(t) = \begin{cases} 2V_{bus}(\frac{t}{T} - \frac{1}{4}) & ,\ kT \le t \le kT + \frac{T}{2} \\ 2V_{bus}(-\frac{t}{T} + \frac{3}{4}) & ,\ kT + \frac{T}{2} \le t \le kT + T \end{cases} \tag{3.14}$$

the time interval $T_{abck}$ may be computed from $u_{abck}$ by setting

$$v_{tri}(T_{ak}) = u_{ak} \qquad v_{tri}(T_{bk}) = u_{bk} \qquad v_{tri}(T_{ck}) = u_{ck} \tag{3.15}$$

which leads to

$$T_{abck} = \frac{T}{2}\left(\frac{1}{2}\mathbf{1}_3 + \frac{u_{abck}}{V_{bus}}\right) \tag{3.16}$$

Substitution of (3.16) into (3.12) yields

$$\bar{v}_{ABCk} = u_{abck} + \frac{1}{2}V_{bus}\mathbf{1}_3 - \operatorname{sgn}(i_{abck})V_{bus}\frac{t_d}{T} \tag{3.17}$$

Under ideal circumstances with $t_d = 0$, (3.17) indicates that each average inverter leg voltage will be equal to its reference signal offset by one-half of the bus voltage. The dc offset is present because inverter leg voltages must be between 0 and $V_{bus}$, even though motor phase voltages should be between $-V_{bus}$ and $+V_{bus}$. Note however that if $t_d \neq 0$, (3.17) indicates that the inverter leg voltages will be distorted in proportion to $V_{bus}\frac{t_d}{T}$.

As an alternative, a modified rule for relating $T_{abck}$ to $u_{abck}$ can be derived, with the goal of compensating the dead time distortion allowed by the simple comparator approach described above. In other words, the uppermost plot of Fig. 3.2 is disregarded and $T_{abck}$ is understood to be an independent variable defining the ideal switching instants. Since the goal is to establish (3.17) but without the dead time perturbation term, one can simply substitute this desired result into the left-hand-side of (3.12) and solve for $T_{abck}$. This procedure, referred to as the inverse approach, results in

$$T_{abck} = \frac{T}{2}\left(\frac{1}{2}\mathbf{1}_3 + \frac{u_{abck}}{V_{bus}} + \operatorname{sgn}(i_{abck})\frac{t_d}{T}\right) \tag{3.18}$$

Substituting (3.18) into (3.12) yields

$$\bar{v}_{ABCk} = u_{abck} + \frac{1}{2}V_{bus}\mathbf{1}_3 \tag{3.19}$$

as expected. This modified switching strategy is superior to the simple comparator approach, since even when $t_d \neq 0$ the average inverter leg voltages will be equal to the reference signals offset by one-half of the bus voltage.

The above analysis provides three useful insights. First, it is clear that the comparator approach cannot compensate for the distortion caused by dead time. Second, it has been established that the inverse approach will remove dead time distortion if accurately programmed. Third, the comparator approach has been shown to be a special case of the inverse approach, corresponding to an assumption that $t_d = 0$. What remains is to establish a relationship between the motor phase voltages and the reference signals. For this purpose, note that $C\mathbf{1}_3 = 0$ and $Cu_{abck} = u_{abck}$. The latter identity is due to the fact that $u_{abc}(t)$ is a balanced three-phase signal determined from $u_{qd}(t)$; in mathematical terms, $K(\theta)C = K(\theta)$ and $CK^T(\theta) = K^T(\theta)$. From (3.17) and (3.6), the comparator approach leads to

$$\bar{v}_{abck} = u_{abck} - C\operatorname{sgn}(i_{abck})V_{bus}\frac{t_d}{T} \tag{3.20}$$

whereas, from (3.19) and (3.6), the inverse approach leads to

$$\bar{v}_{abck} = u_{abck} \tag{3.21}$$

as desired. Hence, the reference signal $u_{abck}$ is properly interpreted as the desired average value of motor phase voltage $\bar{v}_{abck}$. When the comparator approach is used, distortion will generally exist; when the accurately programmed inverse approach is used, no distortion will be present.

Fig. 3.3 provides an overall view of the digital comparator scheme, for the ideal case when $t_d = 0$. The inverter leg voltages are obtained by comparing a three-phase sinusoidal reference signal to the triangular carrier signal. The motor phase voltages are derived from the inverter leg voltages, and their fundamental component voltages are displayed as well. Since $t_d = 0$ in this example, these fundamental components are identical to the reference signals, according to the above analysis.

## 3.3 Piecewise Linear Inverter Model

It is preferable for PWM inverters to have a high switching frequency, in order to reduce switching ripple. Under such circumstances, a standard averaging approximation may be made; the discrete-level motor phase voltages $v_{abc}(t)$ may be replaced by a continuous-time representation of their average values $\bar{v}_{abck}$, without significantly altering the response of the system. This averaging approximation will be used throughout the remainder of this paper.

It has been shown in (3.20) that the comparator approach leads to distorted motor phase voltages. Furthermore, it is important to realize that even the potentially distortionless inverse approach described in (3.21) cannot be perfectly programmed since this would imply perfect knowledge of $T$, $V_{bus}$ and $t_d$. Although one could argue that $T$ should be accurately known in any digital implementation, the other parameters pose a greater problem. The bus voltage is expected to drift in response to various loading conditions, and direct on-line measurement of the bus voltage would require additional interfacing and greater expense, and would suffer from switching noise error as well. The dead time is not always known, especially for off-the-shelf inverters. Moreover, the "effective" dead time of an inverter must account for various switch imperfections and circuit parasitics and thus is not simply equal to an intentionally implemented time delay. In other words, the voltages in Fig. 3.2 would be time delayed and approximately trapezoidal rather than square in shape. All off-on transitions are delayed by $t_{on}$ and all on-off transitions are delayed by $t_{off}$. These delays are accounted for by replacing $t_d$ in (3.12) with

$$t_d' = t_d + t_{on} - t_{off} \tag{3.22}$$

The rising and falling edges may be approximated by ramps of duration $t_r$ and $t_f$, respectively. This effect can be accounted for by replacing $t_d$ in (3.12) with

$$t_d' = t_d + \frac{1}{4}(t_r - t_f) \tag{3.23}$$

Naturally, the presence of both types of delays is accomodated by combining the additive terms in (3.22)–(3.23). Therefore, the effective dead time depends on at least five different parameters which may be unknown.

A realistic input-output model of the inverter, which accounts for all of the above parameter uncertainties, may be expressed in continuous-time by a general piecewise linear function of the form

$$v_{abc}(t) = m(u_{abc}(t) - \sigma_{abc}(t)b) \tag{3.24}$$

where

$$\sigma_{abc}(t) = C\text{sgn}(i_{abc}(t)) \tag{3.25}$$

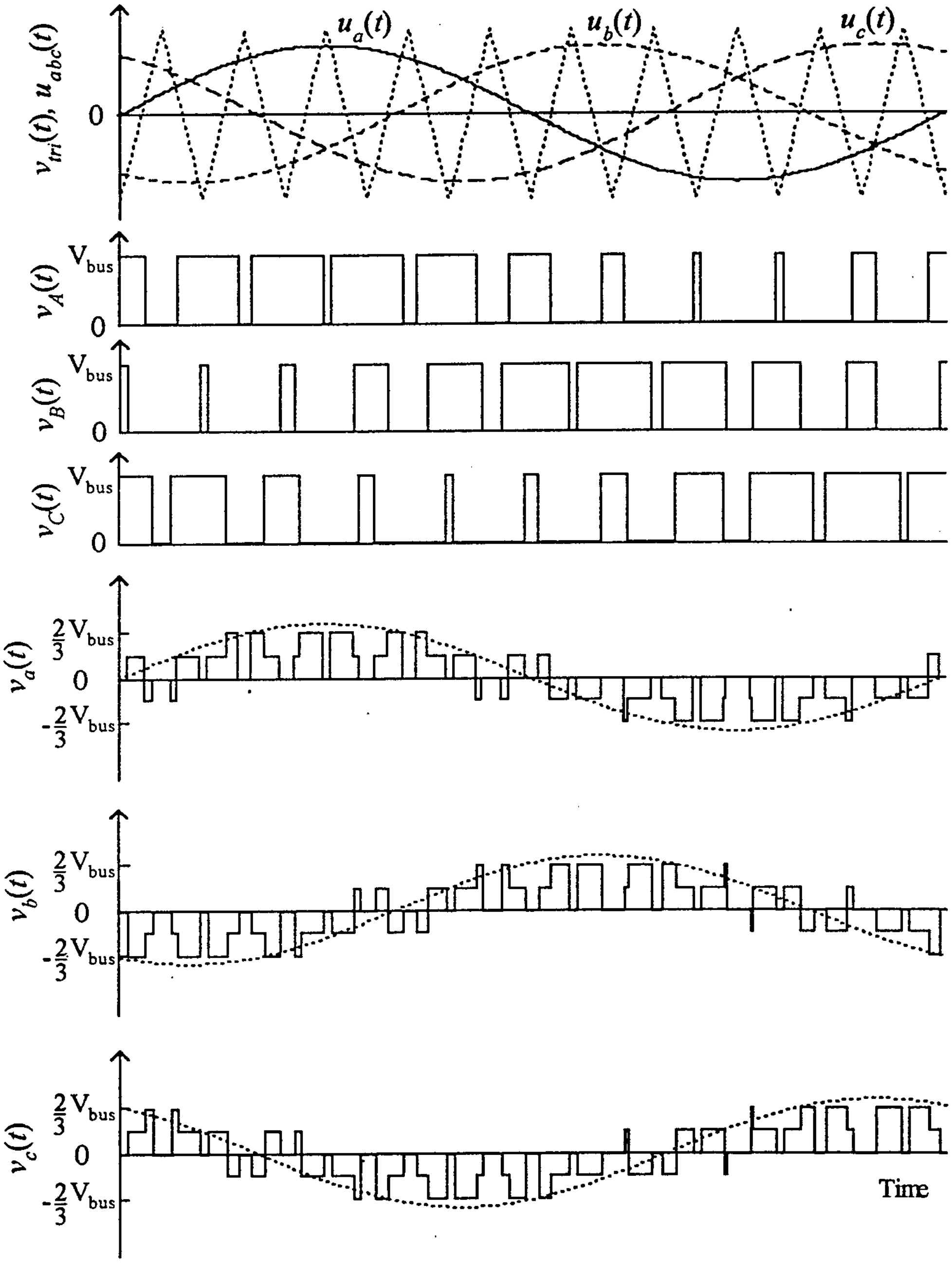

Figure 3.3: Three-phase digital comparator PWM scheme ($t_d = 0$).

and the constant coefficients $m$ and $b$ depend on various inverter parameters and thus may be unknown. For example, the inverter models of the previous section can be put into the new format by defining the slope

$$m = \frac{\hat{T}}{T}\frac{V_{bus}}{\hat{V}_{bus}} \tag{3.26}$$

and the intercept

$$b = \frac{t_d - \hat{t}_d}{\hat{T}}\hat{V}_{bus} \tag{3.27}$$

where the ˆ denotes an approximated value used in (3.16) or (3.18). Although these representations for $m$ and $b$ hold without modification for the inverse approach, they also hold for the comparator approach if $\hat{t}_d$ is taken to be zero. In these parameter assignments, $t_d$ represents the effective dead time which includes the contributions due to turn-on delay, turn-off delay, voltage rise time, and voltage fall time. Since $\sigma_{abc}(t)$ is determined by the direction of motor phase currents only, it is thus available as a measurement even when the inverter parameters are unknown.

Note from (3.24)–(3.25) that the average motor phase voltage exhibits jump discontinuities whenever any phase current reverses direction; this can be expected to occur $6N$ times per mechanical revolution if the phase currents are sinusoidal. when the discontinuities are avoided, the input-output relationship of the inverter is affine. For any fixed $t_d - \hat{t}_d$, the distortion due to effective dead time (i.e. the parameter $mb$) increases as switching frequency and/or bus voltage is increased. Even though the numerator of $b$ may be small, the denominator of $b$ is ideally zero; hence, the ratio $b$ itself may not be negligibly small.

To utilize the piecewise-linear inverter model in control design, it is necessary to transform it into the $qd$ frame of reference. This can be achieved by multiplying both sides of (3.24) by $K(\theta(t))$. The resulting model in the new frame of reference is

$$v_{qd}(t) = m(u_{qd}(t) - \sigma_{qd}(t)b) \tag{3.28}$$

where

$$\sigma_{qd}(t) = K(\theta(t))\text{sgn}(i_{abc}(t)) \tag{3.29}$$

The signal $\sigma_{qd}(t)$, which has constant magnitude and can be directly measured without knowledge of the unknown coefficients $m$ and $b$, is graphically displayed in Fig. 3.4. The six vectors plotted represent all possible values of $\sigma_{qd}(t)$ for a fixed value of $\theta(t)$. Each vector is located within one of six conic sectors identified by dashed lines. Each sector is labeled with ordered permutations of + and −, indicating the signs of $i_a(t)$, $i_b(t)$ and $i_c(t)$, respectively. The actual $\sigma_{qd}(t)$ is determined from either $i_{abc}(t)$ or $i_{qd}(t)$. In the first case, the sector associated with $\text{sgn}(i_{abc}(t))$ is located. In the second case, the sector to which $i_{qd}(t)$ belongs is located. In both cases, $\sigma_{qd}(t)$ is the vector from Fig. 3.4 which is contained in the identified sector.

The distortion due to $m$ and $b$ can now be given a geometrical interpretation in the $qd$ coordinates. Fig. 3.5 (a) shows a reference vector $u_{qd}(t)$ and the six possible values of vector $\sigma_{qd}(t)b$, for some fixed value of $\theta(t)$. Fig. 3.5 (b) shows the corresponding six possible voltage vectors $v_{qd}(t)$ computed from (3.28)–(3.29). The actual voltage vector $v_{qd}(t)$, which depends on the directions of the motor phase currents and on rotor position via $\sigma_{qd}(t)$, terminates on a circle centered at $mu_{qd}(t)$ with radius $2\sqrt{\frac{2}{3}}mb$.

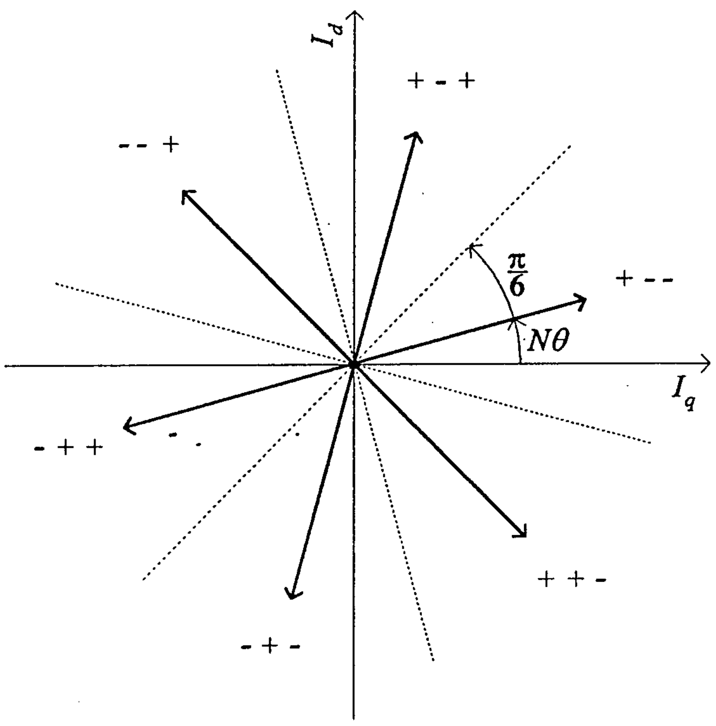

Figure 3.4: Evaluation of $\sigma_{qd}(t)$ from $i_{abc}(t)$ or $i_{qd}(t)$.

Since this circle's radius is constant, the voltage distortion is largest when the magnitude of $u_{qd}(t)$ is small. Fortunately $\sigma_{qd}(t)$ is measured, and hence critical directional properties of the voltage error are known even though the inverter parameters are unknown.

# 4 Adaptive Control Design

The control objective is to achieve asymptotic motion tracking with closed-loop stability, despite the presence of inverter nonlinearities and parameter uncertainty. Adaptive input-output linearization is used as the basis for control design (see Sastry and Isidori 1989 and Kanellakopoulos *et al.* 1991). Since the controller includes on-line parameter estimation, detailed off-line measurements and pre-calibration are not necessary; moreover, the controller can automatically adjust to slowly drifting parameters. Refer to Fig. 1.1 for a block diagram of the overall control system.

## 4.1 Inverter Inverse

As indicated in (3.28)–(3.29) and in Fig. 3.5, the inverter is non-ideal in the sense that $v_{qd}(t) \neq u_{qd}(t)$. However, since the inverter is characterized by an invertible static model, the nonlinearity cancellation technique of Recker (1993) and Tao and Kokotovic (1996) can be applied. Simpy put, the distortion introduced by the inverter can be attenuated by preceding the inverter with a so-called inverter inverse. If the inverter inverse is properly calibrated, all non-ideal features of the inverter are cancelled, and $v_{qd}(t)$ will be linearly proportional to the input of the inverter inverse, $v^{*}_{qd}(t)$.

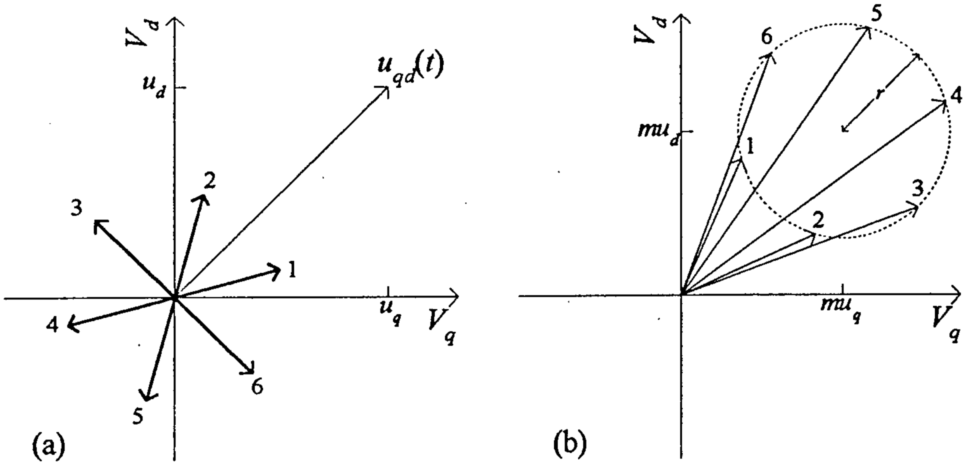

Figure 3.5: Inverter voltage distortion in the $qd$ frame of reference (where $r = 2\sqrt{\frac{2}{3}}mb$).

Note from (2.13)–(2.14) and (3.28)–(3.29) that the overall model contains products of inverter parameters and motor parameter $1/L'$. To provide a linear parameterization, (3.28)–(3.29) is rewritten in the form

$$\frac{1}{L'}v_{qd}(t) = \vartheta_{I1}u_{qd}(t) - \vartheta_{I2}\sigma_{qd}(t) \tag{4.1}$$

where

$$\vartheta_I = \left[\begin{array}{cc} \frac{m}{L'} & \frac{mb}{L'} \end{array}\right]^T \tag{4.2}$$

is the vector of unknown inverter-dependent parameters. The adaptive inverter inverse is defined as

$$u_{qd}(t) = \hat{\vartheta}_{I1}^{-1}(t)\left(v_{qd}^{\star}(t) + \hat{\vartheta}_{I2}(t)\sigma_{qd}(t)\right) \tag{4.3}$$

where $v_{qd}^{\star}(t)$ is the inverter inverse input and where $\hat{\vartheta}_I(t)$ represents the estimated value of $\vartheta_I$.

The relationship between the inverter inverse input $v_{qd}^{\star}(t)$ and the inverter output voltage $v_{qd}(t)$ is

$$\frac{1}{L'}v_{qd}(t) = v_{qd}^{\star}(t) + w(t)\tilde{\vartheta}_I(t) \tag{4.4}$$

where

$$w(t) = \left[\begin{array}{c} w_q(t) \\ w_d(t) \end{array}\right] = \left[\begin{array}{cc} -u_q(t) & \sigma_q(t) \\ -u_d(t) & \sigma_d(t) \end{array}\right] \tag{4.5}$$

and where $\tilde{\vartheta}_I(t) = \hat{\vartheta}_I(t) - \vartheta_I$ denotes parameter estimation error.

Note that $w(t)$ depends only on $\sigma_{qd}(t)$ and $u_{qd}(t)$, and can thus be computed without knowledge of $\vartheta_I$ and without measurement of $v_{qd}(t)$. In the ideal case where $\hat{\vartheta}_I(t) = \vartheta_I$ for all $t \geq 0$, the inverter output voltage obeys $\frac{1}{L'}v_{qd}(t) = v_{qd}^{\star}(t)$.

## 4.2 Estimated Normal Form

The complete model of the ac motor drive, which includes the motor and load dynamics (2.11)–(2.14) as well as the cascade combination of the inverter inverse and the inverter (4.4), is given by

$$\dot{\theta}(t) \;\; = \;\; \omega(t) \tag{4.6}$$

$$\begin{aligned}\dot{\omega}(t) &= -\vartheta_{L1}\omega(t) + N\vartheta_{L2}i_q(t) & (4.7)\\ \dot{i}_q(t) &= -N(\vartheta_{M1} + i_d(t))\omega(t) - \vartheta_{M2}i_q(t) + v_q^\star(t) + w_q(t)\tilde{\vartheta}_I(t) & (4.8)\\ \dot{i}_d(t) &= Ni_q(t)\omega(t) - \vartheta_{M2}i_d(t) + v_d^\star(t) + w_d(t)\tilde{\vartheta}_I(t) & (4.9)\end{aligned}$$

where the vector of unknown motor-dependent parameters is

$$\vartheta_M = \begin{bmatrix} \frac{\lambda'_m}{L'} & \frac{R}{L'} \end{bmatrix}^T \qquad (4.10)$$

and the vector of unknown load-dependent parameters is

$$\vartheta_L = \begin{bmatrix} \frac{B}{J} & \frac{\lambda'_m}{J} \end{bmatrix}^T \qquad (4.11)$$

Since two inputs are present in $v_{qd}^\star(t)$, two outputs shall be selected at this stage; the mechanical output $\theta(t)$ is of greatest interest for motion control applications, whereas the electrical output $i_d(t)$ is chosen to provide some control of flux (a secondary concern). With this choice of outputs and with parameter uncertainty neglected, it is easily verified that this ac motor drive system has global relative degree $\{3, 1\}$, since the determinant of the decoupling matrix is $N\vartheta_{L2} \neq 0$.

To prepare for adaptive input-output linearization, consider the estimated acceleration defined by

$$\alpha(t) = -\hat{\vartheta}_{L1}(t)\omega(t) + N\hat{\vartheta}_{L2}(t)i_q(t) \qquad (4.12)$$

where $\hat{\vartheta}_L(t)$ is the estimated value of $\vartheta_L$. As shown in Kanellakopoulos *et al.* (1991), since all unknown parameters of the motor drive system are separated from the control inputs by no more than one integration, a change of variables from $q$-axis current to estimated acceleration will lead to certain advantages. In contrast, note that a change of variables from $q$-axis current to true acceleration (as suggested in Sastry and Isidori 1989) would instead lead to overparameterization and other disadvantages.

Using the change of variables suggested above, i.e. replacing $q$-axis current with estimated acceleration, the ac motor drive model is transformed into the estimated normal form

$$\begin{aligned}\dot{\theta}(t) &= \omega(t) & (4.13)\\ \dot{\omega}(t) &= \alpha(t) + \omega(t)\tilde{\vartheta}_{L1}(t) - Ni_q(t)\tilde{\vartheta}_{L2}(t) & (4.14)\\ \dot{\alpha}(t) &= f_q(t) + N\hat{\vartheta}_{L2}(t)v_q^\star(t) + N\hat{\vartheta}_{L2}(t)w_q(t)\tilde{\vartheta}_I(t) & (4.15)\\ \dot{i}_d(t) &= f_d(t) + v_d^\star(t) + w_d(t)\tilde{\vartheta}_I(t) & (4.16)\end{aligned}$$

where $\tilde{\vartheta}_L(t) = \hat{\vartheta}_L(t) - \vartheta_L$ represents parameter estimation error and

$$\begin{aligned}f_q(t) &= \left(-\dot{\hat{\vartheta}}_{L1}(t) + \hat{\vartheta}_{L1}(t)\vartheta_{L1} - N^2\hat{\vartheta}_{L2}(t)(\vartheta_{M1} + i_d(t))\right)\omega(t)\\ &\quad + N\left(\dot{\hat{\vartheta}}_{L2}(t) - \hat{\vartheta}_{L1}(t)\vartheta_{L2} - \hat{\vartheta}_{L2}(t)\vartheta_{M2}\right)i_q(t) & (4.17)\\ f_d(t) &= Ni_q(t)\omega(t) - \vartheta_{M2}i_d(t) & (4.18)\end{aligned}$$

Note that if one neglects parameter estimation errors, this new model possesses a special structure. The mechanical output $\theta(t)$ is separated from control input $v_q^\star(t)$ by a chain of three integrators, with all nonlinearities located in the $v_q^\star(t)$ equation. The electrical output $i_d(t)$ is separated from control input $v_d^\star(t)$ by one integrator, with all nonlinearities located in the $v_d^\star(t)$ equation. Consequently, cancellation of all nonlinearities, with mechanical-electrical decoupling, will be possible by proper choice of $v_{qd}^\star(t)$.

## 4.3 Motion Controller

The motion controller is derived by applying input-output linearization after replacing all unknown parameters in the estimated normal form by their estimated values, yielding

$$v_{qd}^{\star}(t) = \begin{bmatrix} N\hat{\vartheta}_{L2}(t) & 0 \\ 0 & 1 \end{bmatrix}^{-1} \left( \begin{bmatrix} -\hat{f}_q(t) \\ -\hat{f}_d(t) \end{bmatrix} + \Delta(t) \right) \tag{4.19}$$

where

$$\begin{aligned} \hat{f}_q(t) &= \left(-\dot{\hat{\vartheta}}_{L1}(t) + \hat{\vartheta}_{L1}(t)\hat{\vartheta}_{L1}(t) - N^2\hat{\vartheta}_{L2}(t)(\hat{\vartheta}_{M1}(t) + i_d(t))\right)\omega(t) \\ &\quad + N\left(\dot{\hat{\vartheta}}_{L2}(t) - \hat{\vartheta}_{L1}(t)\hat{\vartheta}_{L2}(t) - \hat{\vartheta}_{L2}(t)\hat{\vartheta}_{M2}(t)\right) i_q(t) && (4.20) \\ \hat{f}_d(t) &= Ni_q(t)\omega(t) - \hat{\vartheta}_{M2}(t)i_d(t) && (4.21) \end{aligned}$$

and where $\Delta(t)$ represents a linear error feedback. In (4.20)–(4.21), $\hat{\vartheta}_M(t)$ is the estimated value of $\vartheta_M$ and, as usual, $\tilde{\vartheta}_M(t) = \hat{\vartheta}_M(t) - \vartheta_M$ will denote the corresponding parameter estimation error. Implementation of (4.20)–(4.21) will be achieved by replacing the terms $\dot{\hat{\vartheta}}_{L1}(t)$ and $\dot{\hat{\vartheta}}_{L2}(t)$ by the right-hand-sides of the corresponding update laws to be determined in the next section.

For position tracking control, with desired position trajectory $\theta_*(t)$ and desired current trajectory $i_{d*}(t)$, the outer feedback loop is given by

$$\Delta(t) = \begin{bmatrix} -c_{\theta 1}e_{\theta 1}(t) - c_{\theta 2}e_{\theta 2}(t) - c_{\theta 3}e_{\theta 3}(t) + \theta_*^{(3)}(t) \\ -c_{\theta 4}e_{\theta 4}(t) + i_{d*}^{(1)}(t) \end{bmatrix} \tag{4.22}$$

where the error vector is

$$e_\theta(t) = \begin{bmatrix} \theta(t) - \theta_*^{(0)}(t) \\ \omega(t) - \theta_*^{(1)}(t) \\ \alpha(t) - \theta_*^{(2)}(t) \\ i_d(t) - i_{d*}^{(0)}(t) \end{bmatrix} \tag{4.23}$$

and where the feedback gains are chosen such that $s^3 + c_{\theta 3}s^2 + c_{\theta 2}s + c_{\theta 1}$ and $s + c_{\theta 4}$ are Hurwitz polynomials. The closed-loop error dynamics are

$$\dot{e}_\theta(t) = A_\theta e_\theta(t) + W_\theta(t)\tilde{\vartheta}(t) \tag{4.24}$$

where

$$\begin{aligned} A_\theta &= \begin{bmatrix} 0 & 1 & 0 & 0 \\ 0 & 0 & 1 & 0 \\ -c_{\theta 1} & -c_{\theta 2} & -c_{\theta 3} & 0 \\ 0 & 0 & 0 & -c_{\theta 4} \end{bmatrix} && (4.25) \\ W_\theta(t) &= \begin{bmatrix} W_{\theta I}(t) & W_{\theta M}(t) & W_{\theta L}(t) \end{bmatrix} && (4.26) \\ \tilde{\vartheta}(t) &= \begin{bmatrix} \tilde{\vartheta}_I^T(t) & \tilde{\vartheta}_M^T(t) & \tilde{\vartheta}_L^T(t) \end{bmatrix}^T && (4.27) \end{aligned}$$

The regressor submatrices are defined by

$$W_{\theta I}(t) = \begin{bmatrix} 0 & 0 \\ 0 & 0 \\ -N\hat{\vartheta}_{L2}(t)u_q(t) & N\hat{\vartheta}_{L2}(t)\sigma_q(t) \\ -u_d(t) & \sigma_d(t) \end{bmatrix} \tag{4.28}$$

$$W_{\theta M}(t) = \begin{bmatrix} 0 & 0 \\ 0 & 0 \\ N^2\hat{\vartheta}_{L2}(t)\omega(t) & N\hat{\vartheta}_{L2}(t)i_q(t) \\ 0 & i_d(t) \end{bmatrix} \tag{4.29}$$

$$W_{\theta L}(t) = \begin{bmatrix} 0 & 0 \\ \omega(t) & -Ni_q(t) \\ -\hat{\vartheta}_{L1}(t)\omega(t) & N\hat{\vartheta}_{L1}(t)i_q(t) \\ 0 & 0 \end{bmatrix} \tag{4.30}$$

For velocity tracking control, with desired velocity trajectory $\omega_*(t)$ and desired current trajectory $i_{d*}(t)$, the outer feedback loop is given by

$$\Delta(t) = \begin{bmatrix} -c_{\omega 1}e_{\omega 1}(t) - c_{\omega 2}e_{\omega 2}(t) + \omega_*^{(2)}(t) \\ -c_{\omega 3}e_{\omega 3}(t) + i_{d*}^{(1)}(t) \end{bmatrix} \tag{4.31}$$

where the error vector is

$$e_\omega(t) = \begin{bmatrix} \omega(t) - \omega_*^{(0)}(t) \\ \alpha(t) - \omega_*^{(1)}(t) \\ i_d(t) - i_{d*}^{(0)}(t) \end{bmatrix} \tag{4.32}$$

and where the feedback gains are chosen such that $s^2 + c_{\omega 2}s + c_{\omega 1}$ and $s + c_{\omega 3}$ are Hurwitz polynomials. The closed-loop error dynamics are

$$\dot{e}_\omega(t) = A_\omega e_\omega(t) + W_\omega(t)\tilde{\vartheta}(t) \tag{4.33}$$

where

$$A_\omega = \begin{bmatrix} 0 & 1 & 0 \\ -c_{\omega 1} & -c_{\omega 2} & 0 \\ 0 & 0 & -c_{\omega 3} \end{bmatrix} \tag{4.34}$$

$$W_\omega(t) = \begin{bmatrix} W_{\omega I}(t) & W_{\omega M}(t) & W_{\omega L}(t) \end{bmatrix} \tag{4.35}$$

$$\tilde{\vartheta}(t) = \begin{bmatrix} \tilde{\vartheta}_I^T(t) & \tilde{\vartheta}_M^T(t) & \tilde{\vartheta}_L^T(t) \end{bmatrix}^T \tag{4.36}$$

The regressor submatrices are defined by

$$W_{\omega I}(t) = \begin{bmatrix} 0 & 0 \\ -N\hat{\vartheta}_{L2}(t)u_q(t) & N\hat{\vartheta}_{L2}(t)\sigma_q(t) \\ -u_d(t) & \sigma_d(t) \end{bmatrix} \tag{4.37}$$

$$W_{\omega M}(t) = \begin{bmatrix} 0 & 0 \\ N^2\hat{\vartheta}_{L2}(t)\omega(t) & N\hat{\vartheta}_{L2}(t)i_q(t) \\ 0 & i_d(t) \end{bmatrix} \tag{4.38}$$

$$W_{\omega L}(t) = \begin{bmatrix} \omega(t) & -Ni_q(t) \\ -\hat{\vartheta}_{L1}(t)\omega(t) & N\hat{\vartheta}_{L1}(t)i_q(t) \\ 0 & 0 \end{bmatrix} \tag{4.39}$$

## 4.4 Parameter Adaptation and Stability Analysis

As shown above, the combined effect of the nonlinearity cancellation loop and the pole placement loop is to achieve closed-loop error dynamics governed by

$$\dot{e}(t) = Ae(t) + W(t)\tilde{\vartheta}(t) \tag{4.40}$$

where $A$, $e(t)$, and $W(t)$ depend on the control objective. Although $\tilde{\vartheta}(t)$ is an unknown perturbation to the error dynamics, both $e(t)$ and $W(t)$ may be computed from directly measured signals. Now consider the Lyapunov function candidate

$$V(t) = e^T(t)Pe(t) + \tilde{\vartheta}^T(t)\Gamma^{-1}\tilde{\vartheta}(t) \tag{4.41}$$

where $\Gamma$ is a positive-definite symmetric adaptive gain matrix and $P$ is the positive-definite symmetric matrix which solves the Lyapunov equation

$$A^T P + PA = -Q \tag{4.42}$$

given any positive-definite symmetric matrix $Q$. Time differentiating both sides of (4.41) gives

$$\dot{V}(t) = -e^T(t)Qe(t) + 2\tilde{\vartheta}^T(t)\left(\Gamma^{-1}\dot{\tilde{\vartheta}}(t) + W^T(t)Pe(t)\right) \tag{4.43}$$

Selecting the parameter update law

$$\dot{\hat{\vartheta}}(t) = -\Gamma W^T(t)Pe(t) \tag{4.44}$$

reduces (4.43) to

$$\dot{V}(t) = -e^T(t)Qe(t) \leq 0 \tag{4.45}$$

Even though the update law (4.44) guarantees that $V(t)$ is non-increasing, it may lead to another problem. Specifically, note that the possibility of division by zero exists in both the inverter inverse (4.3) and in the motion controller (4.19). However, under the reasonable assumption that positive constants $\vartheta_{I1}^0$ and $\vartheta_{L2}^0$ are known such that

$$\vartheta_{I1} > \vartheta_{I1}^0 \qquad \vartheta_{L2} > \vartheta_{L2}^0 \tag{4.46}$$

it is possible to use projection on (4.44) in order to guarantee that division by zero will not occur while also guaranteeing that $\dot{V}(t) \leq 0$ continues to hold (see Ioannou and Sun 1996).

In summary, the complete adaptive control system consists of the adaptive inverter inverse (4.3), the adaptive inner-loop of the motion controller (4.19), the adaptive outer-loop of the motion controller (4.22) or (4.31), and the parameter update law (4.44) modified by projection. A Lyapunov function $V(t)$ satisfying $\dot{V}(t) \leq 0$ has been found, which guarantees that tracking error $e(t)$ and parameter error $\tilde{\vartheta}(t)$ are bounded and confined to a closed ellipsoidal region in the error space. Application of Barbalat's Lemma (see Ioannou and Sun 1996) allows the further conclusion that $e(t) \to 0$ as $t \to \infty$, i.e. that the tracking error converges to zero asymptotically. The boundedness of all signals in the closed-loop system, as well as the asymptotic tracking capability, are guaranteed for all bounded initial conditions and all bounded reference trajectories.

There are several special cases for which the adaptive control system simplifies. For example, if any parameter vector $\vartheta_I$, $\vartheta_M$, or $\vartheta_L$ is known a priori, then this known vector does not need to be estimated on-line. Instead, one would simply plug the known vector into the adaptive inverter inverse or adaptive motion controller as necessary, and the corresponding update law would be disregarded. This concept becomes particularly clear when the parameter update laws are expressed in the component form

$$\dot{\hat{\vartheta}}_I(t) \;=\; -\Gamma_I W_I^T(t)Pe(t) \tag{4.47}$$

$$\dot{\hat{\vartheta}}_M(t) = -\Gamma_M W_M^T(t) P e(t) \tag{4.48}$$

$$\dot{\hat{\vartheta}}_L(t) = -\Gamma_L W_L^T(t) P e(t) \tag{4.49}$$

where regressors $W_I(t)$, $W_M(t)$ and $W_L(t)$ are defined in (4.28)–(4.30) or (4.37)–(4.39) depending on the control objective.

# 5 Simulation Results

A computer simulation was performed to support the results presented in this paper. All parameters of the inverter-motor-load combination are assumed to be unknown, and the control objective is velocity tracking. The inverter parameters are: $m = 0.8$ (unitless) and $b = 3$ V. The motor and load parameters are: $B = 0.0005$ kg-m$^2$/s, $J = 0.0001$ kg-m$^2$, $R = 3.4\ \Omega$, $L' = 0.5$ H, $\lambda'_m = 0.0827$ Wb and $N = 2$. Hence,

$$\begin{aligned} \vartheta_I &= \begin{bmatrix} 1.6 & 4.8 \end{bmatrix}^T \\ \vartheta_M &= \begin{bmatrix} 0.165 & 6.8 \end{bmatrix}^T \\ \vartheta_L &= \begin{bmatrix} 5 & 827 \end{bmatrix}^T \end{aligned}$$

The initial parameter estimates are chosen to be

$$\begin{aligned} \hat{\vartheta}_I(0) &= \begin{bmatrix} 1.8 & 0 \end{bmatrix}^T \\ \hat{\vartheta}_M(0) &= \begin{bmatrix} 0.149 & 6.12 \end{bmatrix}^T \\ \hat{\vartheta}_L(0) &= \begin{bmatrix} 6.5 & 578.9 \end{bmatrix}^T \end{aligned}$$

This choice corresponds to assuming an ideal inverter, motor parameters within 10% and load parameters within 30% of their true values. The gains are chosen to be

$$\begin{aligned} c_\omega &= \begin{bmatrix} -40 & -22 & -15 \end{bmatrix}^T \\ P &= \begin{bmatrix} 1.79 & -3 & 0 \\ -3 & 5.591 & 0 \\ 0 & 0 & 0.2 \end{bmatrix} \\ \Gamma &= \mathrm{diag}\left\{3\times10^{-8},\ 3\times10^{-6},\ 2\times10^{-9},\ 1.2\times10^{-5},\ 7\times10^{-5},\ 0.5\right\} \end{aligned}$$

and the projection parameters are selected to be

$$\vartheta^0_{I1} = \frac{1}{3}\vartheta_{I1} \quad \vartheta^0_{L2} = \frac{1}{3}\vartheta_{L2}$$

Although not necessary, projection was also used on all other parameter estimates to keep them positive; this option enhances parameter convergence. During the first 2 seconds, no parameter adaptation is performed and the controller uses the fixed initial parameter estimates.

As shown in Figs. 5.1–5.6, the motor is commanded to track the velocity trajectory

$$\omega_*(t) = 50\cos(2\pi t)$$

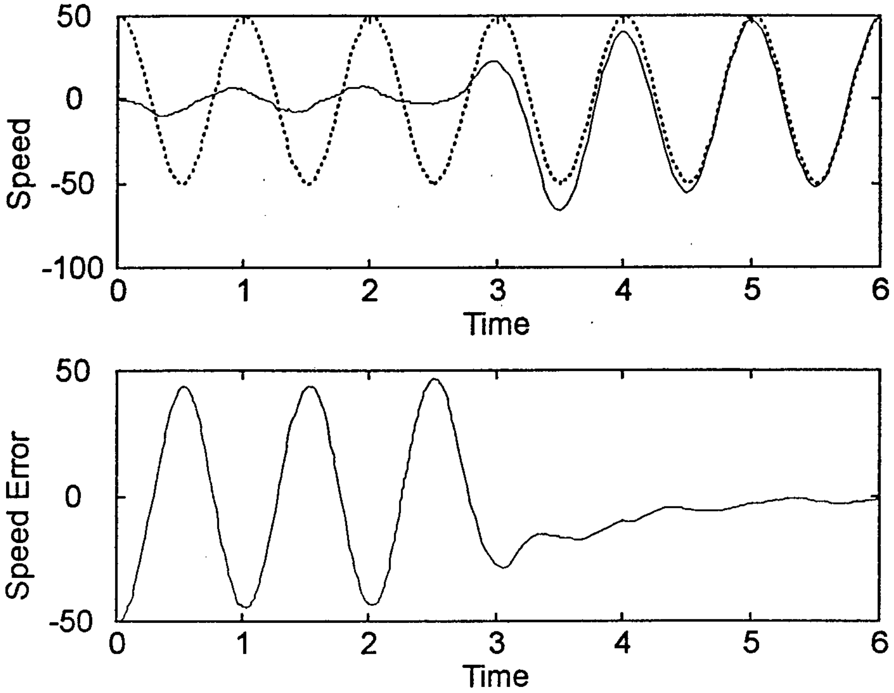

Figure 5.1: Speed and speed error.

This trajectory can be tracked by the example motor without requiring large voltage magnitudes, because both the friction torque and the acceleration torque are relatively small; hence, the voltage distortion introduced by the inverter can be expected to have a significant influence on the overall system response. Direct-axis current is commanded to be constant at 0.

During the first 2 seconds when adaptation is disabled, a large speed tracking error persists and the inverter output voltage exhibits significant jump discontinuities. If fact, voltage discontinuities may be expected to occur roughly 12 times per second, for the uncompensated inverter, due to the choice of motion trajectory. After about 1 second of adaptation, the voltage errors are reduced to near zero and the voltage discontinuities are essentially eliminated; furthermore, the motor and load parameter estimates have begun to approach steady-state values. Consequently, the velocity response becomes nearly linear after this 1 second of adaptation, and the velocity tracking error is reduced essentially to zero after several more seconds of operation. Note that the parameter estimation error also converges to zero in this simulation.

# 6 Conclusion

This paper has presented a new state-feedback adaptive motion control scheme for inverter-fed ac motor drives. Inverter output voltage measurements are not required. The model on which the control scheme is based includes various inverter nonlinearities, the electromechanical dynamics of the motor, and the mechanical load. The control scheme guarantees global stability, and provides asymptotic motion tracking, even when none of the parameters of the inverter-motor-load combination are known. At most six

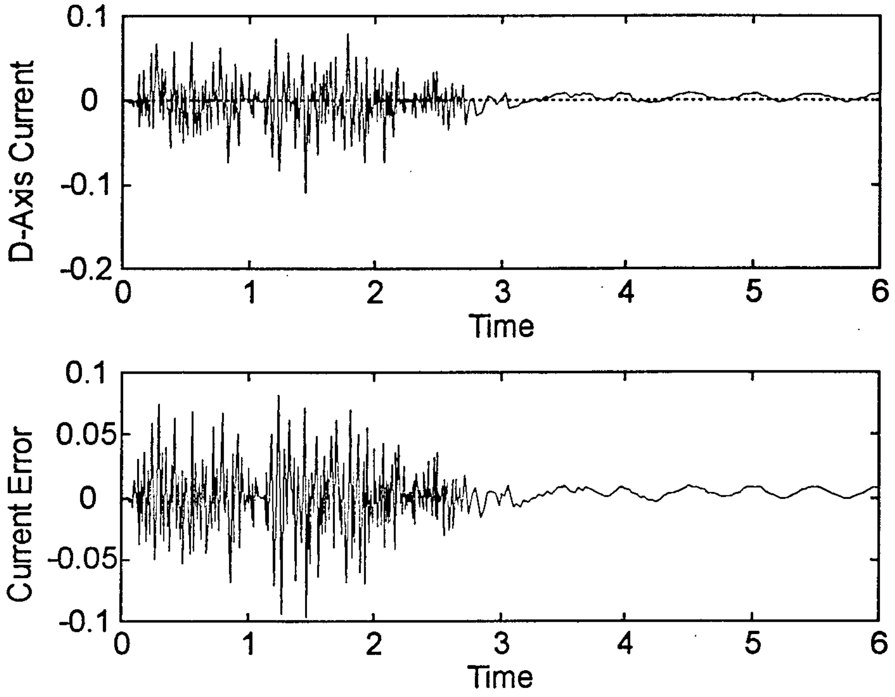

Figure 5.2: Current and current error.

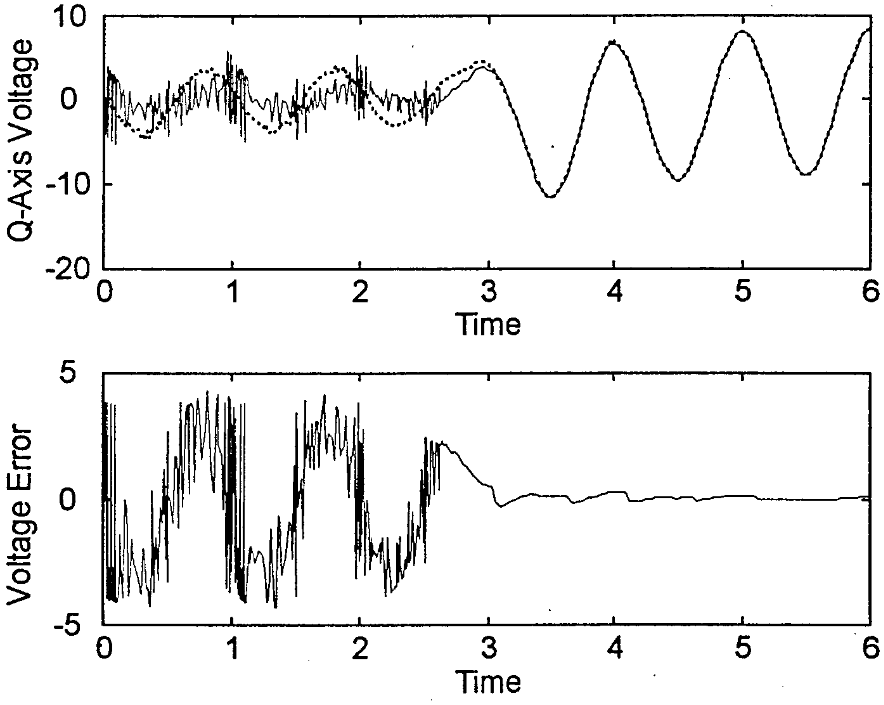

Figure 5.3: Desired and applied $q$-axis voltage.

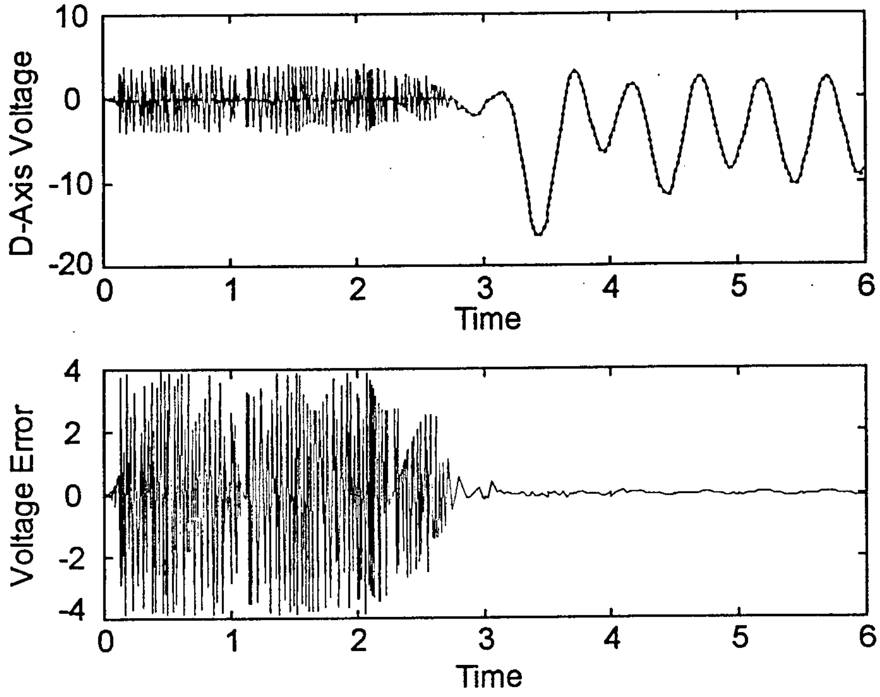

Figure 5.4: Desired and applied *d*-axis voltage.

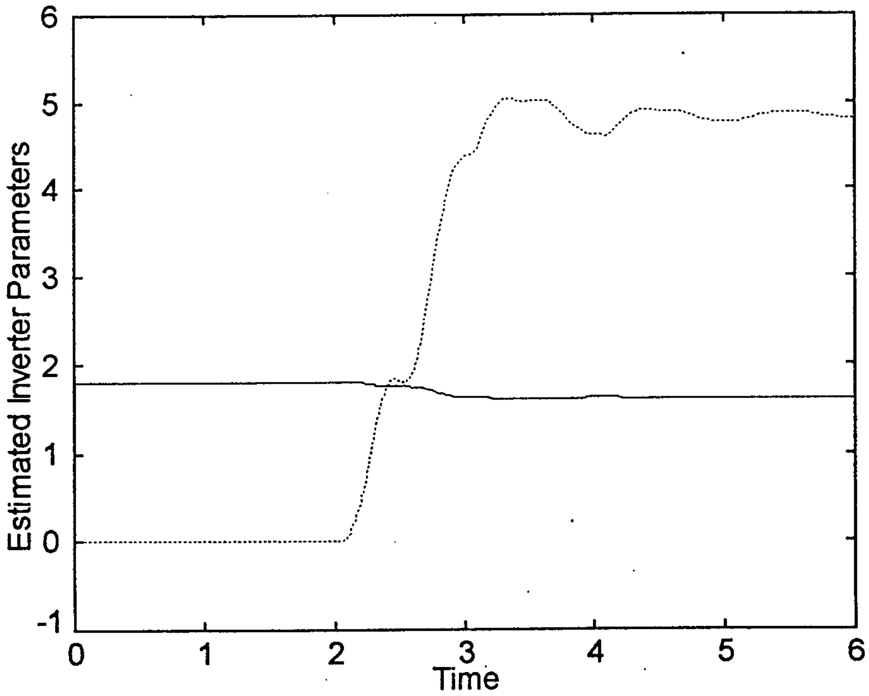

Figure 5.5: Estimated inverter parameters.

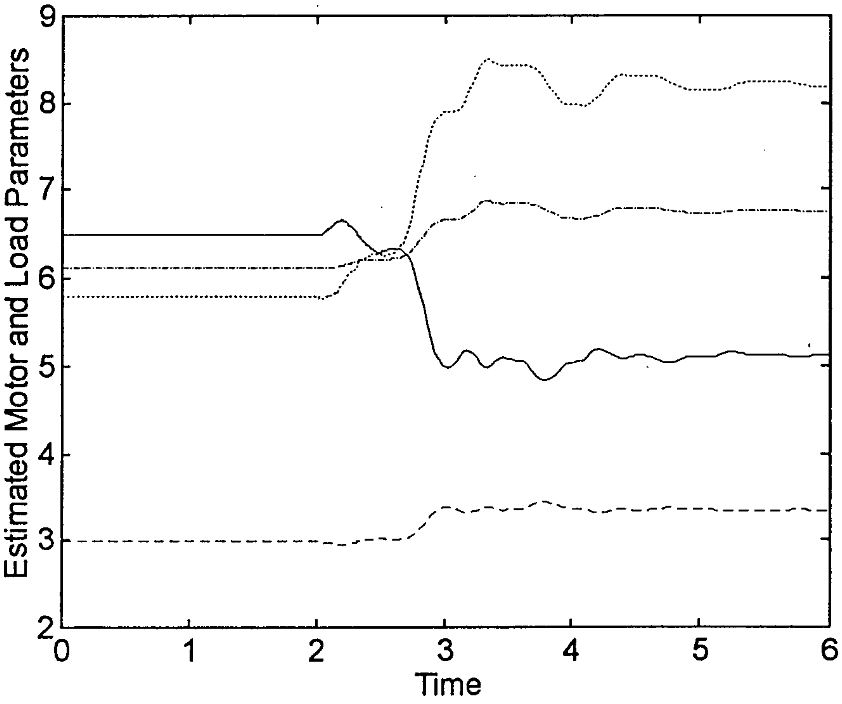

Figure 5.6: Estimated motor and load parameters, where $\hat{\vartheta}_{M1}$ and $\hat{\vartheta}_{L2}$ have been scaled by 20 and 0.01.

parameters need to be estimated on-line; fewer will suffice given a priori parameter knowledge.

Although the inverter switching logic outlined in this paper considers only two possibilities, it is not difficult to show that the proposed piecewise-linear inverter model pertains equally well to other switching schemes such as space-vector modulation. When the proposed linearization-based motion controller is extended to other types of ac motors, the only complication that may arise is a decoupling matrix dependence on current or flux in addition to parameter estimates. In such a case, parameter projection alone cannot guarantee nonsingularity of the decoupling matrix. Consequently, the stability region becomes local rather than global, since initial conditions must be restricted to an ellipsoidal region of the error space in order to guarantee that the adaptive system will not encounter any singularity.

## REFERENCES

CHOI, J. W., AND SUL, S. K., 1996, Inverter output voltage synthesis using novel dead time compensation. *IEEE Transactions on Power Electronics*, **11**, 221–227.

HOLTZ, J., 1994, Pulsewidth modulation for electronic power conversion. *Proceedings of the IEEE*, **82**, 1194–1214.

IOANNOU, P. A., AND SUN, J., 1996, *Robust Adaptive Control* (Upper Saddle River, NJ: Prentice-Hall).

KANELLAKOPOULOS, I., KOKOTOVIC, P. V., AND MARINO, R., 1991, An extended direct scheme for robust adaptive nonlinear control. *Automatica*, **27**, 247–255.

KHAN, W., AND TAYLOR, D. G., 1996, Adaptive control of dc motor drives with converter nonlinearities. *International Journal of Control*, under review.

KRAUSE, P. C., 1986, *Analysis of Electric Machinery* (New York, NY: McGraw-Hill).

MOHAN, N., UNDELAND, T. M., AND ROBBINS, W. P., 1989, *Power Electronics: inverters, Applications, and Design* (New York, NY: John Wiley & Sons).

MURAI, Y., WATANABE, T., AND IWASAKI, H., 1987, Waveform distortion and correction circuit for PWM inverters with switching lag-times. *IEEE Transactions on Industry Applications*, **23**, 881–886.

RECKER, D., 1993, *Adaptive Control of Systems Containing Piecewise Linear Nonlinearities*, Ph.D. Thesis, University of Illinois at Urbana-Champaign.

SASTRY, S. S., AND ISIDORI, A., 1989, Adaptive control of linearizable systems. *IEEE Transactions on Automatic Control*, **34**, 1123–1131.

SEPE, R. B., AND LANG, J. H., 1994, Inverter nonlinearities and discrete-time vector current control. *IEEE Transactions on Industry Applications*, **30**, 62–70.

SIRA-RAMIREZ, H., TARANTINO-ALVARADO, R., AND LLANES-SANTIAGO, O., 1993, Adaptive feedback stabilization in PWM-controlled DC-to-DC power supplies. *International Journal of Control*, **57**, 599–625.

SUKEGAWA, T., KAMIYAMA, K., MIZUNO, K., MATSUI, T., AND OKUYAMA, T., 1991, Fully digital, vector-controlled PWM VSI-fed AC drives with an inverter dead-time compensation strategy. *IEEE Transactions on Industry Applications*, **27**, 552–559.

TAO, G., AND KOKOTOVIC, P. V., 1996, *Adaptive Control of Systems with Actuator and Sensor Nonlinearities* (New York, NY: Wiley).

# Modeling and Control of Digital PWM Systems Using Averaging*

Mohammed Al-Numay and David G. Taylor†

Georgia Institute of Technology
School of Electrical and Computer Engineering
Atlanta, GA 30332-0250 USA

E-mail: david.taylor@ece.gatech.edu
Phone: 404-894-8910
Fax: 404-894-4641

Paper in Preparation for
IEEE Transactions on Control Systems Technology

## 1 Continuous-Time System Description

This paper considers PWM systems as described by

$$\dot{x}(t) = \begin{cases} A_1 x(t) + B_1 u(t) & , t \in \mathcal{T}_1 \\ A_2 x(t) + B_2 u(t) & , t \in \mathcal{T}_2 \end{cases} \tag{1.1}$$

$$y(t) = \begin{cases} C_1 x(t) & , t \in \mathcal{T}_1 \\ C_2 x(t) & , t \in \mathcal{T}_2 \end{cases} \tag{1.2}$$

where $u \in R^m$ is the input vector, $x \in R^n$ is the state vector, and $y \in R^p$ is the output vector. The system switches between two topologies, $(A_1, B_1, C_1)$ and $(A_2, B_2, C_2)$, with switching instants determined by

$$\mathcal{T}_1 := \bigcup_{n=0}^{N-1} [(kN+n)T, (kN+n)T + d_k T) \tag{1.3}$$

$$\mathcal{T}_2 := \bigcup_{n=0}^{N-1} [(kN+n)T + d_k T, (kN+n)T + T) \tag{1.4}$$

where $T$ is the switch period, $NT$ is the control period, $d_k \in [0,1]$ is the switch duty ratio, and $k$ is the discrete-time index. The block diagram representation of system (1.1)–(1.2) is displayed in Fig. 1.1, and the switching function defined by (1.3)–(1.4) is illustrated in Fig. 1.2. Note that

---

*This work was supported in part by the National Science Foundation under grant ECS-9158037, by the Office of Naval Research under grant N00014-96-1-0926, and by a graduate fellowship funded through King Saud University of Riyadh, Saudi Arabia.

†All correspondence should be addressed to this author.

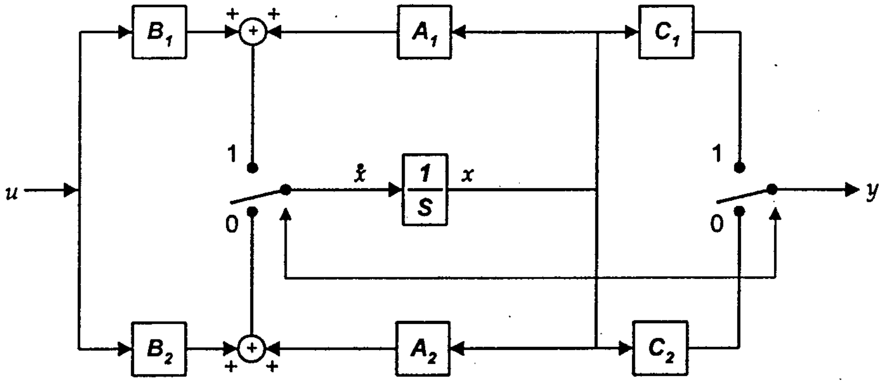

Figure 1.1: Block diagram of PWM system.

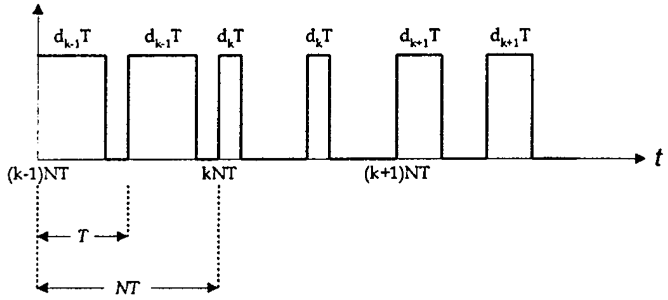

Figure 1.2: Switching function for $N = 2$.

the switch maintains a constant duty ratio throughout each control cycle; duty ratio updates occur every $N$th switch cycle. Ideally $N = 1$, but it is sometimes necessary to choose $N > 1$ so that fast switching may be achieved despite potentially slow control computation. All auxiliary inputs will be assumed to be piecewise-constant, i.e. $u(t) = u_k$ for all $t \in [kNT, (k+1)NT)$.

The continuous-time output signal $y(t)$ contains switching ripple. A related signal which is more appropriate for control design is the one-cycle-average output, defined by

$$y^*(t) := \frac{1}{NT} \int_{t-NT}^{t} y(\tau)\, d\tau \tag{1.5}$$

The averaging interval is set to $NT$, since the switch operates with constant duty ratio over intervals of length $NT$.

## 2 Discrete-Time Large-Signal Model

It is desired to compute, without approximation, the evolution of all system variables at the sampling instants, $t = kNT$. Since the state and output equations (1.1)–(1.2) are piecewise-linear with respect to time $t$, the desired discrete-time model can be obtained symbolically. Using the notations $x_k := x(kNT)$ and $y_k^* := y^*(kNT)$, the result is

$$x_{k+1} = \mathcal{A}(d_k)x_k + \mathcal{B}(d_k)u_k \tag{2.1}$$

$$y_{k+1}^* = \mathcal{C}(d_k)x_k + \mathcal{D}(d_k)u_k \tag{2.2}$$

where the input nonlinearities $\mathcal{A}(d)$, $\mathcal{B}(d)$, $\mathcal{C}(d)$ and $\mathcal{D}(d)$ are given by

$$\mathcal{A}(d) := \mathcal{A}_1(d)^N \tag{2.3}$$

$$\mathcal{B}(d) := \sum_{i=1}^{N} \mathcal{A}_1(d)^{i-1}\mathcal{B}_1(d) \tag{2.4}$$

$$\mathcal{C}(d) := \frac{1}{N}\left(\sum_{i=1}^{N} \mathcal{C}_1(d)\mathcal{A}_1(d)^{i-1}\right) \tag{2.5}$$

$$\mathcal{D}(d) := \frac{1}{N}\left(N\mathcal{D}_1(d) + \sum_{i=1}^{N-1}(N-i)\mathcal{C}_1(d)\mathcal{A}_1(d)^{i-1}\mathcal{B}_1(d)\right) \tag{2.6}$$

where $\mathcal{A}_1(d)$, $\mathcal{B}_1(d)$, $\mathcal{C}_1(d)$ and $\mathcal{D}_1(d)$ denote the input nonlinearities specialized to the case of $N = 1$. These latter functions are in turn defined by

$$\mathcal{A}_1(d) := \Phi_2((1-d)T)\Phi_1(dT) \tag{2.7}$$

$$\mathcal{B}_1(d) := \Phi_2((1-d)T)\Gamma_1(dT) + \Gamma_2((1-d)T) \tag{2.8}$$

$$\mathcal{C}_1(d) := C_1\Phi_1^*(dT) + C_2\Phi_2^*((1-d)T)\Phi_1(dT) \tag{2.9}$$

$$\mathcal{D}_1(d) := C_1\Gamma_1^*(dT) + C_2\left(\Phi_2^*((1-d)T)\Gamma_1(dT) + \Gamma_2^*((1-d)T)\right) \tag{2.10}$$

where

$$\Phi_i(t) := e^{A_i t} \tag{2.11}$$

$$\Gamma_i(t) := \int_0^t e^{A_i\tau}B_i\, d\tau \tag{2.12}$$

$$\Phi_i^*(t) := \frac{1}{T}\int_0^t \Phi_i(\tau)\, d\tau \tag{2.13}$$

$$\Gamma_i^*(t) := \frac{1}{T}\int_0^t \Gamma_i(\tau)\, d\tau \tag{2.14}$$

The large-signal model (2.1)–(2.2), which provides the cycle-to-cycle trajectory for the one-cycle-average value of any signal in the PWM system, is reported here for the first time.

Note that the averaging operation adds "sensor" dynamics to the system; as a consequence, the large-signal model (2.1)–(2.2) is not in standard state-space form. By defining the augmented state vector $x^* \in R^{n+p}$ such that

$$x_k^* := \begin{bmatrix} x_k \\ \mathcal{C}(d_{k-1})x_{k-1} + \mathcal{D}(d_{k-1})u_{k-1} \end{bmatrix} \tag{2.15}$$

an equivalent representation of the large-signal model is given by

$$x_{k+1}^* = \mathcal{A}^*(d_k)x_k^* + \mathcal{B}^*(d_k)u_k \tag{2.16}$$

$$y_k^* = C^*x_k^* \tag{2.17}$$

where

$$\mathcal{A}^*(d) := \begin{bmatrix} \mathcal{A}(d) & 0_{n\times p} \\ \mathcal{C}(d) & 0_{p\times p} \end{bmatrix} \tag{2.18}$$

$$\mathcal{B}^*(d) := \begin{bmatrix} \mathcal{B}(d) \\ \mathcal{D}(d) \end{bmatrix} \tag{2.19}$$

$$C^* := \begin{bmatrix} 0_{p\times n} & I_{p\times p} \end{bmatrix} \tag{2.20}$$

State feedback control design for this system will generally require not only measurement of the circuit's state, but also computation of the sensor's state from nonlinear functions $\mathcal{C}(d)$ and $\mathcal{D}(d)$ and available signals.

To illustrate the advantages of the new one-cycle-average large-signal model, consider the following example. Simulations of buck, boost and buck-boost converters are shown in Fig. 2.1, using three different simulation models. The first simulations use the continuous-time model (1.1)–(1.2) to obtain continuous-time outputs $y(t)$; the results are shown by the solid-line ripple waveforms. The second simulations use the new discrete-time model (2.16)–(2.17) to obtain discrete-time outputs $y_k^*$; the results are identified by the triangles. The third simulations use the traditional discrete-time model (not explicitly shown here) to obtain un-averaged discrete-time outputs $y_k := y(kNT)$; the results are identified by the circles. Note that the traditional discrete-time model returns sample values of the continuous-time output waveform which, unfortunately, may correspond to the peak, valley, or some intermediate point of the ripple waveform. In contrast, the new discrete-time model does not return sample values of the continuous-time output waveform, but rather sample values of the continuous-time one-cycle-average output waveform. Hence, the new discrete-time model provides the most useful representation of the PWM system's response.

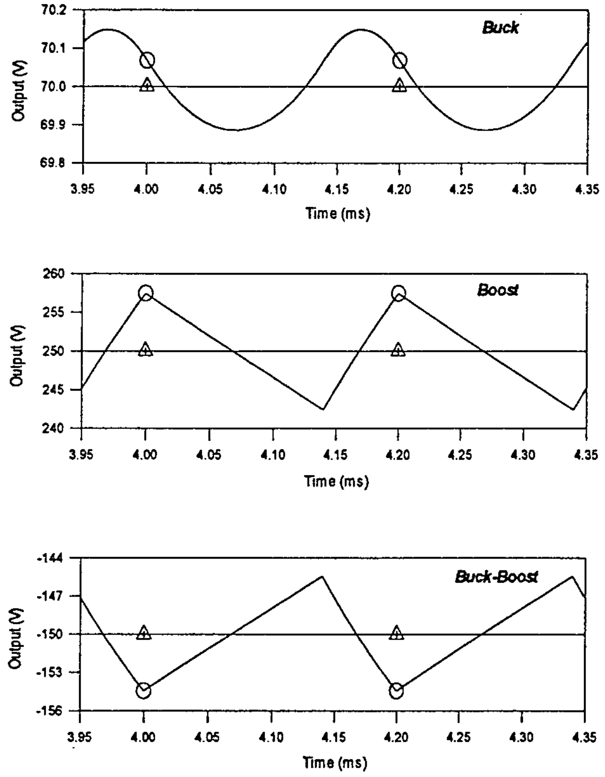

Figure 2.1: Comparison of model responses.

IEEE Conf on Industrial
+ Commercial Power Systems
May 1997, Philadelphia PA

# POLYMER CURRENT LIMITERS FOR LOW-VOLTAGE POWER DISTRIBUTION SYSTEMS[1]

Mark H. McKinney, Charles W. Brice, and Roger A. Dougal
Department of Electrical and Computer Engineering
University of South Carolina

**Abstract—Low-voltage power distribution systems are often protected from overcurrent conditions by fuses, low-voltage power circuit breakers, and molded-case circuit breakers. As changes are made to the power distribution system, the short-circuit duty imposed on the switchgear often increases. This increased short circuit duty may necessitate the replacement of many of the devices in the system, including the circuit breaker if the rating of the breaker is exceeded. One approach to avoiding the replacement of over-dutied switchgear is to use a current limiter to decrease the short-circuit current. This paper discusses the use of polymer current limiters for the protection of over-dutied circuit breakers. Polymer current limiters are widely used in appliances, electronic power supplies and other low-power applications. Power distribution applications of polymer current limiters and simulation results showing potential problems and approaches to their solutions are given. We will begin with an introduction to the functional properties of polymer current limiters, then describe how those properties drive the selection of associated components such as a shunt link and the molded case circuit breaker. Finally, we will describe applications of the PCL in a hierarchic low voltage power distribution structure. Particular emphasis is placed on methods for tailoring the time-current curve to achieve coordination with low-voltage circuit breaker characteristics.**

## I. INTRODUCTION

Any material with a sufficiently strong positive temperature coefficient of resistivity can be used to make a current limiting device. For this class of devices, the insertion loss is small because the resistance is low when conducting rated current. During fault conditions, however, the increased current causes ohmic heating which raises the temperature of the element and hence its resistivity (i.e., the material forms a *thermistor*). A positive feedback situation ensues, causing recursive heating and resistance increase, thus ensuring that the peak fault current is substantially limited. Current limiting fuses operate on this principle. We consider in this paper the use of a polymer current limiter (PCL) in a power system application, and describe how the specifications for the PCL must be carefully coordinated with those of two other necessary elements, the shunt link and the circuit breaker.

Polymer current limiters are fabricated from a polymer material (e.g., polyethylene) filled with conducting particles (e.g., carbon black) to the point that the conducting particles become contiguous, forming conducting chains throughout the material. These polymer conductors generally have positive temperature coefficients (PTC) of resistance that are especially large near phase transitions of the polymer [1],[2]. This is illustrated in Fig 1 which shows the graph of resistivity as a function of temperature for a common carbon-filled polyethylene thermistor. The dramatic increase in resistivity near 130°C is caused by polymer expansion at the phase transition (corresponding to melting) which breaks the conducting chains and isolates the individual carbon black particles. Crosslinking of the polymer conveniently prevents liquefication, so even when the polymer is heated above its melting point, its physical characteristics are preserved [3].

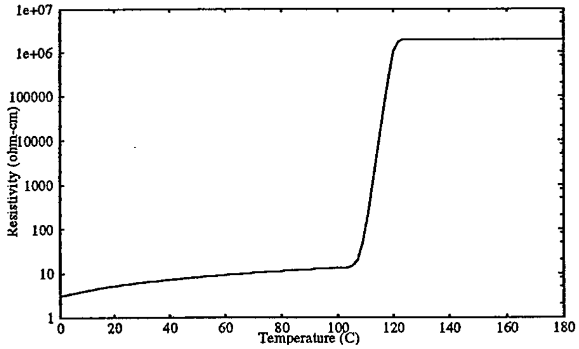

*Figure 1 Typical resistivity vs. Temperature for a polyethylene and carbon black polymer current limiter.*

PTC thermistors of this type are widely used as the sole device for current limiting in low-power applications such as automotive or telephonic systems [4],[5],[6]. Their properties of self-recovery and rapid response to excessive currents are particularly appealing in these situations. Those

---

[1] This research was sponsored by the Naval Surface Warfare Center, Annapolis, MD and by the Office of Naval Research.

same properties make them attractive for applications in low-voltage power distribution systems as was discussed in a previous paper [7]. But when used in a system with relatively high available power, a polymer current limiter is not, by itself, a suitable circuit protection device. Rather, it must be used in conjunction with another element such as a circuit breaker, to effect a total disconnect of a faulty circuit branch. The switching properties of the PCL and of the circuit breaker are not mutually compatible, though, so a third element, a shunt link, must also be used.

The necessity of the shunt link can be understood by considering the switching properties of the PCL. First, due to the rapid response time of the PCL, it can open before the appropriate circuit breaker trips, leaving only the PCL to absorb all of the energy of the fault. Second, if the system current is abruptly quenched, a large inductive voltage spike appears across the PCL for a significant time, imposing an excessively large peak power and peak electric field on the PCL. The shunt link effectively decreases the dI/dt requirement and hence the peak power and field requirements. In a sense, the shunt link is a rugged device into which the necessary system energy can be gracefully deposited. The combined system has a configuration as shown in Fig 2. Design of the collective system is somewhat complicated; since both the polymer current limiter and the shunt resistor must be specified so as to properly coordinate with the circuit breaker. For a detailed description of the design of the shunt link see Ref. 8.

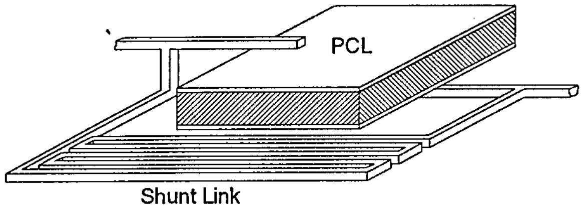

*Figure 2 Polymer current limiter with a shunt link*

This paper discusses coordination and specification issues that must be addressed in order to properly apply polymer current limiters in low-voltage power distribution systems. In particular:

- Prevention of thermal damage to the PCL during heavy short circuits
- Management of pre-heating due to load currents and high ambient temperatures
- Coordination with other devices including circuit breakers, fuses, transformer damage curves and motor starting inrush currents.

Solutions to these problems are demonstrated by means of detailed simulations of the polymer current limiter behavior [8]. We show that thermal damage may be avoided by specification of a proper shunt link, and that the shape of the time-current curve of the PCL may be controlled by proper selection based on cross-sectional area, electrode mass, and thermal conductivity of the composite material. For a variety of reasons, including simplicity of the presentation of results and the fact that the switching action of a PCL occurs on a time scale short compared to a 60 Hz cycle, all results presented in this paper are derived by using a DC power system model with circuit breaker curves adjusted accordingly [9].

## II. MATHEMATICAL SIMULATIONS

Two models were used to obtain the data presented in this paper. The time-current curves were obtained by modeling the PCL-electrode system as a thermal circuit as shown in figure 3. The power dissipated in the polymer is represented by the current source on the left, and the ambient temperature is represented by the source on the right. $C_{sink}$ and $R_{sink}$ are the heat capacity and thermal resistance, respectively, of the electrode attached to PCL The time to switch was defined as the time required for the temperature of the polymer to reach 120°C as once the temperature reaches this point, switching is eminent.

This model was confirmed by a more complex finite element model. This model has correlated favorably with existing device measurements and includes a sophisticated analysis of many electro-thermal properties and characteristics of the PCL material. This model was used to determine all internal temperatures, currents, and energies relating to the PCL and its switching action in an actual power distribution system. For a more detailed description of this model, readers are directed to [8].

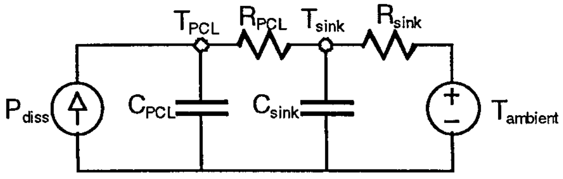

*Figure 3 Thermal model of PCL/Electrode system*

## III. ENERGY ABSORPTION LIMITS OF PCL

Self-recovery is an important advantage of polymer current limiters, but the ability for self-recovery is dependent on limiting PCL energy absorption during a system fault. Energy absorption during a fault was investigated using the simple circuit shown in figure 4. A 0.4 mm thick carbon black/polyethylene PCL device with a cross sectional area of 10 cm$^2$, a low temperature resistance of 12mΩ and a high temperature resistance of 400kΩ was used.

Figure 5 shows the system current following closure of the short circuit. The system current rose initially at a rate limited by the system inductance, then, once the PCL switched, precipitously decreased to near zero in less than a millisecond. The abrupt current interruption resulted in a large inductive voltage across the PCL. The internal temperatures of the polymer exceeded 500°C in a matter of milliseconds, while the device absorbed 450 J of energy. This temperature lies beyond both the functional limits of the polyethylene polymer and range of validity of the model. This clearly indicates an unacceptably large energy absorption in the PCL. Energy absorption can be constrained to lie within the limits of the PCL by placing a low value resistor in parallel with the PCL, as shown in Figure 6.

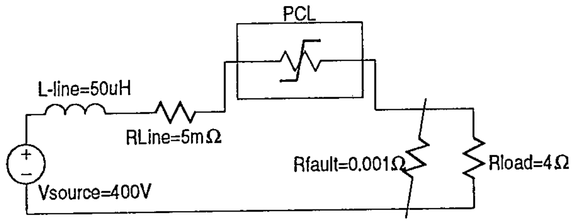

*Figure 4 Simple power distribution system utilizing PCL*

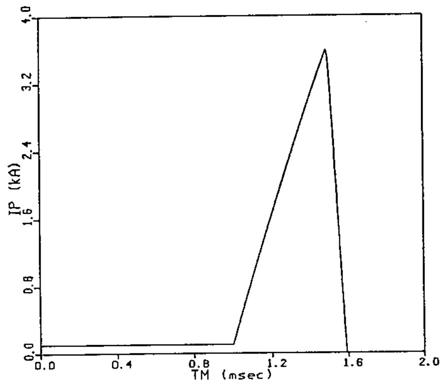

*Figure 5 Current through PCL without shunt link*

Incorporating the shunt link into the numerical simulation, we find that the internal temperatures never substantially exceeded the melting point of polyethylene (125 °C) and the energy dissipated in the PCL was a manageable 50 J. In this configuration, the PCL commutates the current into the shunt link reducing the amount of energy that the PCL itself must absorb. This system does not stop the flow of current entirely, but limits the let-through current to a value determined by the shunt link, in this case, 2 kA. This current is sufficient to trip the circuit breaker without damaging it. The tradeoff for using the shunt link is that the higher let-through current requires that the shunt link have a large energy dissipation rating.

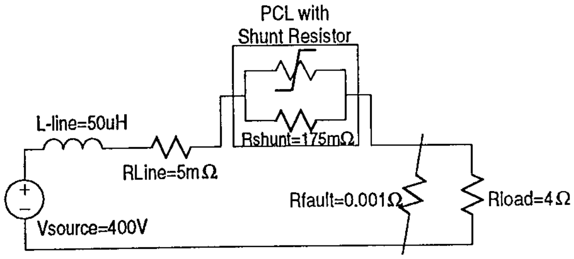

*Figure 6 Simple power distribution system utilizing a PCL and a shunt link.*

Specification of the correct shunt link is somewhat complicated. One desires to have a small resistance so that current is most effectively commutated into it from the PCL. On the other hand, the smaller the shunt resistance, the larger the energy absorption requirement for the link. In the end, the resistance of the shunt resistor depends mostly on ensuring coordination between hierarchic levels of circuit breakers. Then the energy absorption rating of the resistor is determined by the time between the switching of the PCL and the circuit breaker.

## IV. ENVIRONMENTAL CONSIDERATIONS

The switching action of a PCL depends on its temperature so it is inevitable that the ambient conditions will affect its performance. The two most important environmental factors are the ambient temperature and the circuit load. Both of these factors can change the internal temperature of the device, and thus increase or decrease the response time of the PCL.

The response time is essentially the time required to heat the PCL from its equilibrium temperature to the switching temperature. The melting point of polyethylene is near 120°C so the maximum allowable operating temperature must lie well below this point. Each degree of change in the operating temperature results in a corresponding change in the response time. Figure 7a shows how the switching times of a polyethylene PCL vary as the ambient temperature ranges from 0°C up to 75°C, its useful operating range.

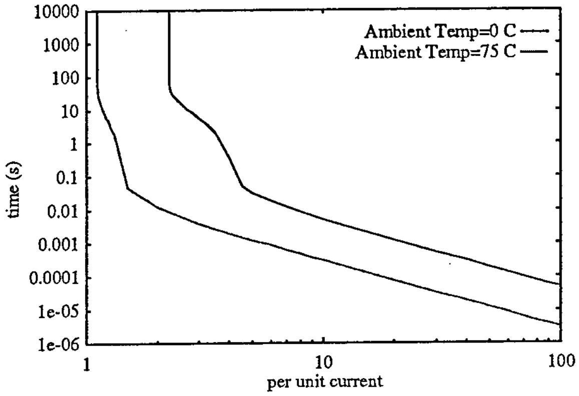

*Figure 7a Variation of trip time with increasing ambient temperature for a PCL with a melting temperature of 120.°C.*

Figure 7b shows the effect of changing the initial load current. While this does not have nearly as dramatic of an effect on the switching time of the device, it nonetheless can be a significant factor in determining the switching characteristics of a PCL device.

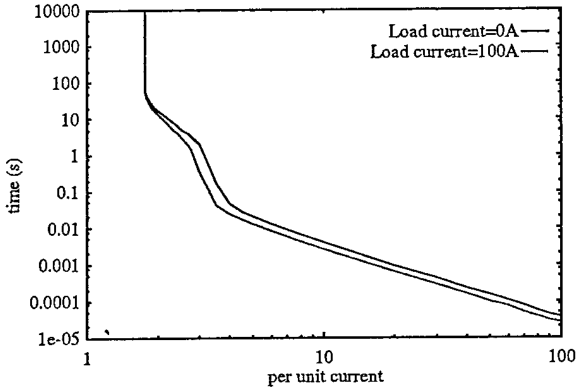

*Figure 7b Variation of trip time with increasing load current for a PCL with a melting temperature of 120.°C.*

As can be seen from these figures, lower internal temperatures, caused by either low load currents or low ambient temperatures, lead to slower switching times - as would be expected. This can result in loss of switching coordination allowing a fault current to reach levels higher than the breaker can safely interrupt. Conversely, if either load currents or ambient temperatures are too high, the internal temperature of the device is higher, causing the switching action to occur more rapidly, thereby again losing coordination with the circuit breaker.

The ability to extract heat from the device is important; in particular the nature of the electrode / PCL contact is critical. This junction can be a significant barrier to heat flow because of void spaces in the contact area due to surface roughness. The effectiveness of this contact can be quantified by the thermal contact coefficient, and is given by

$$h_c = \frac{1}{L_g}\left(\frac{A_c}{A}\frac{2k_E k_P}{k_E + k_P} + \frac{A_v}{A}k_f\right) \quad \left(\frac{W}{m^{2\,\circ}C}\right),$$

where $L_g$ is the thickness of the void spaces, $A_c$ is the contact area, $A_v$ is the void space area, A is the total cross-sectional area, and $k_E$, $k_P$ and $k_F$ are the thermal conductivities of the electrode, polymer, and fluid filling the voids, respectively. By increasing the pressure of the contact and/or minimizing surface roughness, $L_g$ is minimized and the contact area is maximized. Additionally, if a fluid with a higher thermal conductivity than air is used to fill the void spaces, $h_c$ will be maximized, thus allowing the device to remain cooler.

The primary loss of coordination is brought about by the fact that the melting temperatures of most polymers are fairly close to the 75°C maximum operating temperature. Because the low-resistivity portion of the ρ vs. T graph (figure1) is not flat, and in fact increases in slope as the temperature approaches the melting point, a positive feedback situation can arise causing premature switching of the device. The simplest solution to this premature switching is to use a material that has a higher melting point, thus making a 75°C swing in operating temperatures a less significant portion of the materials' low-resistivity state. Figures 8a and 8b show the responses of a device fabricated from a composite with a melting temperature of 150°C, 30°C above that of polyethylene. Although the graphs are similar to those in figure 7, upon close examination, it can be seen that the effects of ambient temperature and load currents are ameliorated to some extent, but the switch takes longer to react, resulting in larger peak currents.

## V. MODIFYING TIME-TO-TRIP CURVES

When used in an electrical distribution system, PCLs in series with circuit breakers may serve at least two purposes. As mentioned above, the PCL can limit the peak fault current to a value that the circuit breaker can safely interrupt as well as ensuring coordination between branch and feeder circuit breakers. Coordination is defined as an isolation of a fault at the lowest possible level of a hierarchic switching structure. Satisfying both of these purposes simultaneously presents many challenges.

Figure 9 shows the trip time characteristics for a typical branch circuit breaker and trip times of a feeder circuit breaker normalized to the rating of the branch circuit breaker . Both circuit breakers have complicated time-current curves, which can be divided into three zones: a long delay zone, a short delay zone, and an instantaneous trip zone (LT-ST-IT). While some circuit beakers have simpler switching characteristics involving only long delay and instantaneous zones (LT-IT), it will be clear that coordination with LT-ST-IT circuit breakers is the more challenging prospect. Long time delays are programmed into the breaker trip-time curve to prevent tripping during transient overcurrent situations such as those encountered when starting a motor. These long delays especially complicate the coordination problem between the circuit breakers and the PCL.

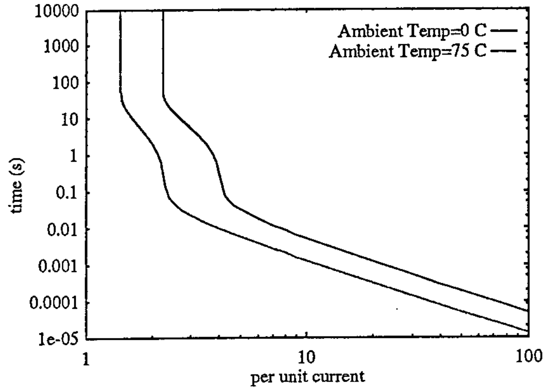

*Figure 8a Variation of trip time with increasing ambient temperature for a PCL with a melting temperature of 150.°C.*

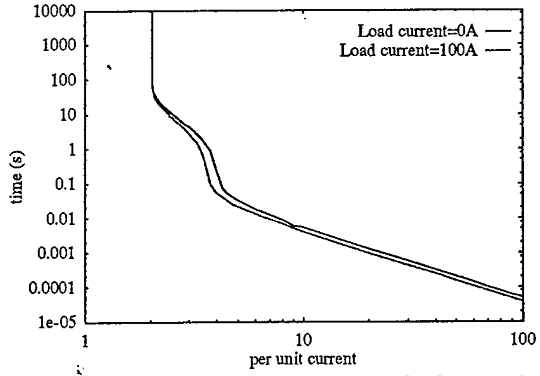

*Figure 8b Variation of trip time with increasing load current for a PCL with a melting temperature of 150.°C.*

Above 10x rated current, most circuit breakers operate in the instantaneous trip mode to rapidly isolate short circuit faults. The maximum instantaneous fault current that can flow in any system depends on the system inductance and the system voltage. In many applications, the system inductance is so low that fault currents can exceed the instantaneous trip current by a substantial margin even before the circuit breaker mechanism can be actuated. In this case, two things may happen: the circuit breaker may fail to interrupt the current if the peak current exceeds the peak interruption rating of the breaker; or both circuit breakers (the feeder and the branch) may trip. The latter condition represents a loss of coordination between the circuit breakers which results in the undesirable condition of trouble-free circuits energized by the same feeder circuit being left without power.

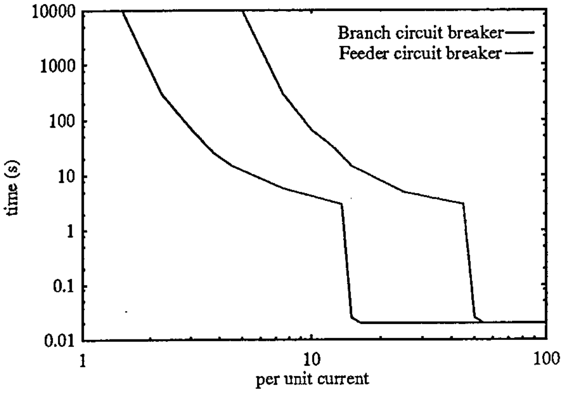

*Figure 9 Typical time-current curves for branch and feeder circuit breakers*

Shown in figure 10 is a typical graph of time to switch for a PCL superimposed over the graphs for typical branch and feeder circuit breakers from figure 9. Note that when the CB operates in the long delay stage (~1.5-5 times rated current), the PCL will switch in a fraction of the time of the CB. This causes two complications. First, the PCL (or its shunt resistor) could absorb an excessive amount of energy and become damaged before the circuit breaker could trip. Second, due to the large time delay between the switching action of the PCL and the CB, the advantage of having a delay built into the circuit breaker is lost.

It is important to note that at low to moderate overcurrents it is advantageous for the PCL to switch slower than the branch circuit breaker in order to allow short duration over-currents. At high overcurrents, however, it is important for the PCL to switch faster than the feeder circuit breaker but slower than the branch circuit breakers in order to achieve the desired current limiting action without causing undesired switching of other circuits feeding off of the same circuit breaker.

At extremely high overcurrents, the switch-time of the PCL is essentially irrelevant for the portion of the curve which lies below the maximum di/dt as moderated by the system voltage and inductance. This is shown in figure 10 and is described by the equation:

$$\frac{di}{dt} = \frac{V}{L_{sys}}.$$

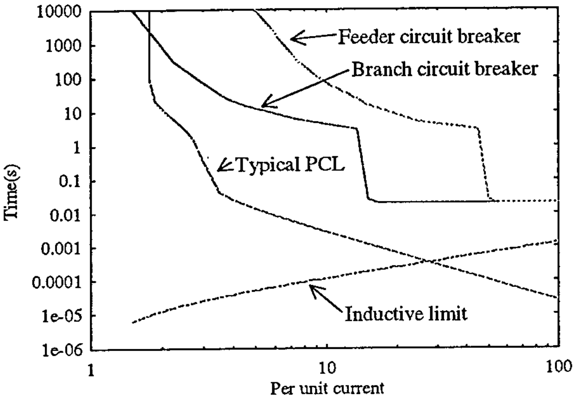

*Figure 10 Comparison of PCL time-current curve with circuit breaker curves showing poor coordination.*

Utilizing the thermal model of the polymer, certain critical parameters were determined to alter the shape of the PCL curve to better match that of the circuit breaker. These parameters can be altered within the limitations of the manufacturing technology to allow a PCL to be developed to match a great number of systems.

### *A. Cross Sectional Area Variations*

As a first approach, the simplest way to keep the PCL curve to the right of the branch circuit breaker is to increase the cross-sectional area of the PCL. Time vs. overcurrent curves are shown in figure 11 for several different PCLs, each with a different cross-sectional area. As can be seen, larger cross-sectional areas shift the entire curve to the right. Although the knee in the graph flattens slightly with larger areas, very little useful change in the shape of the curve is achieved. Using this approach, the PCL could be made large enough to prevent switching during the long-delay section of the branch circuit breaker. There are two problems with this approach, however. First, the device is now offering no protection below its new, higher threshold value. In essence, all that has been done, is that a higher rated device has been substituted for a lower rated one. Second, this is not an acceptable solution with regards to the feeder circuit. In order to prevent the feeder circuit breaker from tripping, the long delay portion of the PCL curve needs to lie to the left of the feeder circuit breaker curve. This is not possible in many systems by simply changing the area of the device as the long delay section of the circuit breaker and PCL curves would cross. It is evident then that the knee of the PCL curve needs to be altered in order to get ideal coordination between the PCL and the circuit breakers.

### *B. Electrode Mass Variations*

By increasing the mass of the electrode attached to the PCL, the time constant associated with the heat capacity and thermal contact resistance is altered, moving the top inflection point of the knee to higher values, as shown in figure 12.

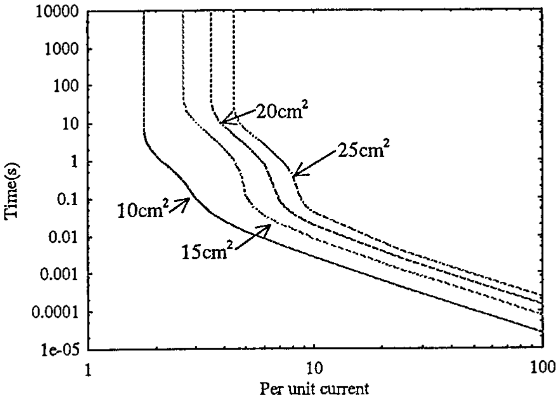

*Figure 11 Variation of trip time for various cross sectional areas.*

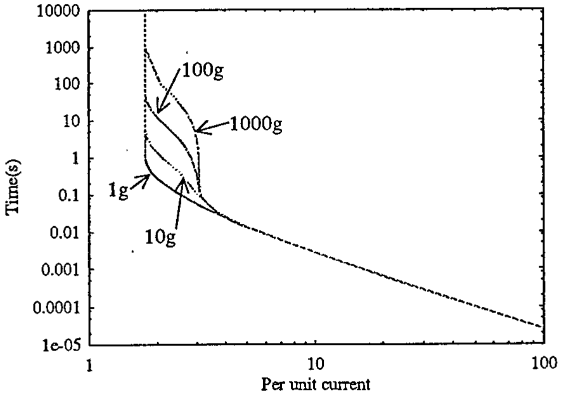

*Figure 12 Variation of trip time for various electrode masses.*

At the two extremes, i.e. for a massless electrode or for an electrode of infinite mass, there would be only one inflection point and no knee in the graph.

### *C. Thermal Conductivity Variations*

The locations of the vertical asymptotes corresponding to the limiting cases are independent of the mass of the electrode but can be altered by varying the thermal conductivity of the polymer material itself. This effect is clearly shown in figure 13.

As the thermal conductivity of the polymer increases the vertical asymptote corresponding to an infinite electrode mass moves to higher current values. An additional effect of increasing the thermal conductivity is that the entire curve (including the long delay portion) shifts to higher current values. This is completely expected as the devices depend on self-heating to switch and can be compensated by decreasing the cross-sectional area of the device enough to compensate for the shift. This will not affect the height or width of the knee in the graph, just the position on the current axis.

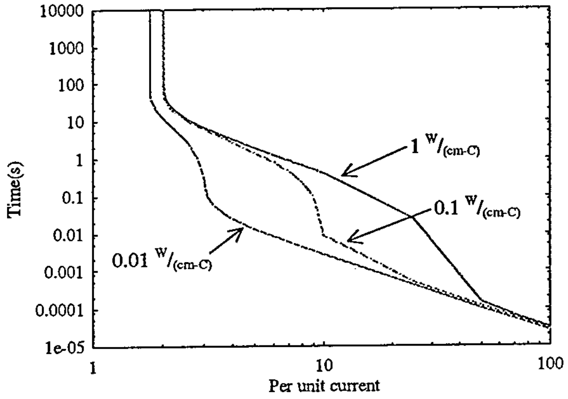

*Figure 13 Variation of trip time for various thermal conductivities.*

By altering the cross-sectional area, electrode mass, and polymer thermal conductivity, it is theoretically possible to match nearly any circuit breaker design. By adjusting the necessary design parameters, appropriate PCL curves were obtained and are shown in figure 14.

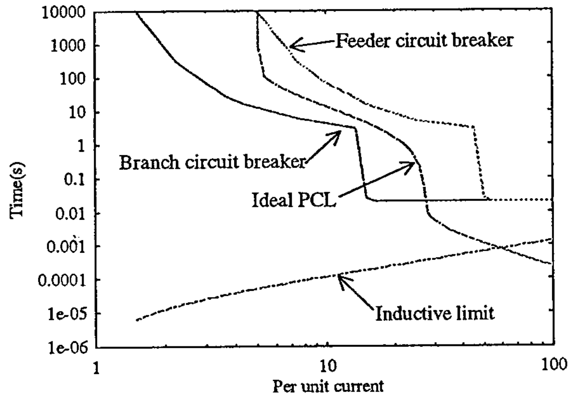

*Figure 14 Proper coordination between PCL and circuit breakers.*

In practice, the limiting values of these parameters will be determined by both physical and design constraints, thus limiting the design flexibility. The electrode mass and cross-sectional area will be limited by size constraints of the applications. Changing the thermal conductivity of the material would prove difficult without adversely affecting other material parameters. However, altering the effective thermal conductivity of the PCL could be accomplished without affecting the electrical characteristics by slicing the device into thin sections and sandwiching thermal masses in between the layers.

## VI. CONCLUSION

We have presented a comprehensive analysis of the necessary design considerations for utilizing a polymer current limiter in a low voltage power distribution system. Several problems associated with using a PCL in a high energy environment are investigated and appropriate solutions are presented.

The effectiveness of a shunt link in dissipating destructive amounts of energy during heavy short circuits was analyzed utilizing models of the system with and without a shunt link. An appropriately designed shunt link was shown to prevent the destruction of the PCL and facilitate coordination with other system devices.

The effects of steady state load and ambient temperature conditions on the switching characteristics of a PCL/shunt link system was investigated. The effect of reducing the influence of these environmental factors by increasing the melting point of the polymer material was presented.

Finally, it was shown that, theoretically, the trip time characteristics of a PCL can be arbitrarily manipulated to match a circuit breaker's characteristics by varying three of the PCL's design parameters: the cross-sectional area, the electrode mass and the thermal conductivity of the polymer material. The electrode mass is a completely independent variable while the area and polymer thermal conductivity are linked and must be balanced.

This paper is intended to introduce and explore the feasibility of utilizing the characteristics of specifically designed polymeric materials as current limiting devices in low voltage power distribution systems. As this application of this technology has not been thoroughly explored, there is a need for more extensive research. Of particular importance, is the interaction with other current limiting devices that may be present within the system, such as current limiting circuit breakers.10 Future plans include the inclusion of a mathematical model of a current limiting circuit breaker in the same system to explore this interaction. Finally, while some experimental data based on real-world situations has been obtained to add validity to the models used more experimental analysis needs to be conducted to prove the accuracy of the models as they apply to the application proposed here.

## VII. REFERENCES

[1] M. Blaszkiewicz, D.S, McLachlan, R.E. Newnham, "The volume fraction and temperature dependence of the resistivity in carbon black and graphite polymer composites: an effective media-percolation approach", *Polymer Engr. and Sci.*, **32**, No. 6, pp 421-425, March 1992.

[2] F. Bueche, "A new class of switching materials", *J. Appl. Phys.*, **44**, No. 1, pp 532-533, January 1973.

[3] M. Narkis, A. Ram, Z. Stein, "Effect of crosslinking on carbon-black/polyethylene switching materials", *J. Appl. Poly. Sci.*, **25**, pp 1515-1518, January 1980.

[4] M. Valencia, "Self-resetting PTC-polymer devices guard against overcurrent damage", *EDN*, **41**, pp 131-137, January 18, 1996.

[5] M. Stoessl, "Positive Temperature coefficient conductive polymer resistors protect electronic equipment", *Power Control in Motion*, pp 50-55, June 1993.

[6] F. Doljack, "PolySwitch PTC Devices - A new low resistance conductive polymer-based PTC device for overcurrent protection", *IEEE Trans. Components, Hybrids and Manuf. Tech.*, **CHMT-4**, No. 4, pp 372-378, December 1981.

[7] C.W. Brice, R.A. Dougal, J.L. Hudgins, "Review of technologies for current limiting low-voltage circuit breakers", *IEEE Trans. On Industry Appl.*, **32**, No. 5, pp 1005-1010, September/October 1996.

[8] R.A. Dougal, "Current limiting thermistors for high-power applications", *IEEE Trans. on Power Elect.*, **11**, No. 2, March 1996.

[9] G.D. Gregory, "Applying low-voltage circuit breakers in direct current systems", *IEEE Trans. on Industry Appl.*, **31**, No. 4, July/Aug. 1995.

[10] B. DiMarco, S.R.Hanson, "Interplay of Energies in Circuit Breaker and Fuse Combinations", *IEEE Trans. on Industry Appl.*, **29**, No. 3, May/June 1993.

**MARK H. MCKINNEY** attends the University of South Carolina. He received a B.S. degree in electrical engineering from USC in 1993, and an M.E. in 1995. He is currently working on his Ph.D. in polymer current limiting devices. His research interests also include high-energy spark gaps and optically controlled semiconductor switches.

**CHARLES W. BRICE** (M '76, SM '83) attended the School of Electrical Engineering at the Georgia Institute of Technology, receiving the BEE degree in 1971, the MSEE degree in 1972 and the PhD degree in 1977. He is an Associate Professor in the Department of Electrical and Computer Engineering at the University of South Carolina in Columbia, SC. He was a member of the faculty of the Department of Electrical Engineering at Texas A&M University from 1977 to 1983. His fields of interest are electric power systems, control systems, and electric machines.

**ROGER A. DOUGAL** (S '75, M '83, SM '94) was born in Champaign, Illinois in 1956. He received the B.S. degree in electrical engineering at Texas Tech University, Lubbock, in 1978, then remained there to earn the M.S. degree in 1980 for work on infrared lasers, and the Ph.D. degree in 1983 for research on laser-triggered switching of gas-filled spark gaps. He joined the Faculty of the Department of Electrical and Computer Engineering, University of South Carolina, in 1983, where his research interests focus on physical electronics. He has spent summers at the Los Alamos National Laboratory ('78, '79) and at the Lawrence Livermore National Laboratory ('89). Dr. Dougal has been honored as a Carolina Research Professor, and as a Litman Distinguished Professor of Engineering.

Submitted to Automatica (revised once)

# Global Asymptotic Stability of Indirect Field-Oriented Speed Control of Induction Motors

Levent U. Gökdere[†§], M. A. Simaan[‡] and Charles W. Brice[†]

[†]Department of Electrical & Computer Engineering
University of South Carolina
Swearingen 3A80
Columbia, SC 29208

[‡]Department of Electrical Engineering
University of Pittsburgh
Pittsburgh, PA 15261

## ABSTRACT

In this short paper, we show that the indirect field-oriented controller for induction motors guarantees the global asymptotic stability of speed tracking error for time-varying speed and rotor flux references. The load torque is assumed to be constant but is unknown.

*Key words*: Indirect field-oriented method, induction motor, speed control.

---

[§] Corresponding author. Tel: (803) 777-9314; Fax: (803) 777-8045; E-mail: gokdere@ece.sc.edu.

## INTRODUCTION

The indirect field-oriented method for induction motor control is one of the most common types of field-oriented methods used in industrial applications since it does not require flux sensor (or flux estimator) to measure (or estimate) the rotor flux (Vas, 1990). Recently, Ortega and Taoutaou (1996) proved that the indirect field-oriented method provides asymptotic tracking of constant speed reference (assuming that the rotor flux reference is constant).

In this short paper, the results in Ortega and Taoutaou (1996) are improved to include time-varying speed and rotor flux references. The load torque is assumed to be constant but is unknown.

## A CURRENT-COMMAND *d-q* MODEL OF INDUCTION MOTOR

Let $\boldsymbol{\lambda}_{\mathrm{dq}}^{\mathrm{T}} := [\lambda_{\mathrm{d}}\ ,\ \lambda_{\mathrm{q}}]$, $\mathbf{i}_{\mathrm{dq}}^{*\mathrm{T}} := [i_{\mathrm{d}}^{*}\ ,\ i_{\mathrm{q}}^{*}]$, $\omega$ and $\theta$ denote, respectively, the transpose of the rotor flux vector, transpose of the commanded stator current vector, rotor speed and rotor position. Then, a current-command *d-q* (direct-quadrature) model of an induction motor is given by

$$\frac{d\boldsymbol{\lambda}_{\mathrm{dq}}}{dt} + \omega_s \mathbf{J}\boldsymbol{\lambda}_{\mathrm{dq}} + \frac{R_r}{L_r}\boldsymbol{\lambda}_{\mathrm{dq}} = \frac{R_r M}{L_r}\mathbf{i}_{\mathrm{dq}}^{*} \tag{1}$$

$$J\frac{d\omega}{dt} = \tau - f\omega - \tau_L \tag{2}$$

$$\frac{d\theta}{dt} = \omega \tag{3}$$

where $\omega_s$ is the slip frequency, $\tau$ is the electrical torque, $\tau_L$ is the load torque, $R_r$ is the rotor resistance, $L_r$ is the rotor self inductance, $M$ is the mutual inductance, $J$ is the rotor moment of inertia, $f$ is the viscous friction coefficient and **J** is a two by two skew-symmetric matrix. The electrical torque is given by

$$\tau = -\frac{2n_p M}{n_{ph} L_r} \boldsymbol{\lambda}_{\mathbf{dq}}^{\mathrm{T}} \mathbf{J} \mathbf{i}_{\mathbf{dq}}^{*} \tag{4}$$

where $n_p$ is the number of pole pairs and $n_{ph}$ is the number of phases.

In the above model, the electrical variables are defined in a reference frame which rotates at an angular speed of $\omega_s + n_p \omega$.

In the indirect field-oriented control, $\mathbf{i}_{\mathbf{dq}}^{*}$ and $\omega_s$ are the control inputs and chosen as (Nabae *et al.* (1980))

$$\mathbf{i}_{\mathbf{dq}}^{*} := \begin{bmatrix} \dfrac{\lambda_d^*}{M} + \dfrac{L_r}{R_r M} \dfrac{d\lambda_d^*}{dt} \\ \dfrac{n_{ph} L_r}{2n_p M} \dfrac{\tau^*}{\lambda_d^*} \end{bmatrix} \tag{5}$$

$$\omega_s := \frac{n_{ph} R_r}{2n_p} \frac{\tau^*}{\lambda_d^{*2}} \tag{6}$$

where $\lambda_d^*$ is the $d$ component of reference rotor flux vector, which is defined as

$$\boldsymbol{\lambda}_{\mathbf{dq}}^{*} := \begin{bmatrix} \lambda_d^* \\ 0 \end{bmatrix} \tag{7}$$

and $\tau^*$ is the reference torque, whose value is determined by the control system designer.

Note that $\lambda_{dq}^*$ is aligned with the *d* axis of the *d-q* reference frame since *q* component of $\lambda_{dq}^*$ is defined to be equal to zero. Furthermore, the magnitude of $\lambda_{dq}^*$ is $\lambda_d^*$ which, in this paper, is assumed to be time-varying.

In Ortega and Taoutaou (1996), a simplified version of the indirect field-oriented controller is considered since the speed and flux references are assumed to be constant. Otherwise, the indirect field-oriented controllers in this paper and in Ortega and Taoutaou (1996) are exactly equivalent to each other.

The following analysis shows that the flux tracking error is exponentially stable at the origin ( This was also reported in Espinosa-Pérez, Ortega and Nicklasson (1997)). Later, it will be shown that the speed tracking error can be forced to converge asymptotically to the origin by proper choice of reference torque $\tau^*$.

## EXPONENTIAL STABILITY OF FLUX TRACKING ERROR

Let us define flux tracking error as

$$\tilde{\lambda}_{dq} := \begin{bmatrix} \tilde{\lambda}_d \\ \tilde{\lambda}_q \end{bmatrix} := \lambda_{dq} - \lambda_{dq}^* \qquad (8)$$

Substituting $\lambda_{dq} = \lambda_{dq}^* + \tilde{\lambda}_{dq}$ in (1) results in

$$\frac{d\tilde{\boldsymbol{\lambda}}_{\mathrm{dq}}}{dt}+\omega_s\mathbf{J}\tilde{\boldsymbol{\lambda}}_{\mathrm{dq}}+\frac{R_r}{L_r}\tilde{\boldsymbol{\lambda}}_{\mathrm{dq}}=\frac{R_rM}{L_r}\mathbf{i}_{\mathrm{dq}}^{\,*}-\frac{d\boldsymbol{\lambda}_{\mathrm{dq}}^{*}}{dt}-\omega_s\mathbf{J}\boldsymbol{\lambda}_{\mathrm{dq}}^{*}-\frac{R_r}{L_r}\boldsymbol{\lambda}_{\mathrm{dq}}^{*} \tag{9}$$

By direct substitution of (5), (6) and (7), we can show that

$$\mathbf{i}_{dq}^{\,*}=\frac{L_r}{R_rM}\frac{d\boldsymbol{\lambda}_{\mathrm{dq}}^{*}}{dt}+\omega_s\frac{L_r}{R_rM}\mathbf{J}\boldsymbol{\lambda}_{\mathrm{dq}}^{*}+\frac{1}{M}\boldsymbol{\lambda}_{\mathrm{dq}}^{*} \tag{10}$$

As a result, error equation (9) becomes

$$\frac{d\tilde{\boldsymbol{\lambda}}_{\mathrm{dq}}}{dt}+\omega_s\mathbf{J}\tilde{\boldsymbol{\lambda}}_{\mathrm{dq}}+\frac{R_r}{L_r}\tilde{\boldsymbol{\lambda}}_{\mathrm{dq}}=0 \tag{11}$$

Consider the candidate Lyapunov function

$$V=\frac{1}{2}\tilde{\boldsymbol{\lambda}}_{\mathrm{dq}}^{\mathrm{T}}\tilde{\boldsymbol{\lambda}}_{\mathrm{dq}}. \tag{12}$$

Assuming that the solution $\tilde{\boldsymbol{\lambda}}_{\mathrm{dq}}$ to equation (11) is unique and continuous for $t \geq 0$, then, the derivative of $V$ with respect to time along the trajectory of $\tilde{\boldsymbol{\lambda}}_{\mathrm{dq}}$ is

$$\frac{dV}{\mathrm{dt}}=\tilde{\boldsymbol{\lambda}}_{\mathrm{dq}}^{\mathrm{T}}\frac{d\tilde{\boldsymbol{\lambda}}_{\mathrm{dq}}}{dt}=-\tilde{\boldsymbol{\lambda}}_{\mathrm{dq}}^{\mathrm{T}}\left(\omega_s\mathbf{J}\tilde{\boldsymbol{\lambda}}_{\mathrm{dq}}+\frac{R_r}{L_r}\tilde{\boldsymbol{\lambda}}_{\mathrm{dq}}\right)=-\frac{R_r}{L_r}\tilde{\boldsymbol{\lambda}}_{\mathrm{dq}}^{\mathrm{T}}\tilde{\boldsymbol{\lambda}}_{\mathrm{dq}}=-\frac{2R_r}{L_r}V \tag{13}$$

which is negative definite. It follows that

$$\left|\tilde{\boldsymbol{\lambda}}_{\mathrm{dq}}\right|=\sqrt{2V}=\sqrt{2V(0)}e^{-\frac{R_r}{L_r}t}=\left|\tilde{\boldsymbol{\lambda}}_{\mathrm{dq}}(0)\right|e^{-\frac{R_r}{L_r}t}\ \text{for } t\ \geq\ 0 \tag{14}$$

That is, the flux tracking error is exponentially decreasing with a rate of convergence equal to the rotor time constant $\frac{L_r}{R_r}$.

## ASYPTOTIC STABILITY OF SPEED TRACKING ERROR

Let us choose the reference torque as

$$\tau^* = J\frac{d\omega^*}{dt} + f\omega^* - Jk_i\int_0^t\left(\omega - \omega^*\right)dt - Jk_p(\omega - \omega^*) \tag{15}$$

where $\omega^*$ is the reference values of $\omega$. Feedback gains $k_i$ and $k_p$ are positive constants.

Considering the torque equation (2) and reference torque (15), we can write

$$\frac{de_2}{dt} = \frac{1}{J}\left(\tau - \tau^*\right) - k_i e_1 - \left(k_p + \frac{f}{J}\right)e_2 - \frac{\tau_L}{J} \tag{16}$$

where $e_1 := \int_0^t\left(\omega - \omega^*\right)dt$ and $e_2 := \omega - \omega^*$.

For any $\tau^*$, the following holds:

$$\tau^* = -\frac{2\mathrm{n_p} M}{\mathrm{n_{ph}} L_r}\boldsymbol{\lambda}_{\mathbf{dq}}^{*\mathbf{T}}\mathbf{J}\mathbf{i}_{\mathbf{dq}}^* \tag{17}$$

This can be proven by substituting the explicit values of $\mathbf{i}_{\mathbf{dq}}{}^*$ given by (5) and $\boldsymbol{\lambda}_{\mathbf{dq}}^*$ given by (7) in (17).

Subtracting (17) from (4) gives

$$\tau - \tau^* = -\frac{2n_p M}{n_{ph} L_r} \tilde{\boldsymbol{\lambda}}_{\mathrm{dq}}^{\mathrm{T}} \mathbf{J} \begin{bmatrix} \dfrac{\lambda_d^*}{M} + \dfrac{L_r}{R_r M}\dfrac{d\lambda_d^*}{dt} \\ \dfrac{n_{ph} L_r}{2n_p M}\dfrac{\tau^*}{\lambda_d^*} \end{bmatrix} \tag{18}$$

which, using (15), can be written explicitly as

$$\tau - \tau^* = -J\frac{\tilde{\lambda}_d}{\lambda_d^*}\left(k_i e_1 + k_p e_2\right) - \frac{2n_p M}{n_{ph} L_r} \tilde{\boldsymbol{\lambda}}_{\mathrm{dq}}^{\mathrm{T}} \mathbf{J} \begin{bmatrix} \dfrac{\lambda_d^*}{M} + \dfrac{L_r}{R_r M}\dfrac{d\lambda_d^*}{dt} \\ \dfrac{n_{ph} L_r}{2n_p M}\dfrac{\left(J\dfrac{d\omega^*}{dt} + f\omega^*\right)}{\lambda_d^*} \end{bmatrix} \tag{19}$$

Substituting (19) in equation (16), we can obtain total mechanical error system as

$$\dot{\mathbf{e}} = \left(\mathbf{A}_1 + \mathbf{A}_2(t)\right)\mathbf{e} + \mathbf{b}\left(u(t) - \frac{\tau_L}{J}\right) \tag{20}$$

where

$$\mathbf{e} := \begin{bmatrix} e_1 \\ e_2 \end{bmatrix}, \ \mathbf{A}_1 := \begin{bmatrix} 0 & 1 \\ -k_i & -\left(\dfrac{f}{J} + k_p\right) \end{bmatrix}, \ \mathbf{A}_2(t) := \frac{\tilde{\lambda}_d}{\lambda_d^*}\begin{bmatrix} 0 & 0 \\ -k_i & -k_p \end{bmatrix},$$

$$\mathbf{b} := \begin{bmatrix} 0 \\ 1 \end{bmatrix} \text{ and } u(t) := -\frac{2n_p M}{n_{ph} L_r J} \tilde{\boldsymbol{\lambda}}_{\mathrm{dq}}^{\mathrm{T}} \mathbf{J} \begin{bmatrix} \dfrac{\lambda_d^*}{M} + \dfrac{L_r}{R_r M} \dfrac{d\lambda_d^*}{dt} \\ \dfrac{n_{ph} L_r}{2n_p M} \dfrac{\left( J \dfrac{d\omega^*}{dt} + f\omega^* \right)}{\lambda_d^*} \end{bmatrix}.$$

In (20), $\mathbf{A}_1$ is Hurwitz for $k_i$ and $k_p > 0$ since $\frac{f}{J} > 0$. However, depending on the initial value of the flux tracking error $\tilde{\boldsymbol{\lambda}}_{\mathrm{dq}}$, the eigenvalues of $\mathbf{A}_1 + \mathbf{A}_2(t)$ might be in the open right-half complex plane for a time interval determined by the rotor time constant $\frac{L_r}{R_r}$. During this time interval, the norm of $\mathbf{e}$, and in turn $\tau^*$, will grow. As a result, the stator currents may saturate. Taking this into account, let us make the following assumption:

$$\left| \tilde{\boldsymbol{\lambda}}_{\mathrm{dq}}(0) \right| \le \left| \boldsymbol{\lambda}_{\mathrm{dq}}^*(t) \right| \text{ for } t \ge 0 \tag{21}$$

Then, the eigenvalues of $\mathbf{A}_1 + \mathbf{A}_2(t)$ will never be in the open right-half complex plane.

Note here that condition (21) is consistent with the practical implementations. For example, for $\boldsymbol{\lambda}_{\mathrm{dq}}^{\mathrm{T}}(0) := [0\ ,\ 0]$ and $0 < \lambda_d^*(0) \le \lambda_d^*(t)$ (see Bodson, Chiasson and Novotnak (1995) for the selection of flux references in induction motors), condition (21) holds.

Suppose that $\omega^*$ and $\lambda_d^*$ are continuous, bounded, have bounded and continuous first-order derivatives, and $\lambda_d^*$ is bounded away from zero.

Furthermore, the load torque $\tau_L$ is constant. Then, considering the exponential stability of $\tilde{\lambda}_{dq}$, we can say that equality (20) represents an exponentially stable linear time-varying system perturbed by a constant disturbance (Khalil (1992)), which means speed tracking error $e_2$ will converge asymptotically to the origin.

## CONCLUSION

In the indirect field-oriented control of induction motors, the global asymptotic stability of speed tracking error is achieved for time-varying speed and flux references.

## ACKNOWLEDGMENT

This work was supported by the Office of Naval Research under Grant N00014-96-1-0926.

automatica

# REFERENCES

Bodson, M., J. Chiasson and R. Novotnak (1995). A Systematic Approach to Selecting Flux References for Torque Maximization in Induction Motors. *IEEE Trans. on Control Systems Technology*, **3**, 388-397.

Espinosa-Pérez, R. Ortega and P.J. Nicklasson (1997). Torque and Flux Tracking of Induction Motors. *Int. Journal on Robust and Nonlinear Control*, **7**, 1-9.

Khalil, H. (1992). *Nonlinear Systems*. Macmillan, New York.

Nabae, A., K. Otsuka, H. Uchino and R. Kurosawa (1980). An Approach to Flux Control of Induction Motors Operated with Variable-Frequency Power Supply. *IEEE Trans. on Industry Applications*, **16**, 342-350.

Ortega, R. and D. Taoutaou (1996). Indirect Field-Oriented Speed Regulation for Induction Motors Is Globally Stable. *IEEE Trans. on Industrial Electronics*, **43**, 340-341.

Vas, P. (1990). *Vector Control of AC Machines*. Clarendon Press, Oxford.

Submitted to IEEE Transactions on Control Systems Technology

# A Passivity-Based Controller for Saturated Induction Motors

Levent U. Gökdere[†§], M. A. Simaan[‡] and C. W. Brice[†]

[†]Department of Electrical & Computer Engineering
University of South Carolina
Swearingen 3A80
Columbia, SC 29208

[‡]Department of Electrical Engineering
University of Pittsburgh
Pittsburgh, PA 15261

## ABSTRACT

In this paper, we design, and also experimentally verify, a passivity-based controller that forces an induction motor which has significant magnetic saturation to track a time-varying optimal flux trajectory. As a result, we are able to provide close tracking of a time-varying speed/position trajectory that requires close to the maximum torque achievable by the motor within the voltage and current limits.

*Key words*: Induction motor, magnetic saturation, passivity-based controller.

---

[§] Corresponding author. Tel: (803) 777-9314; Fax: (803) 777-8045; E-mail: gokdere@ece.sc.edu.

# LIST OF FIGURES

1 Block diagram for the current-command passivity-based control of the induction motor. .......... 11

2 Magnetization curve of the induction motor. .......... 11

3 Estimated (solid) and reference (dashed) speeds in radians per second versus time in seconds. .......... 12

4 Speed error in radians per second versus time in seconds. .......... 12

5 Measured (solid) and reference (dashed) positions in radians versus time in seconds. .......... 12

6 Position error in encoder counts (1 count = $2\pi / 2880$ radians) versus time in seconds. .......... 12

7 $\left|\hat{\lambda}_{dq}\right|$ (solid) and $\left|\lambda^{*}_{dq}\right|$ (dashed) in Webers versus time in seconds. .......... 12

## I. INTRODUCTION

In high-performance motion control applications, selection of the rotor flux reference is an important issue since the maximum torque achievable by the motor depends on the rotor flux level. At low speeds, the rotor flux is held constant at some maximum value within the voltage and current limits to extract the maximum torque from the motor. At higher speeds, the rotor flux level is decreased to prevent the stator voltages from saturating. In brief, the selection of time-varying, rather that constant, rotor flux reference is essential to obtain maximum performance from the motor without saturating the stator voltages.

Bodson *et al.* [1] and Novotnak *et al.* [2, 3] introduced time-varying optimal flux trajectories for induction motors to obtain maximum positive torque during acceleration (motor mode) and minimum negative torque during deceleration (generator mode) under the voltage and/or current constraints.

In this paper, we design, and also experimentally verify, a passivity-based controller that forces the induction motor to track the time-varying optimal flux trajectory without knowledge of the rotor electrical state variables (i.e., rotor fluxes or currents). As a result, we are able to provide close tracking of a time-varying speed/position trajectory, which requires close to the maximum torque achievable by the motor within the voltage and current limits, without having to measure (or estimate) the rotor electrical sate variables. The passivity-based controller in this paper takes into account the magnetic saturation effects.

## II. A CURRENT-COMMAND PASSIVITY-BASED CONTROLLER for INDUCTION MOTORS

A current-command *d-q* model of the induction motor can be given by

$$\frac{d\lambda_{dq}}{dt} + \left(\frac{R_r}{L_r}\right)\lambda_{dq} = \left(\frac{R_r M}{L_r}\right)\mathbf{i}^*_{dq} \tag{1}$$

$$J\frac{d\omega}{dt} = \tau - f\omega \tag{2}$$

$$\frac{d\theta}{dt} = \omega \tag{3}$$

where $\lambda_{dq}$ is the rotor flux vector, $\mathbf{i}^*_{dq}$ is the reference stator current vector, $\omega$ is the motor angular speed, $\theta$ is the motor angular position, $\tau$ is the electrical torque (the torque produced by the motor), $R_r$ is the rotor resistance, $L_r$ is the rotor inductance, $M$ is the mutual inductance, $J$ is the rotor moment of inertia and $f$ is the viscous friction coefficient. The electrical torque is given by

$$\tau = -\frac{2n_p M}{n_{ph} L_r}\lambda^T_{dq}\mathbf{J}\mathbf{i}^*_{dq} \tag{4}$$

where $n_p$ is the number of pole pairs, $n_{ph}$ is the number of phases, $\lambda^T_{dq}$ is the transpose of $\lambda_{dq}$ and $\mathbf{J}$ is a two by two skew-symmetric matrix.

In the above model, the electrical variables are defined in a special *d-q* reference frame whose angular position with respect to the fixed stator reference frame is $n_p\theta$.

The current-fed induction motor version of the passivity-based controller developed by Ortega *et al.* [4, 5, 6] is given by

$$\mathbf{i}^*_{dq} = \begin{bmatrix} \cos\alpha & -\sin\alpha \\ \sin\alpha & \cos\alpha \end{bmatrix} \begin{bmatrix} \dfrac{\beta(t)}{M} + \dfrac{L_r}{R_r M}\dfrac{d\beta(t)}{dt} \\ \dfrac{n_{ph}L_r}{2n_p M}\dfrac{\tau^*}{\beta(t)} \end{bmatrix} \tag{5}$$

where $\alpha$ is the solution of

$$\frac{d\alpha}{dt} = \frac{n_{ph}R_r}{2n_p}\frac{\tau^*}{\beta(t)^2} \tag{6}$$

In (5) and (6), $\beta(t)$ is the magnitude of the reference rotor flux vector and $\tau^*$ is the reference torque. The reference rotor flux vector is defined as

$$\lambda^*_{dq} = \beta(t)\begin{bmatrix} \cos\alpha \\ \sin\alpha \end{bmatrix}$$

and the reference torque is chosen as

$$\tau^* = J\frac{d\omega^*}{dt} + f\omega^* - Jk_1\int_0^t \left(\theta - \theta^*\right)dt - Jk_2\left(\theta - \theta^*\right) - Jk_3\left(\omega - \omega^*\right) \tag{7}$$

where $\theta^*$ and $\omega^* = \dfrac{d\theta^*}{dt}$ are the reference values of $\theta$ and $\omega$, respectively. Feedback gains $k_1$, $k_2$ and $k_3$ are positive constants.

It can be shown that current-command passivity-based controller (5) provides exponential tracking of time-varying speed/position and flux trajectories.

The current-command passivity-based controller is equivalent to the well-known indirect (strictly feedforward) field-oriented controller (the *de facto* industry standard) [5]. Implementations of the indirect field-oriented controllers based on the linear and saturated magnetic models of the induction motor can be found in [7] and [8], respectively.

## III. INCORPARATION of MAGNETIC SATURATION EFFECTS INTO PASSIVITY-BASED CONTROLLER

Levi *et al.* [8], Heinemann *et al.* [9], Sullivan *et al.* [10, 11] developed field-oriented controllers based on saturated magnetic models of the induction motor. An input-output linearization controller, which takes the saturation effects into account, was designed by Novatnak *et al.* [2, 3].

In [2, 3, 9], saturation is assumed to be entirely in the main flux path of the induction motor. That is, the change in the mutual inductance due to saturation in the material is considered and the changes in the stator and rotor leakage factors are neglected. Using the same approach, we can rearrange passivity-based controller (5) as

$$\mathbf{i}_{dq}^{*} = \begin{bmatrix} \cos\alpha & -\sin\alpha \\ \sin\alpha & \cos\alpha \end{bmatrix} \begin{bmatrix} f_m^{-1}(\beta(t)) + \dfrac{L_r}{R_r M}\dfrac{d\beta(t)}{dt} \\ \dfrac{n_{ph}L_r}{2n_p M}\dfrac{\tau^{*}}{\beta(t)} \end{bmatrix} \tag{7}$$

where $f_m^{-1}(\cdot)$ is the inverse of the magnetization curve function of the induction motor. In (7), the nominal values of $L_r$ and $M$ are used. This is reasonable since $\frac{L_r}{M} = 1 + \sigma_r$, where $\sigma_r$ is the rotor leakage factor [12], and the change in $\sigma_r$ due to the saturation is neglected.

For the values of $\beta(t)$ which remain in the linear magnetic region, $f_m^{-1}(\beta(t)) = \frac{\beta(t)}{M}$ with $M$ constant so that (7) reduces to (5).

## IV. SPEED ESTIMATOR

The passivity-based technique requires the knowledge of the speed and position to achieve speed/position tracking control. In a typical experimental setup, only position measurements are available and hence, a speed estimator must be implemented in real-time to compute the speed.

The easiest way to estimate the speed is the numerical differentiation of the position outputs from the optical encoder. That is

$$\hat{\omega} = \frac{\theta(nT) - \theta((n-1)T)}{T} \tag{8}$$

where $\hat{\omega}$ is the estimated speed, $T$ is the sample period and $\theta(nT)$ is the position measurement at $t = nT$. However, a $2880$ pulses per revolution (resolution of $\frac{2\pi}{2880}$ radians) encoder is used in the experimental setup and computing $\hat{\omega}$ by (8) may cause an error in the speed estimate up to $\frac{2\pi}{2880T}$.

Lorenz *et al.* [13] and Bodson *et al.* [14] proposed, and also experimentally verified, speed estimators based on the dynamic model of the motor and the positions measurements. In this paper, the following speed estimator was used [13] :

$$\frac{d\hat{\theta}}{dt} = \hat{\omega} + l_1\left(\theta - \hat{\theta}\right) \tag{9}$$

$$\frac{d\hat{\omega}}{dt} = \frac{\tau^*}{J} - \frac{f}{J}\hat{\omega} + l_2\left(\theta - \hat{\theta}\right) \tag{10}$$

where, again $\hat{\omega}$ is the estimate of the speed, $\hat{\theta}$ is the estimate of the position, and $l_1$, $l_2$ are the estimator gains.

Fig. 1 shows a block diagram for the passivity-based control of the induction motor.

## V. OPTIMAL FLUX TRAJECTORY

Bodson *et al.* [1] and Novotnak *et al.* [2, 3] introduced, and also experimentally verified, time-varying optimal flux trajectories to extract maximum positive torque during acceleration (motor mode) and minimum negative torque during deceleration (generator mode) from the induction motor under the voltage and/or current constraints.

In this paper, $\beta(t)$, the magnitude of the rotor flux vector, was chosen as the solution of

$$\frac{d\beta(t)}{dt} = M\eta\left(-f_m^{-1}(\beta(t)) + \frac{1}{\mu\beta(t)\delta_{sopt}(\omega^*)}\frac{d\omega^*}{dt}\right) \qquad (11)$$

where $\eta := \frac{R_r}{L_r}$, $\mu := \frac{2n_p M}{n_{ph} J L_r}$ and $\delta_{sopt}(\omega^*)$ is the solution to the saturated magnetics optimal torque problem [2, 3].

## VI. EXPERIMENTAL RESULTS

Current-command passivity-based controller (7) was tested on an experimental setup which consisted of (i) a 3-phase, 6-pole, 1-Hp, squirrel cage induction motor, (ii) a Motorola DSP96002 (floating point processor) ADS system, (iii) a data acquisition board, and (iv) three 20 kHz PWM amplifiers (±150 Volts and ±10 Amperes). The parameters of the induction motor are listed in Table I. The position measurements were obtained through a 2880 pulses per revolution (resolution of $\frac{2\pi}{2880}$ radians) line encoder.

TABLE I

INDUCTION MOTOR PARAMETERS

| | |
|---|---|
| $M$ | 0.225 H |
| $L_r$ | 0.244 H |
| $L_s$ | 0.244 H |
| $R_r$ | 2.1 Ω |
| $R_s$ | 1.85 Ω |
| $J$ | 0.0185 N-m-s$^2$ |
| $f$ | 0.0 N-m/rad/sec |

Fig. 2 shows the magnetization curve of the induction motor which was determined by Novotnak [3].

In the experiment, a point-to-point position move was carried out in which the motor was accelerated from the rest to a speed of 170 radians per second in 0.486 seconds and decelerated from 170 radians per second to 0 radians per second in 0.449 seconds. This type of mechanical trajectory was chosen since it requires 90% of the maximum positive torque achievable by the motor used in the experiment under the voltage and current limits [2, 3].That is, the motor must produce close to the maximum torque to accelerate from the rest to 170 radians per second in 0.486 seconds. The magnitude of the reference rotor flux vector was chosen as the solution of (11).

Fig. 3 shows estimated speed $\hat{\omega}$ and reference speed $\omega^*$ (the two are so close that they are indistinguishable in the figure). Fig. 4 is a plot of speed error $\hat{\omega} - \omega^*$. Fig. 5 shows measured position $\theta$ and reference position $\theta^* = \int_0^t \omega^* dt$ ( the two are so close that they are indistinguishable in the figure). Fig. 6 is a plot of position error $\theta - \theta^*$ . Note that in Fig. 6, the final position error is one encoder count ($1\,\text{count} = \frac{2\pi}{2880}$ radians), that is, within the encoder resolution. The position error during the entire move is within $21$ encoder counts. In brief, a close tracking of time-varying speed and position trajectories was achieved.

An input-output linearization controller [2, 3] was also able to provide tracking of the same mechanical trajectory by keeping the final position error at the end of the run within the encoder resolution. But, during the entire run, the position error reached values as high as 64 encoder counts.

To achieve the maximum torque at the beginning of the move, the rotor flux must be at its maximum value [2, 3]. Therefore, the rotor flux was ramped up from zero to its maximum value of $1.1$ Webers before the motor was commanded to move at $t = 0.125$ seconds. Fig. 7 shows the magnitudes of the estimated rotor flux vector and reference rotor flux vector. The rotor flux vector was estimated off-line by solving the following equation:

$$\frac{d\hat{\boldsymbol{\lambda}}_{dq}}{dt} + \left( \frac{R_r M}{L_r} \frac{f_m^{-1}\left(\left|\hat{\boldsymbol{\lambda}}_{dq}\right|\right)}{\left|\hat{\boldsymbol{\lambda}}_{dq}\right|} \right) \hat{\boldsymbol{\lambda}}_{dq} = \left( \frac{R_r M}{L_r} \right) \mathbf{i}_{dq} \qquad (12)$$

where the components of $\mathbf{i}_{dq}$ were collected from the experiment.

## VII. CONCLUSIONS

In this paper, we designed, and also experimentally verified, a current-command passivity-based controller that forces an induction motor which has significant magnetic saturation to track time-varying speed/position and flux trajectories without knowledge of the rotor electrical state variables. Also, we used a speed estimator, which is based on the dynamic model of the induction motor and the position measurements, to remove the need of measuring the motor speed.

## ACKNOWLEDGMENT

The same experimental setup as in [2, 3] was used. Dr. R. T. Novotnak of Aerotech Inc. is thanked for his continuous help and suggestions.

Finally, this work was supported in part by the Office of Naval Research under Grant N00014-96-1-0926.

[illegible] for Saturated Induction Motors

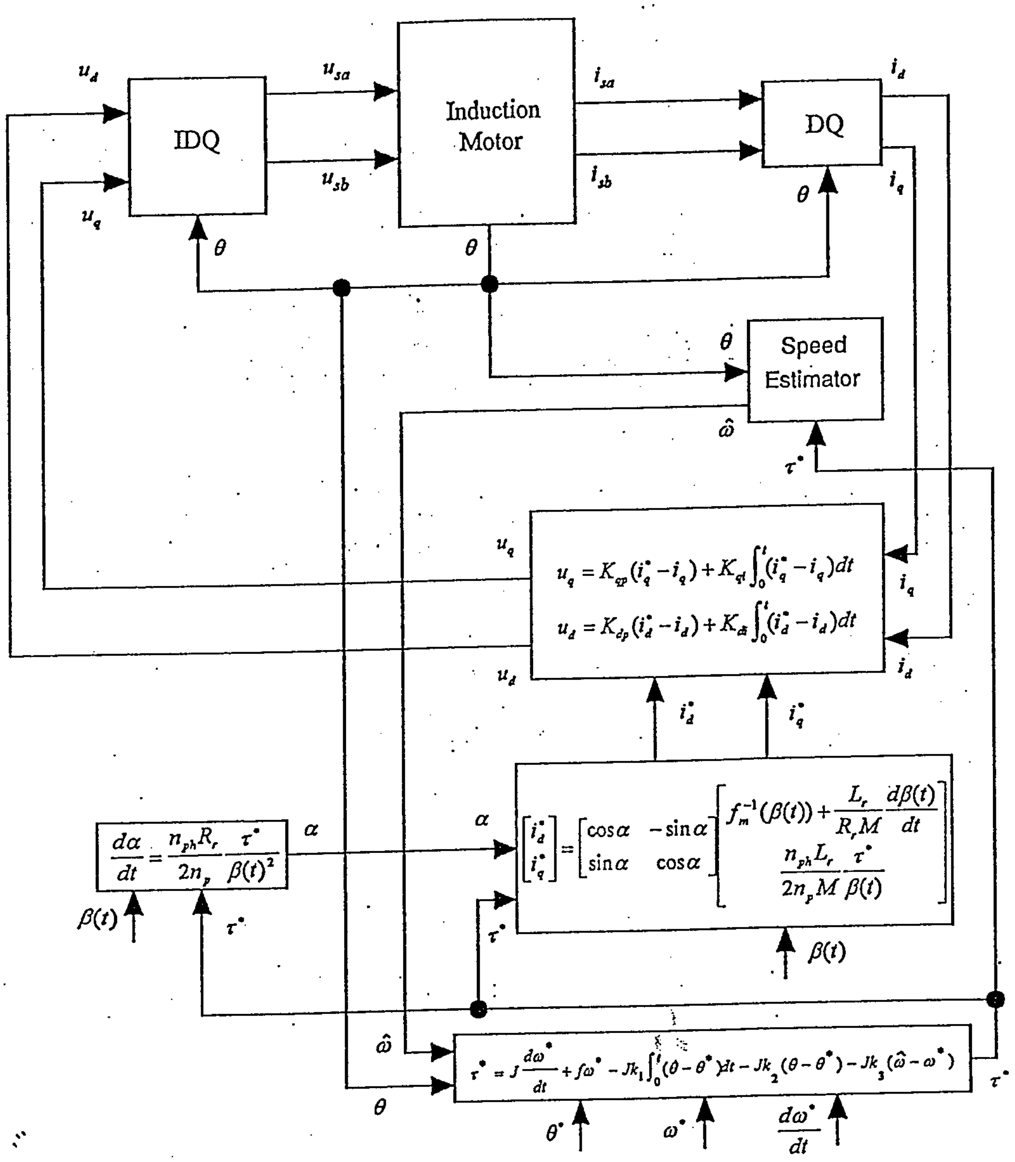
$u_d$
$u_{sa}$
IDQ
Induction Motor
$i_{sa}$
DQ
$i_d$
$u_q$
$u_{sb}$
$i_{sb}$
$\theta$
$i_q$
$\theta$
$\theta$
$\theta$
Speed Estimator
$\hat{\omega}$
$\tau^*$
$u_q$
$u_q = K_{qp}(i_q^* - i_q) + K_{qi}\int_0^t (i_q^* - i_q)dt$
$u_d = K_{dp}(i_d^* - i_d) + K_{di}\int_0^t (i_d^* - i_d)dt$
$i_q$
$u_d$
$i_d$
$i_d^*$
$i_q^*$
$\frac{d\alpha}{dt} = \frac{n_{ph}R_r}{2n_p}\frac{\tau^*}{\beta(t)^2}$
$\alpha$
$\alpha$
$\begin{bmatrix} i_d^* \\ i_q^* \end{bmatrix} = \begin{bmatrix} \cos\alpha & -\sin\alpha \\ \sin\alpha & \cos\alpha \end{bmatrix} \begin{bmatrix} f_m^{-1}(\beta(t)) + \frac{L_r}{R_r M}\frac{d\beta(t)}{dt} \\ \frac{n_{ph}L_r}{2n_p M}\frac{\tau^*}{\beta(t)} \end{bmatrix}$
$\beta(t)$
$\tau^*$
$\tau^*$
$\beta(t)$
$\hat{\omega}$
$\tau^* = J\frac{d\omega^*}{dt} + f\omega^* - Jk_1\int_0^t(\theta - \theta^*)dt - Jk_2(\theta - \theta^*) - Jk_3(\hat{\omega} - \omega^*)$
$\tau^*$
$\theta$
$\theta^*$
$\omega^*$
$\frac{d\omega^*}{dt}$

Fig. 1. Block diagram for the current-command passivity-based control of the induction motor.

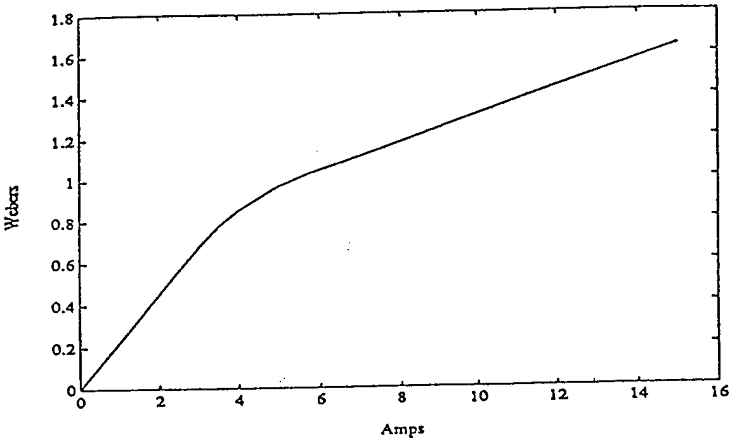

Fig. 2. Magnetization curve of the induction motor.

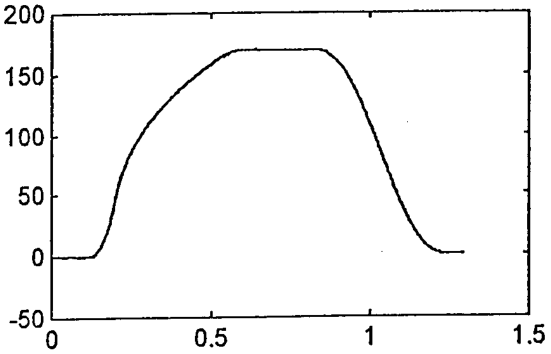

Fig. 3. Estimated (solid) and reference (dashed) speeds in radians per second versus time in seconds.

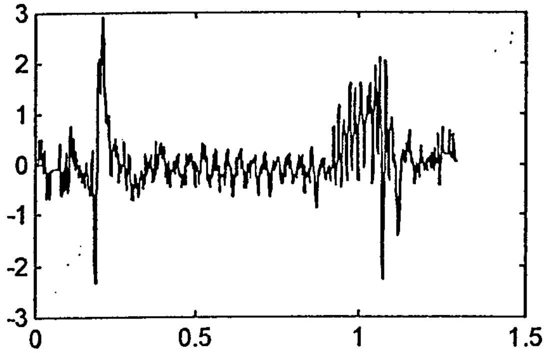

Fig. 4. Speed error in radians per second versus time in seconds.

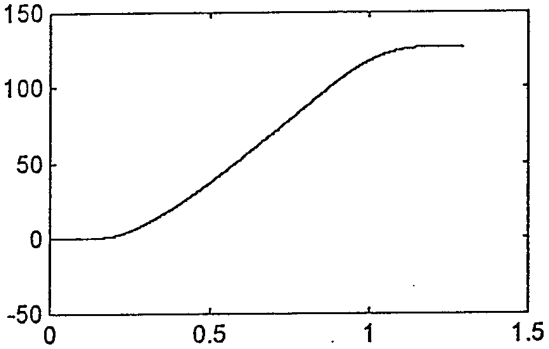

Fig. 5. Measured (solid) and reference (dashed) positions in radians versus time in seconds.

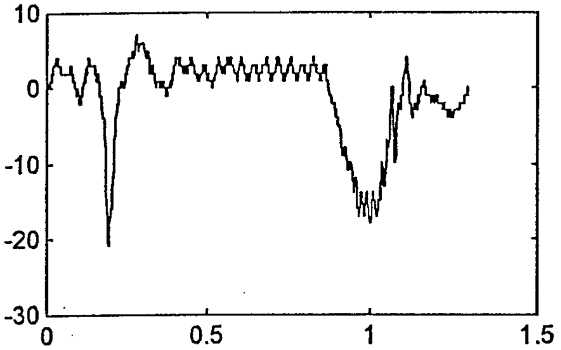

Fig. 6. Position error in encoder counts versus time in seconds (1 count = $2\pi / 2880$ radians).

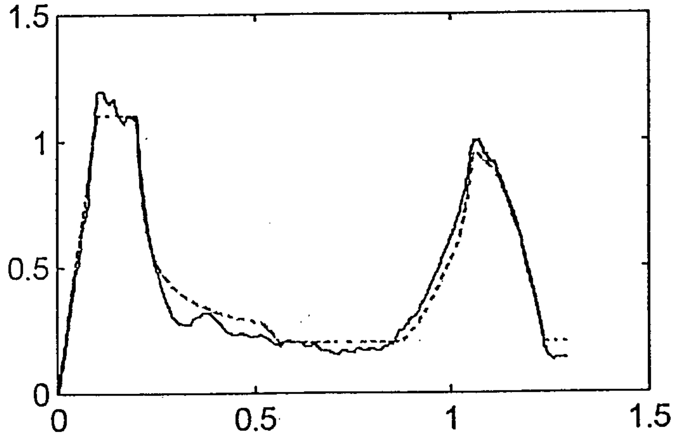

Fig. 7. $|\hat{\lambda}_{dq}|$ (solid) and $|\lambda^{*}_{dq}|$ (dashed) in Webers versus time in seconds.

# REFERENCES

[1] M. Bodson, J. N. Chiasson, and R. T. Novotnak, "A systematic approach to selecting flux references for torque maximization in induction motors," *IEEE Trans. Control Systems Technology*, vol. 3, pp. 388-397, December 1995.

[2] R. T. Novotnak, J. Chiasson, and M. Bodson, "High performance motion control of an induction motor with magnetic saturation," in *Proceedings of the 34th IEEE Conference on Decision & Control*, pp. 2145-2150, December 1995, New Orleans, LA.

[3] R. T. Novotnak, "Nonlinear control of an induction motor by input/output linearization: Theory and experiment," Ph.D. thesis, University of Pittsburgh, 1995.

[4] G. Espinosa and R. Ortega, "State observers are unnecessary for induction motor control," *Systems and Control Letters*, vol. 23, pp. 315-323, 1994.

[5] R. Ortega, P. J. Nicklasson, and G. Espinosa, "On speed control of induction motors," *Automatica*, vol. 32, pp. 455-460, March 1996.

[6] G. Espinosa, P. J. Nicklasson, and R. Ortega, "Control of induction motors in the field weakening region," in *Proceedings of the 34th IEEE Conference on Decision & Control*, pp. 2151-2152, December 1995, New Orleans, LA.

[7] A. Nabae, K. Otsuka, H. Uchino, and R. Kurosawa, "An approach to flux control of induction motors operated with variable-frequency power supply," *IEEE Trans. Industry Applications*, vol. 16, pp. 342-349, May/June 1980.

[8] E. Levi, S. Vukosavic, and V. Vuckovic, “Saturation compansation schemes for vector controlled induction motor drives,” in *Proceedings of the IEEE Power Electronics Specialists Conference*, pp. 591-598, June1990, San Antonio, TX.

[9] G. Heinemann and W. Leonhard, “Self-tuning field-oriented control of an induction motor drive, in *Proceedings of the International Power Electronics Conference*, pp. 465-472, April 1990, Tokyo, Japan.

[10] C. R. Sullivan and S. R. Sanders, “Modeling the effects of magnetic saturation on electrical machine control systems,” in *Proceedings of the IFAC Nonlinear Control System Design Symposium*, pp. 136-143, June 1992, Bordeaux, France.

[11] C. R. Sullivan, C. Kao, B. M. Acker and S. R. Sanders, “Control systems for induction machines with magnetic saturation,” *IEEE Trans. Industrial Electronics*, vol. 43, pp. 142-152, February 1996.

[12] W. Leonhard, *Control of Electrical Drives*. New York: Springer-Verlag, 1985.

[13] R. D. Lorenz and K. W. Patten, “High-resolution velocity estimation for all-digital, ac servo drives,” *IEEE Trans. Industry Applications*, vol. 27, pp.701-705, July/August 1991.

[14] M. Bodson, J. Chiasson, and R. Novotnak, “Nonlinear speed observer for high-performance induction motor control,” *IEEE Trans. Industrial Electronics*, vol. 47, pp.337-343, August 1995.

Submitted to IEEE Transactions on Industrial Electr

# Incorporation of Magnetic Saturation Effects into Passivity-Based Control of Induction Motors

Levent U. Gökdere[†§], M. A. Simaan[‡] and C. W. Brice[†]

[†]Department of Electrical & Computer Engineering
University of South Carolina
Swearingen 3A80
Columbia, SC 29208

[‡]Department of Electrical Engineering
University of Pittsburgh
Pittsburgh, PA 15261

## ABSTRACT

It is well known that saturation of the magnetic material will cause deterioration in the trajectory tracking performance of the controllers based on the linear (nonsaturated) magnetic model of the induction motor. In this paper, we design a passivity-based controller taking into account saturation of the magnetic material in the main flux path of the induction motor to provide precise tracking of time-varying speed, position and flux trajectories. The proposed controller does not require knowledge of the rotor electrical state variables (i.e., rotor fluxes or currents). As a result, there is no need for a sensor (or state estimator) to measure (or compute) the rotor electrical state variables. Experimental results show that the passivity-based controller provides close tracking of time-varying speed, position and flux trajectories without knowledge of the rotor electrical state variables.

*Key words*: Induction motor, magnetic saturation, passivity-based control.

---

[§] Corresponding author. Tel: (803) 777-9314; Fax: (803) 777-8045; E-mail: gokdere@ece.sc.edu.

## LIST OF FIGURES

1 The block diagram for the current-command passivity-based control of the induction motor. .......... 7

2 Magnetization curve of the induction motor. .......... 8

3 Estimated (solid) and reference (dashed) speeds in radians per second versus time in seconds. .......... 13

4 Speed error in radians per second versus time in seconds. .......... 13

5 Measured (solid) and reference (dashed) positions in radians versus time in seconds. .......... 14

6 Position error in encoder counts (1 count = $2\pi / 2880$ radians) versus time in seconds. .......... 14

7 $\left|\hat{\lambda}_{dq}\right|$ (solid) and $\left|\lambda^*_{dq}\right|$ (dashed) in Webers versus time in seconds. .......... 15

8 $i_d$ (solid) and $i_d^*$ (dashed) in Amperes versus time in seconds. .......... 15

9 $i_q$ (solid) and $i_q^*$ (dashed) in Amperes versus time in seconds. .......... 16

10 Speed error in radians per second versus time in seconds (linear magnetics). .......... 16

11 Position error in encoder counts (1 count = $2\pi / 2880$ radians) versus time in seconds (linear magnetics). .......... 17

12 $\left|\hat{\lambda}_{dq}\right|$ (solid) and $\left|\lambda^*_{dq}\right|$ (dashed) in Webers versus time in seconds (linear magnetics). .......... 17

# I. INTRODUCTION

Control algorithms for induction motors are usually developed assuming that saturation does not occur in the magnetic material making up the flux paths. However, in practice, saturation does occur very frequently with a significant impact on the motor dynamics. Thus, the effects of saturation have to be taken into account if applications require precise speed and position tracking control.

Heinemann *et al.*[1], Levi *et al.*[2] and Sullivan *et al.*[3, 4] have developed field-oriented controllers based on saturated magnetic models of the induction motor. An input-output linearization controller, which takes into account the saturation effects, was designed by Novotnak *et al.*[5, 6].

In [1, 5, 6], saturation is assumed to be entirely in the main flux path of the induction motor. That is, the change in the mutual inductance due to saturation in the magnetic material is considered and the changes in the stator and rotor leakage factors are neglected. In this paper, using the same approach, we design, and also experimentally verify, a passivity-based controller that provides precise tracking of time-varying speed, position and flux trajectories even if the motor is operated in magnetic saturation regions. The proposed controller does not require knowledge of the rotor electrical state variables (i.e., rotor fluxes or currents). As a result, there is no need for a sensor (or state estimator) to measure (or compute) the rotor electrical state variables.

The work in this paper is an extension of the work [7] in which, following Ortega *et al.*[8,9,10], Gökdere *et al.* [7] designed, and also experimentally verified, a passivity-based controller under the assumption of linear (nonsaturated) magnetics.

## II. A CURRENT-COMMAND *d-q* MODEL of INDUCTION MOTOR

Consider a general *d-q* (direct-quadrature) reference frame whose angular position with respect to the fixed stator reference frame is $\phi$ where $\phi$ is an arbitrary angle. In this reference frame, a current-command *d-q* model of the induction motor can be given by

$$\frac{d\boldsymbol{\lambda}_{\mathrm{dq}}}{dt} + \omega_s \mathbf{J} \boldsymbol{\lambda}_{\mathrm{dq}} + \frac{R_r}{L_r} \boldsymbol{\lambda}_{\mathrm{dq}} = \frac{R_r M}{L_r} \mathbf{i}^*_{\mathrm{dq}} \tag{1}$$

$$J \frac{d\omega}{dt} = \tau - f\omega \tag{2}$$

$$\frac{d\theta}{dt} = \omega \tag{3}$$

where $\boldsymbol{\lambda}_{\mathrm{dq}}$ is the rotor flux vector, $\mathbf{i}^*_{\mathrm{dq}}$ is the reference stator current vector, $\mathbf{J}$ is the two by two skew-symmetric matrix, $\omega_s$ is the slip frequency, $\omega$ is the motor angular speed, $\theta$ is the motor angular position, $\tau$ is the electrical torque (the torque produced by the motor), $R_r$ is the rotor resistance, $L_r$ is the rotor inductance, $M$ is the mutual inductance, $J$ is the rotor moment of inertia and $f$ is the viscous friction coefficient [7]. The slip frequency and electrical torque are given by

$$\omega_s \overset{\Delta}{=} \frac{d\phi}{dt} - n_p \omega \tag{4}$$

and

$$\tau = -\frac{2n_p M}{n_{ph} L_r} \boldsymbol{\lambda}_{\mathbf{dq}}^T \mathbf{J} \mathbf{i}_{\mathbf{dq}}^* \tag{5}$$

where $n_p$ is the number of pole pairs, $n_{ph}$ is the number of phases and $\boldsymbol{\lambda}_{\mathbf{dq}}^T$ is the transpose of $\boldsymbol{\lambda}_{\mathbf{dq}}$.

Because angle $\phi$ is arbitrary, the definition of slip frequency (4) is not the definition normally used for induction motor.

## III. A CURRENT-COMMAND PASSIVITY-BASED CONTROLLER for INDUCTION MOTORS

In the current-command passivity-based control of induction motors, both $\mathbf{i}_{\mathbf{dq}}^*$ and $\phi$ are considered as the control inputs. Specifically, $\mathbf{i}_{\mathbf{dq}}^*$ is given by

$$\mathbf{i}_{\mathbf{dq}}^* \overset{\Delta}{=} \begin{bmatrix} \frac{\lambda_d^*}{M} + \frac{L_r}{R_r M} \frac{d\lambda_d^*}{dt} \\ \\ \frac{n_{ph} L_r}{2n_p M} \frac{\tau^*}{\lambda_d^*} \end{bmatrix} \tag{6}$$

and $\phi$ is chosen as the solution of

$$\frac{d\phi}{dt} = \frac{n_{ph} R_r}{2n_p} \frac{\tau^*}{\lambda_d^{*2}} + n_p \omega \tag{7}$$

where $\tau^*$ is the reference torque and $\lambda_d^*$ is the $d$ component of the reference rotor flux vector [7] (see also [8, 9, 10] for more information about passivity-based control of induction motors). The reference torque is given by

$$\tau^* = J\frac{d\omega^*}{dt} + f\omega^* - Jk_1\int_0^t\left(\theta-\theta^*\right)dt - Jk_2\left(\theta-\theta^*\right) - Jk_3(\omega-\omega^*) \qquad (8)$$

where $\theta^*$ and $\omega^* = \frac{d\theta^*}{dt}$ are the reference position and reference speed, respectively. Feedback gains $k_1$, $k_2$ and $k_3$ are positive constants.

In the current-command passivity-based control of induction motors, exponential tracking of time-varying speed, position and flux trajectories is achieved.

## IV. INCORPORATION of MAGNETIC SATURATION EFFECTS into PASSIVITY-BASED CONTROLLER

In [1, 5, 6], saturation is incorporated assuming that it is entirely in the main flux path of the induction motor. That is, the change in the mutual inductance due to saturation of the magnetic material is considered and the changes in the stator and rotor leakage factors are neglected.

Using the approach in [1, 5, 6], we can then rearrange reference stator current vector (6) as

$$\mathbf{i}_{\mathrm{dq}}^* \overset{\Delta}{=} \begin{bmatrix} f_m^{-1}(\lambda_d^*) + \frac{L_r}{R_r M}\frac{d\lambda_d^*}{dt} \\ \\ \frac{n_{ph} L_r}{2n_p M}\frac{\tau^*}{\lambda_d^*} \end{bmatrix} \qquad (9)$$

where $f_m^{-1}(\cdot)$ is the inverse of the magnetization curve function of the induction motor. In (9), the nominal values of $L_r$ and $M$ are used. This is reasonable since $\frac{L_r}{M} = (1+\sigma_r)$, where $\sigma_r$ is the rotor leakage factor [11], and the change in $\sigma_r$ due to saturation is neglected. For the values of $\lambda_d^*$ which remain in the linear magnetic region, $f_m^{-1}(\lambda_d^*) = \frac{\lambda_d^*}{M}$ with $M$ constant so that (9) reduces to (6).

## V. SPEED ESTIMATOR

The passivity-based technique requires the knowledge of the speed and position to achieve speed and position tracking control. In a typical experimental setup, only position measurements are available and hence, a speed estimator must be implemented in real-time to compute the speed. Following Lorenz *et al.* [12], Bodson *et al.* [13] introduced a speed estimator based on the dynamic model of the induction motors. However, the speed estimator in [13] uses the estimated value of the rotor flux. To remove the need of estimating the rotor flux, Gökdere *et al.*[7] modified the speed estimator in [13] as following:

$$\frac{d\hat{\theta}}{dt} = \hat{\omega} + l_1\left(\theta - \hat{\theta}\right) \tag{10}$$

$$\frac{d\hat{\omega}}{dt} = \mu\lambda_d^* i_q - \frac{f}{J}\hat{\omega} + l_2\left(\theta - \hat{\theta}\right) \tag{11}$$

In (10) and (11), $\hat{\omega}$ is the estimate of the speed, $\hat{\theta}$ is the estimate of the position, $l_1$, $l_2$ are the estimator gains and $\mu \overset{\Delta}{=} \frac{2\mathrm{n_p} M}{n_{ph} J L_r}$.

Gökdere *et al.*[7] have experimentally shown that speed estimator (10)-(11) works well for the passivity-based control of induction motor.

The block diagram for the current-command passivity-based control of the induction motor is shown in Figure 1.

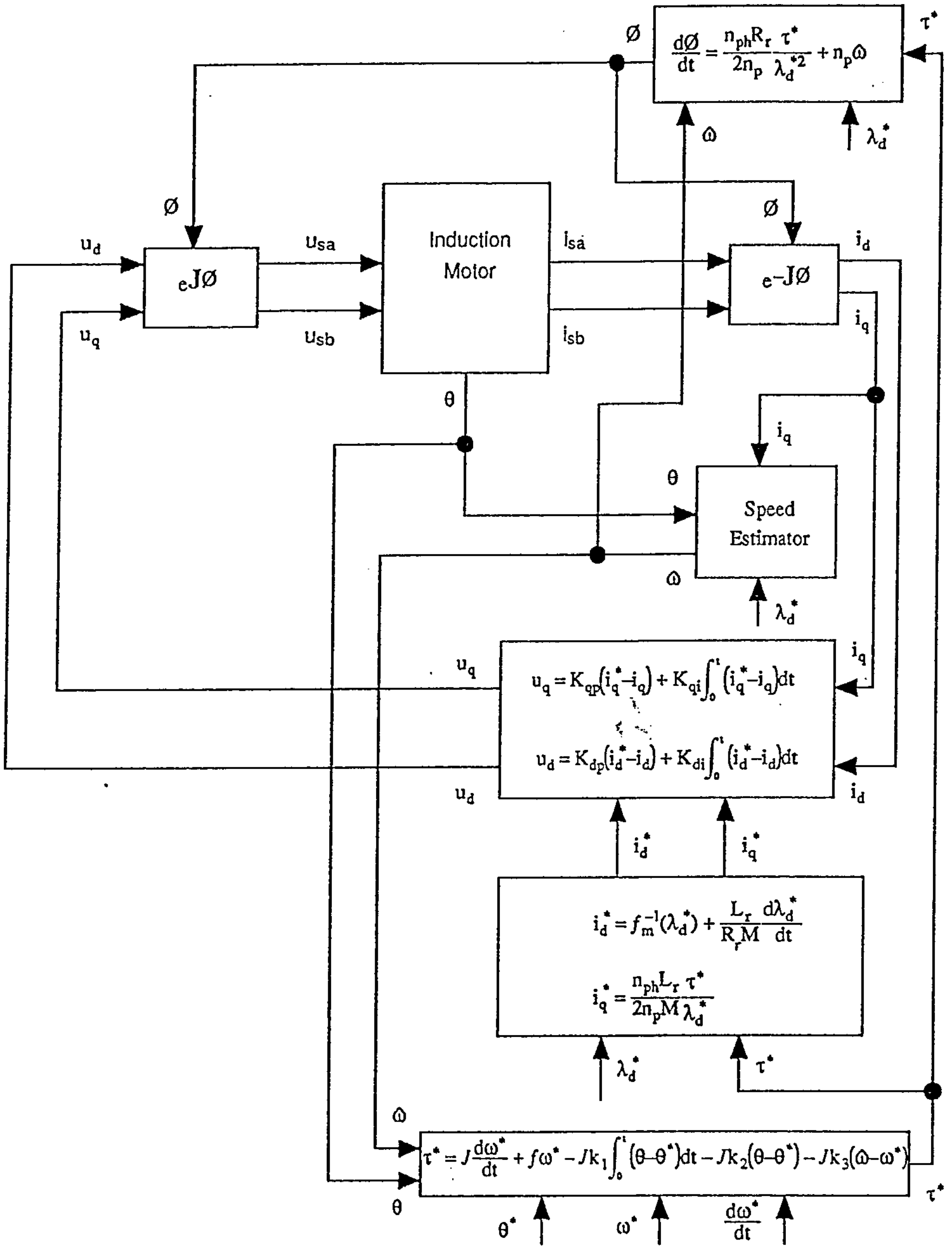

$\emptyset$
$\frac{d\emptyset}{dt} = \frac{n_{ph}R_r}{2n_p}\frac{\tau^*}{\lambda_d^{*2}} + n_p\hat{\omega}$
$\tau^*$
$\hat{\omega}$
$\lambda_d^*$
$\emptyset$
$\emptyset$
$u_d$
$u_q$
$eJ\emptyset$
usa
usb
Induction Motor
isa
isb
$e^{-J\emptyset}$
$i_d$
$i_q$
$\theta$
$i_q$
$\theta$
Speed Estimator
$\hat{\omega}$
$\lambda_d^*$
$u_q$
$i_q$
$u_q = K_{qp}(i_q^* - i_q) + K_{qi}\int_0^t (i_q^* - i_q)dt$
$u_d = K_{dp}(i_d^* - i_d) + K_{di}\int_0^t (i_d^* - i_d)dt$
$u_d$
$i_d$
$i_d^*$
$i_q^*$
$i_d^* = f_m^{-1}(\lambda_d^*) + \frac{L_r}{R_r M}\frac{d\lambda_d^*}{dt}$
$i_q^* = \frac{n_{ph}L_r}{2n_p M}\frac{\tau^*}{\lambda_d^*}$
$\lambda_d^*$
$\tau^*$
$\hat{\omega}$
$\tau^* = J\frac{d\omega^*}{dt} + f\omega^* - Jk_1\int_0^t (\theta - \theta^*)dt - Jk_2(\theta - \theta^*) - Jk_3(\hat{\omega} - \omega^*)$
$\theta$
$\tau^*$
$\theta^*$
$\omega^*$
$\frac{d\omega^*}{dt}$

Fig. 1. The block diagram for the current-command passivity-based control of the induction motor.

# VI. EXPERIMENTAL RESULTS

The passivity-based controller (9) was tested on an experimental setup which consisted of (i) a 3-phase, 6-pole, 1-Hp, squirrel cage induction motor, (ii) a Motorola DSP96002 (floating point processor) ADS system, (iii) a data acquisition board, and (iv) three 20 kHz PWM amplifiers (± 150 Volts and ± 10 Amps). The position measurements were obtained through a 2880 pulses/revolution (resolution of 360°/2880=.125°) line encoder. The induction motor parameters are $M = 0.225$ H, $L_r = 0.244$ H, $L_s = 0.244$ H, $R_r = 2.1\ \Omega$, $R_s = 1.85\ \Omega$, $f = 0.0$ N-m/radians/second, and $J = .0185$ N-m-s$^2$. Fig. 2 shows the magnetization curve of the induction motor which was determined experimentally by Novotnak [6].

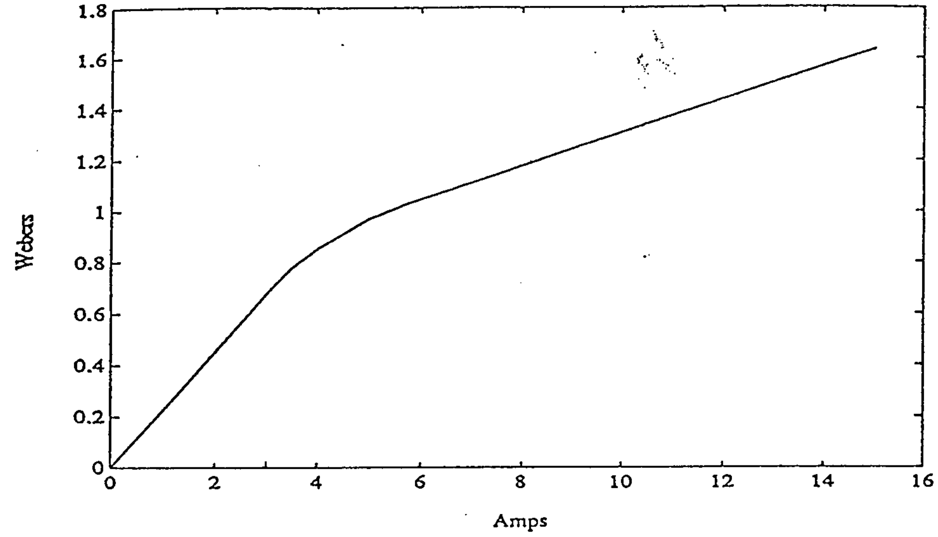

Fig. 2. Magnetization curve of the induction motor.

In the experiment, a point-to-point move was carried out in which the motor was accelerated to a speed of 170 radians/second in 0.486 seconds and decelerated from 170 radians/second to 0 radians/second in 0.449 seconds. This type of mechanical trajectory was chosen since it requires 90% of the maximum positive torque achievable by the motor under the voltage and current constraints [5, 6]. That is, the motor must produce close to the maximum torque to accelerate from 0 to 170 radians/second. The magnitude of the flux reference was chosen as the solution to

$$\frac{d\lambda_d^*}{dt} = \frac{R_r M}{L_r}\left( - f_m^{-1}(\lambda_d^*) + \frac{1}{\mu\delta_{sopt}(\omega^*)\lambda_d^*}\frac{d\omega^*}{dt}\right)$$

where $\delta_{sopt}(\omega^*)$ is the solution to the saturated magnetics optimal torque problem [5, 6].

The PI current-command gains were set as $K_{dp} = 150.0$, $K_{di} = 1500.0$ and $K_{qp} = 110.0$, $K_{qi} = 2500.0$. The PID gains for the speed and position tracking errors were chosen to be $k_1 = 0.0$, $k_2 = 10200.0$, and $k_3 = 120.0$. The speed estimator gains were $l_1 = 4000$ and $l_2 = 400000$. The sample rate was 2.5 kHz.

Figures 3 - 9 show the results. Figure 3 is the plots of estimated speed $\hat{\omega}$ and reference speed $\omega^*$ (the two are so close that they are indistinguishable in this figure). Speed was estimated using estimator (10)-(11). Speed tracking error $\hat{\omega} - \omega^*$ is given in Figure 4. Figure 5 shows measured position $\theta$ and reference position $\theta^* = \int_0^t \omega^* dt$ (again, the two are so close that they are indistinguishable in the figure). Position tracking error $\theta - \theta^*$ is given in Figure 6. Note that in Figure 6, the final position error is one encoder count (1 count = $2\pi / 2880$ radians), that is, within the encoder resolution. The position error during the entire run is within 17 encoder counts. In brief, a close tracking of the time-varying speed and position trajectories was achieved.

An input-output linearization controller [5, 6] was also able to provide tracking of the same mechanical trajectory by keeping the final position error at the end of the run within the encoder resolution. But, during the entire run, the position error reached values as high as 64 encoder counts.

To achieve the maximum torque at the beginning of the move, the flux must be at its maximum value [5, 6]. Therefor, the flux was ramped up from zero to its maximum value of 1.1 Webers before the motor was commanded to move at $t$=0.125 seconds. Fig. 7 shows the magnitudes of estimated rotor flux vector $\hat{\lambda}_{dq}$ and reference rotor flux vector $\lambda^*_{dq}$. The rotor flux vector was estimated off-line by solving the following equation:

$$\frac{d}{dt}\begin{bmatrix}\hat{\lambda}_d \\ \hat{\lambda}_q\end{bmatrix} + \omega_s \mathbf{J}\begin{bmatrix}\hat{\lambda}_d \\ \hat{\lambda}_q\end{bmatrix} + \frac{R_r M}{L_r}\frac{f_m^{-1}(\sqrt{\hat{\lambda}_d^2 + \hat{\lambda}_q^2})}{\sqrt{\hat{\lambda}_d^2 + \hat{\lambda}_q^2}}\begin{bmatrix}\hat{\lambda}_d \\ \hat{\lambda}_q\end{bmatrix} = \frac{R_r M}{L_r}\begin{bmatrix}i_d \\ i_q\end{bmatrix} \tag{12}$$

where $\omega_s = \frac{n_{ph} R_r}{2n_p}\frac{\tau^*}{\lambda_d^{*2}} = \frac{R_r M}{L_r}\frac{i_q^*}{\lambda_d^*}$. The values of $i_d$, $i_q$ and $i_q^*$ were collected from the experiment.

In Fig. 7, the small perturbations around the reference value of the flux are due to the tracking performance of the current loops [7]. That is, the perturbations occur since the stator currents can not track exactly their corresponding references ( see Figures 8 and 9).

For comparison purposes, passivity-based controller (6), which is based on the linear magnetic model, was also implemented to control the same motor along the same mechanical trajectory. The magnitude of the flux reference was chosen as the solution of differential equation

$$\frac{d\lambda_d^*}{dt} = -\frac{R_r}{L_r}\lambda_d^* + \frac{R_r M}{\mu L_r \delta_{lopt}(\omega^*)\lambda_d^*}\frac{d\omega^*}{dt}$$

where $\delta_{lopt}(\omega^*)$ is the solution to the linear magnetics optimal torque problem [14].

The PI current-command gains were set as $K_{dp} = 150.0$, $K_{di} = 1500.0$ and $K_{qp} = 110.0$, $K_{qi} = 2500.0$. The PID gains for the speed and position tracking errors were chosen to be $k_1 = 0.0$, $k_2 = 10200.0$, and $k_3 = 120.0$. The speed estimator gains were $l_1 = 4000$ and $l_2 = 400000$. The sample rate was 2.5 kHz.

Figures 10 - 12 show the results with the controller based on the linear magnetic model. Figure 10 is a plot of the speed tracking error. The position tracking error is given in Figure 11. Note that in Figure 11, the final position error is one encoder count. Moreover, the position error during the entire run is within 23 encoder counts. In brief, a close tracking was achieved even though the controller was based on the linear magnetic model.

An input-output linearization controller based on the linear magnetic model was not able to provide tracking of the same mechanical trajectory [5, 6]. The reason for this is that the input-output linearization technique relies on an estimate of the rotor flux and an estimator based on the linear magnetic model gives an incorrect value for the flux if saturation occurs in the motor.

Fig. 12 shows the flux tracking performance of passivity-based controller (6). From this figure, it is seen that the controller based on the linear magnetic model fails to increase the flux from zero to the maximum value of 1.32 Webers which is well above the linear magnetic region (see the magnetization curve in Fig. 2). Again, the rotor flux vector was estimated off-line by solving equation (12).

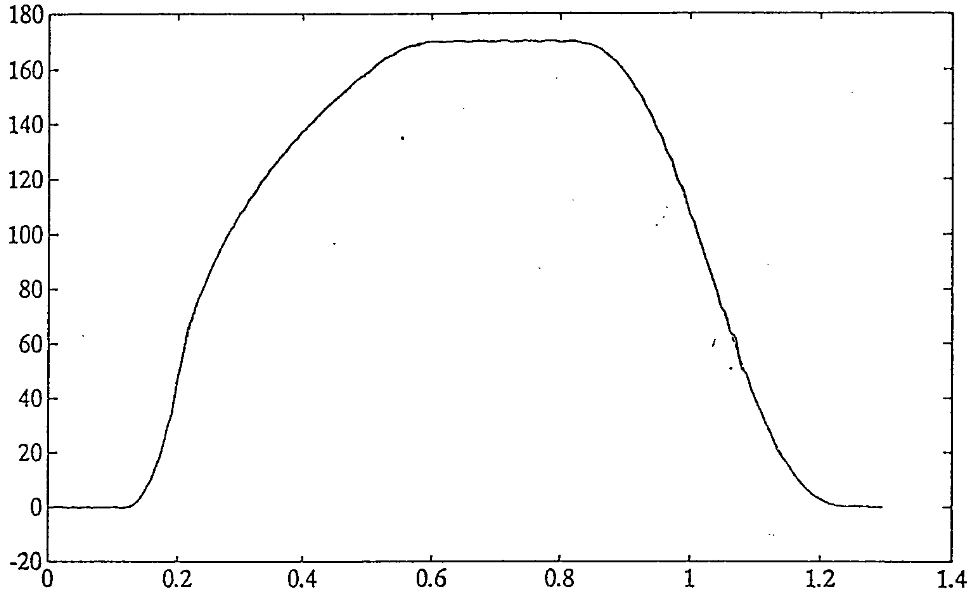

Fig. 3. Estimated (solid) and reference (dashed) speeds in radians per second versus time in seconds.

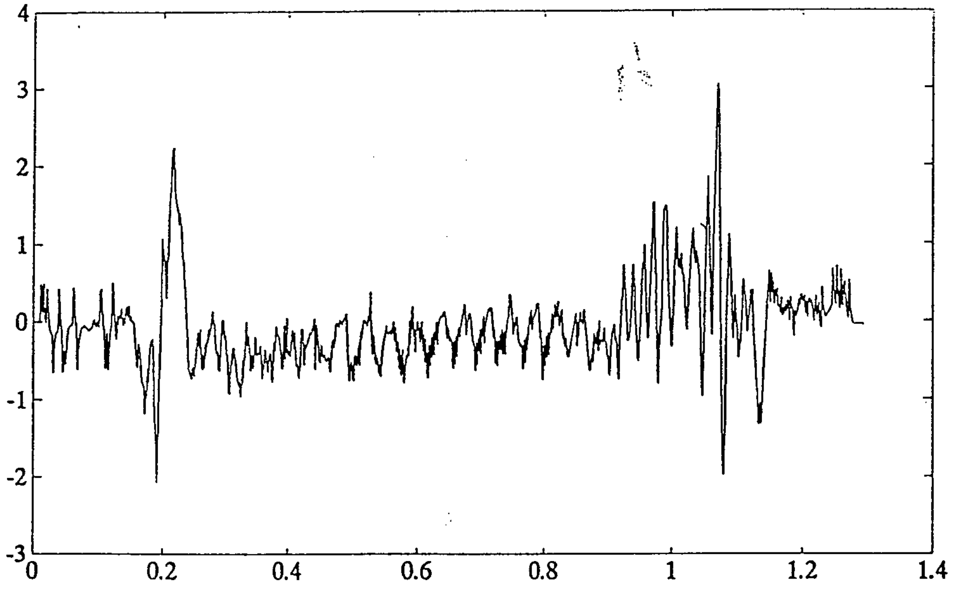

Fig. 4. Speed error in radians per second versus time in seconds.

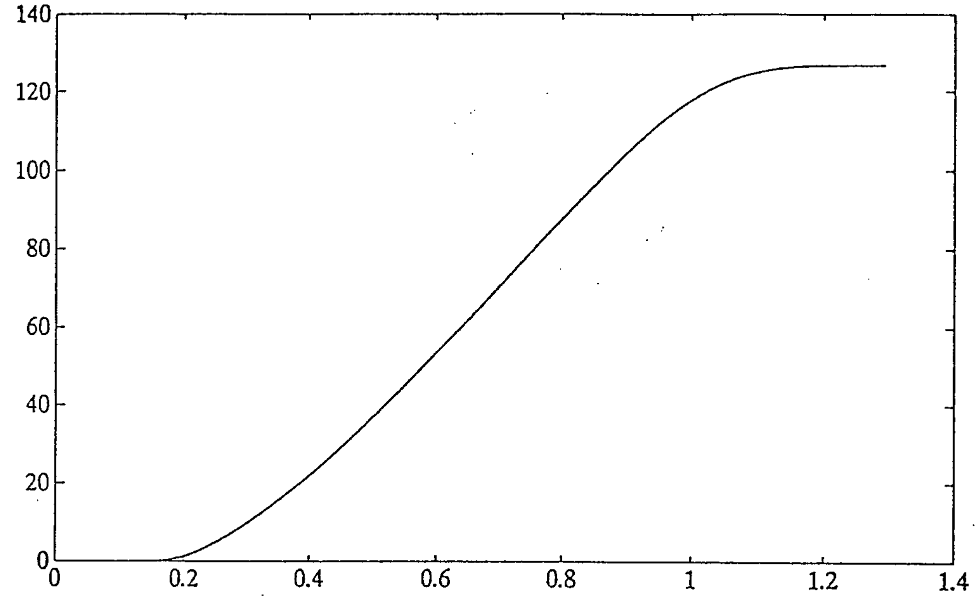

Fig. 5. Measured (solid) and reference (dashed) positions in radians versus time in seconds.

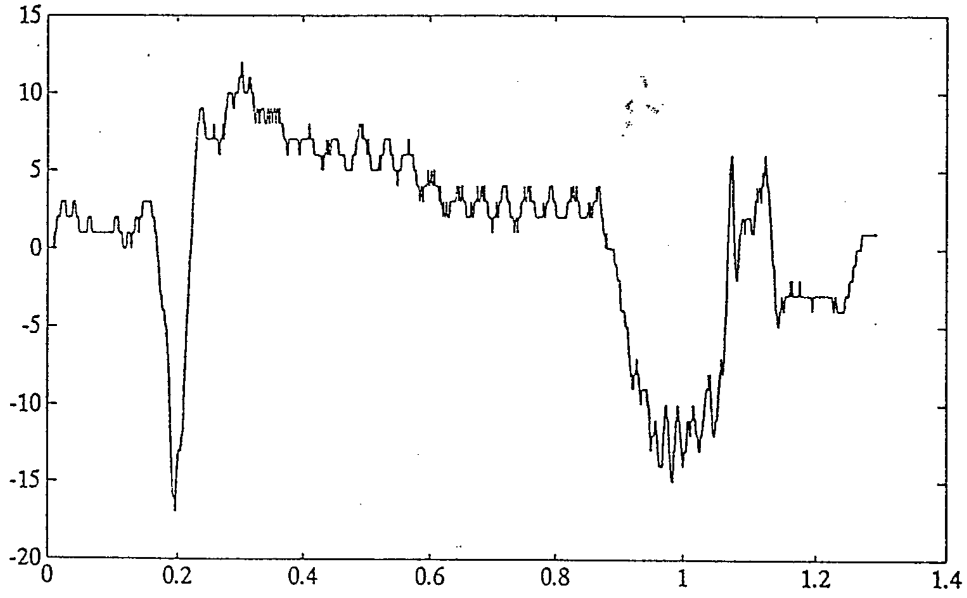

Fig. 6. Position error in encoder counts (1 count = $2\pi/2880$ radians) versus time in seconds.

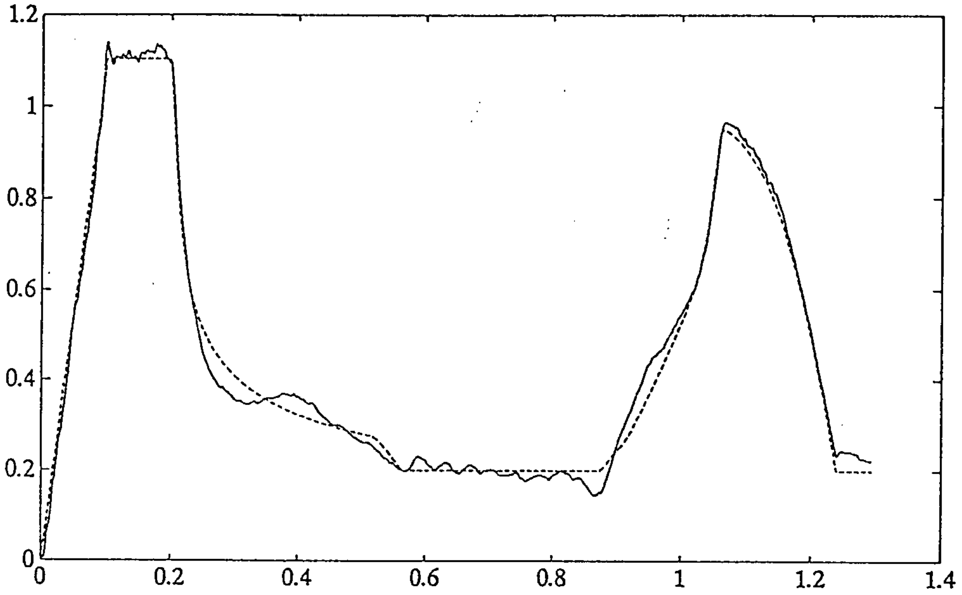

Fig. 7. $\left|\hat{\lambda}_{dq}\right|$ (solid) and $\left|\lambda^{*}_{dq}\right|$ (dashed) in Webers versus time in seconds.

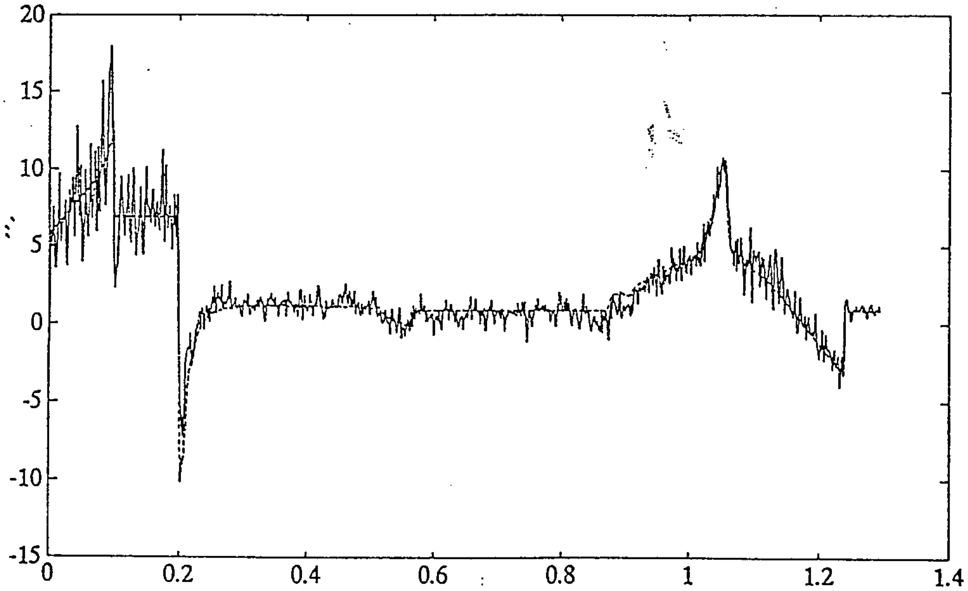

Fig. 8. $i_d$ (solid) and $i_d^*$ (dashed) in Amperes versus time in seconds.

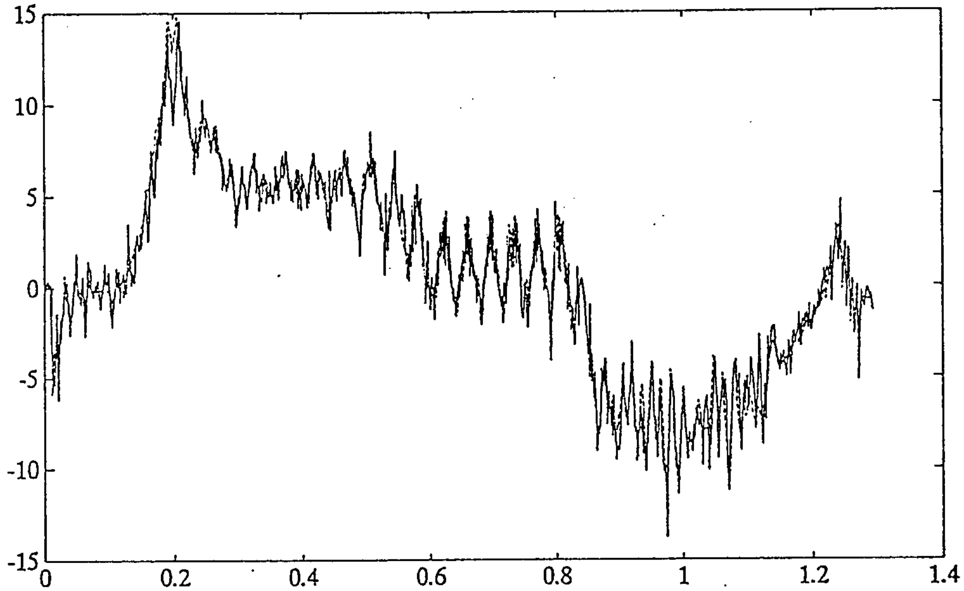

Fig. 9. $i_q$ (solid) and $i_q^*$ (dashed) in Amperes versus time in seconds.

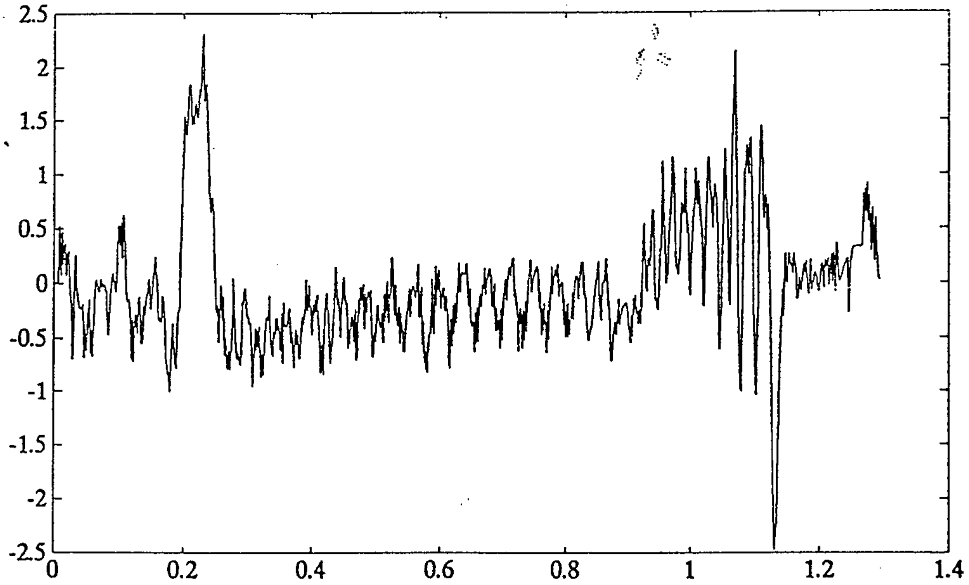

Fig. 10. Speed error in radians per second versus time in seconds (linear magnetics).

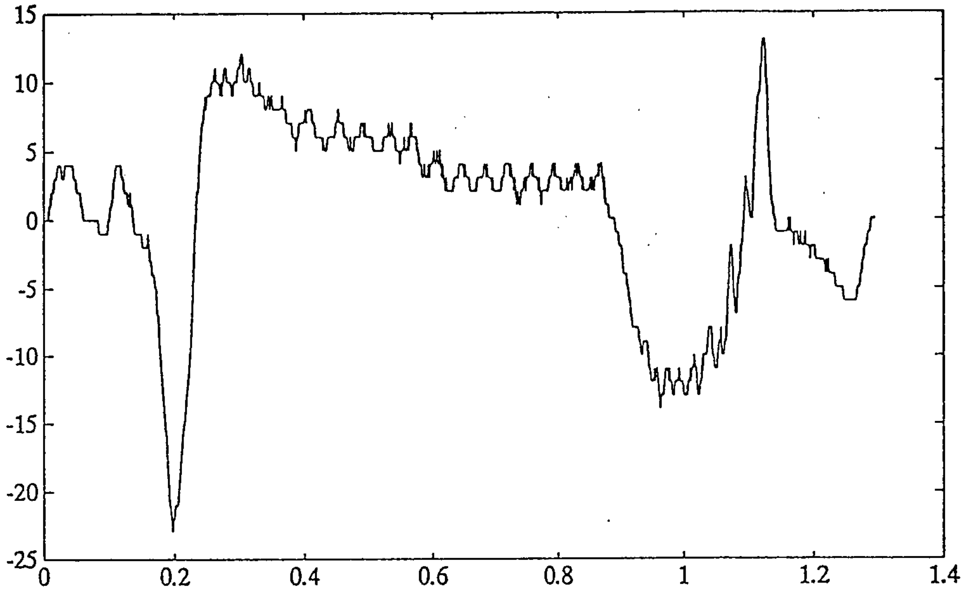

Fig. 11. Position error in encoder counts (1 count = $2\pi / 2880$ radians) versus time in seconds (linear magnetics).

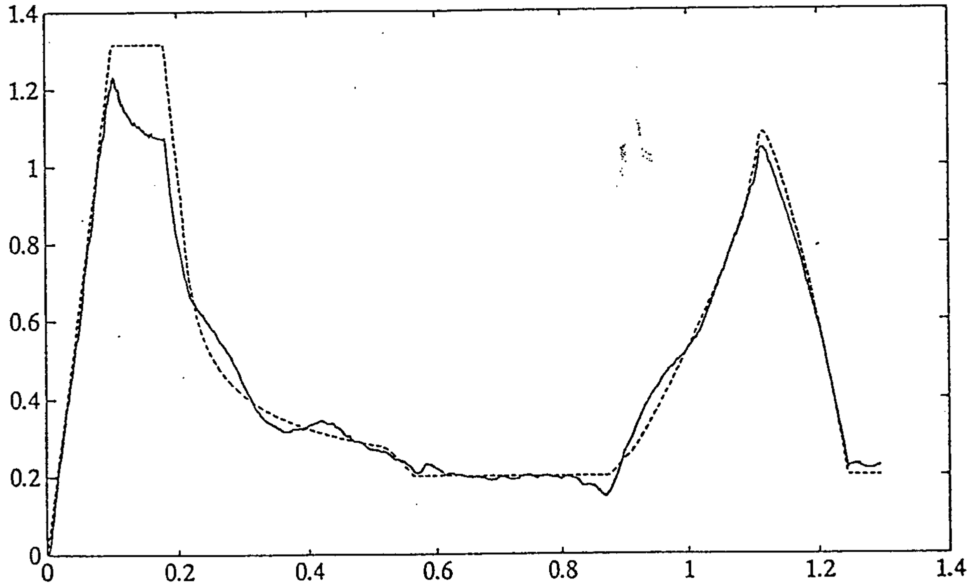

Fig. 12. $\left|\hat{\lambda}_{dq}\right|$ (solid) and $\left|\lambda^*_{dq}\right|$ (dashed) in Webers versus time in seconds (linear magnetics).

## VII. CONCLUSIONS

In this paper, we designed, and also experimentally verified, a current-command passivity-based controller for induction motors which have significant magnetic saturation. The proposed controller provides close tracking of time-varying speed, position and flux trajectories without knowledge of the rotor electrical state variables.

## ACKNOWLEDGEMENT

The experimental setup described in Section VI is the same experimental setup as in [5, 6]. Dr. Robert T. Novotnak of Aerotech Inc. is thanked for his continuous help and suggestions.

The work in this paper was supported in part by the Office of Naval Research under Grant N00014-96-1-0926.

# REFERENCES

[1] G. Heinemann and W. Leonhard, "Self-tuning field-oriented control of an induction motor drive, in *Proceedings of the International Power Electronics Conference*, pp. 465-472, April 1990, Tokyo, Japan.

[2] E. Levi, S. Vukosavic, and V. Vuckovic, "Saturation compansation schemes for vector controlled induction motor drives," in *Proceedings of the IEEE Power Electronics Specialists Conference*, pp. 591-598, June 1990, San Antonio, TX.

[3] C. R. Sullivan and S. R. Sanders, "Modeling the effects of magnetic saturation on electrical machine control systems," in *Proceedings of the IFAC Nonlinear Control System Design Symposium*, pp. 136-143, June 1992, Bordeaux, France.

[4] C. R. Sullivan, C. Kao, B. M. Acker and S. R. Sanders, "Control systems for induction machines with magnetic saturation," *IEEE Trans. Industrial Electronics*, vol. 43, pp. 142-152, February 1996.

[5] R. T. Novotnak, J. Chiasson, and M. Bodson, "High performance motion control of an induction motor with magnetic saturation,: in *Proceedings of the 34th IEEE Conference on Decision & Control*, pp. 2145-2150, December 1995, New Orleans, LA.

[6] R. T. Novotnak, "Nonlinear control of an induction motor by input/output linearization: Theory and experiment," Ph.D. thesis, University of Pittsburgh, 1995.

[7] L. U. Gökdere and M. A. Simaan, "A Passivity-based method for induction motor control," accepted for publication in *IEEE Trans. Industrial Electronics.*

[8] G. Espinosa and R. Ortega, "State observers are unnecessary for induction motor control," *Syst. and Control Letters*, vol. 23, pp. 315-323, 1994.

[9] R. Ortega, P. J. Nicklasson and G. Espinosa, "On speed control of induction motors," *Automatica*, vol. 32, no. 3, pp. 455-460, March 1996.

[10] G. Espinosa, P. J. Nicklasson and R. Ortega, "Control of induction motors in the field weakening region," *IEEE CDC*, New Orleans, LA, 1995.

[11] W. Leonhard, *Control of Electrical Drives*, Springer-Verlag, Berlin, 1985.

[12] R. Lorenz and K. Patten, "High-resolution velocity estimation for all-digital, ac servo drives," *IEEE Transactions on Industry Applications*, vol. 27, no. 4, pp. 701-705, July/August 1991.

[13] M. Bodson, J. Chiasson and R. Novotnak, "Nonlinear speed observer for high-performance induction motor control," *IEEE Transactions on Industrial Electronics*, vol. 47, no. 4, pp. 337-343, August 1995.

[14] M. Bodson, J. Chiasson and R. Novotnak, "A systematic approach to selecting flux references for torque maximization in induction motors," *IEEE Transactions on Control Systems Technology*, vol. 3, no. 4, pp. 388-397, December 1995.

# A Comparison of Passivity-Based and Input-Output Linearization Controllers for Induction Motors

Levent U. Gökdere[†], Marwan A. Simaan[‡] and Charles W. Brice[†]

[†]Department of Electrical & Computer Engineering
University of South Carolina
Swearingen 3A80
Columbia, SC 29208
U.S.A.

[‡]Department of Electrical Engineering
University of Pittsburgh
348 Benedum Hall
Pittsburgh, PA 15261
U.S.A.

*Abstract*— **An experimental and theoretical comparison of passivity-based and input-output linearization controllers for induction motors is presented. The comparison is done taking into account saturation of the magnetic material in the main flux path of the induction motor. Experimental results show that the use of the passivity-based controller results in reduced position tracking errors as compared with the input-output linearization controller.**

## I. INTRODUCTION

The passivity-based [1, 2] and input-output linearization [3, 4, 5] methods are the most recent control methods for induction motors. The current-command passivity-based controller is an indirect (strictly feedforward) field-oriented controller while the current-command input-output linearization controller is a direct field-oriented controller.

The key step with the passivity-based method is the identification of terms, known as *workless forces*, which appear in the dynamic equations of the induction motor but do not have any effect on the energy balance equation of the induction motor [1, 2]. These terms do not influence the stability properties of the induction motor and hence there is no need to cancel them with feedback control. This leads to a simpler control structure and enhances the robustness of the control system.

The input-output linearization method eliminates, in the field-oriented coordinates, the coupling of the rotor flux and speed dynamics [3, 4, 5]. As a result, independent (decoupled) control of the speed and flux is achieved with the input-output linearization method

In this paper, an experimental and theoretical comparison of current-command passivity-based and input-output linearization controllers for induction motors is presented. The comparison is done taking into account the magnetic saturation effects.

## II. PASSIVITY-BASED AND INPUT-OUTPUT LINEARIZATION CONTROLLERS FOR INDUCTION MOTORS

A current-command *d-q* (direct-quadrature) model of the induction motor is given by

$$d\lambda_{dq}/dt + \omega_s \mathbf{J}\lambda_{dq} + (R_r/L_r)\,\lambda_{dq} = (R_r M/L_r)\mathbf{i}_{dq}^{*} \quad (1)$$

$$J d\omega/dt = \tau - f\omega - \tau_L \quad (2)$$

$$d\theta/dt = \omega \quad (3)$$

where $\lambda_{dq}$ is the rotor flux vector, $\mathbf{i}_{dq}^{*}$ is the commanded value of the stator current vector, $\omega$ is the rotor speed, $\theta$ is the rotor angular position, $\tau$ is the electrical torque, $\tau_L$ is the load torque, $\omega_s$ is the slip frequency, $J$ is the rotor moment of inertia, $f$ is the viscous friction coefficient and $\mathbf{J}$ is a two by two skew-symmetric matrix.

---

This work was supported in part by the Office of Naval Research under Grant N00014-96-1-0926.

The current-command passivity-based controller taking into account the magnetic saturation effects is given by

$$\mathbf{i}_{dq}^* := \begin{bmatrix} f_m^{-1}(\lambda_d^*) + \left(L_r/(R_r M)\right)(d\lambda_d^* / dt) \\ \left(n_{ph} L_r/(2n_p M)\right)(\tau^* / \lambda_d^*) \end{bmatrix} \tag{4}$$

and

$$\omega_s := n_{ph} R_r \tau^* / (2\, n_p \lambda_d^{*2}) \tag{5}$$

where $f_m^{-1}$ is the inverse of the magnetization curve function of the induction motor, $\lambda_d^*$ is the reference value of $d$ component of the rotor flux vector, $\tau^*$ is the reference torque, $n_{ph}$ is the number of phases and $n_p$ is the number of pole-pairs. The values of $\lambda_d^*$ and $\tau^*$ are specified by control system designer.

The input-output linearization controller taking into account the magnetic saturation effects can be found in [4, 5].

## III. COMPARISON OF PASSIVITY-BASED METHOD WITH INPUT-OUTPUT LINEARIZATION METHOD

Like the input-out linearization method [3, 4, 5], the passivity-based method allows for the use of time-varying rotor flux references. Thus, the flux level can be adjusted to optimize the torque under the current and voltage bounds (see [6] for torque optimization in induction motors).

In the passivity-based method, the controller does not require knowledge of the rotor flux; therefore, a rotor flux estimator is not needed in contrast with the input-output linearization method. Another disadvantage with the input-output linearization method is that it requires a real-time division by the rotor flux state variable, which is a computational disadvantage.

In the passivity-based method, the discrete values of $1/\lambda_d^*$ have to be stored in the memory of the processor in advance to prevent real-time division by $\lambda_d^*$. This means the passivity-based method requires more memory storage. In the input-output linearization method, implementing the flux estimator requires very little amount of memory (only a couple of lines of programming code).

Like the input-output linearization controller, the passivity-based controller requires knowledge of the speed to achieve speed tracking control. In a typical experimental setup, only position measurements are available through an optical encoder and hence, a speed estimator based on the position measurements must be implemented in real-time to compute the speed.

Finally, unlike the input-output linearization method, in the passivity-based method, the control law is globally defined and is free of singularities [7]. That is, the control law is valid even if the rotor flux is identically zero.

Current-command passivity-based controller (4)-(5) was tested using the same experimental setup as in [4, 5]. Furthermore, for comparison purposes, the same speed/position and flux trajectories as in [4, 5] were considered. The experimental setup consisted of : (i) a 1 horsepower, three-phase induction motor which has significant magnetic saturation, (ii) a Motorola DSP96002 (floating point processor) ADS system, (iii) three 20 kHz PWM amplifiers (±150 Volts and ± 10 Amps) and (iv) a data acquisition board to measure the phase currents and to command the phase voltages to the amplifiers. The sampling frequency was 2.5 kHz. In the experiment, a time-varying speed/position trajectory that requires close to the maximum torque achievable by the motor under the voltage and current constraints was considered [4, 5]. Furthermore, a time-varying optimal flux trajectory was used to force the induction motor to track the mechanical trajectory [4, 5]. Figures 1-3 show some of the results obtained with the passivity-based controller (see [4, 5] for the results obtained with the input-output linearization controller). Fig. 1 is a plot of the estimated speed $\hat{\omega}$ and the reference speed $\omega^*$ (the two are so close that they are indistinguishable in this figure). The speed was estimated using a speed estimator based on the dynamic model of the induction motor and position measurements. Fig. 2 shows the measured position $\theta$ and the reference position $\theta^* = \int_0^t \omega^* dt$ (again, the two are so close that they are indistinguishable in the figure). The position was measured through a 2880 pulse/rev line encoder. The position tracking error $\theta - \theta^*$ is given in Fig. 3. Note that in Fig. 3, the final position error is one encoder count (1 count = $2\pi / 2880$ radians), that is, within the encoder resolution.

From the experimental results, we can conclude that:

1) The use of the passivity-based controller results in reduced position tracking errors as compared with the input-output linearization controller.

2) The passivity-based controller is less sensitive to magnetic saturation than the input-output linearization controller. That is, using linear magnetic model, we can still obtain satisfactory results with the passivity-based controller even though the motor is operated in magnetic saturation region. This is in contrast with the input-output linearization

controller. The reason for the poor performance of an input-output linearization controller based on the linear magnetic model is that the input-output linearization technique relies on an estimate of the rotor flux and an estimator based on the linear magnetic model gives an incorrect value for the flux if saturation occurs in the motor.

3) The input-output linearization controller provides closer tracking of time-varying rotor flux trajectories since the flux tracking control is in the form of closed-loop. Note here that high-performance motion control applications require rapidly changing rotor flux trajectories.

## IV. CONCLUSIONS

The input-output linearization controller provides closer tracking of rapidly changing rotor flux trajectories, which are required for high-performance motion control applications, since the flux tracking control is in the form of closed-loop. However, the experimental results show that the use of the passivity-based controller results in reduced position tracking errors as compared with the input-output linearization controller.

## ACKNOWLEDGMENT

Dr. R. T. Novotnak of Aerotech Inc. is thanked for his continuous help and suggestions.

## REFERENCES

[1] G. Espinosa and R. Ortega, "State observers are unnecessary for induction motor control," *Syst. And Control Letters*, vol. 23, pp. 315-323, 1994.

[2] R. Ortega, P. J. Nicklasson and G. Espinosa, "On speed control of induction motors," *Automatica*, vol. 32, no. 3, pp. 455-460, March 1996.

[3] M. Bodson, J. Chiasson and R. Novotnak, "High-performance induction motor control via input-output linearization," *IEEE Control Systems Magazine*, vol. 14, no. 4, pp. 25-33, August 1994.

[4] M. Bodson, J. Chiasson and R. Novotnak, "High-performance motion control of an induction motor with magnetic saturation," *1995 IEEE CDC*, New Orleans, LA.

[5] R. Novotnak, "Nonlinear control of an induction motor by input/output linearization: Theory and experiment," Ph.D. thesis, University of Pittsburgh, 1995.

[6] M. Bodson, J. Chiasson and R. Novotnak, "A Systematic approach to selecting flux references for torque maximization in induction motors," *IEEE Trans. Control Systems Technology*, vol. 3, no. 4, pp. 388-397, December 1995.

[7] D. Taylor, "Nonlinear control of electric machines: An overview," *IEEE Control Systems Magazine*, vol. 14, no. 6, pp. 41-51, December 1994.

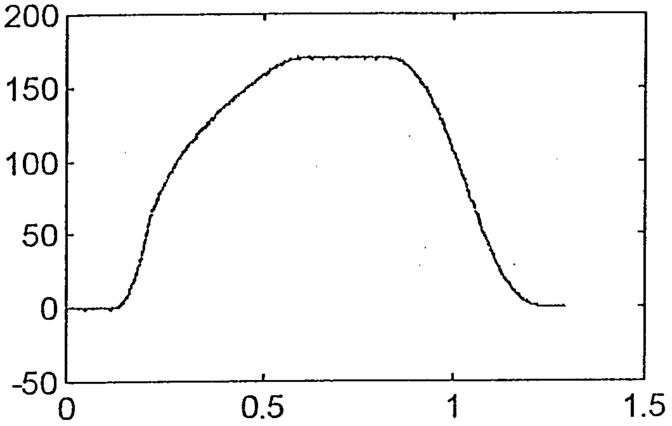

Fig. 1. Estimated (solid) and reference (dashed) speeds in radians per second versus time in seconds.

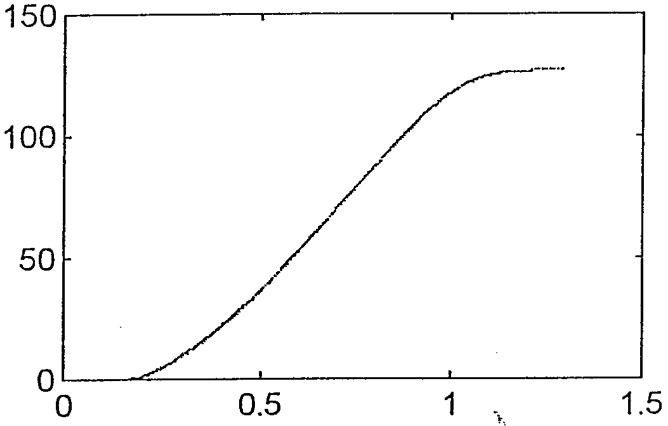

Fig. 2. Measured (solid) and reference (dashed) positions in radians versus time in seconds.

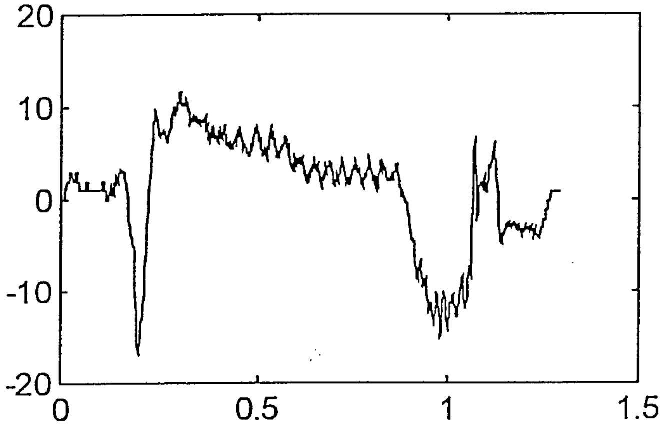

Fig. 3. Position error in encoder counts (1 count = $2\pi / 2880$ radians) versus time in seconds.

# Speed Estimators for Indirect Field-Oriented Control of Induction Motors

Levent U. Gökdere[†], Marwan A. Simaan[‡] and Charles W. Brice[†]

[†]Department of Electrical & Computer Engineering
University of South Carolina
Swearingen 3A80
Columbia, SC 29208
U.S.A.

[‡]Department of Electrical Engineering
University of Pittsburgh
348 Benedum Hall
Pittsburgh, PA 15261
U.S.A.

***Abstract*—Speed estimators for indirect field-oriented control of induction motors are proposed to remove the need of measuring the speed. The speed estimators are based on 1) dynamic model of the induction motor and 2) position measurements obtained through an optical encoder. Experimental results are given to verify the speed estimators.**

## I. INTRODUCTION

Motion controllers for induction motors require precise knowledge of the speed to achieve close tracking of time-varying speed and position trajectories. In applications, the speed is computed through the use of an estimator. This removes the need of measuring the speed.

The easiest way to compute the speed is the discrete differentiation of the position output from an optical encoder. However, at high sample rates and low speeds, this approach results in large errors in the speed estimate. Lorenz *et al.*[1] and Bodson *et al.*[2] have shown, and also experimentally verified, that the use of speed estimators based on the dynamic model of the induction motor results in reduced speed/position tracking errors as compared with an estimator based on the discrete differentiation.

In this paper, we propose, and also experimentally verify, speed estimators for indirect field-oriented control of induction motors. The proposed speed estimators are based on 1) dynamic model of the induction motor, and 2) position measurements obtained through the use of an optical encoder.

## II. SPEED ESTIMATORS FOR INDIRECT FIELD-ORIENTED CONTROL OF INDUCTION MOTORS

Let $\boldsymbol{\lambda}_{\mathrm{dq}}^{\mathrm{T}} := [\lambda_d , \lambda_q]$, $\mathbf{i}_{\mathrm{dq}}^{*\mathrm{T}} := [i_d^* , i_q^*]$, $\omega$, $\theta$ denote, respectively, the transpose of the rotor flux vector, transpose of the commanded stator current vector, rotor speed and rotor position. Then, a current-command *d-q* (direct-quadrature) model of an induction motor is given by

$$\frac{d\boldsymbol{\lambda}_{\mathrm{dq}}}{dt} + \omega_s \mathbf{J}\boldsymbol{\lambda}_{\mathrm{dq}} + \frac{R_r}{L_r}\boldsymbol{\lambda}_{\mathrm{dq}} = \frac{R_r M}{L_r}\mathbf{i}_{\mathrm{dq}}^{*} \tag{1}$$

$$J\frac{d\omega}{dt} = \tau - f\omega - \tau_L \tag{2}$$

$$\frac{d\theta}{dt} = \omega \tag{3}$$

where $\omega_s$ is the slip frequency, $\tau$ is the electrical torque, $R_r$ is the rotor resistance, $L_r$ is the rotor self inductance, $M$ is the mutual inductance, $J$ is the rotor moment of inertia, $f$ is the viscous friction coefficient and $\mathbf{J}$ is a two by two skew-symmetric matrix. The electrical torque is given by

$$\tau = -\frac{2\mathrm{n}_{\mathrm{p}} M}{\mathrm{n}_{\mathrm{ph}} L_r}\boldsymbol{\lambda}_{\mathrm{dq}}^{\mathrm{T}}\mathbf{J}\mathbf{i}_{\mathrm{dq}}^{*} \tag{4}$$

---

This work was supported in part by the Office of Naval Research under Grant N00014-96-1-0926.

where $n_p$ is the number of pole-pairs and $n_{ph}$ is the number of phases.

In the indirect field-oriented control, $\mathbf{i}_{dq}^*$ and $\omega_s$ are the control inputs and defined as

$$\mathbf{i}_{dq}^* := \begin{bmatrix} \lambda_d^* / M + \left(L_r / (R_r M)\right)(d\lambda_d^* / dt) \\ \left(n_{ph} L_r / (2n_p M)\right)(\tau^* / \lambda_d^*) \end{bmatrix} \tag{5}$$

$$\omega_s := \frac{n_{ph} R_r}{2n_p} \frac{\tau^*}{\lambda_d^{*2}} \tag{6}$$

where $\lambda_d^*$ is the $d$ component of reference rotor flux vector $\lambda_{dq}^*$ which is defined as

$$\lambda_{dq}^* := \begin{bmatrix} \lambda_d^* \\ 0 \end{bmatrix} \tag{7}$$

and $\tau^*$ is the reference torque whose value is determined by the control system designer.

Following Lorenz *et al.*[1], Bodson *et al.*[2] introduced, and also experimentally verified, a speed estimator based on the dynamic model of the induction motor. However, the speed estimator in [2] uses the estimated value of the rotor flux. To remove the need of estimating the rotor flux, we modify the speed estimator in [2] as following:

$$\frac{d\hat{\theta}}{dt} = \hat{\omega} + l_1\left(\theta - \hat{\theta}\right) \tag{8}$$

$$\frac{d\hat{\omega}}{dt} = \mu\lambda_d^* i_q - \frac{f}{J}\hat{\omega} + l_2\left(\theta - \hat{\theta}\right) \tag{9}$$

where $\hat{\omega}$ and $\hat{\theta}$ are estimates of the speed and position, respectively, $l_1$, $l_2$ are estimator gains and $\mu := \dfrac{2n_p M}{n_{ph} J L_r}$

In speed estimator (8)-(9), the value of the load torque is assumed to be zero. To incorporate the effects of the load torque, speed estimator (8)-(9) is extended as following [2]:

$$\frac{d\hat{\theta}}{dt} = \hat{\omega} + l_1\left(\theta - \hat{\theta}\right) \tag{10}$$

$$\frac{d\hat{\omega}}{dt} = \mu\lambda_d^* i_q - \frac{f}{J}\hat{\omega} - \frac{\hat{\tau}_L}{J} + l_2\left(\theta - \hat{\theta}\right) \tag{11}$$

$$\frac{d\left(\hat{\tau}_L / J\right)}{dt} = 0 + l_3\left(\theta - \hat{\theta}\right) \tag{12}$$

where $\hat{\tau}_L$ is the estimate of the load torque and $l_3$ is the estimator gain. The estimator models $\dfrac{\hat{\tau}_L}{J}$ as a constant.

Though no analytical proof to guarantee the convergence of $\hat{\omega} \rightarrow \omega$ is given, speed estimators (8)-(9) and (10)-(12) experimentally work well.

## III. EXPERIMENTAL RESULTS

In the experiment, a 6-pole, 1/12 horsepower, two-phase induction motor with a squirrel cage rotor was used. The induction motor is rated at 60 Volts, 2.4 Amps (continuous) and 7300 rpm (revolutions per minute). The motor parameters are $M$ = .011 H, $L_r$ = .014 H, $L_s$ = .014 H, $R_r$ = 3.9 Ω, $R_s$ = 1.7 Ω, $f$ = .00014 N-m/rad/sec, and $J$ = .00011 kg-m$^2$. The hardware setup consisted of a Motorala DSP56001 (fixed point processor) ADS system, two 20 kHz PWM amplifiers (±80 Volts and ±6 Amps), and a data acquisition board to measure the phase currents and to command the phase voltages to the amplifiers. The position measurements were obtained through a 2000 pulse/rev (resolution of $360^\circ/2000 = .18^\circ$) optical encoder. The sampling frequency was 5 kHz.

Applying a simple Euler integration routine, the estimator defined by equations (8) and (9) was implemented on the processor as

$$\hat{\theta}\left((n+1)T\right) = \hat{\theta}(nT) + T\left(\hat{\omega}(nT) + l_1\left(\theta(nT) - \hat{\theta}(nT)\right)\right) \tag{13}$$

$$\hat{\omega}\left((n+1)T\right) = \hat{\omega}(nT) + T\left(\mu\lambda_d^*(nT) i_q(nT) - \frac{f}{J}\hat{\omega}(nT) + l_2\left(\theta(nT) - \hat{\theta}(nT)\right)\right) \tag{14}$$

where $T$ is the sampling period.

Figures 1-4 show the results. Fig. 1 is a plot of the estimated speed $\hat{\omega}$ and the reference speed $\omega^*$ (the two are so close that they are indistinguishable in this figure). The speed tracking error $\hat{\omega} - \omega^*$ is given in Fig. 2. Fig. 3 shows the measured position $\theta$ and the reference position $\theta^* = \int_0^t \omega^* dt$ (again, the two are so close that they are indistinguishable in the figure). The position tracking error $\theta - \theta^*$ is given in Fig. 4. Note that in Fig. 4, the final position error is one encoder count (1 count = $2\pi / 2000$ radians), that is, within the encoder resolution. The position error during the entire run is within four encoder counts. In brief, a close tracking of the time-varying speed and position trajectories was achieved.

In addition to these experimental results, the same speed estimator was implemented replacing $i_q$ with $i_q^*$ in (14) and similar results were obtained.

Finally, speed estimator (10)-(12) was experimentally verified.

## IV. CONCLUSIONS

In the indirect field-oriented control of induction motors, the use of speed estimators based on the dynamic model of the induction motor results in close tracking of time-varying speed and position trajectories.

## ACKNOWLEDGMENT

The same experimental setup as in [2] was used. Dr. R. T. Novotnak of Aerotech Inc. is thanked for his continuous help and suggestions.

## REFERENCES

[1] R. D. Lorenz and K. W. Patten, "High-resolution velocity estimation for all-digital, ac servo drives," *IEEE Trans. on Industry Applications*, vol. 27, pp. 701-705, July/August 1991.

[2] M. Bodson, J. Chiasson and R. Novotnak, "Nonlinear speed observer for high-performance induction motor control," *IEEE Trans. on Industrial Electronics*, vol. 47, pp. 337-343, August 1995.

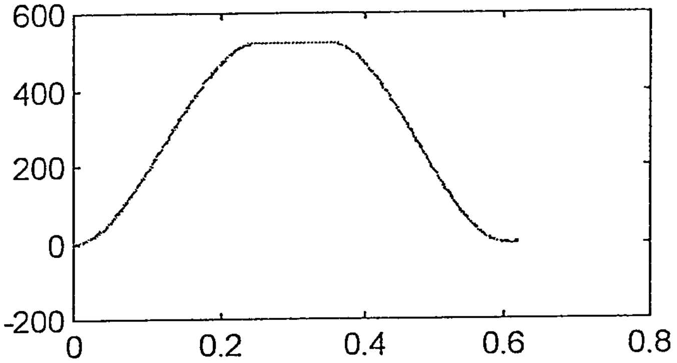

Fig. 1. Estimated (solid) and reference (dashed) speeds in radians per second versus time in seconds.

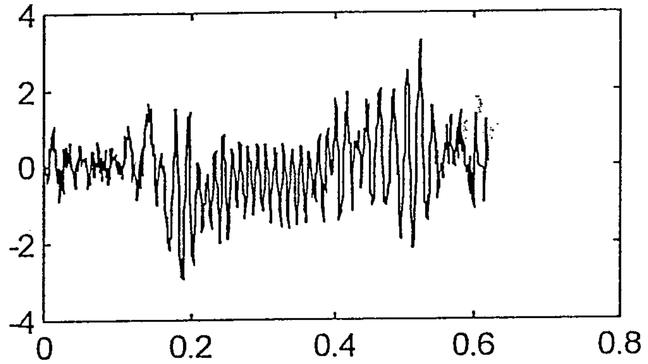

Fig. 2. Speed error in radians per second versus time in seconds.

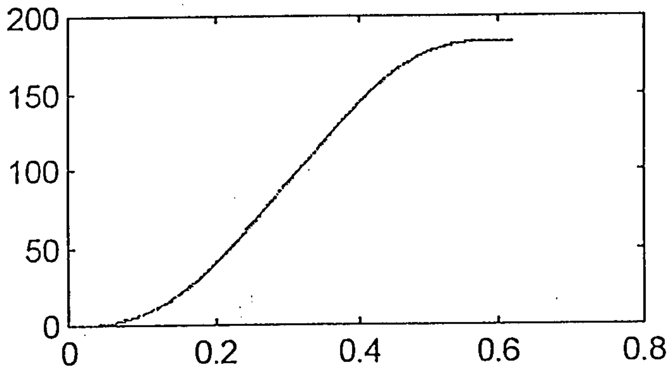

Fig. 3. Measured (solid) and reference (dashed) positions in radians versus time in seconds.

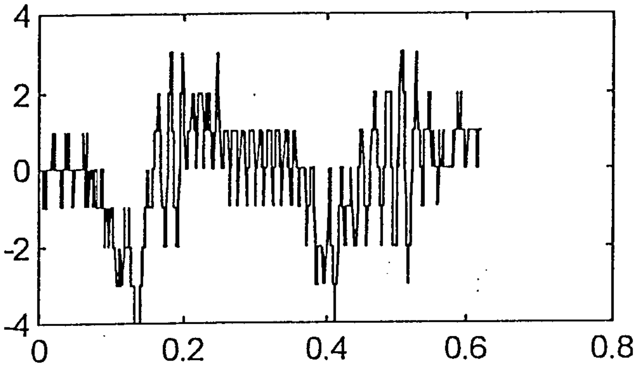

Fig. 4. Position error in encoder counts (1 count = $2\pi / 2000$ radians) versus time in seconds.

# A Passivity-Based Controller for High-Performance Motion Control of Induction Motors

Levent U. Gökdere[†], Marwan A. Simaan[‡] and Charles W. Brice[†]

[†]Department of Electrical & Computer Engineering
University of South Carolina
Swearingen 3A80
Columbia, SC 29208
U.S.A.

[‡]Department of Electrical Engineering
University of Pittsburgh
348 Benedum Hall
Pittsburgh, PA 15261
U.S.A.

***Abstract*—In this paper, we design, and also experimentally verify, a passivity-based controller that forces an induction motor which has significant magnetic saturation to track a time-varying optimal flux trajectory. As a result, we are able to provide close tracking of a time-varying speed/position trajectory that requires close to the maximum torque achievable by the motor within the voltage and current limits.**

## I. INTRODUCTION

In high-performance motion control applications, selection of the rotor flux reference is an important issue since the maximum torque achievable by the motor depends on the rotor flux level. At low speeds, the rotor flux is held constant at some maximum value within the voltage and current limits to extract the maximum torque from the motor. At higher speeds, the rotor flux level is decreased to prevent the stator voltages from saturating. In brief, the selection of time-varying, rather than constant, rotor flux reference is essential to obtain maximum performance from the motor without saturating the stator voltages.

Bodson, Chiasson and Novotnak [1, 2] and Novotnak [3] introduced time-varying optimal flux trajectories for induction motors to obtain maximum positive torque during acceleration (motor mode) and minimum negative torque during deceleration (generator mode) under the voltage and/or current constraints.

In this paper, we design, and also experimentally verify, a passivity-based controller that forces the induction motor to track the time-varying optimal flux trajectory without knowledge of the rotor electrical state variables (i.e., rotor fluxes or currents). As a result, we are able to provide close tracking of a time-varying speed/position trajectory, which requires close to the maximum torque achievable by the motor within the voltage and current limits, without having to measure (or estimate) the rotor electrical state variables. The passivity-based controller in this paper takes into account the magnetic saturation effects.

## II. CURRENT-COMMAND PASSIVITY-BASED CONTROLLER FOR INDUCTION MOTORS

A current-command *d-q* model of the induction motor can be given by

$$\frac{d\boldsymbol{\lambda}_{dq}}{dt} + \left(\frac{R_r}{L_r}\right)\boldsymbol{\lambda}_{dq} = \left(\frac{R_r M}{L_r}\right)\mathbf{i}^*_{dq} \tag{1}$$

$$J\frac{d\omega}{dt} = \tau - f\omega \tag{2}$$

$$\frac{d\theta}{dt} = \omega \tag{3}$$

where $\boldsymbol{\lambda}_{dq}$ is the rotor flux vector, $\mathbf{i}^*_{dq}$ is the reference value of the stator current vector, $\omega$ is the motor angular speed, $\theta$ is the motor angular position, $\tau$ is the electrical torque (the torque produced by the motor), $R_r$ is the rotor

---

This work was supported in part by the Office of Naval Research under Grant N00014-96-1-0926.

resistance, $L_r$ is the rotor inductance, $M$ is the mutual inductance, $J$ is the rotor moment of inertia and $f$ is the viscous friction coefficient. The electrical torque is given by

$$\tau = -\frac{2n_p M}{n_{ph} L_r}\boldsymbol{\lambda}_{dq}^T \mathbf{J}\mathbf{i}_{dq}^* \tag{4}$$

where $n_p$ is the number of pole-pairs, $n_{ph}$ is the number of phases and $\mathbf{J}$ is a two by two skew-symmetric matrix.

In the above model, the electrical variables are defined in a special $d$-$q$ reference frame whose angular position with respect to the fixed stator reference frame is $n_p\theta$.

The current-fed induction motor version of the passivity-based controller developed by Espinosa and Ortega [4] and Ortega, Nicklasson and Espinosa [5, 6] is given by

$$\mathbf{i}_{dq}^* = \begin{bmatrix} \cos\alpha & -\sin\alpha \\ \sin\alpha & \cos\alpha \end{bmatrix} \begin{bmatrix} \dfrac{\beta(t)}{M} + \dfrac{L_r}{R_r M}\dfrac{d\beta(t)}{dt} \\ \dfrac{n_{ph}L_r}{2n_p M}\dfrac{\tau^*}{\beta(t)} \end{bmatrix} \tag{5}$$

where $\alpha$ is the solution of

$$\frac{d\alpha}{dt} = \frac{n_{ph}R_r}{2n_p}\frac{\tau^*}{\beta(t)^2} \tag{6}$$

In (5) and (6), $\beta(t)$ is the magnitude of the reference rotor flux vector and $\tau^*$ is the reference torque. The reference rotor flux vector is defined as

$$\boldsymbol{\lambda}_{dq}^* = \beta(t)\begin{bmatrix} \cos\alpha \\ \sin\alpha \end{bmatrix}$$

and the reference torque is chosen as

$$\begin{aligned} \tau^* = {} & J\frac{d\omega^*}{dt} + f\omega^* - Jk_1\int_0^t \left(\theta - \theta^*\right)dt \\ & - Jk_2\left(\theta - \theta^*\right) - Jk_3\left(\omega - \omega^*\right) \end{aligned}$$

where $\theta^*$ and $\omega^* = \dfrac{d\theta^*}{dt}$ are the reference values of $\omega$ and $\theta$, respectively. Feedback gains $k_1$, $k_2$ and $k_3$ are positive constants.

It can be shown that current-command passivity-based controller (5) provides exponential tracking of time-varying speed/position and flux trajectories.

The current-command passivity-based controller is equivalent to the well-known indirect (strictly feedforward) field-oriented controller (the *de facto* industry standard) [5]. Implementations of the indirect field-oriented controllers based on the linear and saturated magnetic models of the induction motor can be found in [7] and [8], respectively.

## III. INCORPARATION OF MAGNETIC SATURATION EFFECTS INTO PASSIVITY-BASED CONTROLLER

Levi, Vukosavic and Vuckovic [8], Heinemann and Leonhard [9], Sullivan and Sanders [10], and Sullivan, Kao, Acker and Sanders [11] developed field-oriented controllers based on saturated magnetic models of the induction motor. An input-output linearization controller, which takes the saturation effects into account, was designed by Novotnak, Chiasson and Bodson [2] and Novotnak[3].

In [2, 3, 9], saturation is assumed to be entirely in the main flux path of the induction motor. That is, the change in the mutual inductance due to saturation in the magnetic material is considered and the changes in the stator and rotor leakage factors are neglected. Using the same approach, we can rearrange passivity-based controller (5) as

$$\mathbf{i}_{dq}^* = \begin{bmatrix} \cos\alpha & -\sin\alpha \\ \sin\alpha & \cos\alpha \end{bmatrix} \begin{bmatrix} f_m^{-1}(\beta(t)) + \dfrac{L_r}{R_r M}\dfrac{d\beta(t)}{dt} \\ \dfrac{n_{ph}L_r}{2n_p M}\dfrac{\tau^*}{\beta(t)} \end{bmatrix} \tag{7}$$

where $f_m^{-1}(\cdot)$ is the inverse of the magnetization curve function of the induction motor. In (7), the nominal values of $L_r$ and $M$ are used. This is reasonable since $\dfrac{L_r}{M} = 1 + \sigma_r$, where $\sigma_r$ is the rotor leakage factor [12], and the change in $\sigma_r$ due to the saturation is neglected.

For the values of $\beta(t)$ which remain in the linear magnetic region, $f_m^{-1}(\beta(t)) = \dfrac{\beta(t)}{M}$ with $M$ constant so that (7) reduces to (5).

Assuming the rotor flux tracks its reference value while the motor is in the linear magnetic region, then, the flux tracking error remains zero even if the magnitude of the rotor flux vector is increased to the magnetic saturation regions.

## IV. SPEED ESTIMATOR

The passivity-based controller requires the knowledge of the motor speed and position to achieve speed/position tracking control. In a typical experimental setup, only position measurements are available through an optical encoder and hence, a speed estimator must be implemented in real-time to estimate the speed.

The easiest way to estimate the speed is the numerical differentiation of the position outputs from the optical encoder. That is,

$$\hat{\omega} = \frac{\theta(nT) - \theta((n-1)T)}{T} \tag{8}$$

where $\hat{\omega}$ is the estimated speed, $T$ is the sample period and $\theta(nT)$ is the position measurement at $t = nT$. However, a $2880$ pulses per revolution (resolution of $\frac{2\pi}{2880}$ radians) encoder is used in the experimental setup and computing $\hat{\omega}$ by (8) may cause an error in the speed estimate up to $\frac{2\pi}{2880T}$.

Lorenz and Patten [13] and Bodson, Chiasson and Novotnak [14] proposed, and also experimentally verified, speed estimators based on the dynamic model of the motor and the positions measurements. In this paper, the following speed estimator was used [13] :

$$\frac{d\hat{\theta}}{dt} = \hat{\omega} + l_1\left(\theta - \hat{\theta}\right) \tag{9}$$

$$\frac{d\hat{\omega}}{dt} = \frac{\tau^*}{J} - \frac{f}{J}\hat{\omega} + l_2\left(\theta - \hat{\theta}\right) \tag{10}$$

where, again $\hat{\omega}$ is the estimate of the speed, $\hat{\theta}$ is the estimate of the position, and $l_1$, $l_2$ are the estimator gains.

Fig. 1 shows a block diagram for the passivity-based control of the induction motor.

## V. OPTIMAL FLUX TRAJECTORY

Bodson, Chiasson and Novotnak [1, 2] and Novotnak [3] introduced, and also experimentally verified, time-varying optimal flux trajectories to extract maximum positive torque during acceleration (motor mode) and minimum negative torque during deceleration (generator mode) from the induction motor under the voltage and/or current constraints.

In this paper, $\beta(t)$, the magnitude of the rotor flux vector, was chosen as the solution of

$$\frac{d\beta(t)}{dt} = M\eta\left(-f_m^{-1}(\beta(t)) + \frac{1}{\mu\beta(t)\delta_{sopt}(\omega^*)}\frac{d\omega^*}{dt}\right) \tag{11}$$

where $\eta := \frac{R_r}{L_r}$, $\mu := \frac{2n_p M}{n_{ph} J L_r}$ and $\delta_{sopt}(\omega^*)$ is the solution to the saturated magnetics optimal torque problem [2, 3].

## VI. EXPERIMENTAL RESULTS

Current-command passivity-based controller (7) was tested on an experimental setup which consisted of (i) a 3-phase, 6-pole, 1-Hp, squirrel cage induction motor, (ii) a Motorola DSP96002 (floating point processor) ADS system, (iii) a data acquisition board, and (iv) three 20 kHz PWM amplifiers ($\pm 150$ Volts and $\pm 10$ Amperes). The parameters of the induction motor are listed in Table I. The position measurements were obtained through a $2880$ pulses per revolution (resolution of $\frac{2\pi}{2880}$ radians) line encoder.

TABLE I

INDUCTION MOTOR PARAMETERS

| | |
|---|---|
| $M$ | 0.225 H |
| $L_r$ | 0.244 H |
| $L_s$ | 0.244 H |
| $R_r$ | 2.1 Ω |
| $R_s$ | 1.85 Ω |
| $J$ | 0.0185 N-m-s$^2$ |
| $f$ | 0.0 N-m/rad/sec |

Fig. 2 shows the magnetization curve of the induction motor which was determined by Novotnak [3].

In the experiment, a point-to-point position move was carried out in which the motor was accelerated from the rest to a speed of $170$ radians per second in 0.486 seconds and decelerated from $170$ radians per second to $0$ radians per second in 0.449 seconds. This type of mechanical trajectory was chosen since it requires $90\%$ of the maximum positive torque achievable by the motor used in the experiment under the voltage and current limits [2, 3].That is, the motor must produce close to the maximum torque to accelerate from the rest to $170$ radians per second in 0.486 seconds. The magnitude of the reference rotor flux vector was chosen as the solution of (11).

Fig. 3 shows estimated speed $\hat{\omega}$ and reference speed $\omega^*$ (the two are so close that they are indistinguishable in the figure). Fig. 4 is a plot of speed error $\hat{\omega} - \omega^*$. Fig. 5 shows measured position $\theta$ and reference position $\theta^* = \int_0^t \omega^* dt$ ( the two are so close that they are indistinguishable in the figure). Fig. 6 is a plot of position error $\theta - \theta^*$. Note that in Fig. 6, the final position error is one encoder count ($1$ count $= \frac{2\pi}{2880}$ radians), that is, within the encoder resolution. The position error during the entire move is within $21$ encoder counts. In brief, a close tracking of time-varying speed and position trajectories was achieved.

To achieve the maximum torque at the beginning of the move, the rotor flux must be at its maximum value [2, 3]. Therefore, the rotor flux was ramped up from zero to its maximum value of $1.1$ Webers before the motor was commanded to move at $t = 0.125$ seconds. Fig. 7 shows the magnitudes of the estimated rotor flux vector and reference rotor flux vector. The rotor flux vector was estimated off-line by solving the following equation:

$$\frac{d\hat{\lambda}_{dq}}{dt} + \left(\frac{R_r M}{L_r}\frac{f_m^{-1}\left(\left|\hat{\lambda}_{dq}\right|\right)}{\left|\hat{\lambda}_{dq}\right|}\right)\hat{\lambda}_{dq} = \left(\frac{R_r M}{L_r}\right)\mathbf{i}_{dq} \quad (12)$$

where the components of $\mathbf{i}_{dq}$ were collected from the experiment.

## VII. CONCLUSIONS

In this paper, we designed, and also experimentally verified, a current-command passivity-based controller that forces an induction motor which has significant magnetic saturation to track time-varying speed/position and flux trajectories without knowledge of the rotor electrical state variables. Also, we used a speed estimator, which is based on the dynamic model of the induction motor and the position measurements, to remove the need of measuring the motor speed.

## ACKNOWLEDGMENT

The same experimental setup as in [2, 3] was used. Dr. R. T. Novotnak of Aerotech Inc. is thanked for his continuous help and suggestions.

## REFERENCES

[1] M. Bodson, J. N. Chiasson, and R. T. Novotnak, "A systematic approach to selecting flux references for torque maximization in induction motors," *IEEE Trans. Control Systems Technology*, vol. 3, pp. 388-397, December 1995.

[2] R. T. Novotnak, J. Chiasson, and M. Bodson, "High performance motion control of an induction motor with magnetic saturation," in *Proceedings of the 34th IEEE Conference on Decision & Control*, pp. 2145-2150, December 1995, New Orleans, LA.

[3] R. T. Novotnak, "Nonlinear control of an induction motor by input/output linearization: Theory and experiment," Ph.D. thesis, University of Pittsburgh, 1995.

[4] G. Espinosa and R. Ortega, "State observers are unnecessary for induction motor control," *Systems and Control Letters*, vol. 23, pp. 315-323, 1994.

[5] R. Ortega, P. J. Nicklasson, and G. Espinosa, "On speed control of induction motors," *Automatica*, vol. 32, pp. 455-460, March 1996.

[6] G. Espinosa, P. J. Nicklasson, and R. Ortega, "Control of induction motors in the field weakening region," in *Proceedings of the 34th IEEE Conference on Decision & Control*, pp. 2151-2152, December 1995, New Orleans, LA.

[7] A. Nabae, K. Otsuka, H. Uchino, and R. Kurosawa, "An approach to flux control of induction motors operated with variable-frequency power supply," *IEEE Trans. Industry Applications*, vol. 16, pp. 342-349, May/June 1980.

[8] E. Levi, S. Vukosavic, and V. Vuckovic, "Saturation compansation schemes for vector controlled induction motor drives," in *Proceedings of the IEEE Power Electronics Specialists Conference*, pp. 591-598, June1990, San Antonio, TX.

[9] G. Heinemann and W. Leonhard, "Self-tuning field-oriented control of an induction motor drive, in *Proceedings of the International Power Electronics Conference*, pp. 465-472, April 1990, Tokyo, Japan.

[10] C. R. Sullivan and S. R. Sanders, "Modeling the effects of magnetic saturation on electrical machine control systems," in *Proceedings of the IFAC Nonlinear Control System Design Symposium*, pp. 136-143, June 1992, Bordeaux, France.

[11] C. R. Sullivan, C. Kao, B. M. Acker and S. R. Sanders, "Control systems for induction machines with magnetic saturation," *IEEE Trans. Industrial Electronics*, vol. 43, pp. 142-152, February 1996.

[12] W. Leonhard, *Control of Electrical Drives.* New York: Springer-Verlag, 1985.

[13] R. D. Lorenz and K. W. Patten, "High-resolution velocity estimation for all-digital, ac servo drives," *IEEE Trans. Industry Applications*, vol. 27, pp.701-705, July/August 1991.

[14] M. Bodson, J. Chiasson, and R. Novotnak, "Nonlinear speed observer for high-performance induction motor control," *IEEE Trans. Industrial Electronics*, vol. 47, pp.337-343, August 1995.

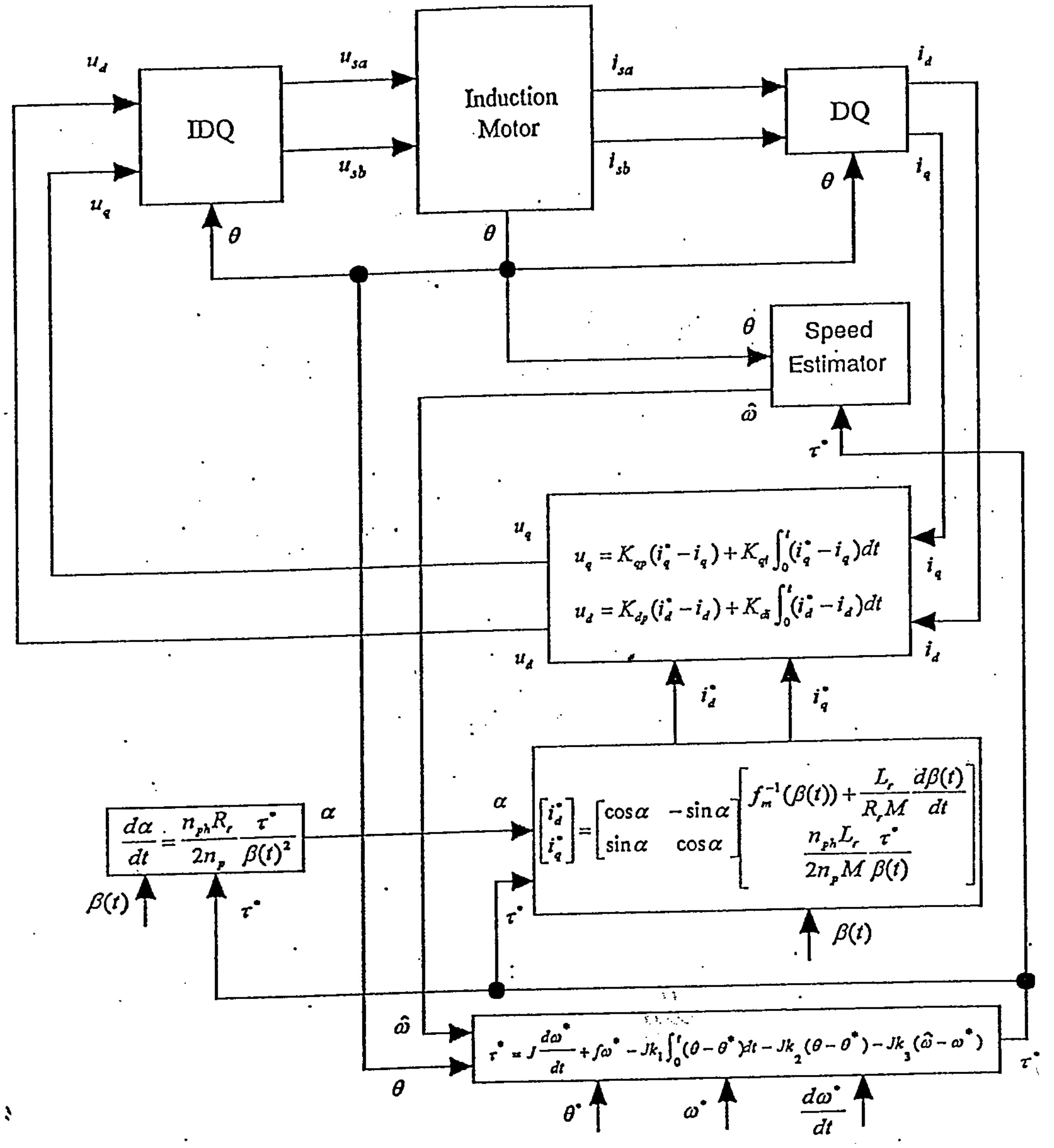
Induction Motor
IDQ
DQ
Speed Estimator
$u_d$
$u_q$
$u_{sa}$
$u_{sb}$
$i_{sa}$
$i_{sb}$
$i_d$
$i_q$
$\theta$
$\hat{\omega}$
$\tau^*$
$u_q = K_{qp}(i_q^* - i_q) + K_{qi}\int_0^t (i_q^* - i_q)dt$
$u_d = K_{dp}(i_d^* - i_d) + K_{di}\int_0^t (i_d^* - i_d)dt$
$i_d^*$
$i_q^*$
$\frac{d\alpha}{dt} = \frac{n_{ph}R_r}{2n_p}\frac{\tau^*}{\beta(t)^2}$
$\alpha$
$\beta(t)$
$\begin{bmatrix} i_d^* \\ i_q^* \end{bmatrix} = \begin{bmatrix} \cos\alpha & -\sin\alpha \\ \sin\alpha & \cos\alpha \end{bmatrix} \begin{bmatrix} f_m^{-1}(\beta(t)) + \frac{L_r}{R_r M}\frac{d\beta(t)}{dt} \\ \frac{n_{ph}L_r}{2n_p M}\frac{\tau^*}{\beta(t)} \end{bmatrix}$
$\tau^* = J\frac{d\omega^*}{dt} + f\omega^* - Jk_1\int_0^t(\theta - \theta^*)dt - Jk_2(\theta - \theta^*) - Jk_3(\hat{\omega} - \omega^*)$
$\theta^*$
$\omega^*$
$\frac{d\omega^*}{dt}$

Fig. 1. Block diagram for the current-command passivity-based control of the induction motor.

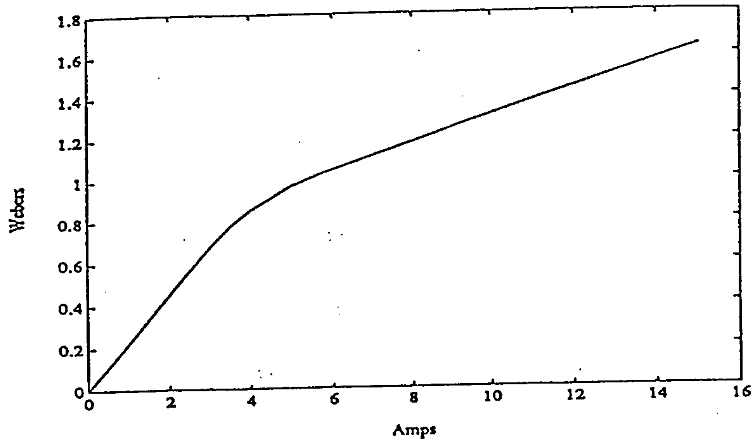

Fig. 2. Magnetization curve of the induction motor.

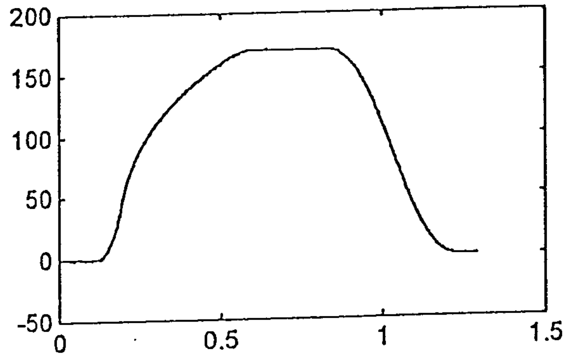

Fig. 3. Estimated (solid) and reference (dashed) speeds in radians per second versus time in seconds.

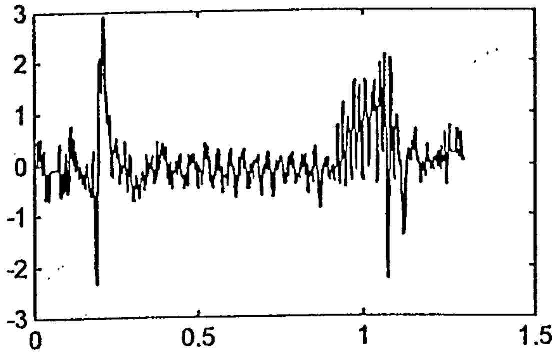

Fig. 4. Speed error in radians per second versus time i seconds.

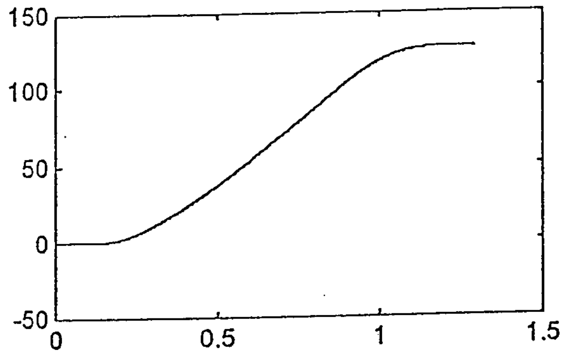

Fig. 5. Measured (solid) and reference (dashed) positions in radians versus time in seconds.

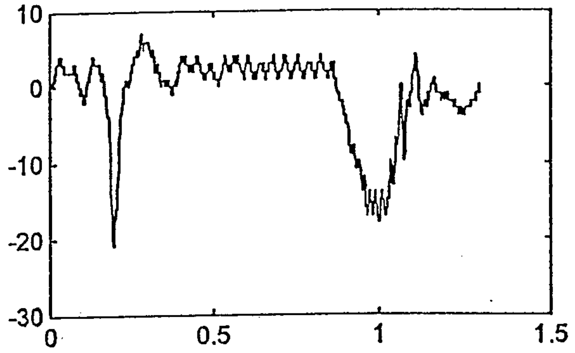

Fig. 6. Position error in encoder counts versus time i seconds (1 count = $2\pi/2880$ radians).

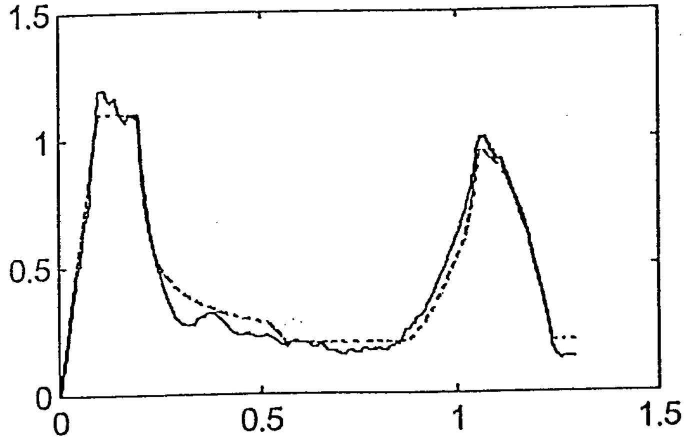

Fig. 7. $\left|\hat{\lambda}_{dq}\right|$ (solid) and $\left|\lambda^{*}_{dq}\right|$ (dashed) in Webers versus time in seconds.